

<b>REPORT DOCUMENTATION PAGE</b>			Form Approved OMB NO. 0704-0188	
Public Reporting burden for this collection of information is estimated to average 1 hour per response, including the time for reviewing instructions, searching existing data sources, gathering and maintaining the data needed, and completing and reviewing the collection of information. Send comment regarding this burden estimates or any other aspect of this collection of information, including suggestions for reducing this burden, to Washington Headquarters Services, Directorate for Information Operations and Reports, 1215 Jefferson Davis Highway, Suite 1204, Arlington, VA 22202-4302, and to the Office of Management and Budget, Paperwork Reduction Project (0704-0188), Washington, DC 20503.				
1. AGENCY USE ONLY (Leave Blank)		2. REPORT DATE - May 7, 2004		3. REPORT TYPE AND DATES COVERED Final Report March 1, 2001 - February 28, 2004
4. TITLE AND SUBTITLE Sub-100nm, Maskless Deep-UV Zone-Plate Array Lithography			5. FUNDING NUMBERS DAAD19-01-0330	
6. AUTHOR(S) Professor Henry I. Smith				
7. PERFORMING ORGANIZATION NAME(S) AND ADDRESS(ES) Massachusetts Institute of Technology Research Laboratory of Electronics 77 Massachusetts Avenue Cambridge, MA 02139-4307			8. PERFORMING ORGANIZATION REPORT NUMBER	
9. SPONSORING / MONITORING AGENCY NAME(S) AND ADDRESS(ES)  U. S. Army Research Office P.O. Box 12211 Research Triangle Park, NC 27709-2211			10. SPONSORING / MONITORING AGENCY REPORT NUMBER  <del>DAAD19-01-0330-1</del>  42428.2-EL	
11. SUPPLEMENTARY NOTES The views, opinions and/or findings contained in this report are those of the author(s) and should not be construed as an official Department of the Army position, policy or decision, unless so designated by other documentation.				
12 a. DISTRIBUTION / AVAILABILITY STATEMENT  Approved for public release; distribution unlimited.			12 b. DISTRIBUTION CODE	
13. ABSTRACT (Maximum 200 words)  Semiconductor lithography is at a crossroads. With mask set costs in excess of \$1M, long mask-turn-around times, and tools that are characterized by their inflexibility and skyrocketing costs (in excess of \$20M), there is need for a new paradigm in lithography. Zone-Plate-Array Lithography (ZPAL) bypasses some of the most pressing problems of current lithography equipment by offering a maskless lithography tool that is scalable, flexible and low cost. It is the departure from a century-old tradition of refractive optics, in combination with the use of advanced micromechanics and fast computing, that enables ZPAL to open up a new application space in lithography. This report covers in detail all levels of the ZPAL system, from the micromechanics, to the diffractive optics, to the control system. Special emphasis is placed on the design, fabrication and characterization of high-numerical-aperture diffractive-optical elements for lithography and imaging. The results achieved provide conclusive evidence that diffractive optics in general, and zone plates in particular, are capable of state-of-the-art lithography and are extendable to the limits of the lithography process. As a result, ZPAL represents the most promising approach to low cost maskless lithography for the semiconductor industry and other areas of nanoscale science and engineering.				
14. SUBJECT TERMS			15. NUMBER OF PAGES	
			16. PRICE CODE	
17. SECURITY CLASSIFICATION OR REPORT UNCLASSIFIED	18. SECURITY CLASSIFICATION ON THIS PAGE UNCLASSIFIED	19. SECURITY CLASSIFICATION OF ABSTRACT UNCLASSIFIED	20. LIMITATION OF ABSTRACT  UL	

## Final Report

Army Research Office  
Grant No. DAAD19-01-1-0330

---

### Introduction:

Lithography is clearly a cornerstone of the semiconductor industry and the information revolution. High-resolution lithography is crucial to a wide variety of devices, from integrated circuits (IC) for computers, to filters for optical communication, to high-density magnetic-information storage. Since the invention of the transistor and the fabrication of the first IC, lithography's goal has been to print reliably smaller and smaller features, leading not only to a high-degree of integration, but also to a dramatic increase in performance, as illustrated in Fig.1-1.

Lithography development has traditionally been dominated by the needs of the semiconductor industry. As a result of the ever-increasing demand for finer features, improved alignment, and higher throughputs within the industry, a rapid acceleration in the complexity and the cost of lithography tools has taken place, causing a bifurcation in the lithography world. Fewer and fewer customers can afford lithographic tools that, although capable of high-resolution and high-throughput, are inherently inflexible and based on a manufacturing model involving millions of chips with fixed designs. As a consequence, customers requiring production alternatives capable of quick-turn-around customized chips have been left out of a market that is increasingly consolidated by a

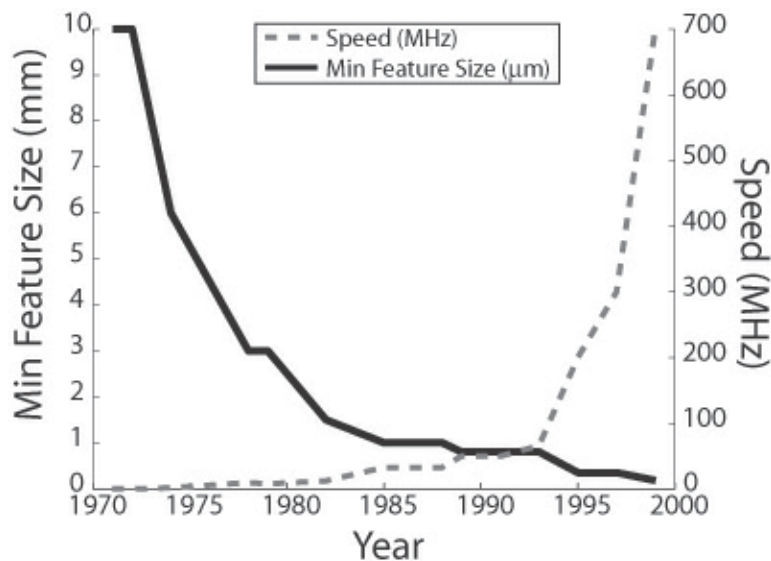


**Figure 1 - 1.** Keeping up with Moore's Law. The graph shows a correlation between the ability to print smaller and smaller features through lithography and the increase in performance (with speed as a metric) of microprocessors (in this case Intel's). Note that being able to get into the sub-1  $\mu\text{m}$  regime has provided a fantastic increase in performance.

handful of semiconductor multinationals. It is in this context of international consolidation and narrow production alternatives that the work presented here acquires its relevance. With the development of a flexible, high-resolution affordable maskless lithography technique, a solution is finally offered to the currently disenfranchised sectors that require advanced nanofabrication processes.

## C h a p t e r 2

### The ZPAL Concept

Zone-Plate-Array Lithography (ZPAL), bypasses some of the most pressing problems of current lithography equipment by developing a maskless lithography tool that will be scalable, flexible and cost-effective. It is the departure from a century-old tradition of refractive optics, in combination with the use of advanced micromechanics and fast computing, that enables ZPAL to open up a new space in the lithography world.

#### 2.1 From Refractive to Diffractive Optics

The advantages of diffractive optics in maskless lithography include: uniformity, high quality, reliability, and cost-effectiveness. *Diffractive* optics are manufactured using highly reliable, mass-production-compatible lithography-based planar-fabrication technology. In contrast, *refractive* optics, even to this day, require both technological sophistication and craftsmanship (including hand grinding and polishing, and macroscopic assembly). *Refractive* optics have the added disadvantage that materials

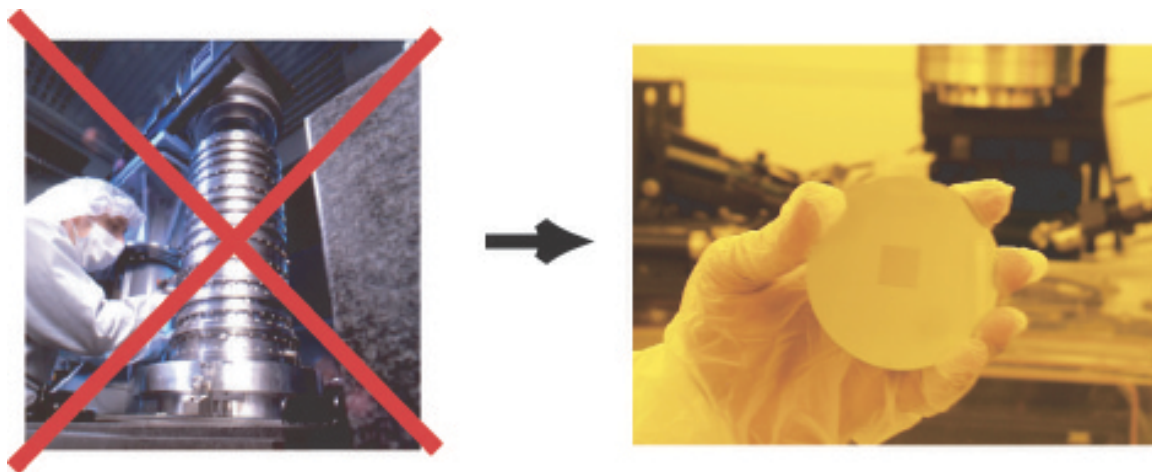


**Figure 2 - 1.** Vision of the power of employing diffractive optics for lithography. Diffractive optics are manufactured using nanofabrication, with techniques similar to those used in chip production

become opaque as wavelength is decreased. In contrast, *diffractive* optics, such as zone plates, can operate at any wavelength; even neutral atoms have been focused [Ref 2-1]. Furthermore, by employing large arrays of diffractive optics, the tradeoff between image resolution and field size can be bypassed. This tradeoff is at the core of much of the complexity and cost of current lithography and microscopy systems. An image of the vision underlying our push for diffractive optics is illustrated in Figure 2-1.

## 2.2 ZPAL System Overview

In conventional semiconductor lithography, glass masks are illuminated with laser light and their image is reduced through a lens onto the substrate to define circuitry. As feature sizes are pushed toward 100 nm and below, lithography is becoming increasingly costly and difficult. Zone-plate-array lithography (ZPAL) is a considerably simpler approach. ZPAL would not have been possible even a few years ago. It is made possible by inexpensive, high-speed computation, advances in nanofabrication, and micromechanics. ZPAL replaces the "printing press" of traditional lithography with a technology more akin to that of a laser printer.



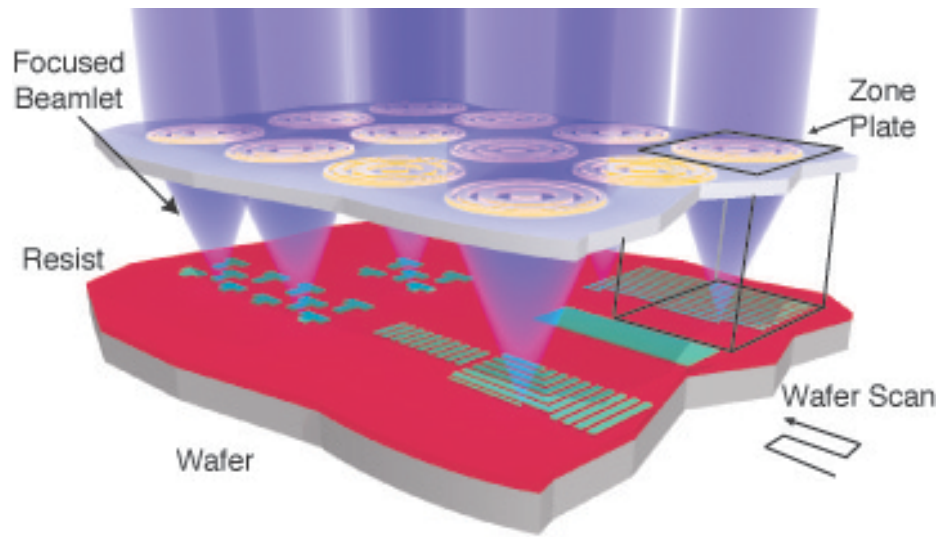


**Figure 2 - 2.** Schematic of zone-plate-array lithography (ZPAL). An array of Fresnel zone plates focuses radiation beamlets onto a substrate. The individual beamlets are turned on and off by upstream micromechanics as the substrate is scanned under the array. In this way, patterns of arbitrary geometry can be created. The resolution of the system is determined by the numerical aperture of the zone plates and the wavelength of light.

Instead of a single, massive lens, an array of one million microfabricated Fresnel-zone-plate lenses is used, each focusing a beam of light onto the substrate. A computer-controlled array of micromechanical mirrors turns the light to each lens on or off as the stage is scanned under the array, thereby printing the desired pattern in a dot-matrix fashion. No mask is required, enabling designers to rapidly change circuit designs.

Zone Plate Array Lithography (ZPAL) is depicted schematically in Figure 2-2. An array of diffractive optical elements (Fresnel zone plates in this case) focuses incident radiation into an array of spots on a substrate. The spot size is approximately equal to the minimum feature size of a zone plate (i.e. the outer zone width). By using micromechanics to independently turn on or off the radiation to each zone plate, and simultaneously scanning the substrate underneath, arbitrary patterns can be generated. ZPAL combines the advantages of maskless lithography with the high throughput of parallel writing provided by an array of zone plates.

ZPAL was first proposed by H. I. Smith in 1996 [Ref 2-2] in a paper which detailed a basic writing strategy and presented a design for a ZPAL system utilizing 4.5 nm radiation from an undulator on a compact synchrotron. Subsequent work presented

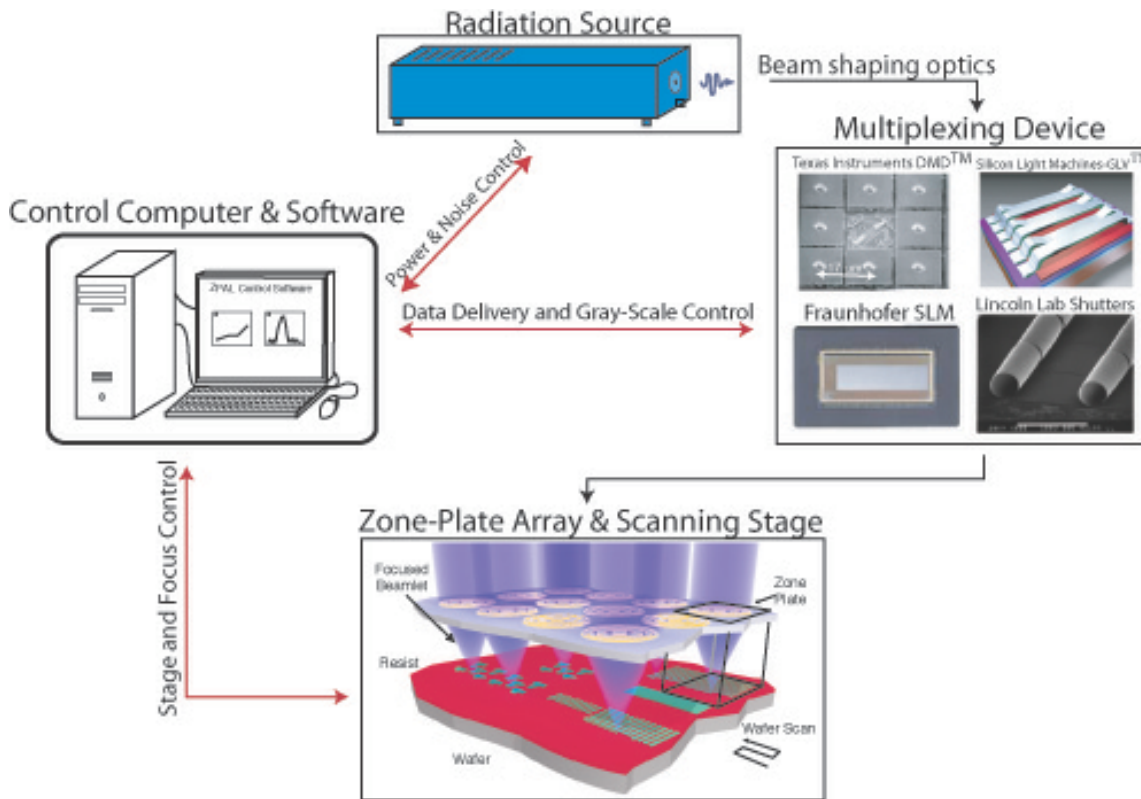


**Figure 2 - 3.** Core elements of a ZPAL system.

resist exposures using phase zone plates in the deep UV ( $\lambda = 193$  nm) and demonstrated rudimentary parallel patterning with a zone-plate array [Ref 2-3,Ref 2-4]. A ZPAL system was then developed at the NanoStructures Lab at MIT that provided the first demonstration of multiplexed lithography with ZPAL [Ref 2-5].

## 2.3 Key Technical Challenges

The area of research covered in this report is multidisciplinary in scope, ranging from nanofabrication, to optical and mechanical design (including extensive use of MEMS), to circuit and software design. This section will discuss some of the key technical challenges.

The core elements of a ZPAL system are depicted in Figure 2-3. The system is comprised of four major components: a radiation source, an array of micromechanical elements, a zone plate array and a scanning stage. A control computer with custom designed hardware and software will provide the necessary control and feedback for the successful integration of the four core ZPAL components.

### 2.3.1 The Radiation Source

Because zone plates can focus any type of radiation of interest in lithography, from blue, to deep UV, to x-rays, and even neutral atoms [Ref 2-1], the zone plate design and the multiplexing can be scaled with the

wavelength to meet future needs (as is the case with many other forms of lithography, by using light of shorter wavelengths, higher resolution can be achieved). While very short wavelengths are appealing in terms of the resolution that can be achieved with them, their use can be costly and flexibility is often sacrificed. A much better solution at the present stage of development of ZPAL technology is to employ tabletop laser sources at UV that don't require the system to operate in vacuum (with the added advantage that glass and fused silica optical elements can still be employed). For these reasons, we have developed ZPAL technology at near UV with lasers operating at 442nm (He-Cd gas laser) and at 400nm (a solid-state laser). The system is capable of achieving sub-wavelength resolution and therefore deep sub-micron lithographic structures.

### 2.3.2 The Micromechanics

It is apparent from Figure 2-2 that if we want each optical element to write independently we have to be able to independently control the illumination of each zone plate. This control is provided by upstream micromechanics. The reason we need micromechanics is because the area of a unit cell, which is the area over which we want to control the illumination, ranges from 10 to 100  $\mu\text{m}^2$ . There are a variety of options available, ranging from the use of micromirrors (such as the DMD manufactured by Texas Instruments [Ref 2-6]), to diffraction based MEMS (such as the Grating Light Valve (GLV) manufactured by Silicon Light Machines [Ref 2-7]) to micro-shutters (prototyped by MIT-Lincoln Laboratory).

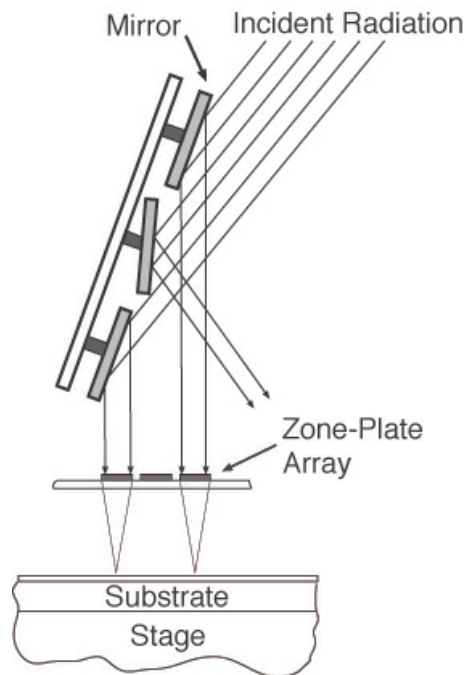


**Figure 2 - 4.** Schematic of a micromirror array for ZPAL. Radiation is modulated by means of micromirrors, which can tilt to two angles by means of electrostatic deflection.

The use of micromirrors for ZPAL is depicted schematically in Figure 2-4. The idea is to place a micromirror array in the path of the radiation beam, so that each mirror, with proper alignment and use of optics, will be responsible for the illumination of an individual zone plate. This is possible because the mirrors can tilt to two positions responding to the control of a computer, and hence, when they are latched in one position the light will be reflected to the appropriate zone plate, and when in the other the radiation will be deflected out of the imaging system.

An alternative micromechanical solution is the Silicon Light Machines Grating Light Valve™ (GLV™) linear array. Although the GLV™ has a smaller number of pixels (1,088) compared to the DMD™ micromirror array (~1 million or more), the higher speed of operation of the GLV™ (20ns rise time as opposed to 20 μs for the DMD™), the fact that gray-scaling is built in, and its diffractive mode of operation (making it compatible with shorter wavelengths, possibly even down to 157nm) have the potential of making the GLV™ a superior choice for ZPAL.

The GLV™ is a micromechanical phase grating consisting of parallel rows of reflective Al ribbons. Alternate rows of ribbons can be pulled down electrostatically in a

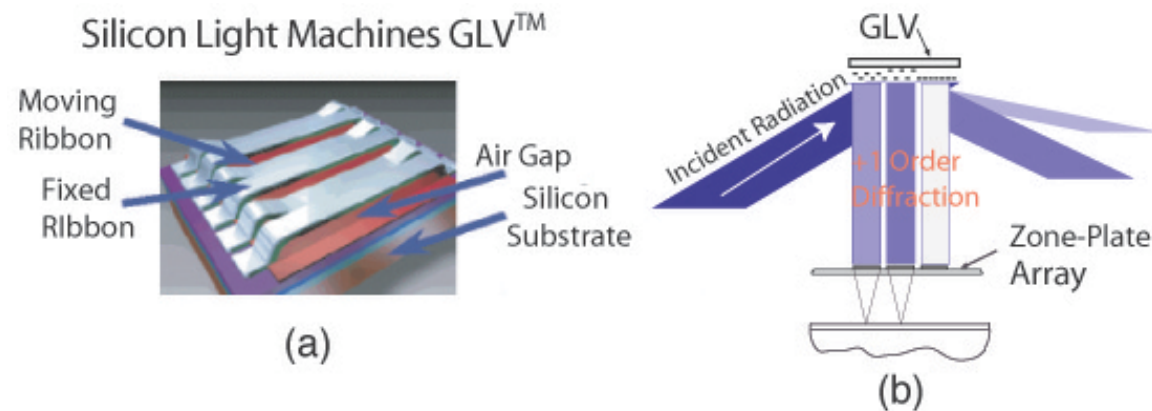


**Figure 2 - 5.** The Silicon Light Machines Grating Light Valve™ (GLV™) (a) one pixel of the GLV™ (each pixel can be thought of as a “mini-grating”), (b) intended implementation of the GLV™ with our linear array of zone plates indicating gray scaling.

controlled manner to create diffraction effects on incident light. When no force is applied, all the ribbons lie in the same plane. If illuminated, incident light will be reflected from their surfaces at the same angle at which it is incident. When alternate ribbons are pulled down, a grating structure is created. In this state, diffraction will produce light at an angle different from that of the incident light.

By alternating between these two states (i.e. from flat ribbons to a grating structure) the GLV™ can switch light ON and OFF. Furthermore, by tuning the applied electrostatic force, the depth to which the ribbons are pulled down can be controlled, impacting the amount of light diffracted into the first order. Grayscale of the incident light can be achieved in this manner. Each of the 1088 pixels present in the linear array can accept

8-bits of grayscaling (256 levels). Since the motion involved in switching the pixels of the GLV™ is small (one-quarter wavelength), the GLV™ is capable of very high switching speeds, with a rise time from the ON to the OFF position of only 20ns [Ref 2-7]. One pixel of the linear array is depicted schematically in Figure 2-5(a), along with the intended implementation in ZPAL, Fig. 2-5(b).

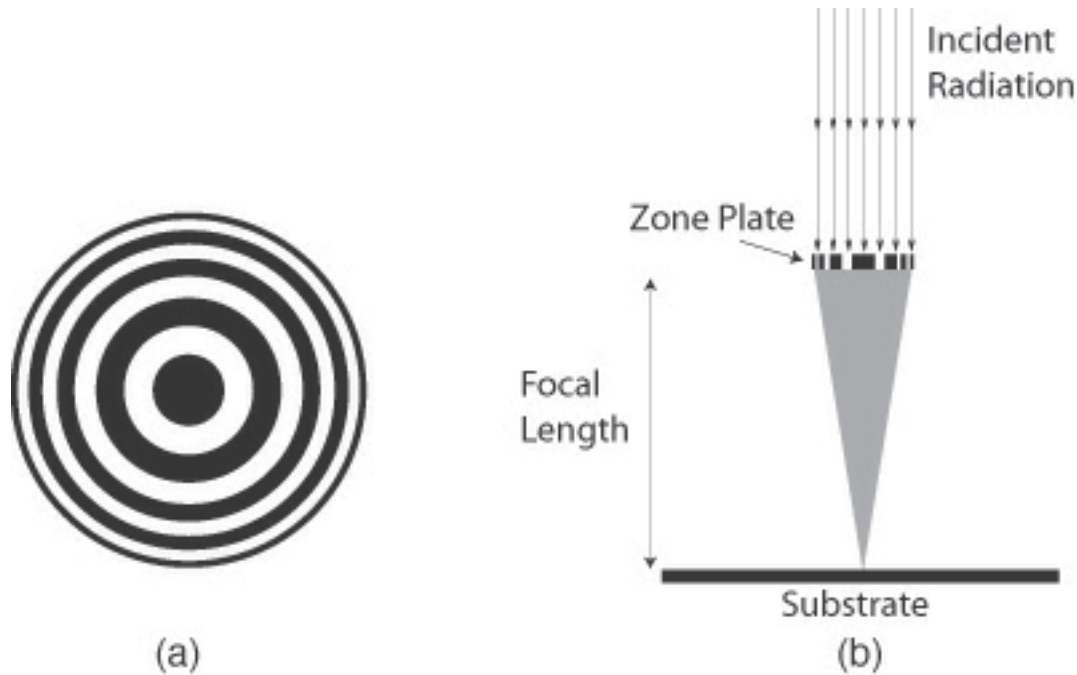


**Figure 2 - 6.** Zone Plates. (a) Top view (b) Cross section

### 2.3.3 The Zone Plate Array

A zone plate is a diffractive optical element of circular symmetry in which the local spatial period depends on the radius in such a way, that the first-order diffracted radiation from any radius value crosses the axis at the same point, the focal length. This concept is illustrated in Figure 2-6. It goes without mention that the zone plates are the core of ZPAL, and that they are the innovative idea of a completely new paradigm in lithography. Chapters 4, 5 and 6 will deal extensively with the theory, design, fabrication, and characterization of these elements.

### 2.3.4 The Scanning Stage

The last of the four major components of ZPAL is a precision movable stage. Its function is to raster scan the substrate over a zone plate unit cell in order to produce the desired patterns. Alternative scanning strategies are also feasible, perhaps desirable, as described, for example, by Feldman [Ref 2-8].

This report presents lithographic results obtained by continuous scan ZPAL. The scanning system utilizes a piezo-actuated stage from Physik Instrumente (model P-770). This model offers a scan range of  $200 \times 200 \mu\text{m}^2$  with a positioning accuracy of less than 10nm. Capacitive sensors are used for position sensing, with custom-built velocity-feedback circuits implemented to enable continuous-velocity scanning.

The stage scans the substrate in a raster fashion. In terms of writing strategy, it is important to differentiate the concepts of spot size, determined by  $w_{\min} = k_1 \lambda / NA$ , and that of pixel size, which refers to the address grid (i.e. the locations on the substrate where spots are flashed at appropriately controlled doses). Based on simulations and previous work [Ref 2-9], 5-bits of grayscale in combination with an address grid of one half the spot size is sufficient to control linewidths to better than 10%. Furthermore, this writing strategy allows all edges of the exposed features to be controlled independently and accurately to a fraction of the spot size.

## References for Chapter 2

[Ref 2-1] Doak RB et. al, Physical Review Letters, 83 (21): 4229-4232, 1999

[Ref 2-2] Henry I. Smith. *A proposal for maskless, zone-plate-array lithography*. J.Vac.Sci.Technol. B, 14(6):4318-4322, Nov/Dec 1996.

[Ref 2-3]Ihsan J. Djomehri,*Zone-Plate-Array Lithography in the Deep UV*, Master's Thesis, Massachusetts Institute of Technology,1998

[Ref 2-4]Ihsan J. Djomehri,T.A.Savas, and Henry I. Smith, *Zone-plate-array lithography in the deep ultraviolet*, J.Vac.Sci.Technol. B, 16(6):3426-3429,Nov/Dec 1998.

[Ref 2-5] D. J. D. Carter, Dario Gil, Rajesh Menon, Mark K. Mondol, H. I. Smith and E. H. Anderson, *Maskless parallel patterning with zone-plate-array lithography*, J.Vac.Sci.Technol. B 17 (6), Nov/ Dec, 1999

[Ref 2-6] Digital Light Processing World Wide Web site: <http://www.dlp.com/>

[Ref 2-7]White papers on Silicon Light Machines GLV technology:  
<http://www.siliconlight.com/htmlpgs/glvtechframes/glvmainframeset.html>

[Ref 2-8] Feldman, M, OSA Proceedings on Soft X-Ray Projection Lithography, 1993, Vol.18

[Ref 2-9] Dario Gil, Rajesh Menon, D. J. D. Carter and H. I. Smith, *Lithographic Patterning and Confocal Imaging with Zone Plates*, J.Vac.Sci.Technol B 18 (6), 2881-2885, Nov/ Dec, 2000

## Extras:

[Ref] Henry I. Smith., *Robust Sub-100 nm Maskless Lithography with Sub-1nm Accuracy*, Proposal to the Army Research Center, 1998

<b>Chapter 2. The ZPAL Concept .....</b>	<b>2</b>
2.1 From Refractive to Diffractive Optics .....	2
2.2 ZPAL System Overview .....	3
2.3 Key Technical Challenges.....	5
2.3.1 The Radiation Source .....	5
2.3.2 The Micromechanics .....	6
2.3.3 The Zone Plate Array .....	8
2.3.4 The Scanning Stage.....	8

### List of Figures:

Figure 2 - 1. Vision of the power of employing diffractive optics for lithography. ....	3
Figure 2 - 2. ZPAL Schematic .....	4
Figure 2 - 3. Core elements of a ZPAL system.....	5
Figure 2 - 4. Schematic of a micromirror array for ZPAL. ....	6
Figure 2 - 5. The Silicon Light Machines Grating Light Valve™ (GLV™).....	7
Figure 2 - 6. Zone Plates. (a) Top view (b) Cross section .....	8

## C h a p t e r    3

# Zone Plate Design and Fabrication

### 3.1 History of Zone Plates

The invention of zone plates originates from the work of Fresnel (1788-1827) on diffraction. In 1808 the Paris Academy proposed the theme of diffraction for a prize, and Fresnel presented a paper [Ref 3-1] synthesizing Huygens's (1629-1695) principle and Young's (1773-1829) Principle of Interference. The resulting theory is now known as the Huygens-Fresnel Principle. Despite strong opposition from Poisson, a member of



the jury and an ardent critic of the wave theory of light, Fresnel won the prize from a jury also composed of Pierre Laplace, Jean B. Biot, Dominique F. Arago, and Joseph L. Gay-Lussac [Ref 3-2].

The paper is worth examining, for it presents the foundations necessary for zone plates to be invented. The most important concept that concerns us in Fresnel's paper is the idea of what later would be called Fresnel Zones. Let's examine where they come from.

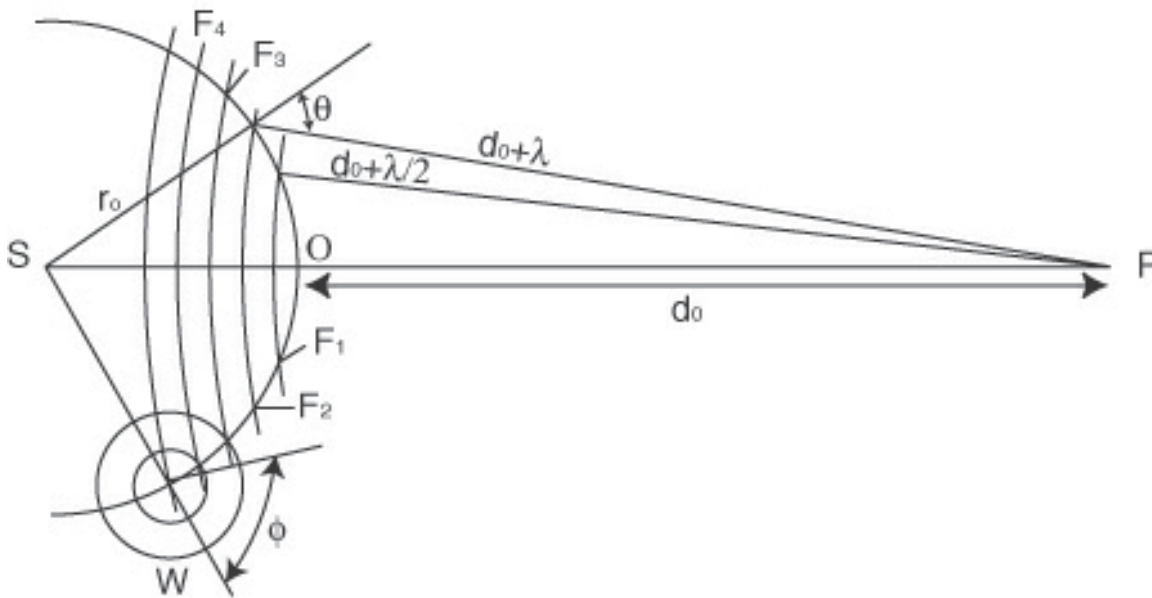


**Figure 3- 1.** The Fresnel Zones

Fresnel's treatment of diffraction was based on the idea of Huygens principle, which states that each point of a wavefront may be regarded as the center of a system of secondary disturbances that gives rise to spherical wavelets. The position of the wavefront at any later time is defined by the common tangent of these waves. The breakthrough came from the realization that by taking into account the mutual interference that takes place between these secondary waves, diffraction effects could be explained. It is in the theoretical development of this explanation of diffraction that the Fresnel zones arise, and as an extension, the Fresnel zone plate.

Fig. 3-1 shows a wavefront arising from a point source at S. Fresnel maintained that the effect of the point source at a point where the light disturbance is to be determined, P, could be found either by allowing this wavefront to proceed until it reaches P, or by dividing the wavefront into small areas so that each one can be assumed to generate one wavelet (see W in the graph). Each of these wavelets then produces an effect at P, which can be summed according to the principle of superposition to give the total effect at P of the point source. Obviously, these two methods should yield identical results, but the second allows the calculation of the effect at P if edges or apertures obscure parts of the wavefront.



Going back to Fig. 3-1 we can see that the shortest distance between the wavefront and P is  $d_0$  ( $=OP$ ). Other parts of the wavefront will cause disturbances at P that are out of phase with that produced by the nearest part (at O) due the difference in length that the light has to travel. This can be analyzed by constructing a set of concentric spheres centered at P with radius  $d_0 + n \lambda/2$ , with  $n = 1, 2, 3, \dots$ . These spheres cut the wavefront at  $F_1, F_2, F_3$ , etc. Let's focus on the first of these circles,  $F_1$ . Within this circle the phase of the disturbances arriving at P varies between 0 and  $\pi$ . If we now look at circle  $F_2$  we see that the disturbances arriving at P from the area between these two circles ( $F_1$  and  $F_2$ ) will have a phase that will vary between  $\pi$  and  $2\pi$ .

Further annuli or zones can be constructed, each having an effect at P varying by  $180^\circ$  of phase. These hypothetical zones are known as **Fresnel zones**. The size of these zones is dependant upon the wavelength of the light used as well as the distance to the point P. It's easy to prove that when we have a spherical wavefront, and the wavelength of the light used is small compared to  $d_0$ , the areas of the zones are all very nearly equal to  $\pi d_0 \lambda$ , and the radii of their boundaries are proportional to the square roots of natural numbers.

As the areas of these zones are equal, we can assume that they produce the same number of secondary wavelets from equal element areas. However, Fresnel had to introduce a correction here. If each wavelet radiated uniformly in all directions, in addition to generating a forward traveling wave, there would also be a reverse wave traveling back towards the source. No such wave is found experimentally, so the radiation pattern of the secondary waves had to be modified. Fresnel introduced an *obliquity* or *inclination factor*, which is a function of  $\theta$  (see Fig. 3-1), in order to describe the directionality of the secondary emissions. To be historically correct, Fresnel postulated the need for it, but it was Kirchhoff who provided an expression for it [Ref 3-2].

We are now at a position to deduce what happens at P. We had assumed that each zone produces the same number of secondary wavelets since they all have equal areas, but, taking into account the obliquity factor, which increases as we go out from the central zone, we can see that the amplitude at P due to the zones will gradually diminish from the central zone outwards. From the way in which the zones have been constructed,

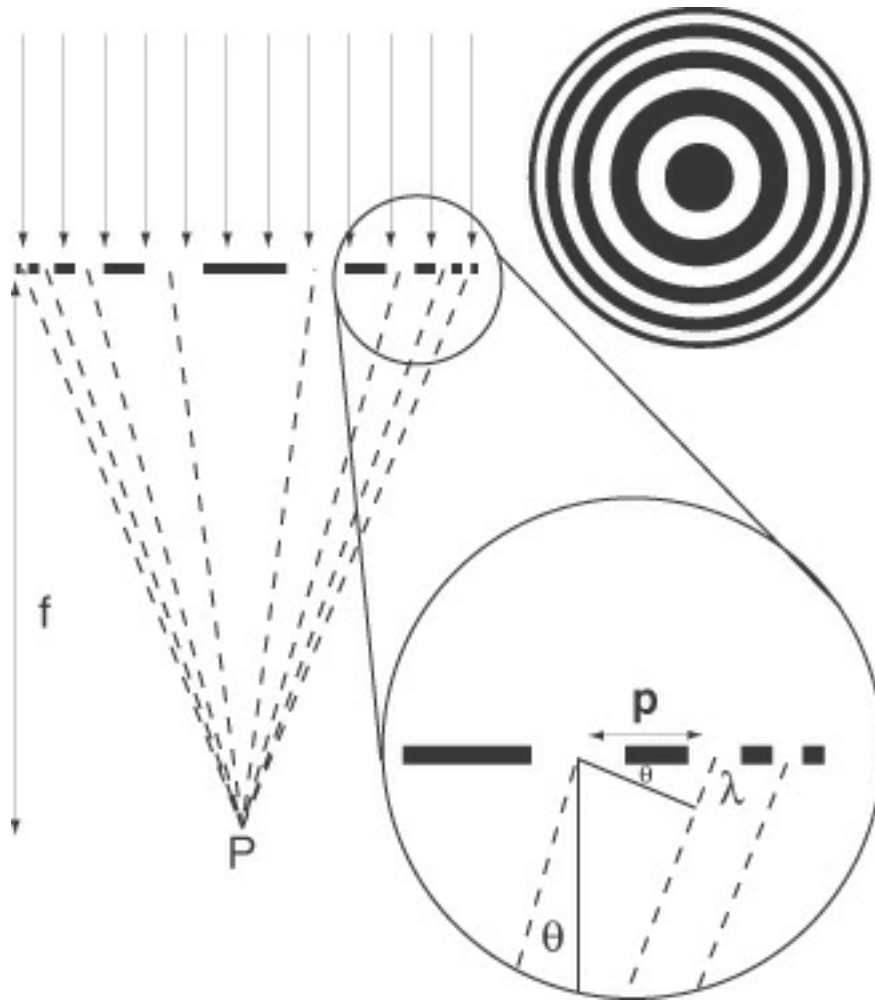


**Figure 3- 2.** Zone plate schematic. Zone plates, like gratings, work by diffraction.

it follows that the effect at P from any one zone is exactly opposite in phase from that of an adjacent zone.

With these concepts in mind, and avoiding the analytical work in favor of doing it just for zone plates in the following section, we are ready to make the jump to the concept of a zone plate. In the previous considerations it was noted that successive Fresnel zones nullify each other due to variations in phase. If we prevent the light propagation from alternate zones from reaching P, that from the remaining zones, since they will all arrive with the same phase, will add up constructively and produce a greatly increased illumination at this point. This concept is illustrated in Fig. 3-2.

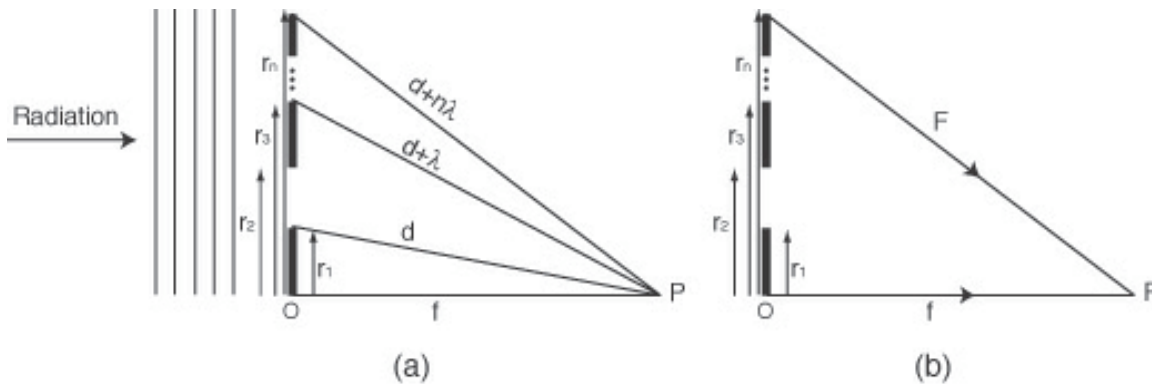


**Figure 3- 3. Zone plate geometry**

An even higher increase in light concentration would be obtained if, instead of blocking alternate zones (amplitude zone plate), the phases of the wavelets from these zones were changed by  $\pi$ . The disturbances from all zones would then arrive at P with the same phase. This is called a phase zone plate.

Let's now take a look in a more quantitative manner at how a zone plate works.

### 3.2 Zone Plate Theory

#### 3.2.1 Geometry of Zone Plates

Fig. 3-3 presents a schematic cross section along a zone plate radius, with a ray diagram indicating the lengths of possible light paths from an incoming plane wave to P. The objective is to derive the necessary expressions for the radii of the zone boundaries. Since we are trying to model a zone plate, we will assume that the total optical path to P via the  $n$ th zone differs by  $\pm\lambda/2$  from the path through the corresponding point on a neighboring zone. To avoid confusions, it should be noted that zones are constituted both by open and closed annuli. If the zone plate is to work efficiently, the difference in path length between any point in an open zone and the corresponding point in the next open zone should be equal to the wavelength of the light used,  $\lambda^1$ .

We determine the values of  $r_n$  by demanding that the optical paths  $F$  and  $f$  (see Fig. 3-3) differ by  $\frac{n\lambda}{2}$ ,

so

$$F = f + \frac{n \cdot \lambda}{2} \quad 3 - 1$$

Since  $r_n^2 = F^2 - f^2$ , we find that

---

<sup>1</sup> There are two basic types of zone plates: amplitude and phase. If alternate zones are blocked, an amplitude zone plate is created. If alternate zones are appropriately phase-shifted, the diffraction emanating from all zones will constructively interfere at the focal spot. These are phase zone plates.

$$r_n = \sqrt{n \cdot \lambda \cdot f + n^2 \cdot \frac{\lambda^2}{4}} \quad 3 - 2$$

The term  $n^2\lambda^2/4$ , which represents the spherical aberration of zone plates, can be ignored for short-wavelength low numerical aperture designs, in which  $f \gg n\lambda/2$ . The numerical aperture of a zone plate, defined as the sine of the maximum angle that gets diffracted by the optic, is given by

$$NA = \sin \theta = \frac{R}{\sqrt{R^2 + f^2}} \quad 3 - 3$$

where  $R$  is the radius of the zone plate and  $f$  is the focal length. Solving for  $f$  in equation 3 – 3, an expression for the focal length of a zone plate in terms of the numerical aperture and the radius can be obtained.

$$f = \frac{R}{NA} \sqrt{1 - NA^2} \quad 3 - 4$$

The above equations are all that are needed to design basic zone plates. The following sequence was used for all the zone plates designed under this grant. First, a *numerical aperture - focal length* combination is chosen. Then, using equation 3-4 and solving for  $R$ , the outer radius of the zone plate is calculated. The next step consists in finding the total number of zones that the resulting optic will have. This can be obtained by rearranging equation 3-2 to obtain:

$$N = \frac{-f + \sqrt{f^2 + R^2}}{\lambda/2} \quad 3 - 5$$

Having  $N$ , the total number of zones, the radii of each of the zones can be calculated by iteratively solving equation 3 - 2 until  $n = N$ .

### *An Intuitive way to Think about Zone Plates*

A useful and intuitive way to think about how a zone plate works is provided by analyzing its behavior in terms of spatial frequencies. The idea behind this approach is to think of a zone plate as an optical element that is created by a combination of a large number of small-area gratings of many different periods. Each one of these gratings generates a plane wave, and each one of them can be described with a characteristic spatial frequency. At the focal plane of the optic, all plane waves interfere, forming a spot. Let's see how such a spot is formed.

### Interference of two plane waves

Let's begin by analyzing what happens when two monochromatic plane waves interfere on a surface, as depicted in Figure 3-4 (a-b). The electric field for both waves is oriented along the  $\hat{z}$  direction (Fig. 3-4(b)), with magnitude  $E_0$ . The phase offset of each wavefront ( $\pi_1, \pi_2$ ) is specified with respect to the origin. The total field at the point of interference is obtained by the superposition of the incoming fields:

$$\begin{aligned}\vec{E} &= E_0 \hat{z} \left[ e^{-jk_{x1}x} e^{-jk_{y1}y} e^{+jk_{z1}z} e^{j\pi_1} + e^{+jk_{x2}x} e^{-jk_{y2}y} e^{+jk_{z2}z} e^{j\pi_2} \right] \\ &= E_0 \hat{z} \cdot e^{-j\frac{1}{2}(k_{x1}x + k_{y1}y - k_{z1}z - \pi_1 - k_{x2}x + k_{y2}y - k_{z2}z - \pi_2)} \\ &\quad \cdot 2 \cos \left[ \frac{1}{2}(k_{x1}x + k_{y1}y - k_{z1}z + k_{x2}x - k_{y2}y + k_{z2}z - \pi_1 + \pi_2) \right]\end{aligned} \quad 3-6$$

The intensity of the aerial image is proportional to  $|\vec{E}|^2$ , and is given by:

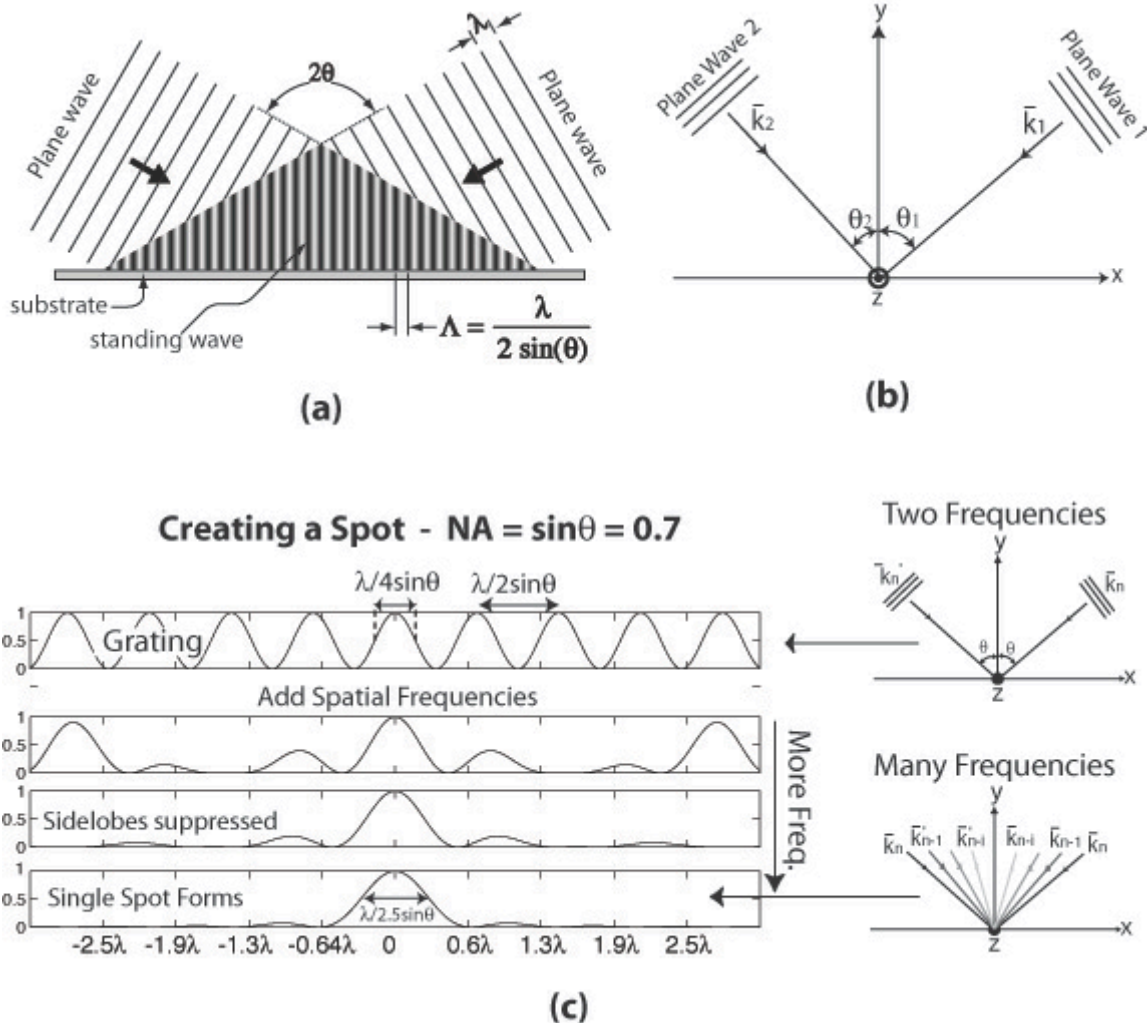


**Figure 3- 4.** When two plane waves interfere standing wave is formed. The period of the resulting periodic pattern is related to the illuminating wavelength and the angle of intersection. By adding plane waves coming from different angles (each angle can be associated with a distinct spatial frequency), a single spot can be formed.

$$\begin{aligned}
|\vec{E}|^2 &= 4E_0^2 \cos^2\left(\frac{1}{2}(k_{x1}x + k_{y1}y - k_{z1}z + k_{x2}x - k_{y2}y + k_{z2}z - \pi_1 + \pi_2)\right) \\
&= 2E_0^2 \left[1 + \cos\left((k_{x1} + k_{x2})x + (k_{y1} - k_{y2})y + (k_{z2} - k_{z1})z - \pi_1 + \pi_2\right)\right]
\end{aligned}
\tag{3-7}$$

For the purpose of this analysis, let's ignore the magnitude of the intensity (this is of little importance if the intensity of this field is to be used for lithography, since the amount of energy that is deposited in the resist can be varied at will simply by changing the exposure time). The important quantity that is to be extracted from equation 3-7 is the periodicity of the resulting standing wave, since this will determine the maximum resolution achievable. In principle, the standing wave should form a perfectly *spatially coherent* periodic pattern. By spatial coherence we mean that by knowing the position of one local minima in the standing wave, one could predict the positions of all the other minima. The spatial coherence of the standing wave is of course related to the spatial and temporal coherence of the interference beams, which is in turn related to the bandwidth and spatial character of the illuminating source.

Equation 3-7 can be rewritten as

$$\begin{aligned}
|\vec{E}|^2 &= 2E_0^2 \left[1 + \cos(\kappa_x x + \kappa_y y + \kappa_z z - \varphi)\right] \\
&= 2E_0^2 \left[1 + \cos(\vec{\kappa} \cdot \vec{r} - \varphi)\right]
\end{aligned}
\tag{3-8}$$

where  $\varphi = \pi_1 - \pi_2$ ,  $\kappa_x = k_{x1} + k_{x2}$ ,  $\kappa_y = k_{y1} - k_{y2}$ , and  $\kappa_z = k_{z2} - k_{z1}$ .

The grating period is hence given by

$$p = \frac{2\pi}{|\vec{\kappa}|} \tag{3-9}$$

In the simple case illustrated in Fig. 3-4(a-b), both incoming waves propagate in the x-y plane, hence  $k_{z1} = k_{z2} = 0$ . Both  $\pi_1$  and  $\pi_2$  are set to zero. From the figure  $k_{x1} = k \sin \theta_1$  and  $k_{x2} = k \sin \theta_2$ , where  $k = 2\pi/\lambda$ . The aerial image at  $y = 0$  is the given by

$$|\vec{E}|^2 = 2E_0^2 \left[1 + \cos(k(\sin \theta_1 + \sin \theta_2)x)\right] \tag{3-10}$$

Therefore the period of the grating is

$$p = \frac{2\pi}{k(\sin \theta_1 + \sin \theta_2)} = \frac{\lambda}{\sin \theta_1 + \sin \theta_2} \quad 3 - 11$$

If  $\theta_1 = \theta_2 = \theta$  Eq. 3-11 reduces to the following expression

$$p = \frac{\lambda}{2 \sin \theta} \quad 3 - 12$$

Since angles of  $\theta \approx 90^\circ$  are possible geometrically with plane waves, the limiting period that can be created is  $\lambda/2$  (this correspond to a numerical aperture of 1). A grating, with a periodicity determined by equation 3-12, created with a NA =  $\sin \theta = 0.7$  is depicted at the top of Fig.3-4(c).

The effect of adding more spatial frequencies is illustrated in Fig.3-4(c). Different plane waves arriving at the origin with different angles interfere in such a way that only the central peak gets reinforced, while all the other periodic peaks (let's call them sidelobes) get progressively smaller and smaller. Note that the width of the central peak, defined at full-width-at-half maximum (FWHM) gets wider as more spatial frequencies are added, growing from a FWHM =  $\lambda/4$  to a FWHM  $\sim \lambda/2.5$  (for a NA=0.7). A zone plates recreates the above analysis in a circular symmetric manner, with different spatial frequencies arriving at the focal spot from a cone of different angles to create a circularly symmetric spot<sup>2</sup>. The spatial frequency description of zone plates also allows us to understand how inner and outer zones contribute differently to the overall shape of the final spot. The outer zones, those having the smallest periods, contribute the high spatial frequencies, and are hence the leading contributors to how small a spot is achievable. The inner zones contribute low spatial frequency components, and are responsible for suppressing the sidelobes surrounding the central spot. Blocking certain areas of the zone plate can hence enable the creation of a finer spot size, but at the prize

---

<sup>2</sup> This simple description does not take into account the vector nature of light. Polarization effects, especially in combination with high-numerical aperture zone plates, can cause spots that lack circular symmetry.

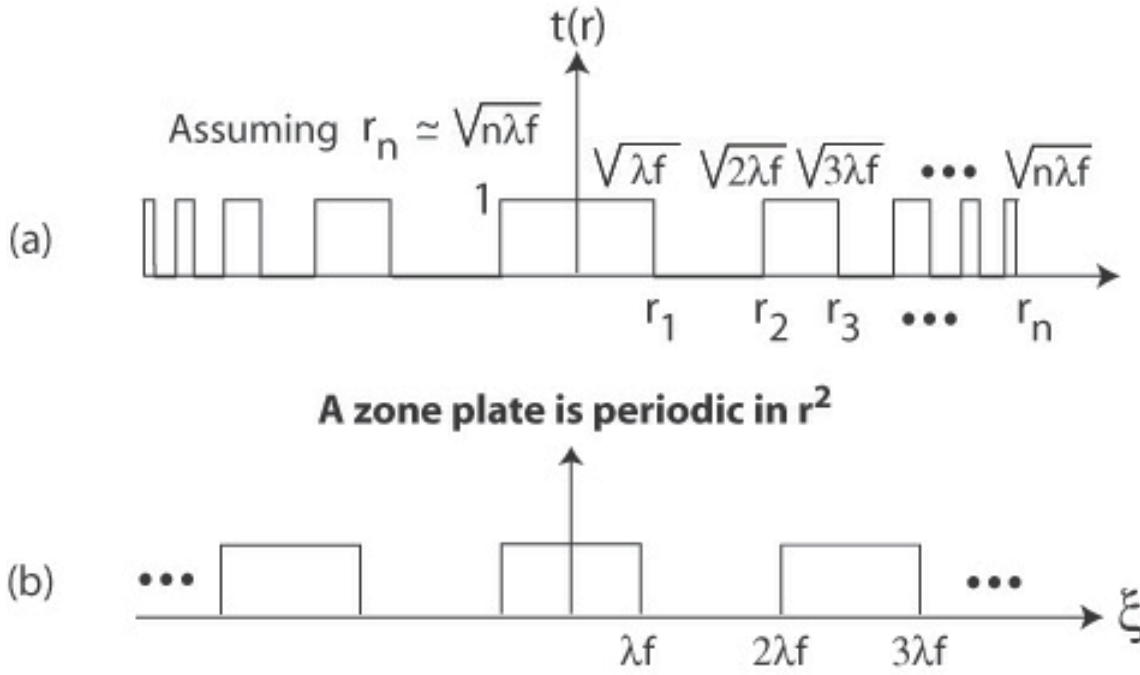


**Figure 3- 5.** (a) Cross section of zone plate. The radius is described using the small angle approximation. (b) A zone plate is periodic in  $r^2$ , and can therefore be analyzed using Fourier analysis.

of higher sidelobes. Well-understood concepts such as apodization can be readily applied to zone plates, with the result of further suppression of the sidelobes. In this manner, one of the virtues of utilizing zone plates for lithography becomes readily apparent: diffractive optics provide many “knobs” that can be tuned in order to maximize or minimize a particular focusing effect. That is, in some cases a smaller spot size might be preferred *even if* the sidelobes increase. By simply controlling what areas of the zone plate are illuminated, such effects can be realized.

Fourier analysis can further provide insight into the focusing behavior of zone plates, especially as it refers to the presence of multiple diffraction orders. Consider the cross section plot of a zone plate illustrated in Fig.3-5. If, for the purpose of simplifying the analysis, we ignore the spherical aberration component of equation 3-2, the expression of the radius of a zone plate can be simplified to the following expression:

$$r_n \approx \sqrt{n\lambda f} \quad 3 - 13$$

where  $n$  is the zone number,  $\lambda$  is the wavelength of light, and  $f$  the focal length.

We can now proceed with the analysis by realizing that zone plates are periodic elements in  $r^2$ , and hence they can be described by a Fourier series decomposition. The transmission function for a zone plate of unity absorption in the opaque zones can be described as:

$$t(\xi) = \frac{1}{2} + \frac{1}{\pi} \left[ \cos 2\pi \frac{\xi}{\Lambda} + \frac{1}{3} \cos 2\pi \frac{3\xi}{\Lambda} + \frac{1}{5} \cos 2\pi \frac{5\xi}{\Lambda} + \dots \right] \quad 3 - 14$$



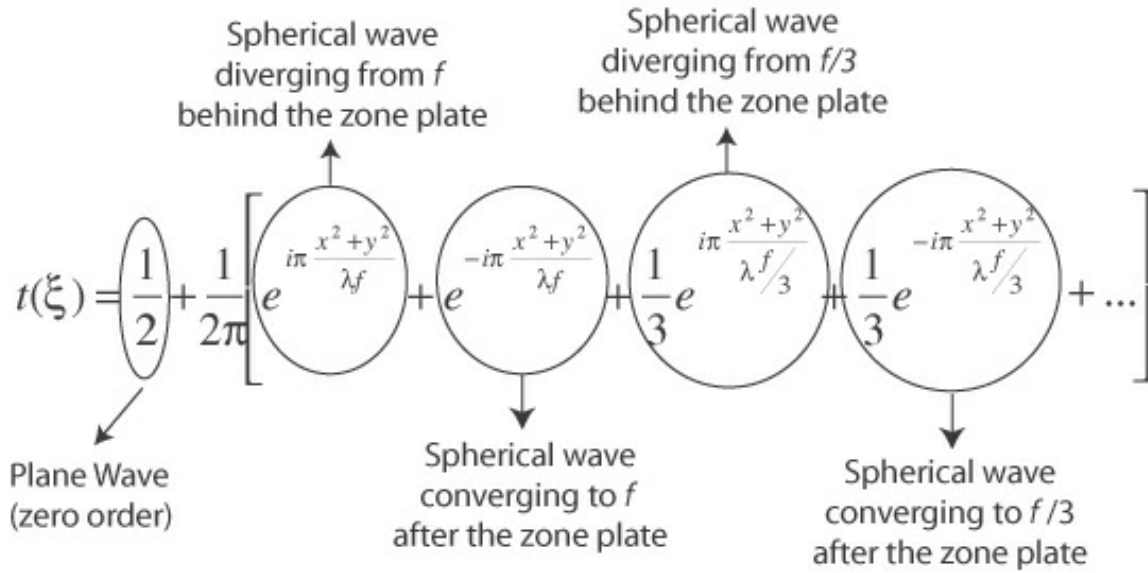
where  $\Lambda = 2\lambda f$ . Substituting for  $\Lambda$  and given that  $\xi = r^2$ , we get

$$t(\xi) = \frac{1}{2} + \frac{1}{\pi} \left[ \cos \frac{\pi r^2}{\lambda f} + \frac{1}{3} \cos \frac{\pi r^2}{\lambda f/3} + \frac{1}{5} \cos \frac{\pi r^2}{\lambda f/5} + \dots \right] \quad 3 - 15$$

Given the circular symmetry of zone plates,  $r^2 = \sqrt{x^2 + y^2}$ . The above equation can then be expressed as:

$$t(\xi) = \frac{1}{2} + \frac{1}{2\pi} \left[ e^{i\pi \frac{x^2+y^2}{\lambda f}} + e^{-i\pi \frac{x^2+y^2}{\lambda f}} + \frac{1}{3} e^{i\pi \frac{x^2+y^2}{\lambda f/3}} + \frac{1}{3} e^{-i\pi \frac{x^2+y^2}{\lambda f/3}} + \frac{1}{5} e^{i\pi \frac{x^2+y^2}{\lambda f/5}} + \frac{1}{5} e^{-i\pi \frac{x^2+y^2}{\lambda f/5}} + \dots \right] \quad 3 - 16$$

Looking at the terms of equation 3-16, we can deduce the following:



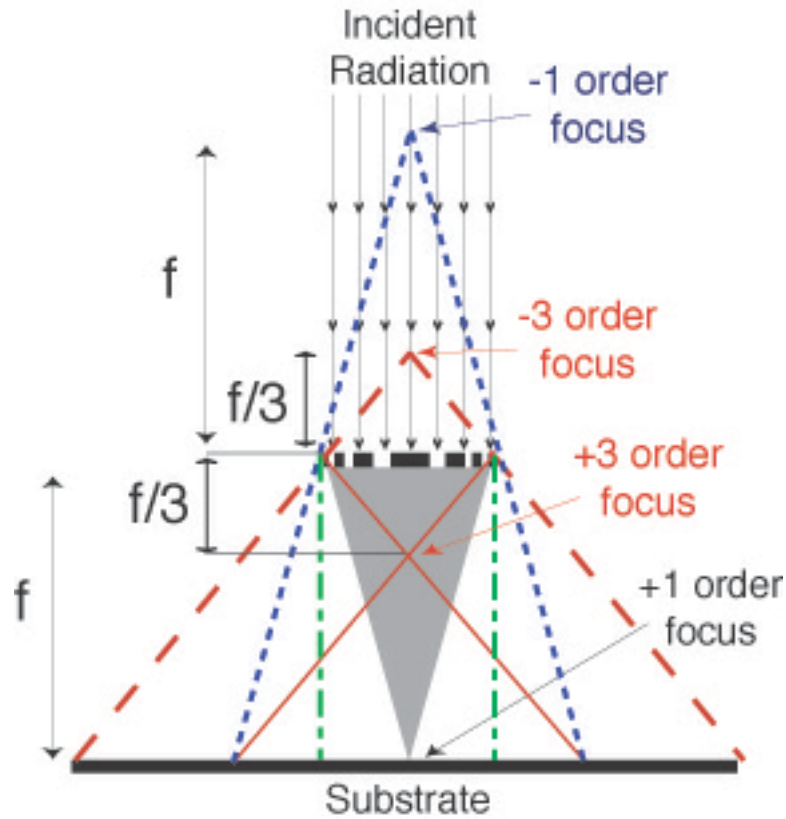


**Figure 3- 6.** Zone plate, being diffracted optical elements, focus light into a number of orders. For a zone plate with a 50-50 duty cycle, only odd orders are present. The zero order can be cancelled in the case of phase zone plates.

Figure 3-6 illustrates the multiple orders that a zone plate generates, as described by equation 3-16.

The analysis presented so far has provided a description of the origin of zone plates, their basic geometrical configuration, as well as how the different focusing orders appear. A spatial frequency analysis has also provided insight on how the main focusing spot is formed. While it is not the objective of this report to expand significantly from the kind of zone plate theory that has been presented so far, it is worth mentioning that in order to fully understand the detailed behavior of these elements, a more rigorous electromagnetic model is needed. A scalar approximation of Maxwell's equations provides a valuable starting point. Below, we briefly outline how such an analysis might proceed.

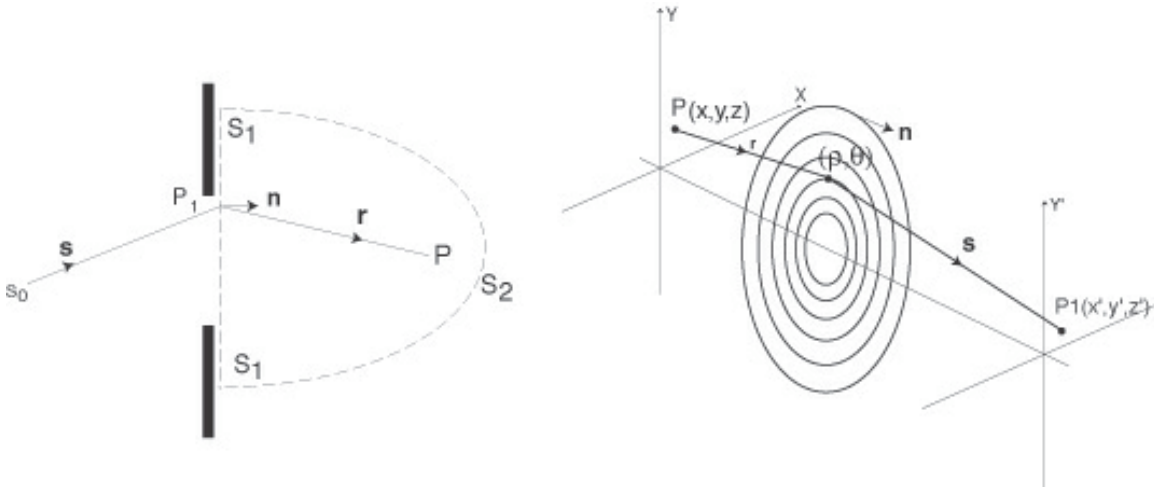


**Figure 3- 7.** Left: Diffraction by an arbitrary aperture. Right: Fresnel-Kirchhoff diffraction for a zone plate.

Fresnel-Kirchhoff diffraction theory provides a rigorous starting point to understand the behavior of light as it encounters a zone plate. We can begin by obtaining an expression of the electric field that results after an electromagnetic wave originating from an arbitrary point encounters an aperture. If we then deconstruct a zone plate as a combination of numerous apertures, an expression for the total field created by the zone plate can be obtained at any arbitrary distance after the zone plate by appropriately adding the diffraction effects of all the apertures. Following the coordinate system defined in Fig. 3-7, the field at  $P$  resulting from an electromagnetic field  $U_o$  that originates from  $S_o$ , taking into account the effect of the aperture placed in between these two points, is given by [Ref 3-3].

$$U(P) = \frac{iU_o}{\lambda} \iint_{\Sigma} \frac{\exp(-ik(r + s))}{rs} \frac{\cos(\mathbf{n}, \mathbf{s}) - \cos(\mathbf{n}, \mathbf{r})}{2} dS \quad 3 - 17$$

For the case of an amplitude zone plate, the above expression can be modified in order to accommodate to the geometrical aperture configuration of these elements to obtain:

$$U(P_1, P) = \sum_{n=1}^{N-1} \frac{iU_o}{\lambda} \int_{\rho=R_n}^{\rho=R_{n+1}} \int_{\theta=0}^{\theta=2\pi} \frac{\exp(-ik(r + s))}{rs} \frac{\cos(\mathbf{n}, \mathbf{s}) - \cos(\mathbf{n}, \mathbf{r})}{2} \rho d\rho d\theta \quad 3 - 18$$

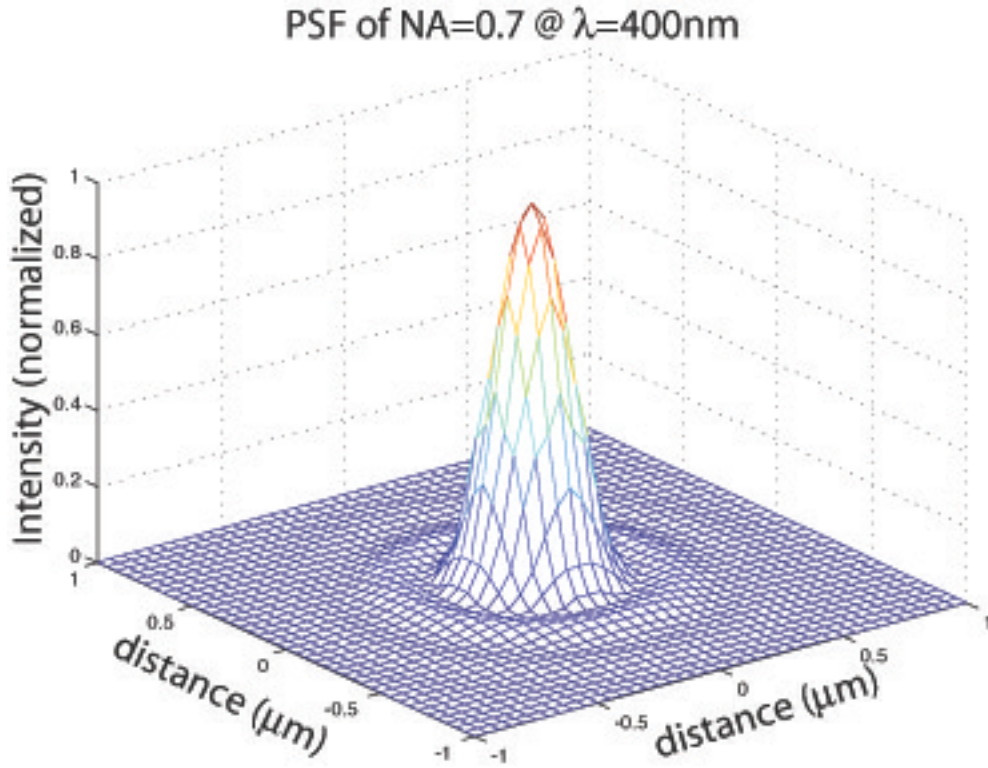


**Figure 3- 8.** Plot of the point-spread-function (PSF) of a NA=0.7 zone plate simulated using a finite-difference time-domain method. Simulation performed by Rajesh Menon.

where  $(\rho, \theta)$  is a point on the zone plate in cylindrical coordinates. The sum on the above expression is only performed over the open zones, that is, it represents the field that would be obtained at  $P_i$  for the case of an amplitude zone plate. In the case of a phase zone plate, all zones contribute to that total field, and equation 3-18 can be modified to obtain:

$$U(P_1, P) = \sum_{n=1}^{N-1} (-1)^{n+\mu} \frac{iU_o}{\lambda} \int_{\rho=R_n}^{\rho=R_{n+1}} \int_{\theta=0}^{\theta=2\pi} \frac{\exp(-ik(r+s)) \cos(\mathbf{n}, \mathbf{s}) - \cos(\mathbf{n}, \mathbf{r})}{rs} \frac{\rho d\rho d\theta}{2} \quad 3-19$$

where  $\mu = 0$ , if the first zone has a  $\pi$  phase shift or else  $\mu = 1$ . Without taking into account the effect of the illuminating source bandwidth, the total intensity distribution at  $P_1$  is given by:

$$I(P_1) = \iint_S |U(P_1, P)|^2 dS \quad 3-20$$

where  $S$  is the cross-sectional area of the source illuminating the zone plate, and  $U(P_1, P)$  is given by equation 3-19.

Scalar diffraction theory, however, fails to account for all the electromagnetic interactions (e.g. polarization), especially for zone plates of very high numerical aperture. In order to take all the effects into

account, one needs to solve the vector form of Maxwell's equations. One of the most efficient methods of solving this problem for diffractive optics is the finite-difference time-domain method. This is used to analyze the performance of zone plates in the thesis of Rajesh Menon [Ref 3-4].

### 3.3. Fabrication Techniques

The first zone plates for visible light were made in the 19<sup>th</sup> century by Lord Rayleigh, Soret, and Wood by photographically demagnifying drawings of zone plates [Ref 3-5]. Through decades of research and improvements in fabrication techniques, zone plates capable of focusing light at almost all ranges of the electromagnetic spectrum, including soft x-rays, were fabricated. It was Baez in 1961 [Ref 3-6] who first constructed zone plates capable of working with extreme ultra-violet and soft x-ray radiation. Because at these wavelengths radiation is absorbed by photographic plates, it was necessary for Baez to either fabricate unsupported zone plates, or support them on very thin transmitting membranes. He was able to fabricate unsupported zone plates for imaging for 253.7 nm radiation. The zone plates consisted of 19 rings of gold with a diameter of 2.6 mm, an outer zone width of 17  $\mu\text{m}$ , and a focal length of 15 cm.

However, it soon became apparent that other techniques besides photo-reduction and mechanical ruling were necessary to fabricate high-resolution zone plates capable of operating at such short wavelengths. The challenges for the fabrication were twofold: the smallest linewidth desired was (and still is) beyond the resolution of optical projection systems, and the number of zones could sometimes be very large. Another important aspect is the placement of the features. For diffraction-limited performance, the errors in the positioning of the each section of each ring has to be a small fraction of the zone period. Baez proposed holography in 1961 to produce zone plates with large number of zones [Ref 3-7]. However, lasers were not yet available at this time, and the requirements for spatial and temporal coherence reduced the intensity of conventional sources too much to be of practical use for the production of high quality zone plates. Holography became an easy method only after high-quality laser sources became available, and interference patterns with huge number of fringes could be produced routinely.

Electron beam systems for the fabrication of fine microcircuit patterns were first developed in the 1960s, and zone plates were often used as test patterns to demonstrate the resolution. Ever since, with holography still being the choice for certain applications, electron-beam lithography has been the main tool for the fabrication of zone plates. The strength of holography is the large field; the strength of e-beam systems, the high resolution and the flexibility [Ref 3-8].

### 3.3.1. Critical Parameters

The fabrication of efficient diffractive optical elements requires the precise patterning of a large number of sub-wavelength binary surface-relief structures. For close to ideal performance, three critical parameters are required: (1) the local duty-cycle of each pair of zones must remain close to 50-50, (2) the period of each pair of zones must be accurately controlled, and (3) the phase-shift between alternate zones must be as close to  $\pi$  as possible. The following three sections detail the need for these three requirements and the impact of errors in each of these critical requirements on the performance of the zone plates.

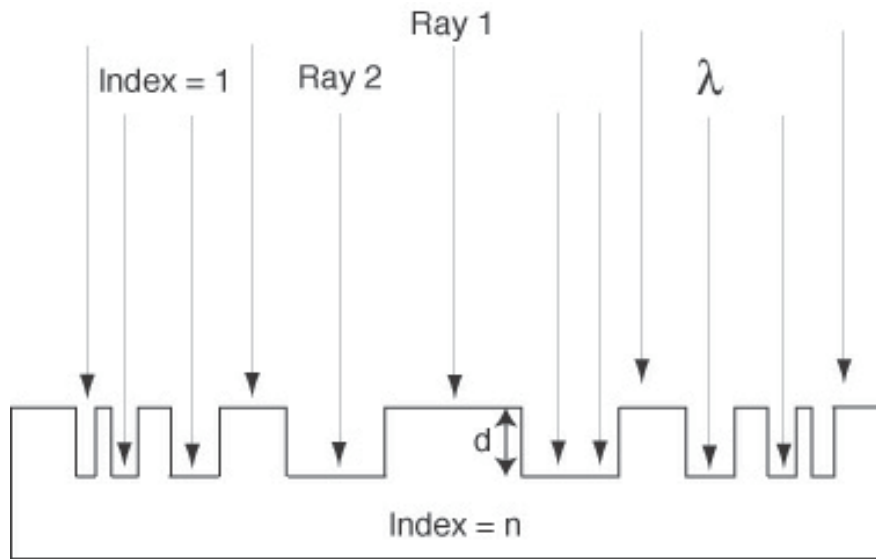


**Figure 3- 9.** Cross-section of a phase zone plate. Alternate zones are phase-shifted to maximize the efficiency into the first order as well as to cancel the zero order.

#### 3.3.1.1 Phase-Shift Errors

Let's begin by calculating an expression for the depth of the groove necessary to obtain a  $\pi$  phase shift between adjacent zones (assuming the zone plates operate in air). If we refer to Fig,3 - 9, we can model the radiation illuminating the zone plate as a plane wave, with a wavefunction  $\Psi$ . Therefore, we can write

$$\Psi = A \cdot e^{i\vec{k} \cdot \vec{r}} \quad 3 - 3$$

$$\text{where } k = \frac{2\pi}{\lambda} \cdot n$$

and  $n$  is now the index of refraction of the material

As the radiation goes through paths 1 & 2 in Fig. 3-9, for path 1, light goes through the material a distance  $d$ , and the wavefunction for light can be written as:

$$\Psi_1 = A \cdot e^{i \cdot \vec{k} \cdot d} = A_1 \cdot e^{i \cdot \frac{2\pi}{\lambda} \cdot n_r \cdot d} \quad 3 - 4$$

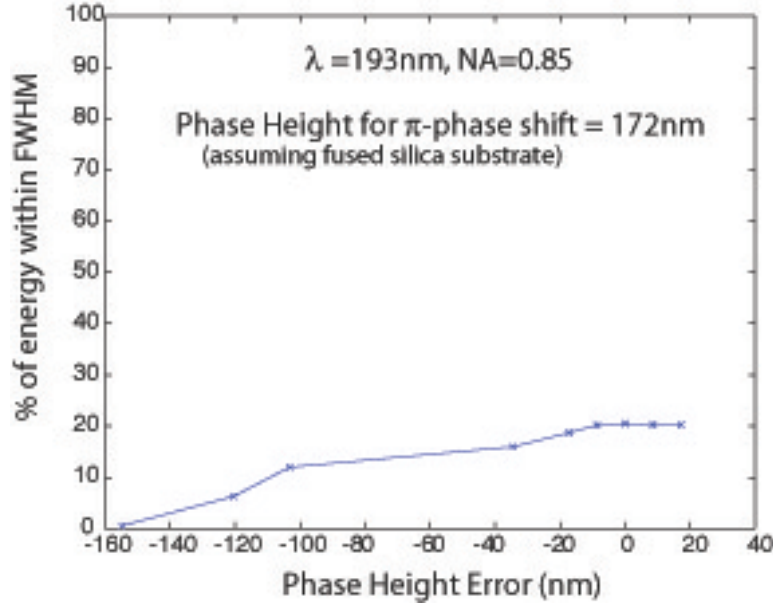


**Figure 3- 10.** Simulation of the first order diffraction efficiency versus phase-height error (phase-shift error). The simulation was performed with a NA = 0.85 at  $\lambda = 193\text{nm}$ . Simulation by Rajesh Menon.

Light going through path 2 will only travel in air, so  $n = 1$ .

$$\Psi_2 = A \cdot e^{i \cdot \vec{k} \cdot d} = A \cdot e^{i \cdot \frac{2\pi}{\lambda} \cdot d} \quad 3 - 5$$

At depth  $d$ , we want a  $\pi$  shift between the radiation that traveled path 1 and the one that traveled path 2, therefore:

$$\Delta\Theta = \pi = \frac{2\pi}{\lambda} \cdot n_r \cdot d - \frac{2\pi}{\lambda} \cdot d = \frac{2\pi}{\lambda} \cdot d \cdot (n_r - 1) \quad 3 - 6$$

Solving for  $d$ :

$$d = \frac{\lambda}{2} \cdot \frac{1}{n_r - 1} \quad 3 - 7$$

Even though fabrication techniques have been developed that can achieve depth control to  $\sim 1\%$ , it is important to understand how phase fabrication errors affect the performance of zone plates. Phase errors can result in a degradation of the focused spot in terms of efficiency, since all zero-order radiation will no longer be cancelled. Fig.3-10 provides a plot illustrating the effect of phase-error on the efficiency of the zone plate.

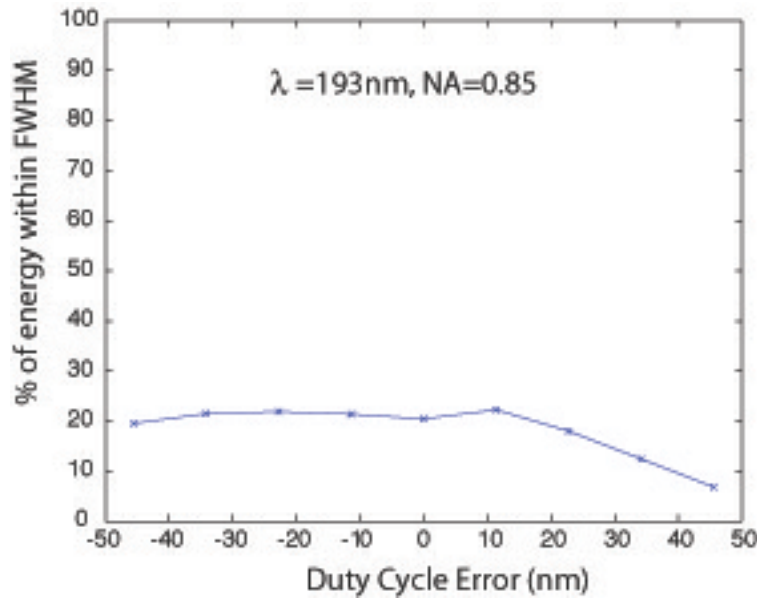


**Figure 3- 11.** First order diffraction efficiency versus duty cycle errors. The simulation was performed with a NA = 0.85 at  $\lambda = 193\text{nm}$ . Simulation by Rajesh Menon.

### 3.3.1.2 Duty-Cycle Errors

Duty-cycle errors are defined as the percent deviation of each pair of zones in a zone plate from their intended linewidths. This concept is easier to explain for the case of a regular grating. A grating with period  $P$  is said to have a 50-50 duty cycle if all the lines and spaces constituting the grating have a width of  $P/2$ . If the lines are wider than the spaces, or vice-versa, the grating's duty cycle is no longer 50-50, and a percent error can be associated with this deviation. As was mentioned earlier, a zone plate can be described as a diffractive element containing a large number of small-area gratings, and locally, they should have duty cycle that are as close to 50-50 as possible. Deviations from such a situation will result in the appearance of even orders in the diffracted radiation, in addition to the always-present odd orders, resulting in a degradation of the focused spot in terms of efficiency. Fig.3-11 provides a plot illustrating the effect of duty-cycle errors on the efficiency of the zone plate.



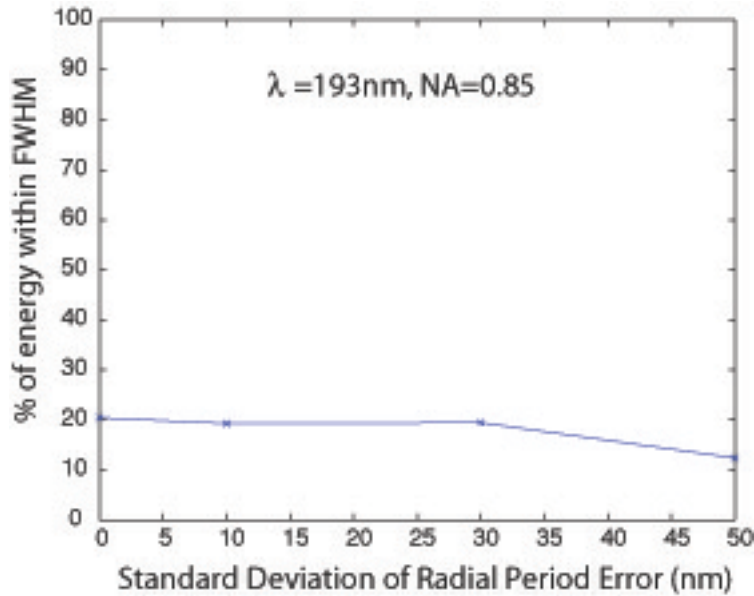


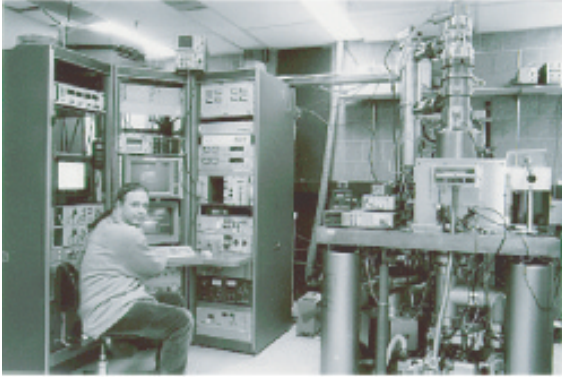
**Figure 3- 12.** Simulation of radial period errors versus zone-plate efficiency at a fixed focal plane. The simulation was performed with a NA = 0.85 at  $\lambda = 193\text{nm}$ . Simulation by Rajesh Menon.

### 3.3.1.3 Radial Period Errors

Radial period control is the determining factor in optimizing how well-tuned zone plates are to the wavelength of choice, in turn determining our ability to control the focal length of the zone plates. This last parameter, the focal length, is critically important, since for large zone-plate arrays that can span many square centimeters in area. Focal length uniformity is paramount if we want all zone plates to create a diffraction-limited spot at the same focal plane. Deviations from a single focal plane will result in different zone plates in the array writing features with different dimensional control, something unacceptable in state-of-the-art lithography. An appropriate metric to analyze this type of error consists in measuring how the PSF degrades in terms of efficiency, for a fixed focal plane, as radial period errors are introduced. Fig.3-12 provides a plot illustrating the effect of radial period errors on the efficiency of the zone plate.

### VS-26 (from I.B.M.)

50 keV Vector Scan System



Resolution: Sub-30nm

### The Raith-150

Variable Voltage (up to 30keV)  
Vector Scan System



Resolution: Sub-20nm

**Figure 3- 13.** Electron beam lithography systems available at the NanoStructures Laboratory at M.I.T.

### 3.3.2 Fabrication of Zone Plates by Means of Electron-Beam Lithography

The fabrication of zone plates requires the definition of large number of circular structures requiring precise width and pitch control. Electron-beam lithography systems are particularly well tailored for this application. The following three sections provide a description of some of the key challenges that have to be solved in order to fabricate high-resolution phase zone plates with good fidelity by means of electron-beam lithography.

Two different electron-beam lithography systems were utilized for the fabrication of zone plates and zone-plate arrays. A picture of the two systems along with some of their key specifications can be seen in Fig.3-13. Both e-beams are vector scan systems capable of high-resolution, but have very different electron-beam optics and acceleration voltages. These considerations can be important, depending on the application requirements.

#### 3.2.2.1 Writing Strategies for Zone Plates

There are a number of important considerations that have to be well understood prior to fabricating circular diffractive elements by means of electron beam lithography.

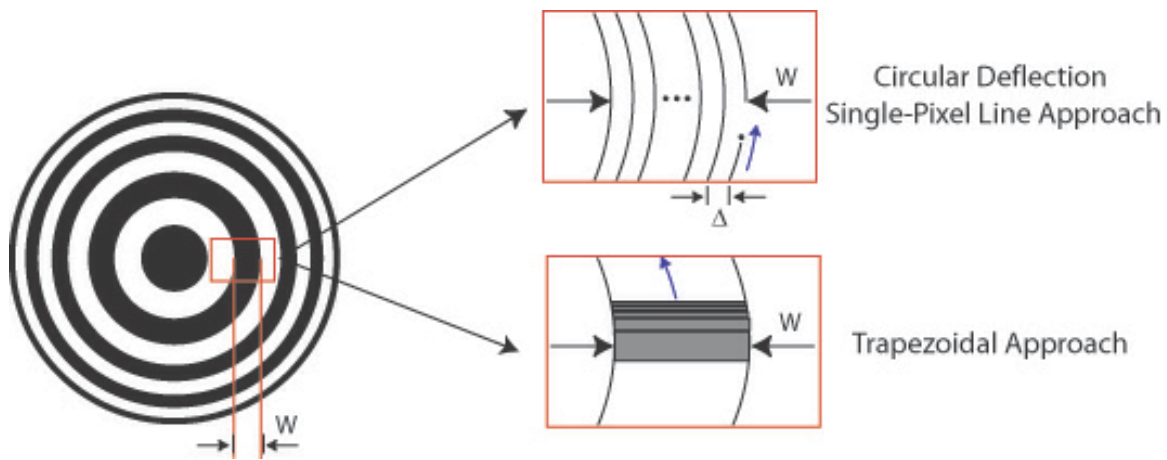


**Figure 3- 14.** Electron beam lithography writing strategies for curved-shaped structures.

They can be summarized as: (1) the challenge of writing circular features for systems that are typically optimized for Manhattan geometries, (2) pattern placement considerations, (3) the presence of proximity effects. This section addresses these three key concerns.

#### Writing Circular Features with E-Beam Lithography

The use of vector-scan electron-beam lithography is most practical when the pattern to be exposed can be efficiently broken down into a set of primitive shapes that the system knows how to fill in. Traditionally, systems are optimized for the generation of trapezoidal structures, which form the basic structures of Manhattan geometries. However, since this writing strategy involves the creation of the desired pattern by adding trapezoids of different sizes, it is very inefficient for circular geometries. For these geometries, with a large number of curved shapes, the trapezoidal process implies an unacceptable tradeoff between storage, writing time and pattern fidelity requirements [Ref 3-9].

We have implemented a solution in the two available e-beam systems at the NanoStructures Laboratory (shown in Fig. 3-13) that is capable of writing structures with curved shapes efficiently, bypassing the trapezoidal approach altogether.

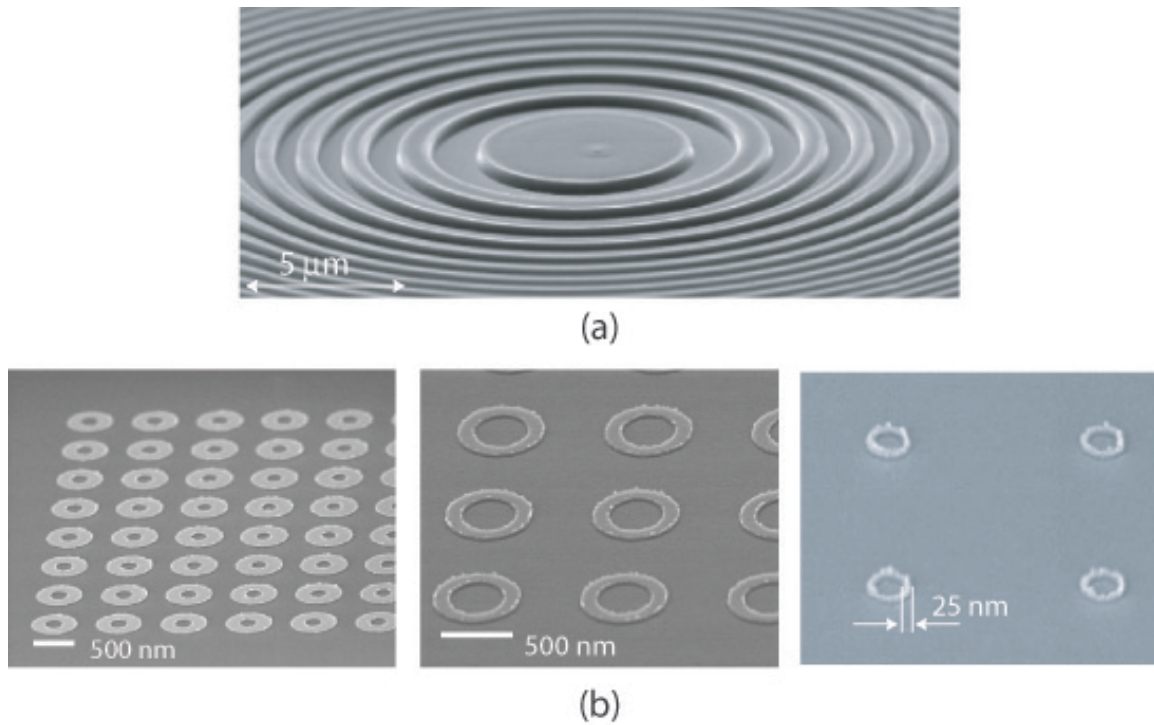


**Figure 3- 15.** Circular structures created with the RAITH-150 electron-beam lithography system. These circular elements were written with the single-pixel-line circular deflection writing strategy. (a) central zones of a zone plate (note the absence of pixilation of the curved elements thanks to the circular deflection of the beam), (b) arrays of magnetic nanorings (as small as 25nm) to be used for magnetic memory applications.

The writing strategy relies on the ability to deflect the beam in a circular manner, and hence create large area circular patterns by the addition of many circular single-pixel scans. A schematic of the *trapezoidal approach* and the *circular deflection technique* applied to the fabrication of circular structures is depicted in Fig. 3 – 14. In the circular deflection technique each zone of the zone plate is broken into an integer number of single-pixel line polygons with more that one thousand points each (therefore creating an excellent approximation to a circle). By exposing sequentially each of these single-pixel circles of increasing radius (the circles are typically spaced 18nm apart, but this spacing can vary at will), zones with precise dimensional control and excellent uniformity can be created. This writing strategy allows for the fast creation on zone plates, with relatively small files that don't require millions of trapezoids to approximate the circular structures of zone plates. Electron beam settling times are also much reduced with this method, since no settling is required during the exposure of each single pixel circle, as opposed to the case requiring large number of trapezoids (for each trapezoid, some beam settling time is involved). The *circular deflection* technique has the added advantage that the dose can be controlled within each zone. This control becomes relevant for diffractive optics applications that require sloped zone profiles and zones with different phase heights (see section 4.1.3 for an analysis on why this turns out to be very useful). Fig. 3-15 contains four scanning electron micrographs showing a variety of circular structures that can be written employing the circular deflection technique. Fig.3-15(a) provides a view of the central zones of a zone plate, and one can note the excellent patterning fidelity that

can be achieved with this technique in terms of concentricity and absence of pixelization effects (resulting in low edge roughness). Circular structures of very small dimensions (with features as small as 25nm) can be readily achieved, as shown in Fig.3-15(b). The figure contains nanoring magnetic elements intended for magnetic memory applications.

Another important consideration concerning the fabrication of diffractive optical arrays by means of electron-beam lithography concerns the ability of e-beam systems to accurately place features on the substrate. Since for the Zone-Plate-Array Lithography application large area patterns must be stitched by means of multiple zone plates, pattern-placement errors introduced by the e-beam lithography tool will be a significant contributor to how well a ZPAL system performs in terms of stitching. There are other key contributors to this overall stitching error budget, namely *angular illumination errors* (i.e. if zone plates are illuminated at an angle, the spot will swivel accordingly, introducing a placement error), and *stage scanning errors* (in ZPAL, pattern control is ultimately limited by how accurately the stage can be scanned). This section considers the pattern placement requirements for e-beam generation of diffraction optical arrays to be utilized in ZPAL systems.

In order to allocate appropriate budget errors, we will assume a ZPAL-tool that will meet the demands of the 100nm node. According to the International Technology Roadmap for Semiconductors 2001, the 100nm node must have 3-sigma Critical Dimension (CD) control values that range from 12.2 nm for DRAM devices to 5.3nm for ASIC devices. Assuming a ZPAL tool employing 1 million diffractive elements, the zone-plates would cover a 10x10cm area (at  $\lambda = 193\text{nm}$  typical zone plate diameters are  $\sim 100\text{ }\mu\text{m}$ ). This area, similar to that of a conventional mask, would have to meet the above-mentioned specs.

In terms of pattern placement, state-of-the-art pattern generators such as Etec's MEBES-eXara electron-beam-lithography system can achieve placement accuracies of  $\sim 20\text{nm}$  (3 sigma) over the area of a mask. Given this fact, the placement accuracy of the writing tool eats up our entire CD error budget for a ZPAL tool (and more). However, it is important to realize that, (1) *local* placement errors are likely to be much smaller (something that can be of use depending on writing strategy), (2) the placement errors can be mapped and later corrected via software in the ZPAL tool, and (3) a solution to improve the pattern placement of e-beam lithography systems exists and can be used to achieve 1 nm pattern placement over large areas (this technique is called Spatial-Phase-Locked Electron-Beam Lithography, SPLEBL).

Spatial-phase-locked e-beam lithography (SPLEBL) is a technique under development at MIT for about 10 years, designed to achieve nanometer-level placement accuracy in e-beam lithography. The technique is unique to MIT. The basic idea is to use fiducial grids, fabricated using interference lithography (or a derivative thereof) to determine the placement of features written with the e-beam by continuously tracking the position of the e-beam. Any deviation of the beam from its intended location on the substrate is sensed, and corrections are fed back to the beam-control electronics to cancel errors in the beam's position. The virtue of interference

lithography (IL) is that the gratings and grids produced have the property of long-range spatial-phase coherence and hence can be used as metrological standards or fiducial grids.

There are several modes of SPLEBL (see Fig.3-16), including the "segmented-grid mode" and the "global-fiducial-grid mode." For fabricating a regular array of zone plates, the segmented-grid mode (SGM) is preferred. In the SGM, a vector-scan e-beam system is used. A grid, produced by IL, is transferred to the substrate upon which the zone plates are to be written, but only in the corners of the e-beam writing field. These grid-based alignment marks might be, for example, about 1 or 2 microns square, and the grid period might be 200 nm. Gold is an ideal material for the grid-based alignment marks; this is the only material that has been used to date. Gold produces a strong secondary-electron or backscattered-electron signal. Alignment of the e-beam scan field

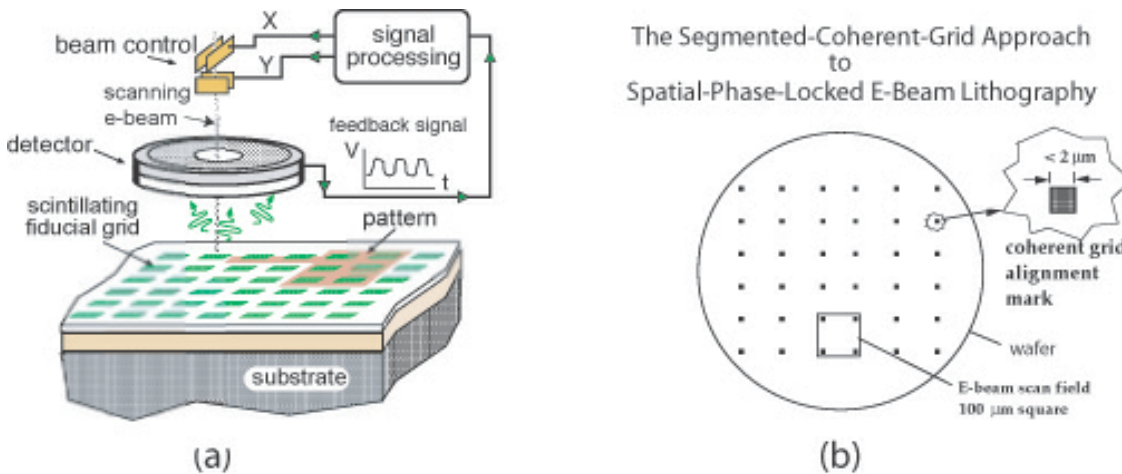


**Figure 3- 16.** Illustration of two modes of spatial-phase-locked e-beam lithography (SPLEBL), (a) the global-fiducial-grid mode, and (b) the segmented-fiducial-grid mode. In (a) a periodic signal is emitted from a grid placed on the substrate as the beam is scanned, enabling a feedback loop to ensure sub-1 nm accuracy of beam placement. In (b) an array of marks, consisting of segments of an interferometrically produced coherent grid, ensure sub-1nm placement via phase detection on the signal from the marks. Such marks could be placed in the spaces between zone plates of a ZPAL array.

relative to the grid-based alignment marks is done using Fourier-domain techniques, as these, in principal, allow alignment to within about 1/2000 of the grating period, or about 0.1 nm.

Experimental results to date have shown an absolute pattern-placement-accuracy, mean plus 3-sigma, of 6 nm. This number is limited by two factors, the least-count of the laser interferometer, and the fact that the SGM is a "look then write" scheme, i.e., drift can occur in the time between the locking and the writing. The real time version of SPLEBL, in which a fiducial grid is patterned over the entire area of the substrate as opposed to only in the corners of the field, has been shown to achieve a pattern-placement accuracy of 1nm [Ref 3-10].

And additional important benefit of employing a technique such as spatial-phase locking is that it would enable one to match the outer periods of zone plates to better than 1 nm, and hence ensure that all zone plates in

the array focus at the same focal plane (to within the depth of focus, which in the case of high-NA zone plates operating at 193nm is about 400nm). This requirement is critical in order to maintain CD control. As was described in Section 3.3.1.3, the focal length of a zone plate is fundamentally determined by the pitch of the zones. The ability to control to sufficient accuracy this pitch will hence determine how repeatable zone plate arrays can be manufactured in terms of focal length.

According to the SIA Roadmap, electron-beam lithography systems must have placement accuracies of 21nm for the 100nm node over the entire area of the mask. This implies that no feature of the mask can be misplaced by more than 20nm from its intended location over a 10x10cm area. This requirement does not contain enough information to assess the quality of the zone plates that can be manufactured by means of commercial high-throughput electron-beam lithography systems. In a way, it provides a worst-case scenario, indicating that any given zone within a zone plate can have a misplacement of  $\pm 20\text{nm}$  with respect to its intended position. That is, according to this placement accuracy, the local pitch of the zone plates can be controlled to no better than 40nm (i.e. since the pitch of our outer-most zones will be 200nm for the 100nm node, all that can be guaranteed is that the pitch will be between 180-220nm, since the previous to last zone could be misplaced  $-20\text{nm}$  from its intended position and the last zone could be misplaced  $+20\text{nm}$  in a worst-case scenario situation). Were this to be the case, it would be impossible to fabricate 1 million zone plates with matched focal lengths by means of electron-beam lithography that adhered to the letter of the SIA specification.

However, this is certainly not what the 20nm placement accuracy metric is indicating. It must be the case that the local pitch control of a state-of-the-art e-beam system is much better than this, closer to the nanometer mark that will be required for the fabrication of large zone-plate arrays. For one, the ability to control the pitch in electron beam lithography is chiefly determined by the accuracy to which the e-beam writing fields can be calibrated. This calibration can be controlled to 1 part in 100,000 if necessary. That is, if 200nm period outer zones are to be written (to achieve 100nm resolution with a ZPAL system), the error in the pitch due to field calibration is in the order of a few picometers. At the same time, it is true that a characteristic of all e-beam systems not operating with SPLEBL is that they are open loop, and that the beam's position with respect to the substrate can drift due to stray fields, vibration, etc. It is indeed quite possible that significant placement errors are present within any given field, but it is more likely that long term drifts due to thermal expansion, sample height variations and stage errors are the key contributors to the 20nm placement



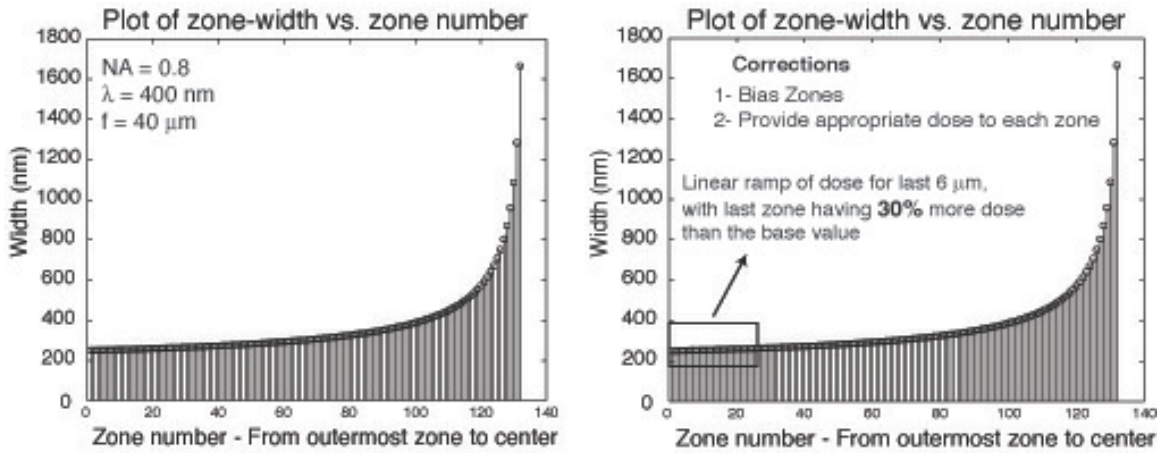


**Figure 3- 17.** Zone plates contain a large number of features requiring precise dimensional control, requiring careful optimization of the e-beam writing strategy to compensate for proximity effects. Left: Plot of the widths of the zones of a zone plate versus zone number. Note that for the 0.8 NA zone plate designed for  $\lambda = 400\text{nm}$ , widths vary continuously from  $\sim 200\text{nm}$  all the way up to  $1.6 \text{ } \mu\text{m}$ . Right: Extensive experimental tests as performed and corrections are applied to compensate for proximity effects. Among the corrections performed, the last zones of the zone plate receive a larger dose than the inner zone's dose.

accuracy, and that locally, for any given zone plate, the pitch of the zone plates can be controlled to a fraction of this value. As a final point, it is worth noting that the chief concern in terms of zone-plate-array fabrication is repeatability from zone plate to zone plate, and that pitch errors can be tolerated so long as they are consistent across the array.

### 3.2.2.2 Proximity Effect Correction for Zone Plates

Although zone plates can be fabricated with the planar process utilizing standard lithographic equipment, careful optimizing has to be performed in order to create diffractive elements with optical performance close to ideal. Zone plates are challenging structures to write with electron-beam lithography systems. So much so that they have long been used as resolution structures to test the performance of e-beam systems. The chief reason for the challenge lies on the circular nature of the pattern (which we have just addressed), and the large number of precisely controlled linewidths that must be achieved in a dense grating like structure. Fig.3-17 illustrates this last point with a plot of the zone width versus the zone number for a  $\lambda = 400\text{nm}$ , 0.8 numerical aperture with a  $40\mu\text{m}$  focal length. As can be seen, zone widths ranging from  $\sim 200\text{nm}$  all the way up to  $1.6 \text{ } \mu\text{m}$  have to be addressed in a continuous manner. The problem is very similar to writing a chirped grating, except that it is done in a radially symmetric fashion.

The radially-symmetric chirped grating present three key challenges for an electron-beam lithography system. *The first* one has to do with astigmatism of the beam. It is very important to properly adjust the beam prior to and during exposure to create round spot with minimized stigmatism, in order to prevent different parts



of the circular zones from having different widths. This problem is somewhat mitigated in that the size of the beam is much smaller than the size of the features being exposed, as is the case when writing zone plates for the UV, where the minimum feature size is well over 100nm and e-beam diameters are less than 20nm.

*The second challenge* has to do with the digital-to-analog converter (DAC), responsible for allowing a discretized digital pattern to be converted into an analog signal (a current) capable of deflecting the beam to the right position on the substrate. Digital-to-analog converters for electron-beam-lithography systems can have different capabilities, ranging from 14 to 16 bits. The VS-26 lithography system available at the NSL has a 14-bit DAC, whereas the RAITH-150 has a 16-bit DAC. A brief calculation will illustrate why this is important. Let's assume that a zone plate has a diameter of  $\sim 200\text{ }\mu\text{m}$ , and therefore we utilize a  $200\text{ }\mu\text{m}$  electron-beam field size. A 14-bit DAC will result in a 12.2nm address grid, where a 16-bit DAC would enable a user to have a 3 nm grid. This can have important consequences for zone plate writing, since the outer zones of high-numerical-aperture zone plates can vary in pitch by figures closer to the nanometer mark than to the tens of nanometer figure.

*The third challenge* concerns the presence of proximity effects in electron-beam lithography. Proximity effects arise because of electron back-scattering from the substrate, with the result that the exposure dose at a given location depends not only on the local incident dose, but also on the dose incident at all points within the electron range [Ref 3-11]. This effect, in combination with the forward spreading of the electron beam, causes the pattern obtained in resist to differ from the geometric pattern addressed by the beam. While this effect has been known for decades, and serious

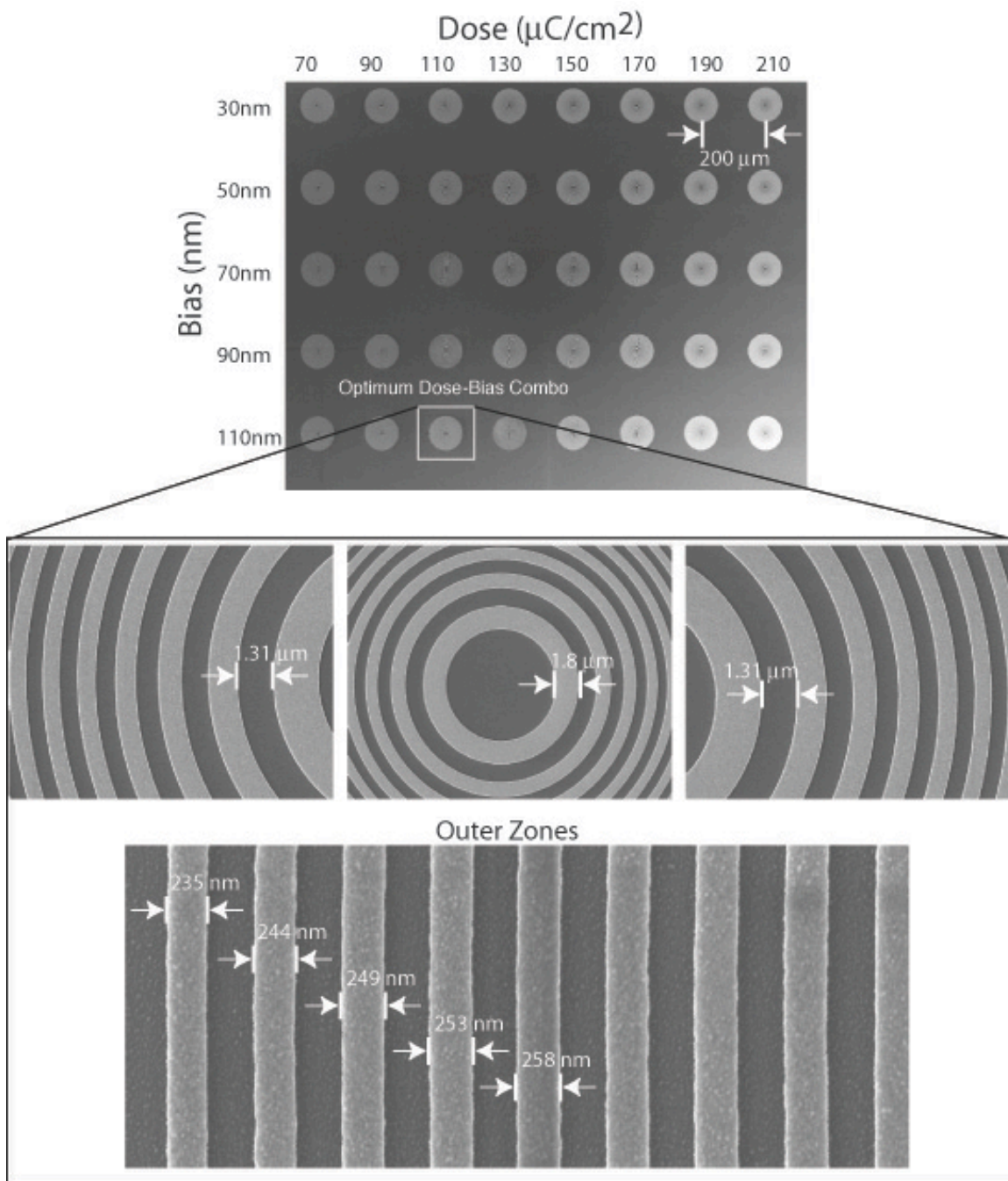


**Figure 3- 18.** Scanning electron micrographs of an array of zone plates exposed with the RAITH-150 at different doses and different biasing aimed at optimizing dimensional control. Each zone plate of the array is inspected and measured in order to tabulate the effect of various dose-bias combinations.

modeling efforts have been undertaken by both industry and academia, there is no standard solution available to the e-beam user community. Because proximity-effect correction depends on the substrate, pattern, acceleration voltage and resist used, no general technique is likely to work for all users. Hence, one must address and solve this problem on a case-by-case basis. To correct for this effect we can: (1) vary the dose applied to each feature, and (2) change the shape and/or width of features to compensate for these effects (changing the width of features is typically known as *biasing*).

Extensive and detailed efforts were undertaken in order to minimize proximity effects for the exposure of zone plates. The process is laborious, but good results can be achieved. It starts by exposing an array of a given zone plate at a large number of doses, as well as with different zone-width biasing combinations, as illustrated in Fig.3-18. Each zone plate of the array is then inspected and measured in order to tabulate the effect of various dose-bias combinations. After selecting the optimal dose-bias combo, some proximity effects will still remain present if a single and uniform bias was provided to all zones of the zone plate. In particular, it is unlikely that the central zones and the outer-most zones will have close to 50-50 duty cycle for the same dose-bias combo. As indicated in Fig. 3-18 (right), this limitation can be tackled by providing a dose correction that can vary according to a specified dose progression for the last X- $\mu\text{m}$  of the zone plate. This again involves an experimental confirmation, with the results depending on the acceleration voltage of the e-beam, the substrate used and the pattern exposed. It was experimentally determined, that for 30keV acceleration voltage, with fused silica substrates, a linear correction for the last 6 $\mu\text{m}$  (this roughly corresponds to the backscattered range at this voltage), in which the dose is increased linearly from the base value up to a 30% higher dose for the last zone, can achieve nearly optimal dimensional control across all the zones of the zone plate. In order to also optimize for sidewall profiles, linear zone plates were fabricated with all the previously mentioned proximity effect correction techniques, with the goal of being able to cleave these samples and look at them edge-on with a scanning electron microscope. A sample of some of the results obtained from these experiments, are shown in Fig.3-19. The linear zone plates were designed to have the exact same dimensions as the ones intended for the final circular zone plates. It is worth noting, that despite the laborious

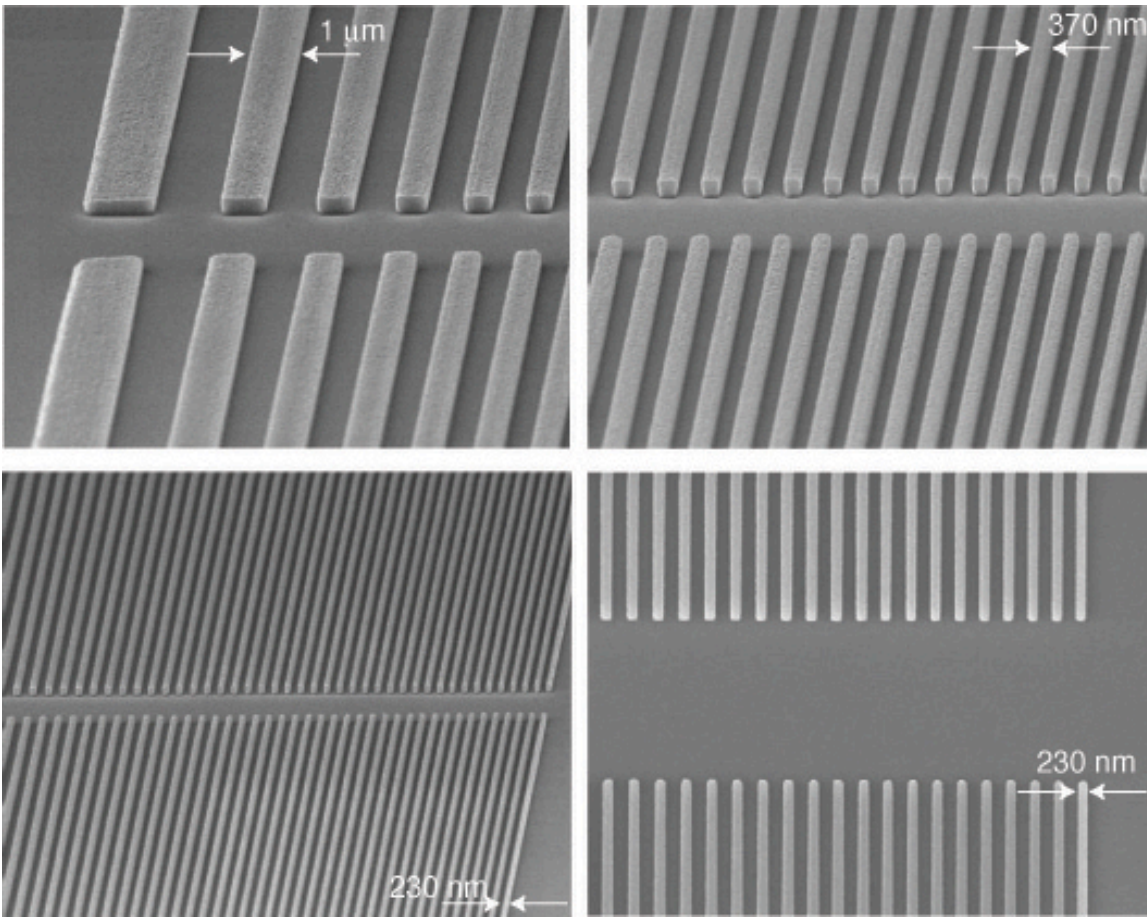


**Figure 3- 19.** Scanning electron micrographs of linear zone plates aimed at testing proximity effect correction schemes and optimizing sidewall profiles. The zone plates were exposed with the RAITH-150, at 30 keV acceleration voltage. The resist utilized was HSQ, a negative spin-on-glass resist from Dow Corning.

nature of the optimization process, the final result was excellent. Zone profiles were smooth and vertical, and duty-cycle control was achieved throughout all zones.

### 3.2.2.3 Choices of Resist

The choice of resist is an important consideration for the fabrication of zone plates and other diffractive elements. While the choice of resist is dependent on a number of other factors having to do with the post-processing of the zone plate substrate, at a minimum it is worth considering what options are enabled by choosing a positive or a negative resist.

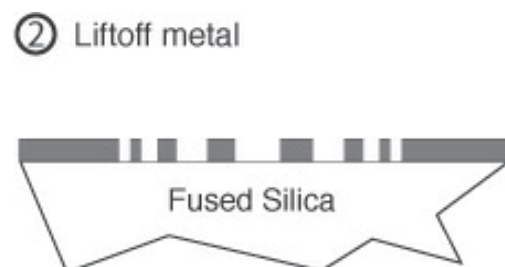
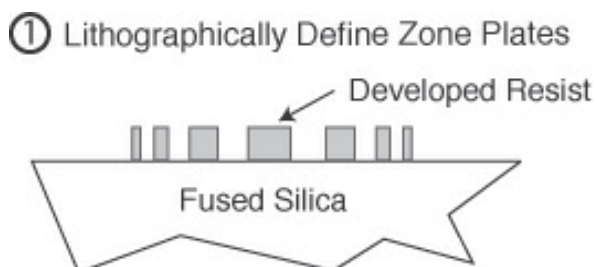


**Figure 3- 20.** A negative resist exposure in combination with a lift-off process provides the simplest fabrication procedure for an amplitude zone plate

As a reminder, in a positive resist the areas that are exposed to radiation will later be removed by mean of a developer, whereas in a negative resist the opposite will occur, that is, only the exposed areas will remain after development.

A negative resist exposure in combination with a lift-off process provides the simplest fabrication procedure for an amplitude zone plate (see Fig.3-20). Amplitude zone plates are clearly not as useful their phase counterpart if they are to be used for lithography applications (ZPAL).

In order to fabricate phase zone plates, processes can be developed with both positive and negative resists. Section 3.2.4 will describe in detail three fabrication procedures aimed at this goal, with the final one, utilizing a negative tone resist, being the preferred and simplest method of all.

### 3.3.3 Fabrication of Zone Plates by means of X-Ray Lithography

X-ray lithography was first suggested by Spears and Smith in 1972 [Ref 3-12, Ref 3-13].The principle of operation is relatively simple. The technique is a shadow-printing scheme, in which a source of radiation (x-rays in this case, with wavelengths between 6 and 14 Å) is shaped by a mask to produce the desired pattern in a resist that is sensitive to the radiation utilized (Fig.3-21). Unlike the situation for electrons and optical photons, it is very difficult to construct any type of optics for x-rays (zone plates are the only exception), and as a consequence, the x-ray exposure setup employs a 1X mask.

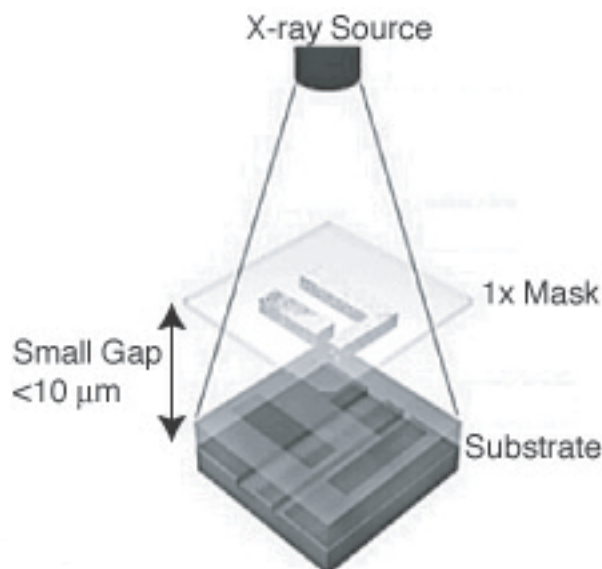


**Figure 3- 21.** X-ray lithography schematic.

The mask and the wafer are maintained in close proximity, typically a distance of the order of a few microns. The resolution, or more precisely, the minimum printable line width  $W$ , is dominated, to first order, by diffractive blurring at the finite wavelength  $\lambda$  and gap  $G$  [Ref 3-14]. The relationship between mask-substrate gap  $G$  and the minimum feature size  $W$  is given by

$$G = \alpha \frac{W^2}{\lambda} \quad 3 - 21$$

where  $\alpha$  is typically in the range 1-1.5 [Ref 3-15, Ref 3-16].

The 1X mask is the heart of the x-ray lithography process, and it consists of an absorber pattern on a thin membrane. The mask structure is dictated by the optical properties of the x-rays. The membrane must be transparent enough to allow for fast exposures, and yet be able to withstand handling and radiation damage. In general, the membrane will be on the order of 1 to 2  $\mu\text{m}$  thick, and be made of low-Z materials for high transmission. Currently used mask membranes are fabricated with silicon, silicon nitride, or silicon carbide, while high Z materials such as gold, tantalum, and tungsten, are used as absorbers [Ref 3-17].

Since exposure is a 1X process, the placement accuracy of the pattern must be within the bounds dictated by the error allocation budget. This implies that the membrane must be rigid enough so that no distortion of the pattern is induced by the handling and exposure process. The membrane is not self-supporting, so it must be fastened to some support to provide the necessary rigidity. The support structure is usually a Pyrex ring. In general, the mask is fabricated starting from a 75 or 100mm silicon wafer, using a variety of techniques, but the fundamental structure of a mask is the same: a thin, uniform membrane is mounted on a structurally rigid holding frame. The pattern is applied on the membrane, typically by means of electron-beam lithography<sup>3</sup>.

### 3.3.3.1 Zone Plates for UV-Radiation

The availability of x-ray lithography systems at the NSL provides an appealing incentive to use them for the fabrication of zone plate arrays. This section briefly describes some of the x-ray lithography masks containing zone plate arrays designed to operate at the UV. An added incentive to develop a mask-based process was provided by the desire to “cast in stone” a zone plate design that had been carefully optimized through e-beam lithography to have nearly perfect dimensional control for all the zones in the zone plates.

---

<sup>3</sup> Pattern distortion is a serious problem in x-ray masks. The distortions are present not only from the writing of the mask via e-beam, but also due to the built-in stress in the absorber. At the NanoStructures Laboratory at MIT, an effort is underway in correcting for such distortions by means of localized heat correction techniques [Ref 3-18].

Although the precise details of the process are included in Appendix A, the key steps are briefly highlighted here. The objective of the process is to create a structure such as the one depicted in Fig 3-22. Starting with a standard x-ray mask, consisting of a 30mm-diameter  $\text{SiN}_x$  membrane supported on a Si ring bonded anodically to a pyrex frame, a thin layer of plating base (10 nm of Ti and 1.8 nm of Au) is evaporated onto the



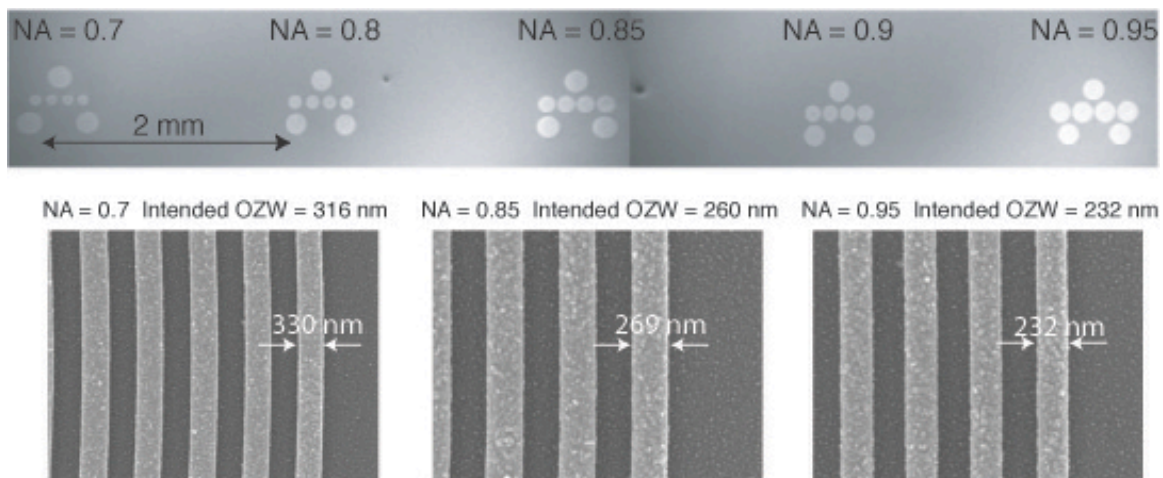
**Figure 3- 22.** Schematic of an X-ray mask.

mask. After spin coating the mask with the desired e-beam resist (PMMA in this case), patterning by means of e-beam lithography can take place. The mask is then developed and gold plated.

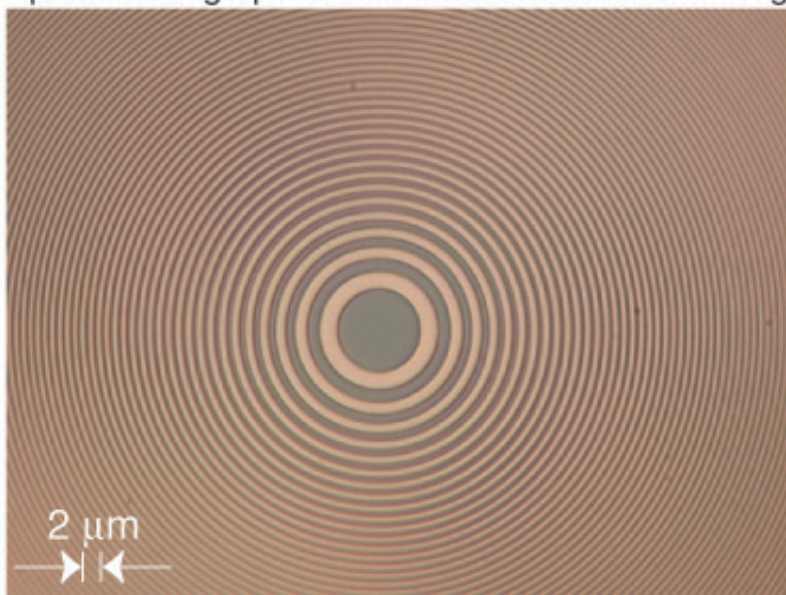
After removing the remaining resist, an absorber relief structure is left on the mask. The process must be optimized by carefully controlling and testing a large number of doses and biases during the e-beam patterning in order to achieve the right duty cycle and dimensional control in the final mask.

Figure 3-23 shows the final result of an x-ray mask with 5 sets of zone plates with numerical apertures ranging from 0.7 to 0.95. Each set of numerical apertures consists of a linear array of 4 zone plates (designed to operate at blue wavelengths) surrounded by 3 zone plates with matched focal lengths but designed to operate at  $\lambda = 633 \text{ nm}$  (these *satellite* zone plates will be used to set the zone plate array at the right focal distance with respect to the substrate to be exposed in a ZPAL system). The top of the figure shows a number of scanning-electron-micrographs illustrating the ability to achieve a duty cycle and outer-zone-width (OZW) dimensional control on the mask, after all the processing is done, that is very close to specification. The bottom of Fig. 3-23 shows an optical micrograph of the central zones of one of the *satellite* zone plates after plating. Following an identical process, x-ray masks with zone plates designed to operate at  $\lambda = 400 \text{ nm}$  containing sets of different numerical apertures, as well as larger linear arrays of zone plates, were also fabricated. All masks were also daughtered (i.e. a copy of the mask resulting in the negative of the *mother*, the original) to safeguard the originals, as well as to enhance the processing capabilities by having masks with different polarities. Different mask polarities enables the possibility the utilization of both positive and negative resists.





Optical Micrograph of Zone Plate Mask after Plating



**Figure 3- 23.** Top: Scanning electron micrographs of x-ray mask with 5 sets of zone plates with numerical apertures ranging from 0.7 to 0.95. By careful processing, close to ideal dimensional control can be achieved. Bottom: Optical micrograph of the central zones of a 0.9 numerical aperture zone plate designed to operate at  $\lambda = 633\text{nm}$ .



### 3.3.3.2 Zone Plates for Short-Wavelength Radiation

One of the key strengths of zone-plate-array lithography comes from its extendibility to be very short wavelengths, making it potentially capable of reaching the limits of the lithographic process. For the wavelength scaling to occur, it is crucial that fabrication techniques are developed to create zone-plate arrays capable of operating in these regimes (from EUV to soft and hard x-rays). Short wavelength zone plates are also crucial for x-ray microscopy applications, and there is a rich body of work that has been devoted to fabricating and testing x-ray zone plates that can have resolution as small as 30nm [Ref 3-19, Ref 3-20].

For hard x-ray microscopy applications (this technique allows one to nondestructively investigate microproperties in the bulk of thick samples), high-aspect-ratio zone plates are required in order to obtain sufficient efficiency into the first order<sup>4</sup>. The high-aspect-ratio (can be several microns high) must be combined with very high resolution, with outer zone widths that can be as small as 25nm. This would imply aspect ratios in excess of 40:1 in photoresist. This is simply not achievable with standard processing, since surface tension during wet photoresist development, the drying process, and the mechanical rigidity of photoresists lead to pattern collapse [Ref 3-21].

X-ray lithography provides a technique that can accommodate the need for high-resolution and high aspect ratios. The process relies on the utilization of self-aligned multiple exposures, as illustrated in Fig.3-24<sup>5</sup>. Starting with a conventional x-ray mask, using a high-resolution negative resist (such as HSQ from Dow Corning), the zone plates are patterned by means of electron-beam lithography. After development, the mask is plated to the maximum thickness that can be achieved (determined by the resist height).

---

<sup>4</sup> The optimal thickness of the zone plate, determined by a  $\pi$ -phase shift requirement, depends on the wavelength,  $\lambda$ , and the absorber/phase shifter material properties. The exact relationship is determined by the following relation:

$$t(\pi) = \lambda/2\delta$$

where  $\delta$  is determined from the complex refractive index,  $n = 1 - \delta - i\beta$

<sup>5</sup> The idea was first proposed by Azalia A. Krasnoperova, et al [Ref 3-22] and developed independently (i.e. reinvented) by the author and by Todd Hastings (also graduate student in the NSL)

## Self-Aligned Fabrication Process for X-Ray Microscopy Zone Plates

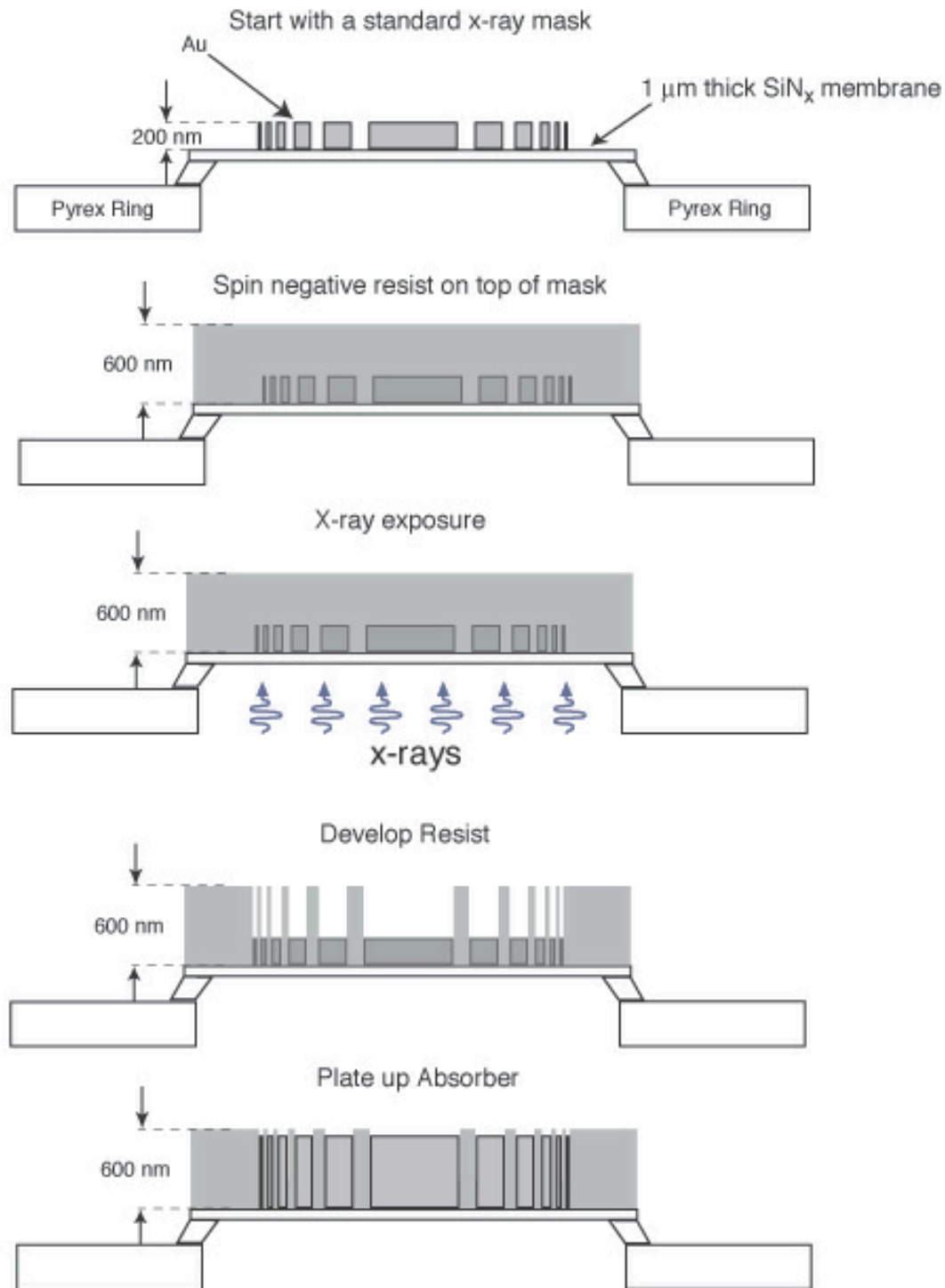


**Figure 3- 24.** Self-aligned x-ray lithography process flow for the fabrication of x-ray microscopy zone plates.

For high-resolution patterning, this height will typically be at most  $\sim 200\text{nm}$ . After plating, another layer of negative resist sensitive to x-ray wavelengths is spun on the mask (HSQ is a good solution, since it is also sensitive to x-rays). The mask is then mounted in the x-ray lithography exposure apparatus and is simply exposed from the back. The existing absorber will prevent the x-rays from reaching the negative resist that sits

on top of the absorber, while all other areas will be exposed. After development, all unexposed areas will be dissolved away (this is why it is important that the resist has a negative tone). The mask can then be plated again, resulting in a higher aspect ratio zone plate with perfect alignment. This process can be repeated until the necessary aspect ratio is obtained.

The details of the process are now described in more detail. The zone plates on the x-ray mask were created by means of x-ray lithography, through a daughtering process of a mask patterned with a RAITH-150 electron-beam lithography system. The resist utilized for the daughtering process was 250nm of PMMA, baked at 180°C for 1h. The x-ray exposure time was 24 hours. A separate exposure with an optical aligner was done in order to remove all the areas surrounding the membrane that were covered with PMMA (this is important to allow an adequate contact area for electroplating). Development was done in a solution of 1:3 methyl isobutyl ketone: isopropanol (MIBK:IPA) for ~90sec (the development was monitored with an AFM). After a 20s O<sub>2</sub> clean, the mask was plated in a gold bath having the following parameters: conductivity = 76.5 mS/cm, temperature = 39°C, current = 14.1mA, resulting in a rate of ~20nm/min. The resulting mask, after the PMMA was removed in an acetone bath, consisted of 220nm-thick gold zone plates.

The mask was then spun-coated with a spin-on-glass negative resist (FoX-16, by Dow Corning, also known as HSQ) at 3000 RPM for 60sec, resulting in a layer 500nm thick. The resist was oven baked at 150°C for 30min, followed by a 220°C bake for another 30min. At this point, the mask was ready for the self-aligned x-ray exposure. A 14h exposure was performed. The mask was then developed in CD-26 (a TMAH based developer) for 20 min. It was then introduced in the plating bath with similar conditions to the ones previously described, except for the fact that the current was 12.9mA, as

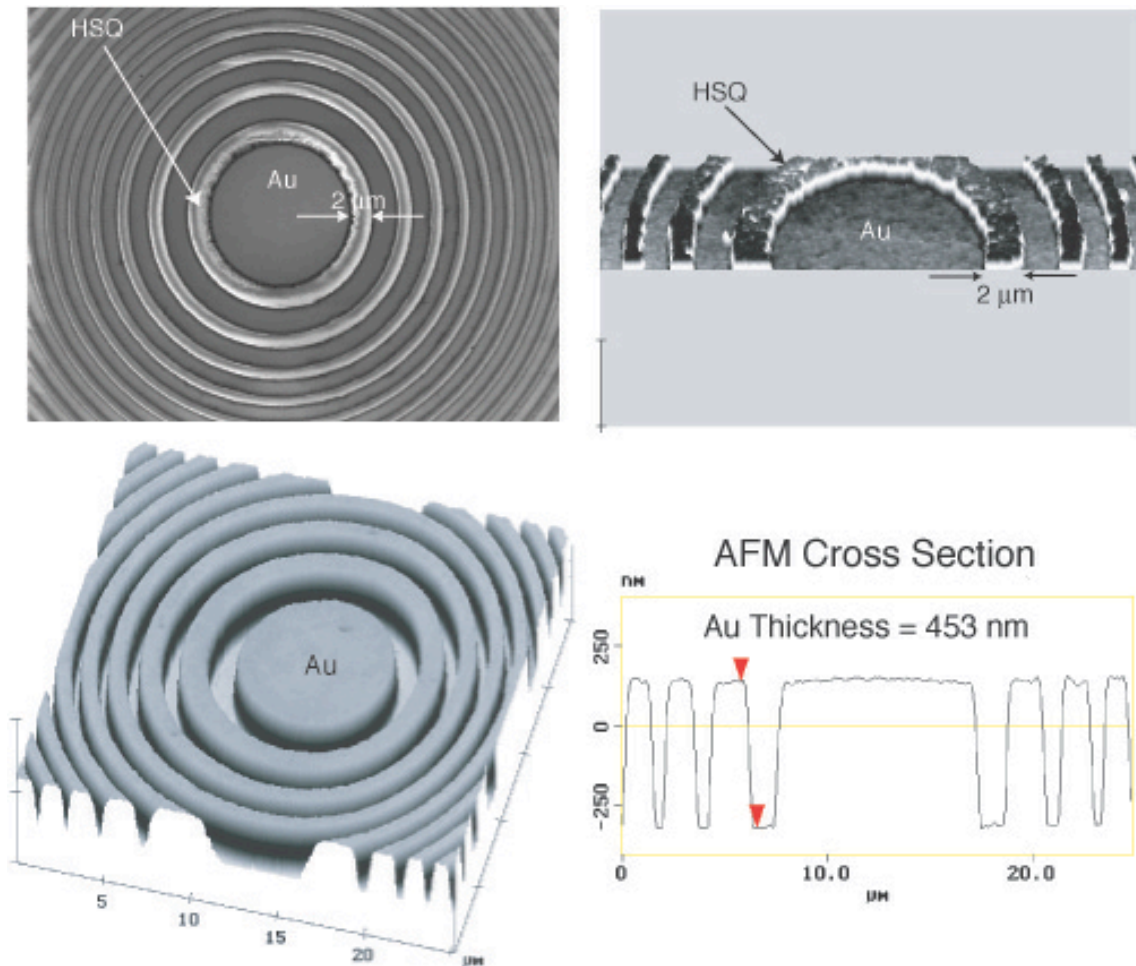


**Figure 3- 25.** Results of self-aligned high-aspect ratio zone plate mask with applications for x-ray microscopy. Top-Left: Scanning electron micrograph of the central zones after the self-aligned electroplating. Top-Right: AFM scan of central zones after electroplating. Bottom: After the resist (HSQ) was removed a high-aspect ratio structure remains, with an absorber thickness that could not be achieved with a single layer exposure.

opposed to 14.1mA, to compensate for the smaller plating area. The plating was monitored by means of an atomic force microscope until the gold reached the top of the resist. Fig.3-25 shows the results of this process, where zone plates were created with an absorber thickness that was 453nm, twice the height achievable with standard single-layer mask-making techniques. Higher absorber thicknesses can be readily achieved by repeating this process a number of times, since it is a self-aligned, self-planarizing technique.

### 3.3.4 Three Zone Plate Fabrication Processes for Lithography Applications

The following sections describe three techniques aimed at the fabrication of zone-plate arrays designed to be used for a ZPAL system operating at the UV. The processes are described chronologically, showing how the eventual final fabrication technique evolved in time from the partial successes of the original processing ideas.

The requirements for fabricating phase zone plates at UV for lithography applications can be clearly defined. *First*, as previously described, it is crucial that the dimensional control of the zones of the zone plates be as close to perfect as possible. Duty-cycle and radial-period errors should be kept to a minimum to enhance the lithographic performance of the elements. *Second*, on the substrate containing the zone plates, as illustrated in Figure 3-26, it is necessary to place an absorbing layer on the areas surrounding the elements. This absorbing layer prevents unwanted radiation from reaching the substrate when the zone plates are used for lithography. Alignment between the absorber layer and the zone plates is critical. The *third* and last key challenge, requires achieving a phase shift of  $\pi$  between alternate zones.

Before embarking on a description of the individual processes, let's analyze in general how these three challenges can be tackled with standard fabrication techniques. The first challenge, of dimensional control, was addressed in detail in previous sections in relation to electron-beam-lithography patterning. It is important to understand, however, that what matters is that the *final* processed zone plate achieves the dimensional control (right duty cycle and so on), and that it is of little use to start with a nearly perfect e-beam patterned zone plate if, after subsequent steps (be it reactive ion etching, be it baking, etc), the painstakingly optimized e-beam defined features are altered. The second challenge, that of placing an absorber in the areas surrounding the zone plates, can be achieved by means of two aligned lithography steps. For example, one lithography step would define the circles that would contain the zone plates (as well as a set of alignment marks), and a second step (after registering to the alignment marks) would write the actual zone plates. How well these two exposures can be aligned will have an impact on the lithographic performance of the optics, since unwanted radiation will leak through the misaligned edges of the absorber.

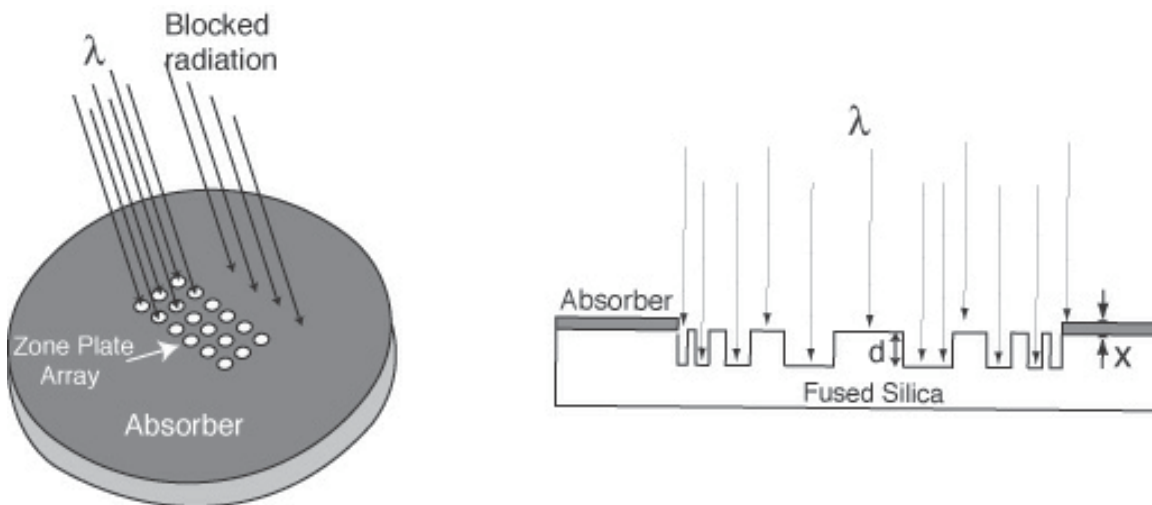


**Figure 3- 26.** Need for an Absorber. (a) Three dimensional view of the diffractive optical array and the substrate underneath. A layer of an absorbing material surrounding the optics is needed in order to prevent undesired radiation from reaching the substrate. (b) Side view of the fused-silica substrate with a phase zone plate etched into it.

Given the fact that zone plates will typically be patterned by means of electron-beam lithography, it is important to realize that aligned exposures with e-beam systems are always complicated and time consuming, since fields have to be aligned one at a time. The final process presented here will bypass the need for this alignment, greatly simplifying the entire procedure. The third challenge, that of creating the right phase-shift between alternate zones, is a relatively less challenging problem than the previous two. Reactive-ion etching in combination with atomic force microscopy provides a process that is both powerful and reliable. The main challenge arises from the large number of features of different dimensions that are present in zone plates, which can result in different etching rates for different areas of the zone plate. Obtaining good sidewall profiles can also be of importance in order to maximize efficiency.

#### **3.3.4.1 The Chromium Process**

The first fabrication approach undertaken is schematically illustrated in Fig.3-27. The objective was to define by means of two aligned lithographic exposures: (1) the circular area that will later contain the zone plates, and (2) the actual zones that define the optic.

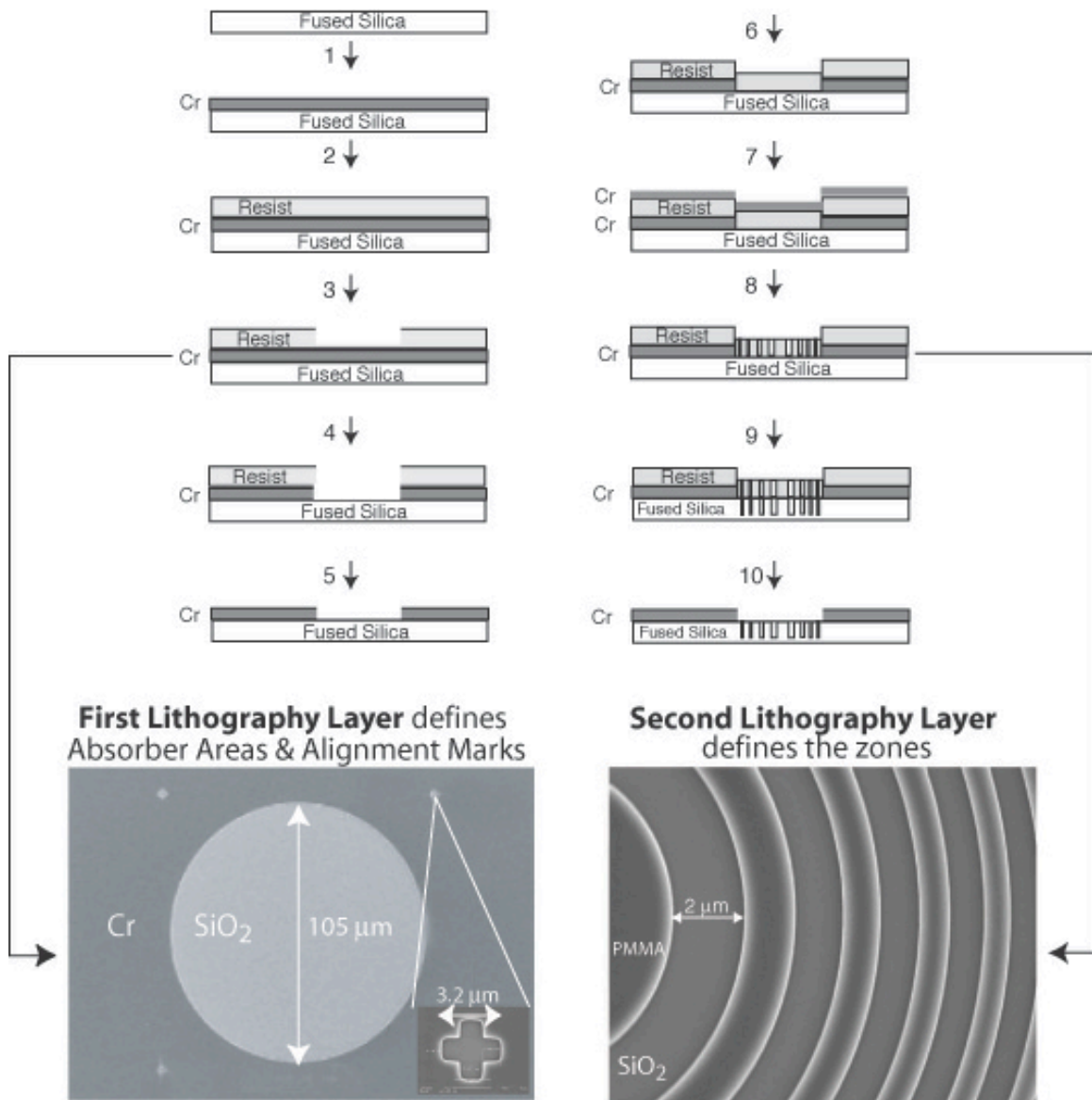


**Figure 3- 27.** *Chromium Fabrication Process* for UV and DUV Zone Plates. Steps 1-5 define the area where the diffractive optics will be placed in subsequent steps. Chromium (Cr) is used as the absorber material in this process, but a number of other materials could also be employed. Steps 6-8 define the diffractive optics. Steps 9-10 transfer the resist patterns into the fused silica substrate by means of reactive-ion-etching.



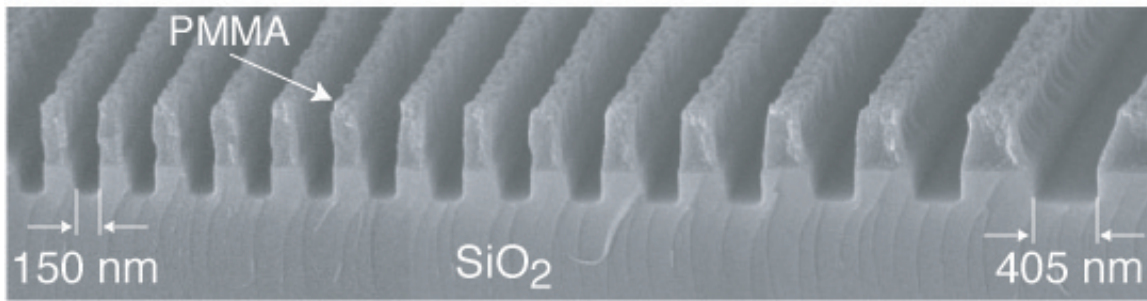


**Figure 3- 28.** Scanning electron micrograph of fused silica sample etched in  $\text{CHF}_3$  with PMMA as a mask. The PMMA was patterned by means of electron beam lithography. The chamber conditions inside the RIE were the following: Pressure = 20 mT, DC Bias = 200V, Gas = 20 sccm of  $\text{CHF}_3$ .

Starting with a fused-silica substrate, a layer of chromium is evaporated. The thickness of this layer is chosen such that it will absorb close to 100% of the incident light at the wavelength of choice. After spinning resist (PMMA was used for this process), the circular apertures are defined, along with a set of alignment marks placed at the edges of each electron-beam lithography field. Once developed, with the resist as a mask, a wet chromium etch removes the Cr that was underneath the area that was exposed.

The substrate is then prepared for the second lithography exposure by spinning resist and evaporating a thin layer of chromium (5 nm) on top to avoid charging during the e-beam exposure. Prior to exposing the zone plates, each field is aligned by appropriately scanning the edges of the previously defined circles and registering to the existing alignment marks. The system then proceeds to expose all the zone plate zones in the manner described in Section 3.2.2.1. Development of the resist defines a relief structure containing the zones. The resist is then used as a mask in a reactive-ion-etching (RIE) step used to create a  $\pi$ -phase shift between alternate zones, as illustrated in Fig.3-28. Process monitoring zone-plates are placed in particular locations on the substrate, allowing one to check etch depths by means of atomic-force-microscopy after locally removing the resist mask through a controlled oxygen ashing step. Great accuracy can be achieved in terms of phase-etch control by such careful processing. The remaining resist is removed through an oxygen etch. The final processing steps consist in covering up the

alignment marks that surround each zone plate of the array. This can be done by spinning a positive resist and by opening up the areas over the alignment marks by means of an optical lithography exposure<sup>6</sup>. After development, chromium is evaporated and a lift-off is performed. The zone plates are now ready.

<sup>6</sup> This exposure was done with an optical microscope. The process is as follows: With a filter preventing the illuminating light from exposing the resist, each alignment mark is located. An iris is closed to illuminate only an area only slightly larger than the mark. The filter is removed for a brief time allowing the white light to reach the substrate and hence locally expose the resist. The process is repeated for each mark, four per zone plate.



While this process provides a viable method for zone plate fabrication, it suffers from some serious deficiencies. Let's briefly analyze them. The first and most serious limitation is created by the chromium wet-etching step. The complications are twofold: (1) the etch is isotropic, making it difficult to control the final dimension of the circle, (which can cause a deleterious misalignment between the outer zones and the absorber), and, (2) chrome on oxide is a problematic combination to etch, with the Cr having a tendency to leave small nanometer-sized islands that can not be removed. This problem is severe, and becomes critical because the small islands of un-etchable Cr serve as a mask in the  $\text{SiO}_2$  RIE step (step 9 in Fig.3-27), causing "grass" in the etched zones. The author could not find a systematic way to solve this problem, despite valiant and desperate efforts that spanned many months. The author still regrets such long, and ultimately wasted, days.

The process suffers from other limitations that are less serious, but that nevertheless hinder the applicability of the technique for large-array manufacturing. The double lithography step requires aligning each zone plate one at a time. This process takes a few seconds per field, if electron-beam lithography is used. If a million zone plates are required, even ignoring the actual zone plate writing time, the process would take millions of seconds (spent just doing alignment), a clearly unacceptable figure.

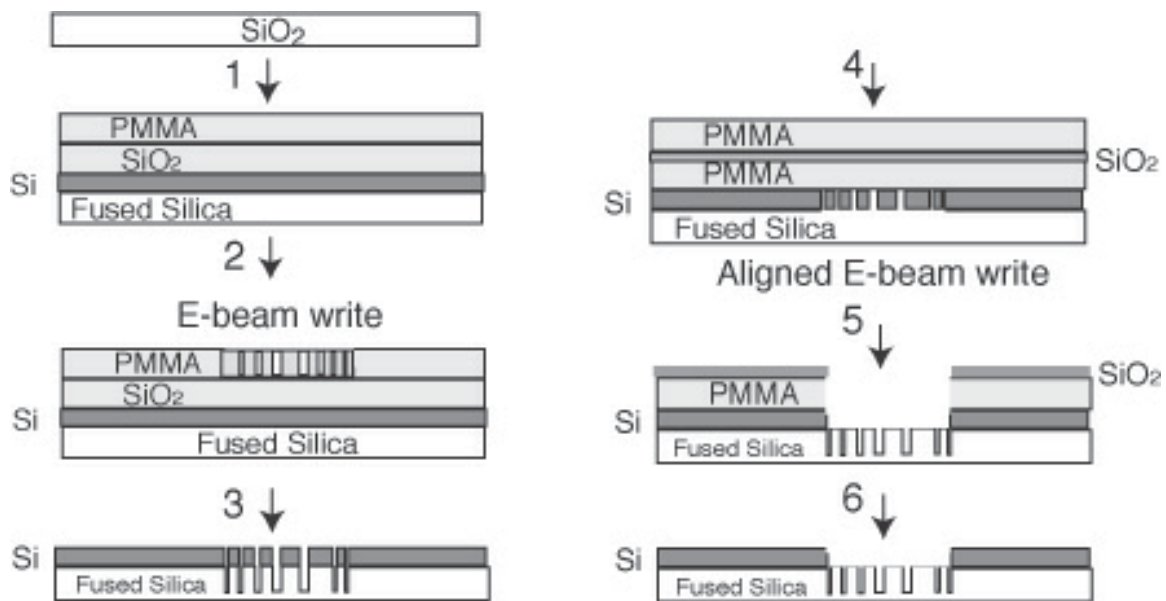


**Figure 3- 29.** *Silicon Fabrication Process* for UV and DUV Zone Plates. Steps 1-3 define the zone plate zones and alignment marks, which get transferred first into silicon, and then into the fused silica. Steps 4-6 remove the silicon mask the remains over the zones.

### 3.3.4.2 The Silicon Process

The desire to remove all wet-etch-based steps became a priority in order to develop a robust zone plate fabrication process. Given the difficulty of etching metals with the RIE capabilities available at the NSL, it was decided to utilize silicon as the absorber layer, instead of chromium. The process is depicted in Fig.3-29. The chief advantage of using Si as an absorber relies on the fact that a dry-etch technique is available to remove it (there are a number of reactive-ion etching recipes, with  $\text{Cl}_2$  being the most widely used).

Starting with a fused silica optical flat, silicon is sputtered. The height of the Si is chosen in order to provide over 99% attenuation at the wavelength of choice ( $\lambda = 442\text{nm}$ ). Silicon dioxide is then evaporated (this oxide layer will serve as a mask to etch the Si). The zone plates are then patterned by means of e-beam lithography. An atomic-force-microscope image of the PMMA after development is shown in Fig.3-30.

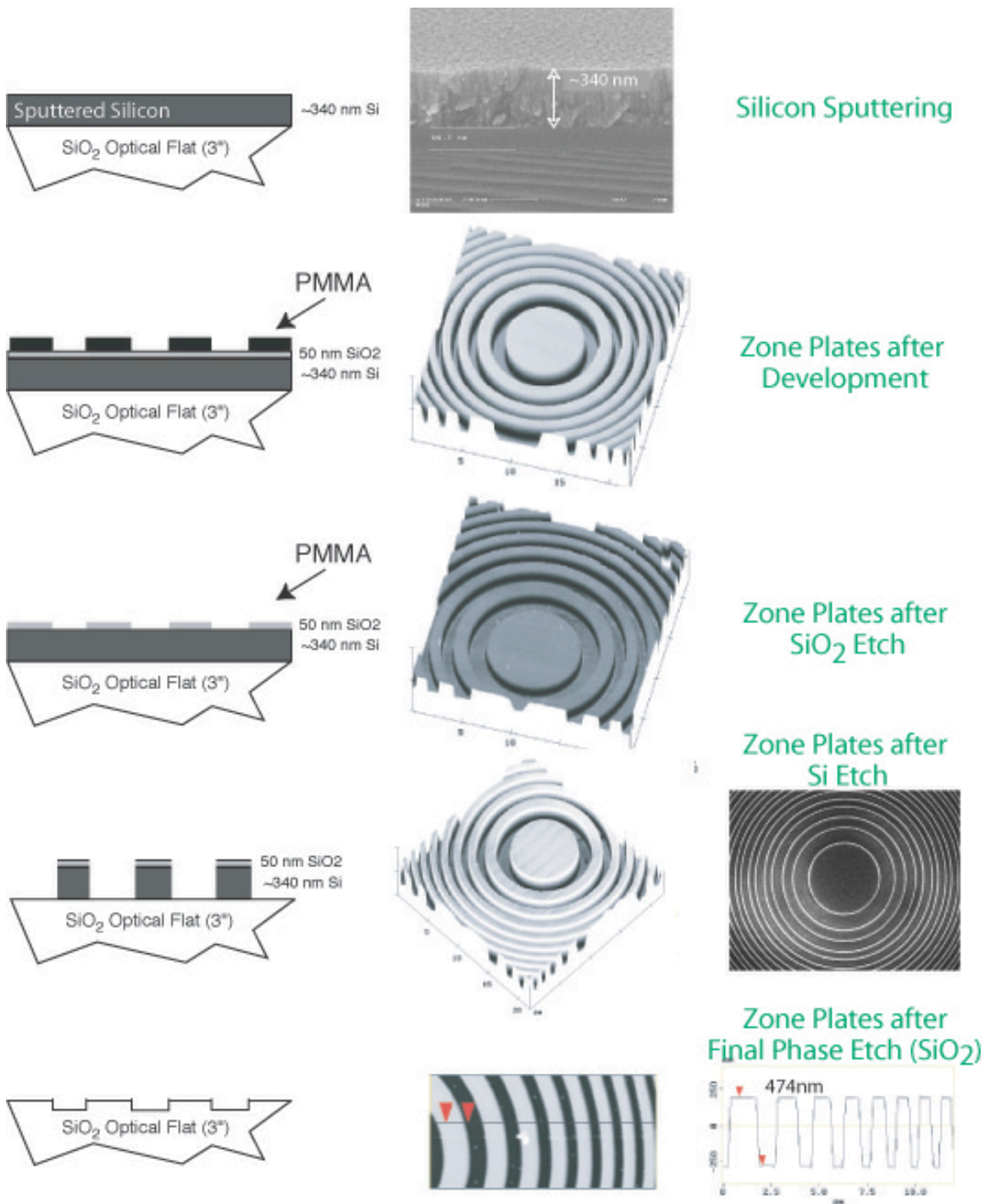


**Figure 3- 30.** Atomic Force Microscope images of fabricated zone plates using the *Silicon Process*. Note that careful processing allows one to obtain almost perfect phase control (see bottom AFM cross-sectional image; the etch goal was actually 474nm)

With the PMMA as mask, the zones get transferred in to the oxide layer, which in turn serves as the mask to etch the silicon layer. This later step is achieved by means of a chlorine etch inside a reactive ion etcher (RIE). At this point, we have a fused-silica substrate that contains zone plates with zones defined in silicon. The final fused-silica etch can now take place. This etch will define a  $\pi$ -phase shift between alternate zones, so careful

control is necessary. The fused silica is etched with  $\text{CHF}_3$  inside a RIE in a series of steps. After each step, the total etched height is measured by means of atomic-force microscopy. Nearly perfect  $\pi$ -phase shifts can be achieved with this technique, as illustrated at the bottom of Fig.3-30, where the goal to create a 474nm etch depth was accomplished with nanometer precision. The remaining steps of the process involve removing the Si that remains on top of the unetched zones. This is done, as is depicted in Fig.3-29 (4-6), through a second aligned exposure and subsequent RIE steps.

The above description provides a big-picture overview of the required process. Although zone plates can indeed be fabricated with this method, it is very complicated, with lots of subtle processing tricks and optimizations that were sometimes hard to reproduce. Fabricating new sets of zone plates with the process took weeks, even once all the parameters were more or less optimized. As is well known to anybody with processing experience, for every new layer that is added to a fabrication procedure, the total processing time goes up by a factor of  $n$ , where  $n$  is a number between 2 and 100, depending on the size of the moon.

Jokes aside, the process does suffer from an excess of complexity. Too many RIE steps made it hard to maintain appropriate duty-cycle control of the zones. In addition, a second aligned lithography e-beam exposure was still required, resulting in all sorts of problems due to the fact that the alignment marks were buried into the fused silica by the time all the zone etching was finished. Being able to image those marks through all the spun-on layers later added was a big challenge. And the fact remains (as was mentioned in the chromium process description) that having to go through a second aligned exposure prevents large array manufacturing.

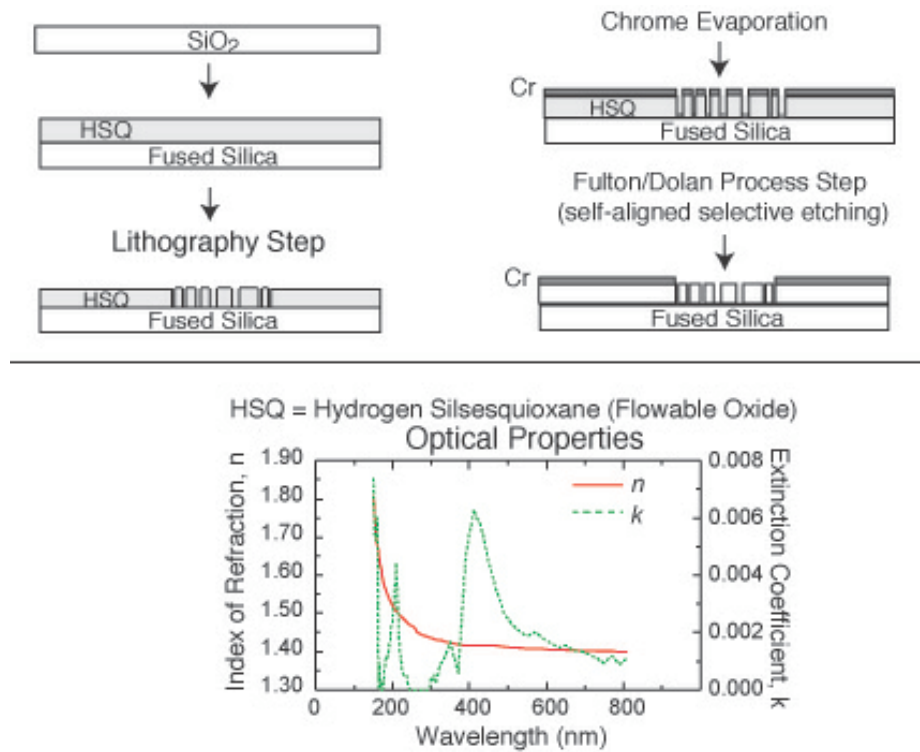


**Figure 3- 31.** Top: Typical sequence of the self-aligned process requiring a single-lithography step. Starting with a transparent blank material, HSQ is spun on it. The thickness of the HSQ is chosen to provide the appropriate phase step for the diffractive optical element. After patterning the elements in HSQ, the absorber material is evaporated. Note that the absorber (chrome in this case) inside the diffractive element and outside is not electrically connected. The absence of electrical connectivity will allow for the absorber within the diffractive elements to be removed by means of a wet-etch Fulton/Dolan technique. Bottom: The optical properties of HSQ are almost identical to those of fused silica.

### 3.3.4.3 The Self-Aligned Process

A solution to all the problems encountered in the two previously described processes has been devised and implemented through the work reported here. This novel fabrication process for zone-plate arrays is capable of high resolution, requires a single lithography step, and no etching (even for the case of phase zone plates). For this process the negative resist HSQ (hydrogen silsesquioxane, by Dow Corning) is used, which is sensitive at both e-beam and x-ray wavelengths. HSQ's extraordinarily high resolution ( $\sim 10\text{nm}$ ) and its glass-like properties make it an optimal choice for fabricating diffractive-optical elements that operate in the UV and DUV regimes. HSQ has an index of refraction very close to that of fused silica, and a negligible absorption down to

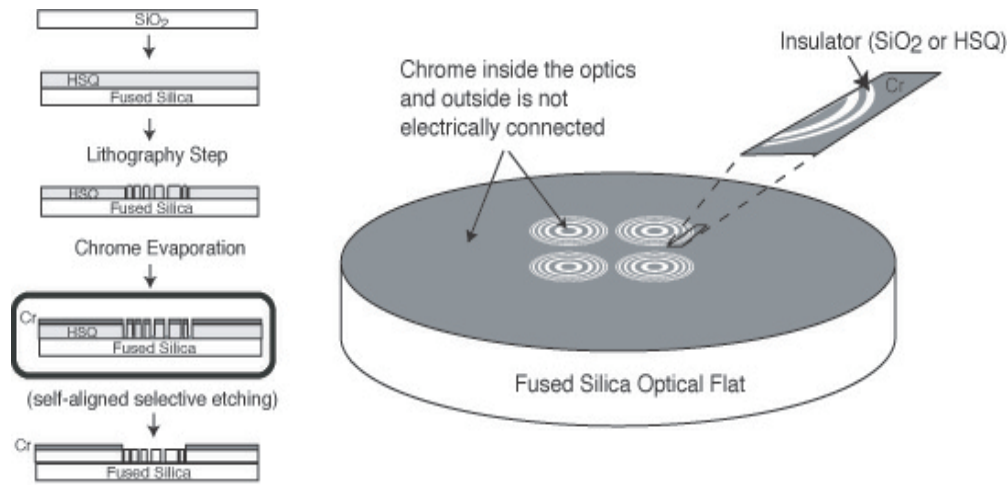


**Figure 3- 32.** Detail of the process after the absorber has been evaporated. Note that the absorber (chrome in this case) inside the diffractive element and outside is not electrically connected. The lack of electrical connectivity will allow for the absorber within the diffractive elements to be removed by means of a wet-etch Fulton/Dolan technique (see Figure 3-34).

157nm. As a result, if the resist is spun to the thickness corresponding to the desired phase step for the optic, patterning and development are the only required steps. The process is schematically illustrated in Fig. 3-32.

The process bypasses the need for a second lithography step while achieving perfect alignment between the absorber and the zones of the zone plates. The solution arises from the realization that if one patterns the zone plate and then evaporates the absorber material onto the substrate, the absorber material (typically a metal) that lands in the trenches and on top of the zones is not electrically connected to the metal area surrounding the zone plates. This situation is depicted in Figure 3-33 (right). Rather than having to perform a second lithography step requiring nanometer level alignment so as to remove the absorber that is on the zones, the lack of electrical connectivity between the metal inside and outside the zone plates allows for the removal of either the inside metal, or the outside metal, with one single high-resolution wet etch step.

The self-aligned wet etch technique was first proposed by T.A. Fulton and G.J.Dolan in 1982 [Ref 3-33, Ref 3-34]. The process, initially named “Brushfire Lithography” and later “Canyon Lithography”, was proposed as a means to speed-up electron-beam lithography writing of chrome-on-glass masks.



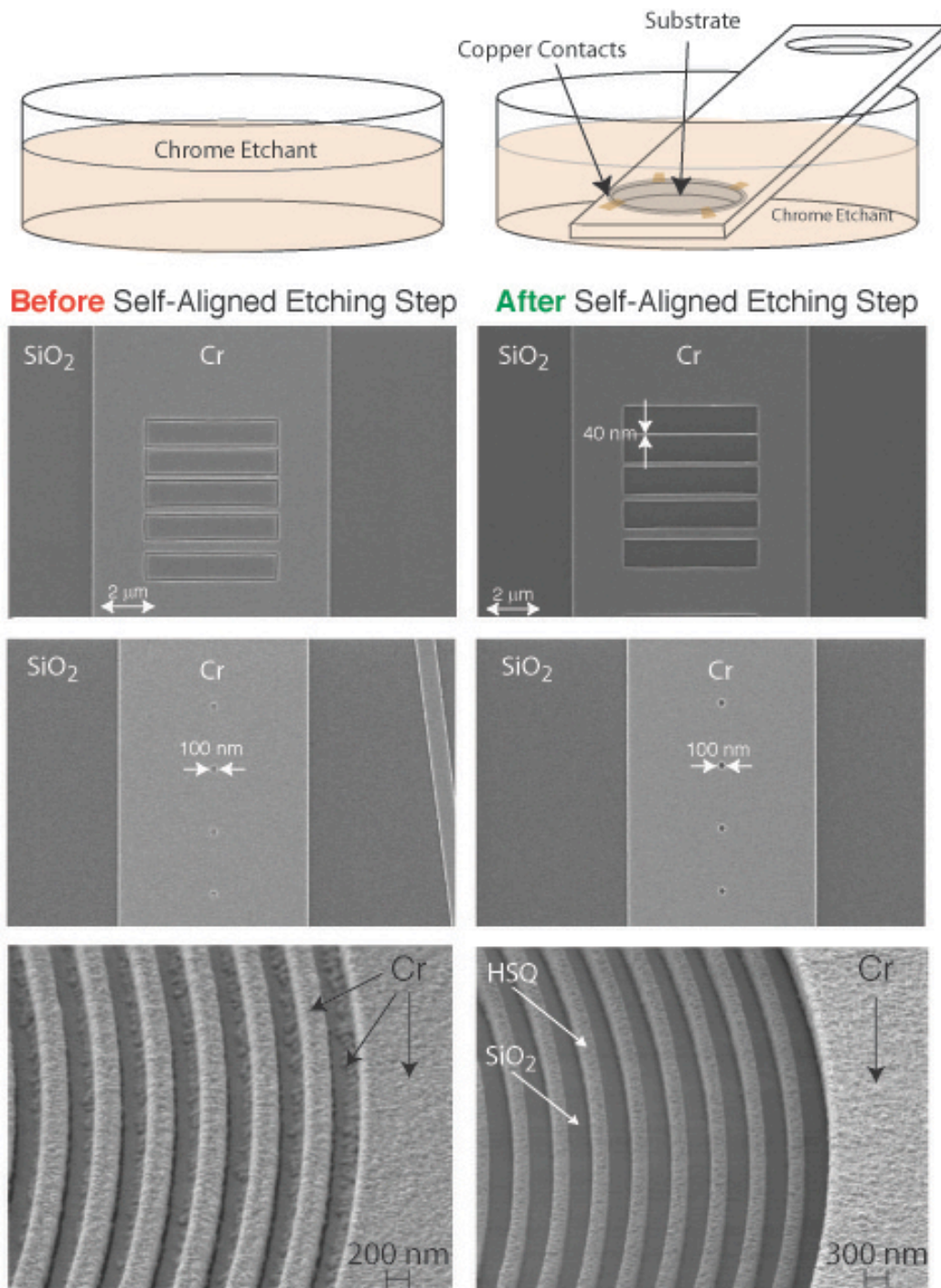


**Figure 3- 33.** Self-aligned etching process results. Top: Schematic illustrating the experimental implementation. Bottom: Scanning electron micrograph of a variety of patterns illustrating the high-resolution capabilities of the process, as well as its applicability to zone plate fabrication. Bottom Right: The Cr from the top of the zones and in the trenches is removed after the self-aligned etching process was applied. Note the perfect alignment between the surrounding absorber and the last zone of the zone plate.

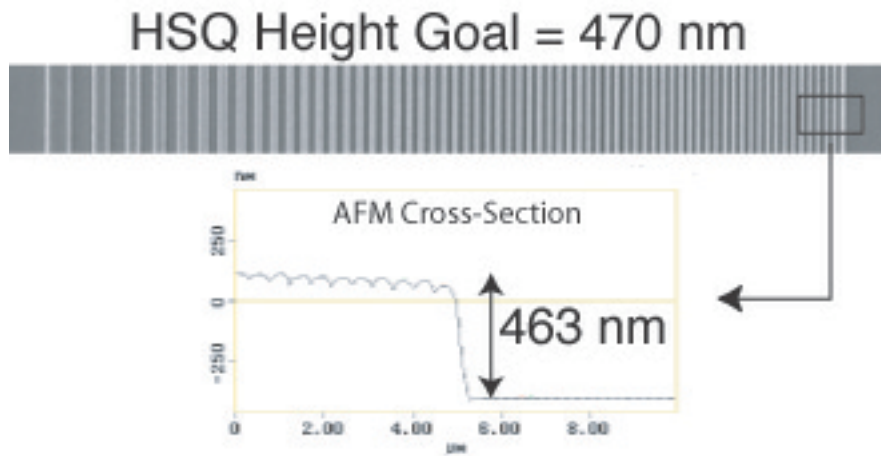


**Figure 3- 34.** By spin-coating the HSQ, the phase shift of the zone plates can be controlled to  $\sim 1\%$ . Top: Scanning electron micrograph of a section of a high-numerical aperture zone plate. Bottom: Atomic force microscope scan of the outer zones of the zone plate. While the trenches in the outer zones can not be resolved due to their small size, the overall height-step can be accurately measured.

Instead of fully exposing a pattern with the e-beam system, only the outlines of the individual features in the pattern are exposed, leaving the completion of the pattern (“the filling in”) to the electrochemical wet etch step. The principle behind the technique arises due to the fact that by biasing electrically connected regions of a metal film at different potentials one can selectively etch, electroplate, or anodize appropriately patterned substrates.

The technique was implemented for the fabrication of zone plates, with chromium as the etching material. Cr is a particularly suitable metal, since the active-passive transition provides a strong inhibition or enhancement of etching rates for suitable bias and etchants [Ref 3-34]. The Fulton-Dolan process is capable of both positive and negative tone etching. In the positive-tone case, the one of interest for zone plate fabrication, all metal that is biased will stay after the substrate is introduced in the etchant, and all parts not electrically connected will be etched away. Figure 3-33 illustrates the experimental implementation of the technique as well as some of the patterning capabilities that can be achieved. The technique is as simple as contacting the Cr metal with copper contacts spaced symmetrically around the edges of the substrate, and then immersing the substrate and the contacts inside chrome etchant (ceric ammonium nitrate). The copper passivates the contacted regions while isolated features etch. In this process copper is consumed and a significant current flows through the chrome film. The resulting voltage variations in the thin film limit the distance over which passivation is effective, so that for large-area patterns the contacts must be sufficiently closely spaced (or the etchant sufficiently diluted) to passivate the desired region. The process latitude of the technique is simply fantastic. The chrome film can be “over-etched” (i.e. left inside etch bath after apparent completion) for as long as one wants without apparent degradation in the final pattern. As can be seen in Fig.3-33, the technique is capable of very high resolution. When applied to zone plate fabrication, perfect alignment between the outer-most zone and the absorber (the Cr) can be achieved.



By spin-coating the HSQ, the phase shift of the zone plates can be controlled to  $\sim 1\%$ , as shown in Figure 3-34. The figure presents an atomic-force-microscope scan of the outer zones of a zone plate. While the trenches in the outer zones can not be resolved due to their small size, the overall height-step can be accurately measured, showing that a 463nm height difference is present (the goal was  $\sim 470\text{nm}$ ). Furthermore, since the height was achieved by spin-coating, all zones of the zone plate have the same phase-step, something that is more difficult to achieve with a reactive-ion-etch based procedure.

The self-aligned process has enabled the capability of fabricating large arrays of zone plates in reasonable times. Figure 3-35 shows the largest high-numerical-aperture array fabricated in this work, with over 1,000 zone plates designed to operate at  $\lambda=400\text{nm}$ . Local duty-cycle was maintained throughout the array, and no errors were detected across the array. The Fulton-Dolan process achieved perfect alignment for all the elements in the array. Local random checks across the array confirmed that the phase height across the zone plates was uniform<sup>7</sup>.

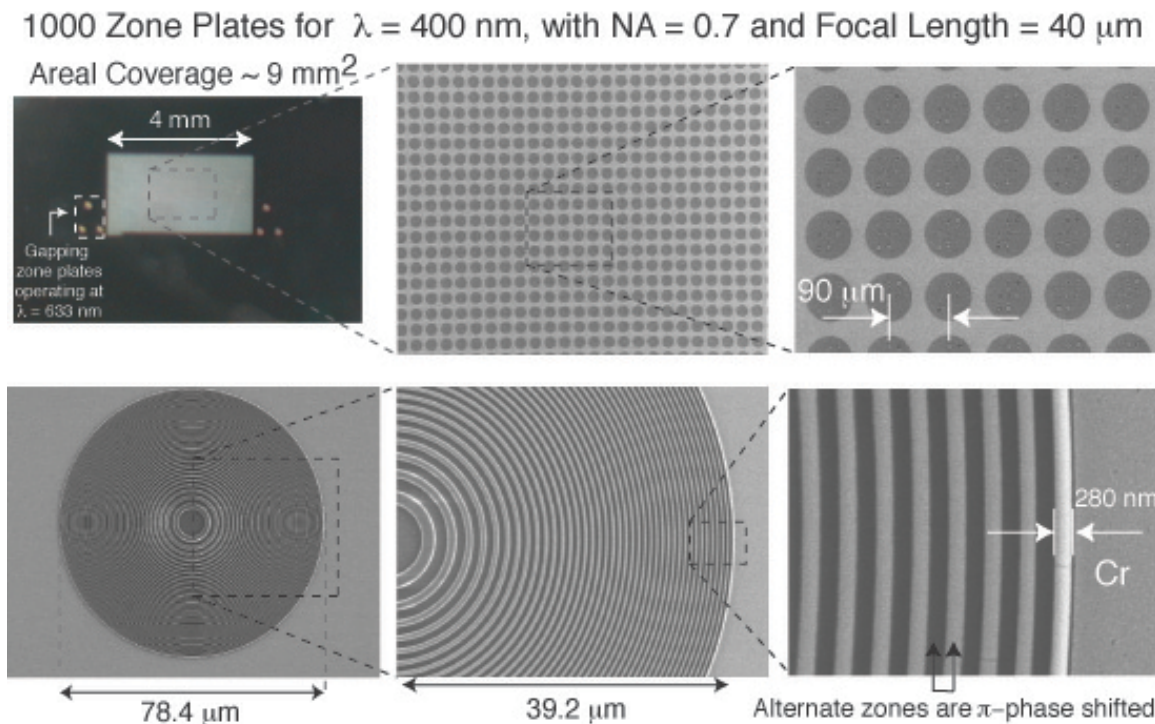


**Figure 3- 35.** Large zone plate arrays can be readily fabricated with our novel process that requires a single lithography exposure and no etching, even for the case of phase zone plates. Top-left: Optical micrograph indicating showing an array containing over 1,000 zone plates with an aerial coverage of  $9 \text{ mm}^2$ . Bottom-right:

<sup>7</sup> More details of the process are provided in Appendix B.

Detail of the outer-most zones. The duty-cycle is very close to 50%, and the phase shift between alternate zones was controlled to about 1%.

#### 3.3.4.4 Order Sorting Apertures

The existence of multiple diffracted orders reduces the available contrast of zone plates in lithography applications. It would therefore be advantageous to include some form of order-sorting aperture in the space between the zone plate and the substrate to be exposed, in order to block all unwanted orders while allowing for first-order to go through. The idea is illustrated in Fig.3-36. Contrast can be dramatically improved in this configuration.

This section briefly presents a possible self-aligned fabrication procedure for the creation of order-sorting apertures. The process is outlined at the top of Figure 3-38. Starting with a phase-zone plate fabricated in fused silica (or HSQ), a thin piece of fused silica is bonded by means of a high-temperature bake. Since for ZPAL the order-sorting

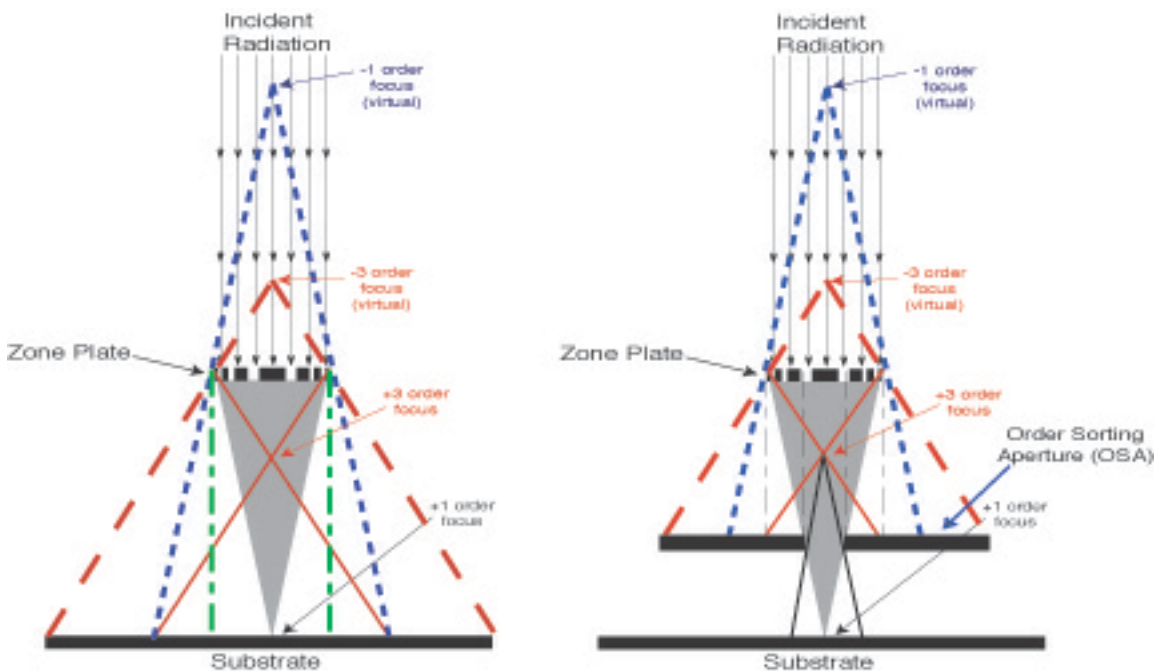
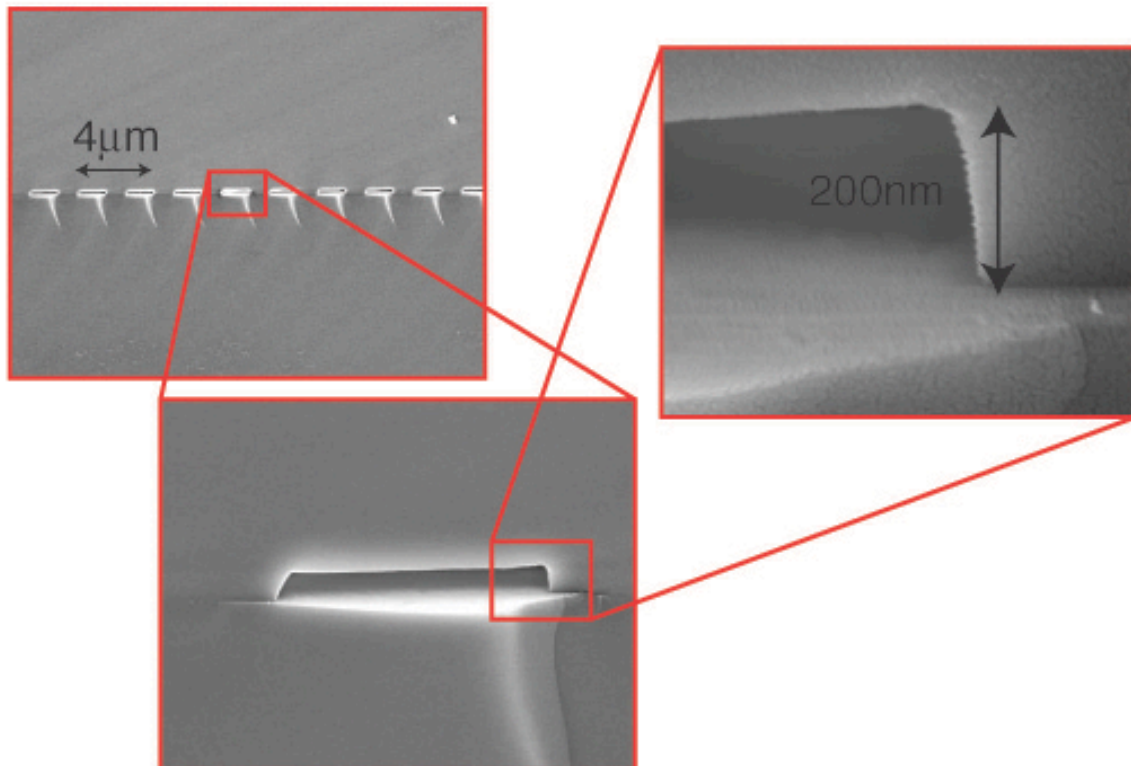
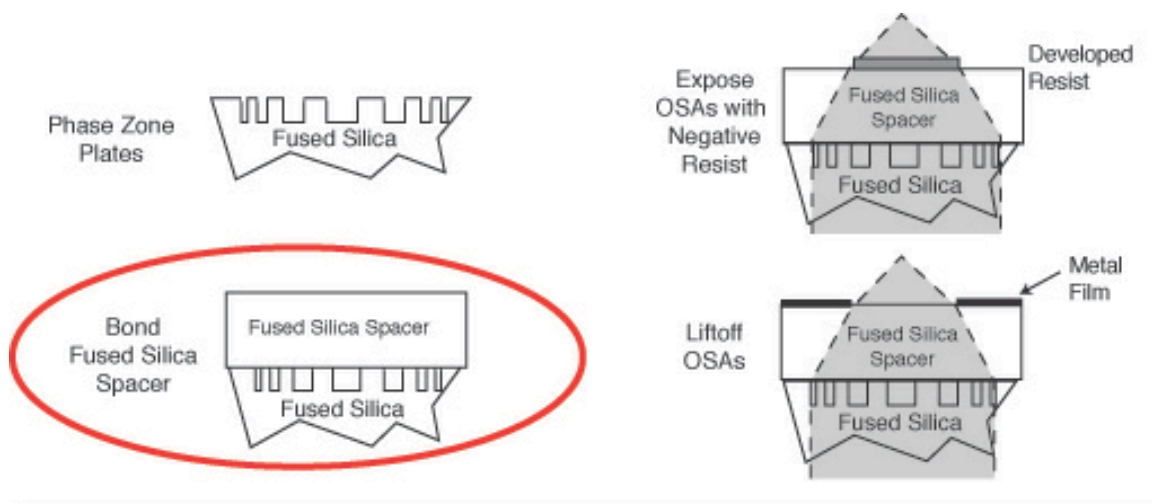


**Figure 3- 36.** Left: The existence of multiple diffracted orders reduces the available contrast of zone plates in lithography applications. Right: Order-sorting apertures can block unwanted orders while allowing first-order diffraction to go through.

aperture will have to be placed between the zone plate substrate and the wafer to be exposed, the bonded piece must be very thin (tens of microns). If need be, a thicker piece might be bonded and then thinned down with a carefully controlled polishing step. The scanning electron micrographs of Figure 3-37 show the first results that

were obtained in our efforts<sup>8</sup> to bond two fused silica wafers (one of them containing a large-area phase grating). The results are very encouraging, indicating that the high-temperature bake ( $\sim 1000^\circ\text{C}$ ) still maintains the grating profiles.

Once bonded, the remaining steps of the process consist of spinning negative resist onto the bonded piece and exposing through the back of the zone plate, as illustrated in Fig.3-37. The converging beam of light will expose the negative resist, which after development, will leave a self-aligned island that can be used in a lift-off process to produce the desired order-sorting aperture.



<sup>8</sup> This work was done in collaboration with Dr. David J. Carter.

**Figure 3- 37.** Top: Process flow for fabricating self-aligned order-sorting apertures. Bottom: Scanning electron micrographs showing the results of bonding two fused silica wafers (one of them containing a large-area phase grating). Note that the visible spikes coming down from the edges of the bonded grooves are an artifact of the cleave. The results are very encouraging, indicating that the high-temperature bake still maintained the grating profiles.

### 3.4 Replication Techniques

If ZPAL is ever to be commercially introduced in the marketplace, it is crucial that viable zone plate manufacturing techniques are developed. By viable, we mean expanding beyond small-array manufacturing in a laboratory setting, to arrays containing one million zone plates. It must also be done in a cost-effective manner. The following sections address a number of proposals that have large-array fabrication as a goal.

#### 3.4.1 Throughput in Electron-Beam Lithography: How many zone plates can one make?

If we were to use either of the e-beam systems we have at MIT's NSL, given that each zone plate requires a few minutes to write, a million zone plates would take a couple of years to be completed! This is clearly not an option. With both the RAITH system and the VS-26 (both vector-scan systems), the writing of zone plates is limited to arrays containing thousands of elements, but certainly not hundreds of thousands, let alone one million.

All hope is not lost with the prospect of utilizing e-beam systems for large array manufacturing. It is possible that such arrays could be fabricated utilizing a mask-making electron-beam-lithography tool such as the MEBES system from ETEC [Ref 3-35], since writing time for this tool is pattern-independent. Fabricating an array of 1000x1000, assuming each zone plate is ~100 microns in diameter, would require an area coverage of 10x10cm. This area is similar to a conventional mask, which can be written in 6.5 hours using a 120nm beam size, or 20 hours if a 60nm beam size is utilized [Ref 3-36]. Assuming that a MEBES system can meet all the tolerances for zone plates, the issue of absolute placement of the centers of the zone plates still remains. With a 21nm (3-sigma) pattern placement, and given the fact that in ZPAL this error does not get reduced as is the case of the masks written for steppers (ZPAL is a one-to-one lithography system), it would probably be required to map out these errors once the master plate has been fabricated and then correct via software the writing of the ZPAL tool. The details of how this is to be done remain to be worked out, but this issue of placement is of paramount importance and needs to be carefully addressed. Once again, it is possible that an

implementation of the SPLEBL principle in a high-throughput e-beam system such as the MEBES® eXara™ will make absolute pattern placement budgets of only a few nanometers.

### 3.4.2 Proposals for Large-Array Fabrication

Although in section 3.2.4.3 a fabrication procedure for relatively large zone plate arrays (~1,000) utilizing e-beam lithography in combination with the Fulton-Dolan process was described, it is the opinion of the author that it will be necessary to decouple the effort of fabricating a master zone-plate array, from that of manufacturing (in a cost effective manner) a relative large number of identical zone-plate arrays. A possibility is to employ a mix-match technique that would make use of e-beam lithography for fabricating the master (or part of it) and either *x-ray*, *holographic*, *ZPAL* or *imprint* lithography to replicate it (or fully create it). The main advantage of this methodology, as opposed to relying on electron-beam lithography for the manufacture of identical arrays, lies in the fact that great pains can be taken in the fabrication of one (or a few) zone plate masters that contain very few and well characterized errors. Rather than having a different set of possible errors each time the e-beam writes a new zone plate array, by replicating the well characterized original master, the optics of all ZPAL systems will all behave in the same way.

The following sections address four possible routes that could be undertaken in order to replicate large arrays with high fidelity and in a cost effective manner.

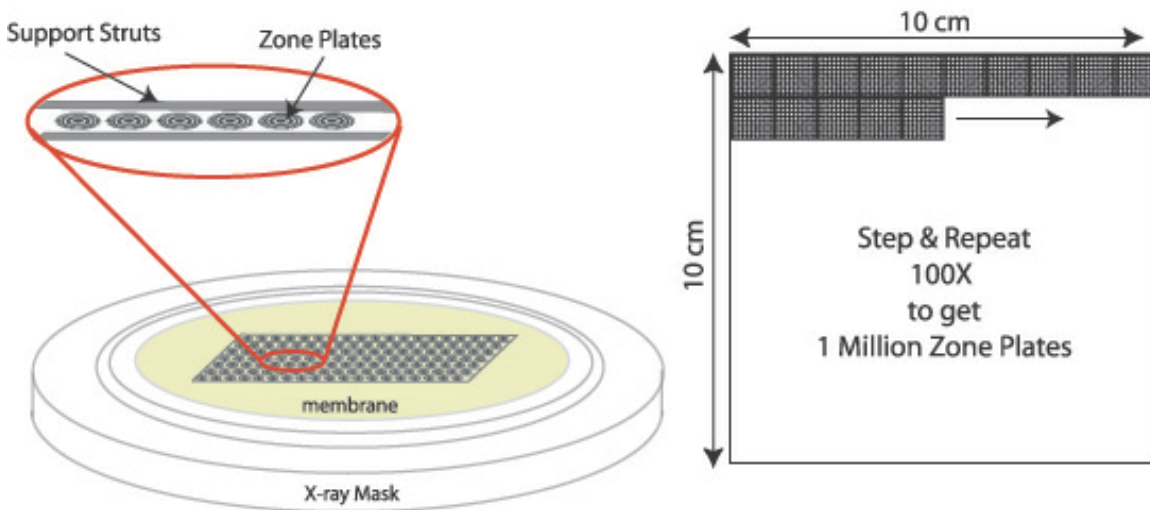


**Figure 3- 38.** Replication of zone plates by means of x-ray lithography. Left: Schematic of an x-ray mask containing an array of zone plates. The zone plates are surrounded by support struts in order to avoid membrane distortions. Right: With an x-ray lithography exposure system, the mask is exposed multiple times (step and repeat) in order to obtain a one-million-zone-plate array.

#### 3.4.2.1 Replication by Means of X-ray Lithography

X-ray lithography provides a viable technique for large array fabrication. The idea is illustrated in Figure 3-38. On an x-ray mask, the maximum tolerable array size that can be e-beam written is plated. The zone plates are placed in between support struts in order to avoid membrane distortions. It is conceivable that 10,000 zone plates, spanning an area of 1cm X 1cm, could be written with an e-beam, even with the two systems available at the NSL. Then, provided an x-ray exposure apparatus with a sufficiently powerful x-ray source is used<sup>9</sup>, 100 exposures would suffice to pattern one million zone plates. The only requirement would be to ensure alignment of the exposed sub-arrays of zone plates by means of a laser-interferometer-controlled stage.

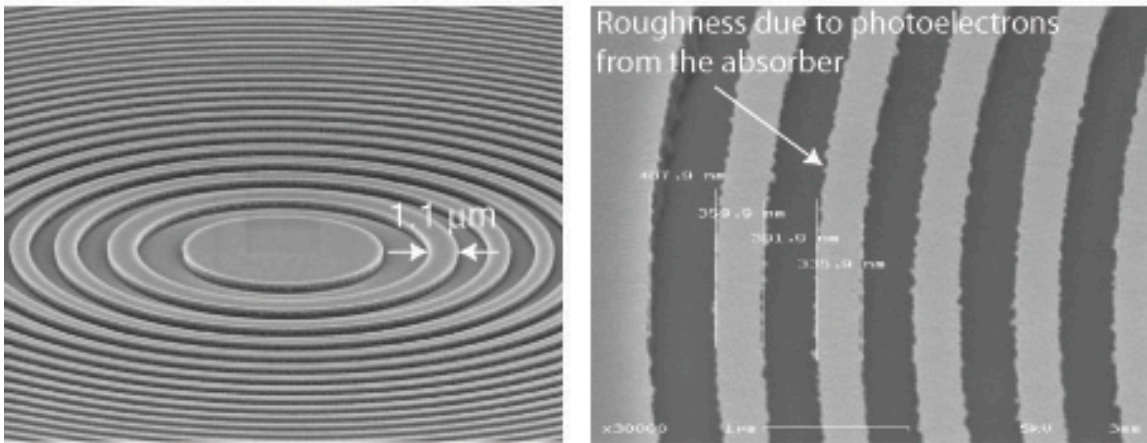
One of the advantages of utilizing an x-ray based process is the fact that HSQ is sensitive at these wavelengths, and hence phase UV-zone plates can be patterned in one shot, as previously described. Experiments were performed in order to optimize this process, with some of the results obtained shown in Fig.3-39.

---

<sup>9</sup> Perhaps the x-ray lithography exposure tool available at University of Wisconsin, Madison, which uses a synchrotron as its x-ray source.



### X-Ray Exposure with 450nm of HSQ



### X-Ray Exposure with 450nm of HSQ + Aquasave

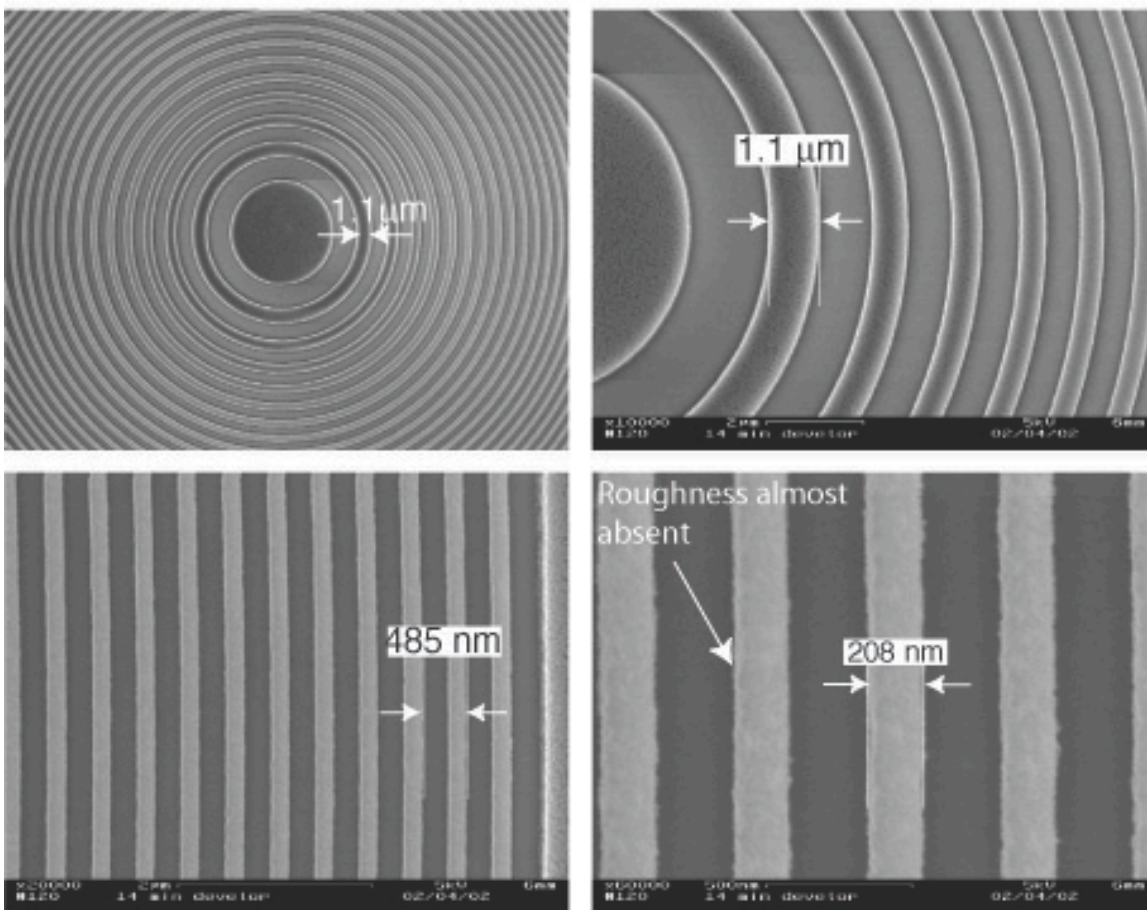


**Figure 3- 39.** The negative resist HSQ can be patterned by means of x-ray lithography. Top: Photoelectrons emitted from the absorber during the exposure causes roughness in the final HSQ pattern. Bottom Four: By adding a layer of Aquasave (a conductive aqueous solution) on top the HSQ, the roughness problem can be almost entirely mitigated.

The results presented in the figure indicate that good patterning can be achieved with this process. The only problem that had to be resolved was the presence of roughness in the zones of the zone plate due to photoelectrons emitted from the absorber during the exposure. The problem was solved by adding a layer of

Aquasave (a conductive aqueous solution) on top the HSQ<sup>10</sup>, as shown in the bottom four scanning electron micrographs of Figure 3-39.

### 3.4.2.2 Replication by Means of Holography

The scheme for reproducing zone plates by means of holography consists of interfering two wavefronts in such a way that the desired Fresnel-zone pattern is obtained. The scheme can work as follows: light is incident on a lens or an array of lenses (these can be a phase or amplitude zone plates, microlens, spatial light modulator pixels, or other phase/amplitude modulating elements which creates the right modulation of the incident wavefront); after being modulated by the lens, the light interferes with another wavefront (which itself might have been modulated by a similar configuration) to create a hologram, which can be recorded to create the pattern for a diffractive element. This interference can be on-axis or off-axis. A few of the possible specific cases are described below. Figure 3-40 illustrates the fact that a zone plate is a hologram.

A uniform plane wave incident on a zone plate (phase or amplitude or a lens) is focused to a first order spot and diverges from there as a spherical wave. Interfering this diverging spherical wave with a plane wave traveling in the opposite direction, and then recording the interference fringes, results in the creation of a zone plate pattern. The geometry of this zone plate would depend on the distance at which the fringes are recorded. If this distance is twice the focal length of the original zone plate, the daughter zone plate is a clone of the original one. The plane waves can be illuminated from the

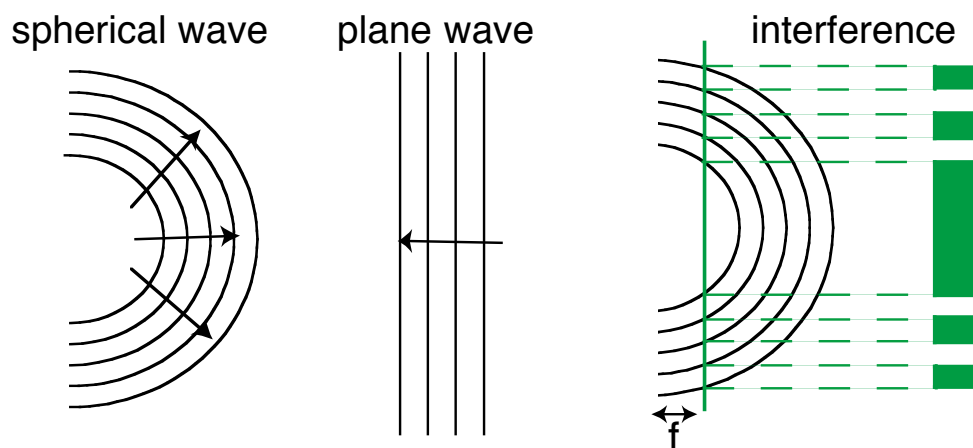


**Figure 3- 40.** A zone plate is a hologram, resulting from the interference of two spherical waves or one spherical wave and one plane wave.

<sup>10</sup> Polyvinylalcohol (PVA) was also tried as a solution, with very mixed results.



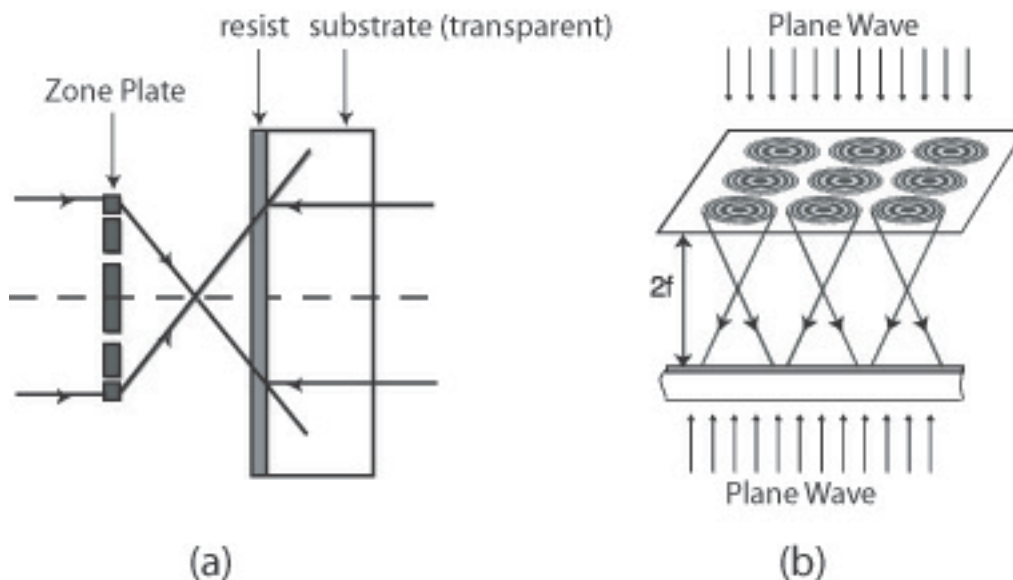


**Figure 3- 41.** Holographic reproduction of zone plates. (a) A uniform plane wave incident on a zone plate) is focused to a first order spot and diverges off as a spherical wave beyond the focal plane of the zone plate. The interference of this diverging spherical wave with a plane wave traveling in the opposite direction, gets recorded in the resist, obtaining the pattern of a zone plate, (b) generalization of this concept to arrays of zone plates.

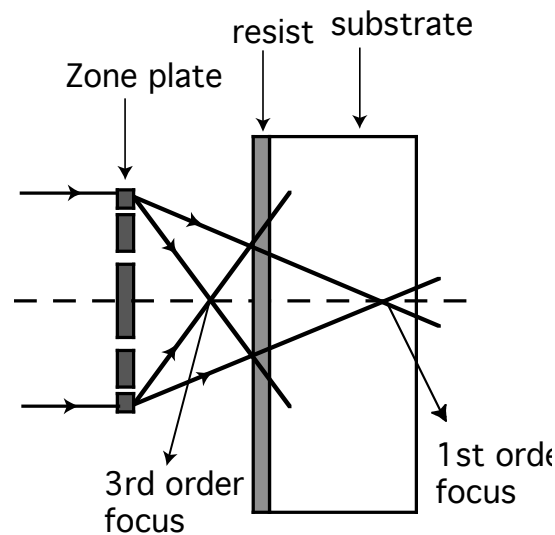


**Figure 3- 42.** The interference of the first and third orders of the same parent zone plate can be recorded in resist to create a daughter zone plate with smaller features.

backside of a glass substrate and the fringes can be recorded in photoresist on the front surface. This scheme is depicted in Figure 3-41.

Another related idea is to use the interference of the first and third orders of the same parent zone plate to create fringes, which could be recorded as a daughter zone plate with smaller features. In this case, plane

waves are incident on the zone plate (phase or amplitude), and after diffracting, several orders will be produced, with the first and the third being the strongest. Now, if a recording medium is placed at a position between the zone plate and its focal plane, a daughter zone plate with higher spatial frequencies is obtained. Figure 3-42 illustrates this scheme.

### 3.4.2.3 Replication by Means of Zone-Plate-Array Lithography

Zone-plate-array lithography also offers the possibility of large array fabrication. One can envision a system, initially operating with a few thousand zone plates, that can write larger and larger arrays of zone plates in parallel. As in a regular ZPAL system, the substrate is scanned underneath the master zone-plate array and the radiation illuminating the elements is flashed at appropriate times to create the desired pattern. No micromechanics would be needed for this application, since all zone plates would be

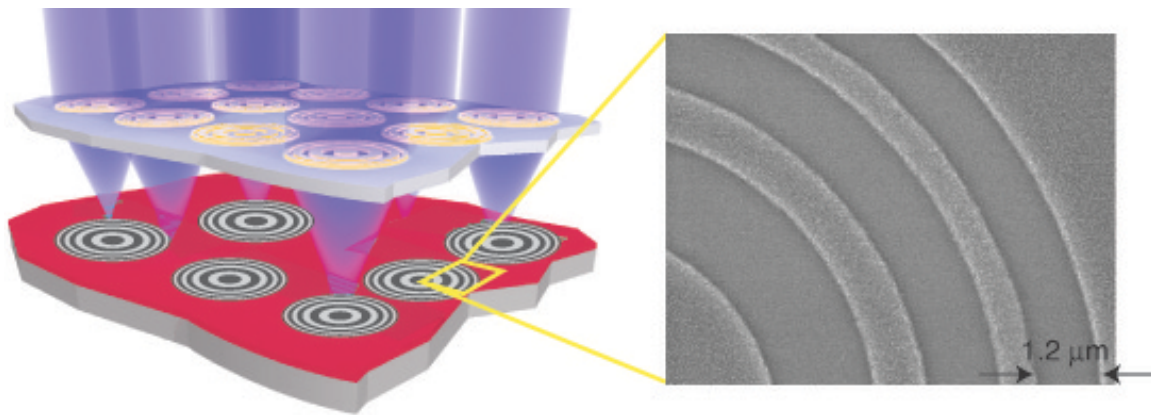


**Figure 3- 43.** Zone plate arrays can be used as means to replicate zone plate arrays. The substrate is scanned underneath the master zone plate array and the radiation illuminating the elements is flashed at appropriate times to create the desired pattern. Right: Scanning electron micrograph illustrating the viability of the technique. The zone plate was patterned by means of a 0.7 numerical aperture master zone plate operating at  $\lambda=400\text{nm}$ .

writing the same pattern (i.e. a zone plate). Figure 3-43 shows a scanning electron micrograph illustrating the viability of the technique. The zone plate was patterned by means of a 0.7 numerical aperture master zone plate operating at  $\lambda = 400\text{nm}$ .

### 3.4.2.4 Replication by Means of Imprint Lithography

Imprint lithography techniques have seen a surge of popularity in recent years due to their extraordinary resolution, ease of use, and potentially low cost. It is not the objective of this section to give a comprehensive

review of the numerous imprint techniques, but rather to simply raise the possibility of replicating the e-beam fabricated diffractive optical arrays by means of one of such techniques.

Some imprint techniques have shown sub-25nm resolution [Ref 3-37], and active research and development has taken place over the last five years in all areas concerning nano-imprint lithography (NIL), from masks, to resists, to processes. NIL patterns a resist by deforming the resist shape through embossing (with a mold), rather than by altering resist chemical structures through radiation . After imprinting the resist, an anisotropic etching is typically used to remove the residue resist

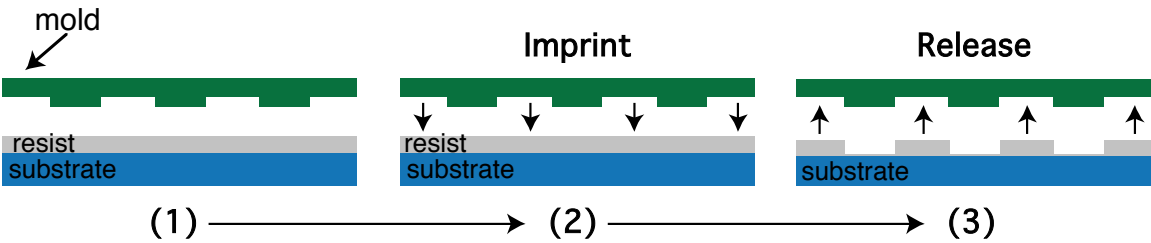


**Figure 3- 44.** Schematic of imprint lithography process

in the compressed area. The nano-imprint lithography process is depicted schematically in Figure 3-44.

While the inability of almost all imprint processes to achieve state-of-the-art multilevel alignment prevents using this process to build large arrays starting with smaller arrays, the technique could prove very cost-effective if used to replicate large number of substrates once a master plate has been fabricated.

<b>Chapter 3. Zone Plate Design and Fabrication .....</b>	<b>10</b>
3.1 History of Zone Plates.....	10
3.2 Zone Plate Theory.....	14
3.2.1 Geometry of Zone Plates .....	14
3.3. Fabrication Techniques .....	24
3.3.1. Critical Parameters .....	25
3.3.1.1 Phase-Shift Errors.....	25
3.3.1.2 Duty-Cycle Errors .....	27
3.3.1.3 Radial Period Errors .....	28
3.3.2 Fabrication of Zone Plates by Means of Electron-Beam Lithography.....	29
3.2.2.1 Writing Strategies for Zone Plates .....	29
3.2.2.2 Proximity Effect Correction for Zone Plates .....	35
3.2.2.3 Choices of Resist.....	39
3.3.3 Fabrication of Zone Plates by means of X-Ray Lithography .....	40
3.3.3.1 Zone Plates for UV-Radiation.....	41

3.3.3.1 Zone Plates for Short-Wavelength Radiation .....	44
3.3.4 Three Zone Plate Fabrication Processes for Lithography Applications.....	47
3.3.4.1 The Chromium Process.....	49
3.3.4.2 The Silicon Process .....	52
3.3.4.3 The Self-Aligned Process .....	56
3.3.4.4 Order Sorting Apertures .....	61
3.4 Replication Techniques .....	63
3.4.1 Throughput in Electron-Beam Lithography: .....	63
3.4.2 Proposals for Large-Array Fabrication.....	64
3.4.2.1 Replication by Means of X-ray Lithography .....	64
3.4.2.2 Replication by Means of Holography.....	67
3.4.2.3 Replication by Means of Zone-Plate-Array Lithography.....	69
3.4.2.4 Replication by Means of Imprint Lithography .....	69

## List of Figures

# Chapter 4

## Zone Plate Characterization

This chapter presents an extensive experimental characterization of zone plates for both lithography and microscopy applications. The elements are characterized in terms of resolution, depth of focus, and efficiency. The results presented provide the first experimental evidence that UV zone plates are capable of diffraction-limited focusing even at very high numerical apertures.

### 4.1 Focusing Performance

#### 4.1.1. Spot Characterization

In Chapter 3, a description of how zone plates focus radiation was provided. A useful rule-of-thumb that can be extracted from the analysis is the following: zone plates can create spots with a resolution (measured at full-width-at-half-maximum -FWHM) that is roughly the size of the outer-most zone. That is, for a given

wavelength  $\lambda$ , the spot size that can be created with a zone plate with an outer-zone-width  $w$ , will also be  $w$  (so long as  $w \geq \lambda/2$ ).

We now present a method for characterizing the resolution capabilities of zone plates for a variety of numerical apertures. All zone plates were fabricated with the

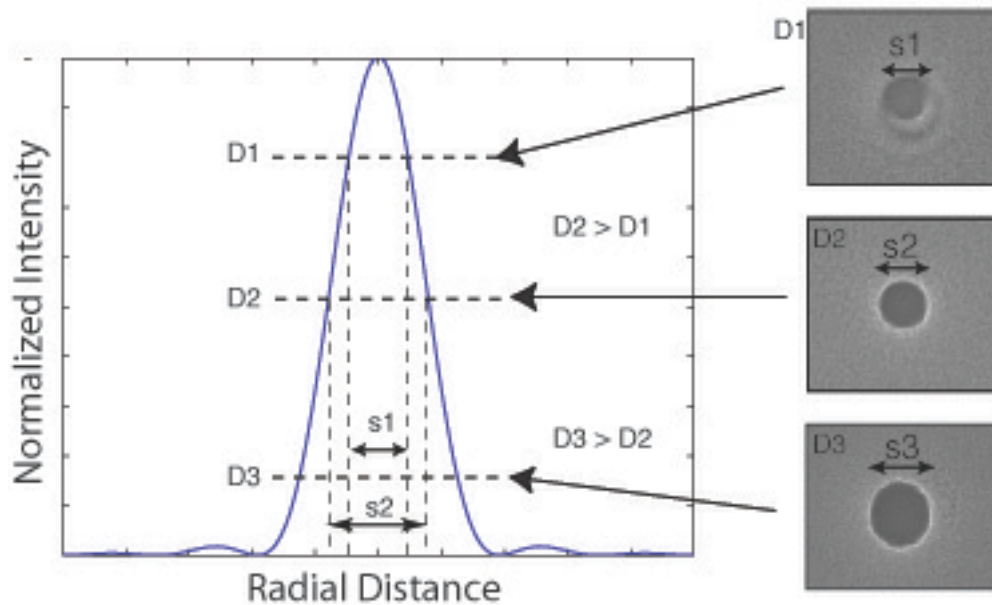


**Figure 4 - 1.** Methodology for extracting the PSF of a zone plate by means of lithographic exposures on resist. The PSF can be sampled by exposing a resist-coated substrate with different illumination intensities. Different exposure dwell times will produce different diameter spots, which can be measured by means of scanning electron microscopy. The information can then be used to reconstruct the PSF, as shown in Figure 4-2.

self-aligned HSQ process described at the end of Chapter 3.

A plot illustrating the methodology used to extract the PSF of a zone plate by means of lithographic exposures on resist is illustrated in Figure 4-1. The idea is to expose spots in different locations of a resist coated substrate, at a large variety of doses. The exposed resist effectively clips (i.e. samples) the point-spread function (PSF) at different levels. By carefully measuring the radii of the exposed spots with a scanning-electron microscope, the full PSF can be reconstructed. From Figure 4-1, it is clear that as the exposure dose increases, the exposed spot gets wider, effectively sampling the PSF at  $D1$ ,  $D2$ ,  $D3$ , etc. Further increases in dose will create in the resist patterns that will indicate the position of the side-lobes. The procedure can then be repeated for zone plates of different numerical apertures and the results compared with the full-vector simulation of the PSF.

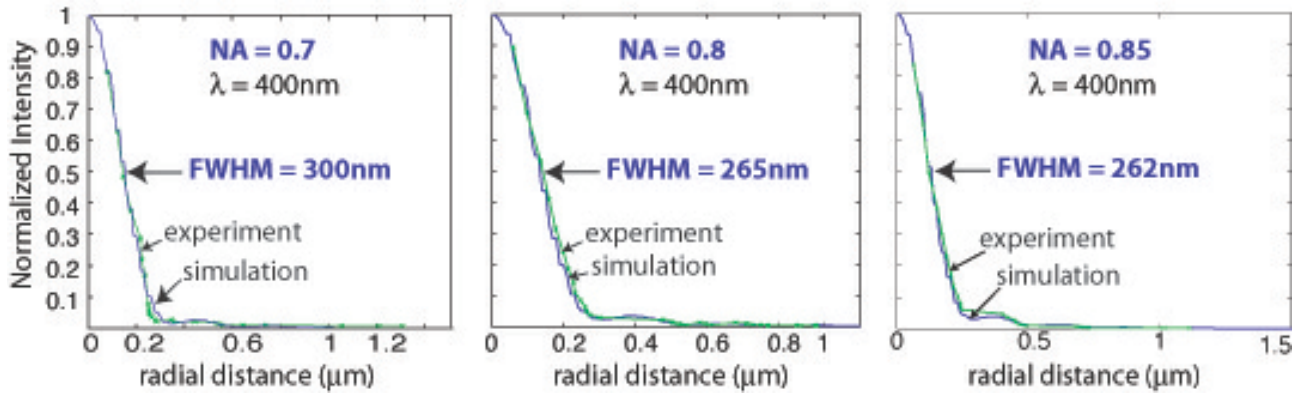


**Figure 4 - 2.** Comparison of the experimentally determined and the simulated PSF of three zone plates with numerical apertures 0.7, 0.8, 0.85 operating at  $\lambda=400\text{nm}$ . Note the excellent agreement between experiment and simulation, from which we can conclude: (1) careful processing allows the fabrication of zone plates with close to ideal performance, and (2) the full-vector simulation procedure is in excellent agreement with experiment.

The results of this process are illustrated in Figure 4 – 2. The figure provides a comparison of the experimentally determined and the simulated PSF of three zone plates with numerical apertures 0.7, 0.8, 0.85 (operating at  $\lambda=400\text{nm}$ ). Note the excellent agreement between experiment and simulation, from which we can conclude: (1) careful processing allows the fabrication of zone plates with close to ideal performance, and (2) the full-vector simulation procedure is in excellent agreement with experiment. And more importantly, the results provide, for the first time, experimental confirmation that high-numerical-aperture zone plates are capable of diffraction-limited performance at the UV.

#### 4.1.2 Depth of Focus

The depth of focus (DOF) of a lens or imaging system is the maximum permitted displacement, away from the focal or image plane, for which the on axis intensity is diminished by some permissible small amount (i.e. the image resolution is only slightly degraded). The quality of the focused spot varies with focus because the relative phase among the rays responsible for forming the PSF change with focus. It is to be expected that the DOF will scale with the wavelength and the numerical aperture.

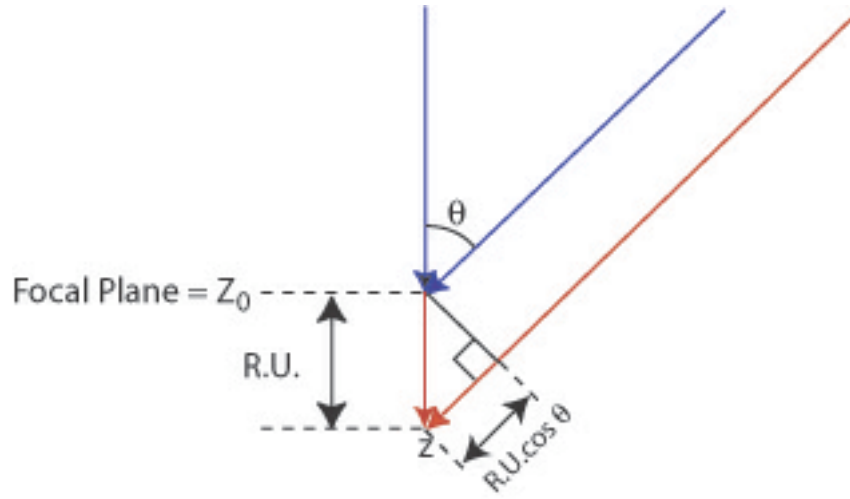


**Figure 4 - 3.** Two rays (spatial frequencies) contributing to spot formation. The depth of focus is proportional to the wavelength and inversely proportional to the square of the numerical aperture.

Consider Figure 4-3, which shows two rays contributing to the spot (PSF) formation, one from the center of the optic (central zone) and one from the edge (the outer-most zone). At focus, the rays interfere at  $z_0$ , at an angle  $\theta$  (the numerical aperture will hence be  $NA = \sin \theta$ ). Let's now consider the defocus case, in which the rays interfere at distance  $z$  away from  $z_0$ . The relative phase change between the two rays will then be:

$$\frac{2\pi}{\lambda}(z - z \cos \theta) \quad 4 - 1$$

It is common practice in the literature [Ref 4-1] to define a depth of focus unit,  $R.U.$  (which stands for Rayleigh Unit), defined as the distance that results in an optical path difference between the two rays of  $1/4\lambda$ . The expression for the  $R.U.$  is then:

$$R.U. = \frac{\lambda}{4} \frac{1}{1 - \cos \theta} = \frac{\lambda}{4} \frac{1}{2 \sin^2(\theta/2)} \cong \frac{\lambda}{4} \frac{1}{2 \left(\frac{NA}{2}\right)^2} \quad 4 - 2$$

$$R.U. = \frac{\lambda}{2NA^2} \quad 4 - 3$$



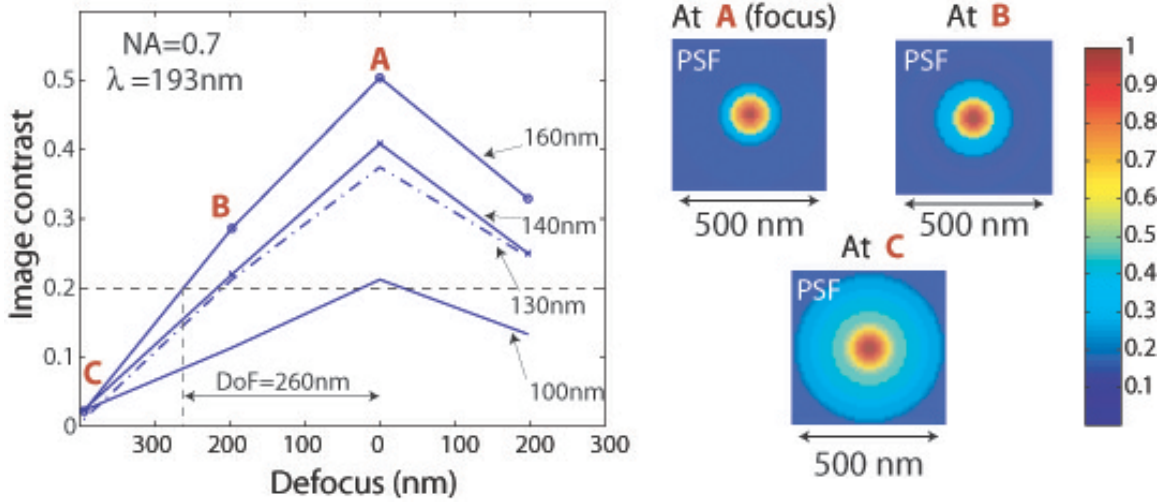


**Figure 4 - 4.** Plot of the impact of defocus on image contrast for ZPAL (operating at  $\lambda=193\text{nm}$ ). Zone plates have a depth-of-focus similar to that of conventional refractive lenses. The depth-of-focus is dependent on the wavelength of the light and the numerical aperture. Defocus is an important consideration in ZPAL, as can be seen in the figure. Left: Simulated plot of image contrast as a function of defocus for dense 1:1 gratings exposed with ZPAL at different resolutions (from 160 nm to 100 nm). Right: Top view of simulated PSF of a 0.7NA zone plate operating at  $\lambda=193\text{nm}$  at different Rayleigh Units (R.U.) of defocus (marked A, B, C in the left graph). Note how the background in creases as the defocus increases (i.e. less energy is going into the diffraction-limited spot).

The quantity  $R.U. = \frac{\lambda}{2NA^2}$  is the Rayleigh unit of defocus. It is proportional to the wavelength and

inversely proportional to the square of the numerical aperture. For the case of a perfect circular lens, with plane wave illumination, it can be shown [Ref 4-2] that one R.U. of defocus corresponds to an on-axis intensity decrease of 20%.

Depth-of-focus is a very important parameter affecting the optical performance of zone plates for lithography applications. Finite resist thickness, focus fluctuations due to wafer topography, zone-plate-substrate non-flatness, and wafer and chuck non-flatness can all cause a decrease in the quality of the final printed patterns. Figure 4 –4 illustrates the impact of defocus on image contrast for a ZPAL system operating at  $\lambda = 193\text{nm}$  (the wavelength required to achieve sub-100nm patterning). Plots of image contrast for simulated dense gratings of different minimum feature sizes are shown as a function of defocus. Mature resist will be able to resolve image contrasts in excess of 0.2. As can be observed, the image contrast is significantly degraded as the defocus increases. One and one-half R.U. of defocus away from perfect focus, results in an image contrast below 0.2 for a 100nm linewidth. We can then conclude, that at  $\lambda=193\text{nm}$ , a zone plate with a 0.7 numerical aperture exhibits a depth-of-focus of  $\sim \pm 200\text{nm}$ , in terms of tolerable image contrast. However, it is important to consider that a number of other factor also contribute to the image contrast that can be achieved with ZPAL (e.g. duty-cycle control, appropriate phase-shifts between alternate zones, and radial period errors, as described in Chapter 3). Given this fact, the tolerance for defocus decreases to a number that has to be quantified

experimentally for each ZPAL system, with an upper bound given by a factor of one to two times the expression obtained in Equation 4-3.

### 4.1.3 Dealing with Multiple Diffraction Orders

This section addressed what is perhaps the most commonly expressed concern regarding the use of zone plates for lithography, namely, whether the presence of multiple diffracted orders in zone plates presents a critical problem for high-resolution lithography. As we will see, while it is true that the existence of multiple orders limits the performance of the zone plates, even with such orders present, zone plates are adequate for state-of-the-art lithography. Alternative diffractive optical designs that can mitigate the presence of multiple orders are also discussed.

#### 4.1.3.1 The Issue of Background in Lithography

Lithography is based on the ability to produce sufficient image contrast in a resist sensitive to some form of radiation. In lithography, pattern formation involves two distinct but interrelated contrasts. The first relates to the image quality at the image plane of the lithographic system. The second contrast relates to the interaction of the aerial image with the resist material. The latter interaction is responsible for the final pattern formation, that is, the *writing in stone* (the literal meaning of lithography). Two contrast metrics are hence present. One relating to the aerial image formed, and the other to the ability of the resist film to take this aerial intensity distribution and convert it into a binary pattern. Understanding this is crucial in order to analyze all forms of lithography, including ZPAL. A fundamental point that is worth remembering through the ensuing discussion is the following:

**A low-contrast aerial image can result in a high-quality lithographic pattern *provided* the resist has enough contrast and conversely.**

Contrast is defined as

$$contrast = \frac{max - min}{max + min} \quad 4 - 4$$

where *max* and *min* are, respectively, the maximum and minimum intensity values in the final image to be resolved by the resist.

## Photoresist Interaction with the Aerial Image

Photoresist is typically an organic polymeric compound that changes its solubility in another chemical (known as developer) as a result of radiation exposure. The performance of any photoresist can be characterized by its contrast curve. Figure 4-5 depicts the contrast curve for a fictitious positive resist. The thickness of resist remaining after development is plotted against exposure dose (plotted in log scale for clarity).

Near  $E_0$ , we can represent the contrast curve by the following equation

$$T = T_0 \gamma \ln \left( \frac{E_0}{E} \right) \quad 4 - 5$$

where  $T$  is the thickness of resist remaining,  $T_0$  is the initial resist thickness,  $\gamma$  is the resist contrast,  $E_0$  is the dose at which no resist remains (clearing dose) and  $E$  is the exposure dose. This equation is illustrated by the dotted linear portion of the curve in Figure 4-5. We want to relate the image contrast to the resist contrast. We need only consider the

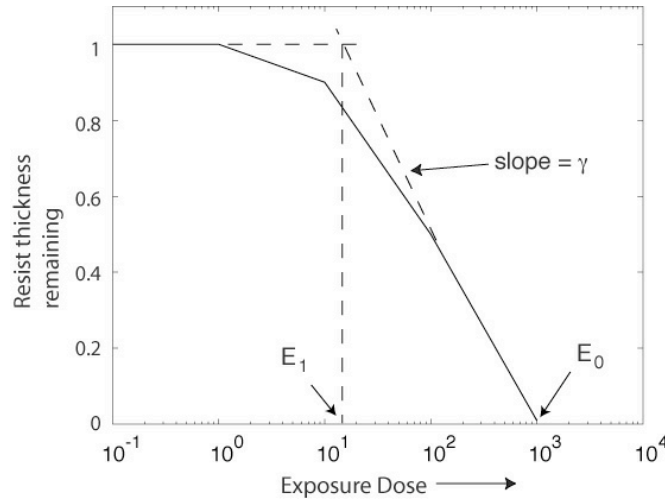


**Figure 4 - 5.** Typical contrast curve of a positive photoresist. Thickness of photoresist remaining is plotted as a function of the exposure dose.

minimum of image intensity  $I_{min}$  and the maximum of image intensity  $I_{max}$ . It is clear that for  $I_{min} < E_1$  and  $I_{max} > E_0$ , the resist will produce the desired “binary” image with vertical sidewalls. These conditions imply

$$\begin{aligned} I_{min} &< E_1 \\ I_{max} &> E_0 \end{aligned} \quad 4 - 6$$

This further means

$$C = \frac{I_{\max} - I_{\min}}{I_{\max} + I_{\min}} > \frac{E_0 - E_1}{E_0 + E_1} \quad 4 - 7$$

$$C_{\min} = \frac{e^{\frac{1}{\gamma}} - 1}{e^{\frac{1}{\gamma}} + 1} \quad 4 - 8$$

In Figure 4-6, the minimum resolvable image contrast ( $C_{\min}$ ) is plotted against the resist contrast ( $\gamma$ ). From this plot, we can see that to resolve an image that has a contrast of about 0.2, a resist contrast,  $\gamma$ , better than 2.5 is needed. As was described in Chapter 1,

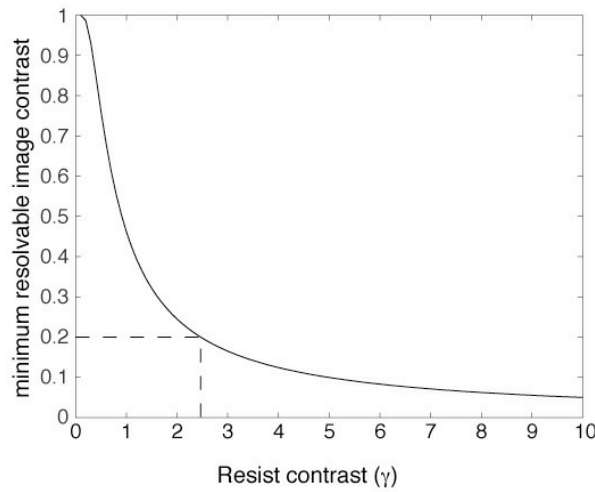


**Figure 4 - 6.** The minimum resolvable image contrast is plotted against the resist contrast. Note that in order to resolve an image of contrast about 0.2, the resist contrast must be better than 2.5. Mature resists are able to resolve image contrasts as low as 0.2.

resist technology has improved tremendously (recall Fig.1-9), with dramatic effects on the quality of the patterning that can be achieved with any given lithographic system. Mature resists are able to resolve image contrasts as low as 0.2.

### The Effect of Zone-Plate Background Radiation in Lithography

The first point that is important to get across regarding the effect of multiple orders on lithography applications, is that the background power in zone plates, although of the same order-of-magnitude as the first-order power, is **spread over a very large area**. An important metric to understand in lithography is that the power-density (i.e. power per unit area) of the radiation incident on the photoresist defines the quality of the printed pattern. On a first pass, it is tempting to provide the following analysis for the case of zone plates (let's call it the *Simple Analysis*). It goes as follows:

### “Simple Analysis”:

“If, at best, only 40% of the light goes into the first order, the remaining 60% will go into unwanted areas on the substrate; the 40-60 split seems intuitively an insufficient number for state-of-the-art lithography. After all, *most of the light* is going to areas where we don’t want it to go, isn’t it?”

Anonymous ZPAL Critic

In order to answer the concerns expressed by the “simple analysis”, one must begin by realizing that patterning in ZPAL is achieved by the incoherent addition of spots. When a single spot is exposed, it is true that 40% of the radiation goes into the spot, and 60% is spread over a much larger area. However, this spreading results in a *power density* for the unexposed pixels that is drastically lower than that of exposed pixels. It is simply wrong to reach the conclusion that the *overall* pattern will receive only 40% of the radiation into the desired areas, and that 60% will go into areas intended to remain unexposed. The error lies in not realizing that part of the background radiation also goes into areas that *are* intended to be exposed. In this manner, an exposed pixel will *always* receive a *higher* exposure dose than all unexposed pixels in its vicinity.

An example will help: Consider the case of exposing a dense 1:1 line/space grating. The “simple analysis” would predict that 40% of the radiation would go into the lines (the exposed areas), and that 60% would go to the spaces (the intended unexposed areas). The grating would not be resolved. However, given that for a grating one half of the total number of pixels are exposed, 1/2 of the 60% background will end up in the exposed pixel areas, with the result that the lines will receive 70% of the radiation (40% from direct exposure + 30% from indirect exposure), and the spaces only 30%. The grating will be readily resolved. This example showcases a general fact that is true for all patterns. If the point-spread function (this function determines how energy is distributed each time a spot is exposed) is well known, it is always possible to account for the background so as to include its contribution to the exposed areas (this is part of the science of proximity effect correction). The image contrast is hence much better than it at first appears. The caveats are that (1) the PSF has to be sufficiently well characterized<sup>11</sup>, (2) dose control for each pixel is necessary, and (3) a pattern dependent dose correction needs to be applied<sup>12</sup>

Let’s proceed with an experimental confirmation of the ability of phase-zone plates to provide sufficient contrast for state-of-the-art lithographic patterning. In

---

<sup>11</sup> As shown in Figure 4-2, our simulations provide excellent agreement with experiment (i.e. we know the PSF of zone plates very well).

<sup>12</sup> This is not necessarily a problem, since it is a calculation that can be done offline prior to exposure. For some results showing the implementation of this technique see section 5.2.1.3 in Chapter 5.

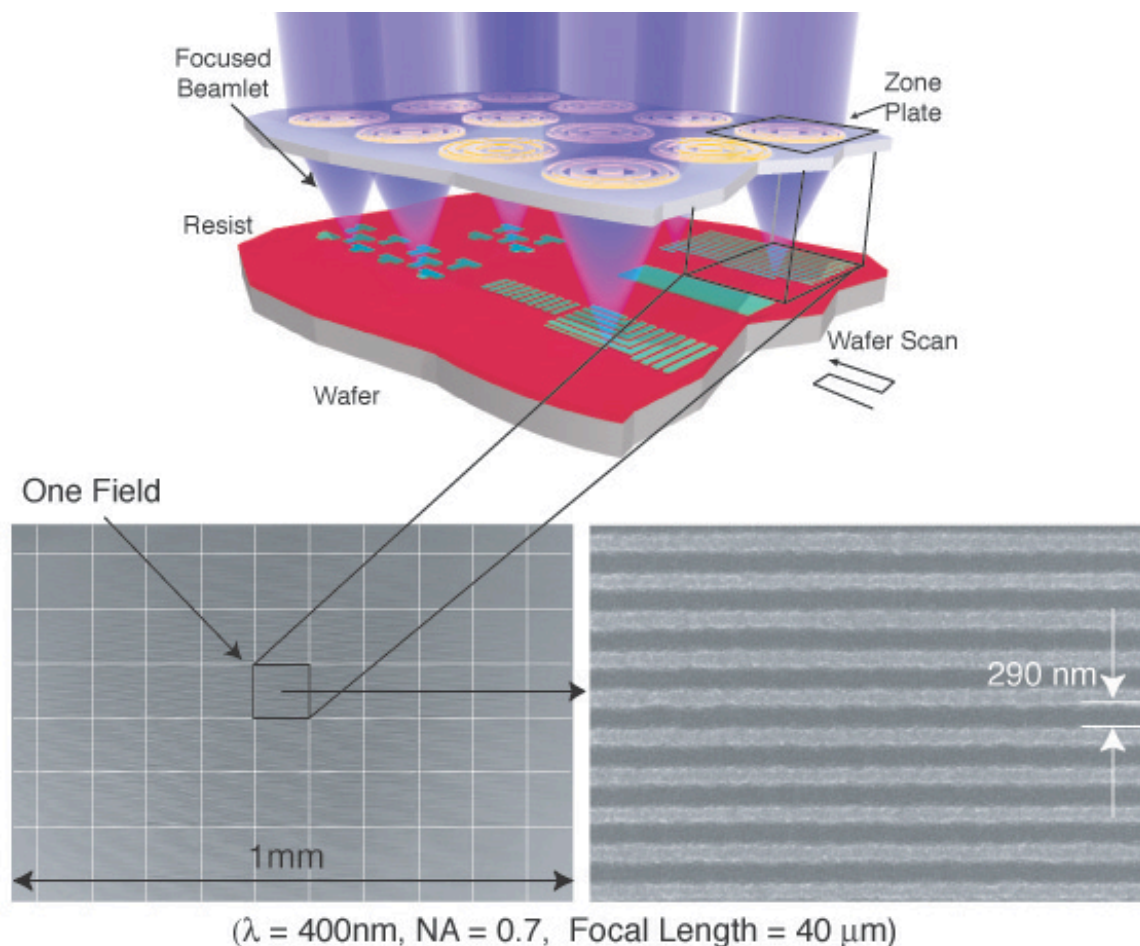


**Figure 4 - 7.** Top: Schematic of the ZPAL system without the micromechanics. Large area patterns are created by stitching adjacent fields, with a field defined as the square area located underneath any given zone plate (a field, depicted with black lines, is shown in the figure). Bottom-left: Proof that full-field patterning is possible with ZPAL despite the existence of multiple orders. A dense pattern with 300nm lines and spaces was exposed (with 400nm light). The total patterned area contained 1,000 fields, spanning a  $10\text{mm}^2$  area. Bottom-right: Zoomed in SEM of the center of the full field grating.

ZPAL, large areas are written by stitching together multiple fields, as is done in scanning-electron-beam lithography. While what defines a field in ZPAL depends on the writing strategy, for simplicity a field can be defined as the square area enclosing the projection onto the substrate of an individual zone plate (i.e. for a zone plate with  $100 \mu\text{m}$  diameter, the field size will be a  $100\mu\text{m} \times 100\mu\text{m}$  square located directly underneath the zone plate). Each zone plate is “responsible” for patterning the field that lies directly underneath it, and stitching at the edges of the fields allows features to be connected with patterns written in adjacent fields.

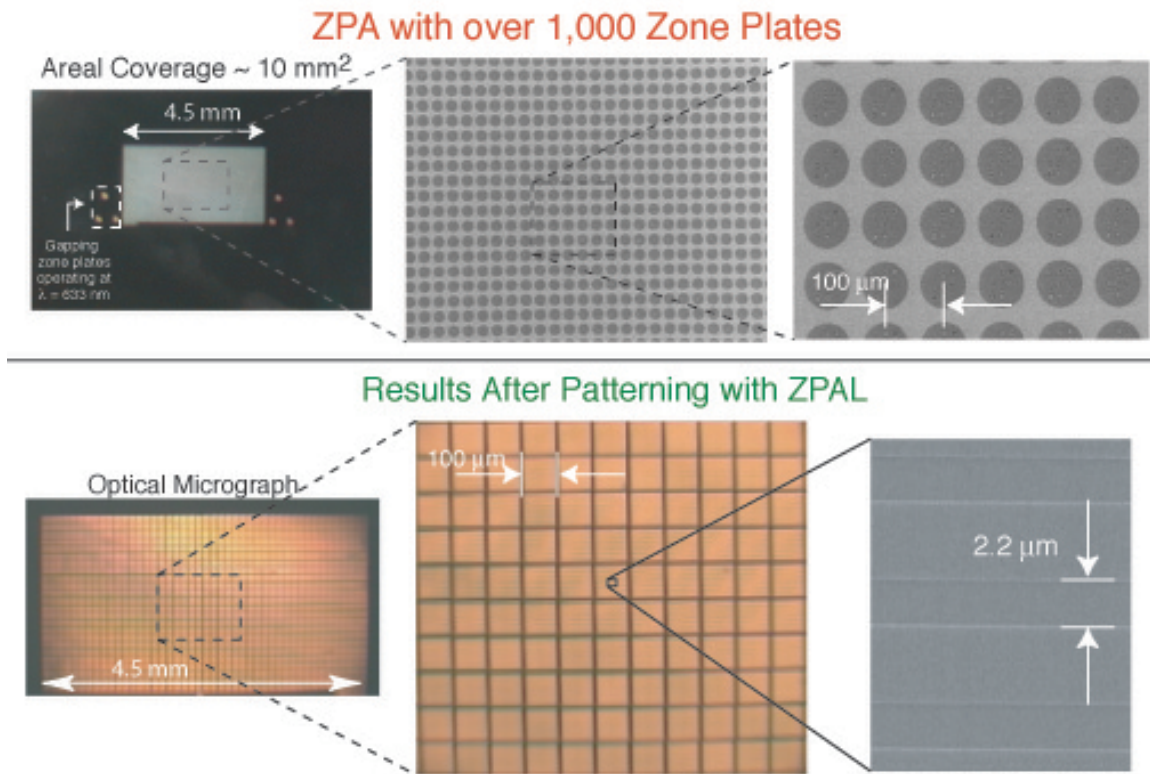


**Figure 4 - 8.** Massive parallelism can be achieved with ZPAL. Top: Optical and scanning electron micrographs of a zone plate array containing over 1,000 zone plates, spanning a  $10\text{mm}^2$  area. Bottom: Lithographic results obtained with the large zone plate array. The exposed pattern is a  $6\mu\text{m}$  period grating with a total area of  $10\text{mm}^2$ . Bottom Right: Scanning electron micrograph of a small section of the  $10\text{mm}^2$  grating.

For the purpose of experimentally evaluating contrast, it is sufficient to pattern full fields at the maximum resolution. If this test is passed, it is clear that entire wafers could be patterned by combining large numbers of fields written in parallel. Figure 4-7 demonstrates that full fields, with dense lines and spaces patterned at the minimum feature size of the zone plate, can be written with high-NA ZPAL. The top of the figure is a schematic of ZPAL (without the micromechanics) illustrating the previously described concept of parallel writing by stitching multiple fields. The bottom of the figure contains an experimental result in which  $100\mu\text{m} \times 100\mu\text{m}$  fields were exposed with a 0.7 NA zone plate operating at  $\lambda=400\text{nm}$  and a focal length of  $40\mu\text{m}$ . The exposed pattern consists of 1:1 dense lines and spaces with  $300\text{nm}$  features (the exposure wavelength is  $400\text{nm}$ ). The zoomed in SEM at the bottom-right of Figure 4-7 provides a clear view of what the pattern looks like, namely a  $600\text{nm}$ -period, dense 1:1 grating. For contrast purposes, only next-neighbor fields will affect patterning, due to the highly localized structure of the point-spread function. The results presented in Fig.4-7 and Fig.4-8, present full-field ZPAL patterns that were exposed in the presence of a very large number of neighboring fields. The results confirm that ZPAL will be able to pattern dense full fields at the diffraction limit even with arrays of one million elements or more<sup>13</sup>. In conclusion, high-numerical-aperture zone plates are

<sup>13</sup> As a matter of fact, a zone plate located at the center of an array containing 7 hexagonal close-packed zone plates will pattern identically to a zone plate located in the center of an array containing 1 million or more zone plates.

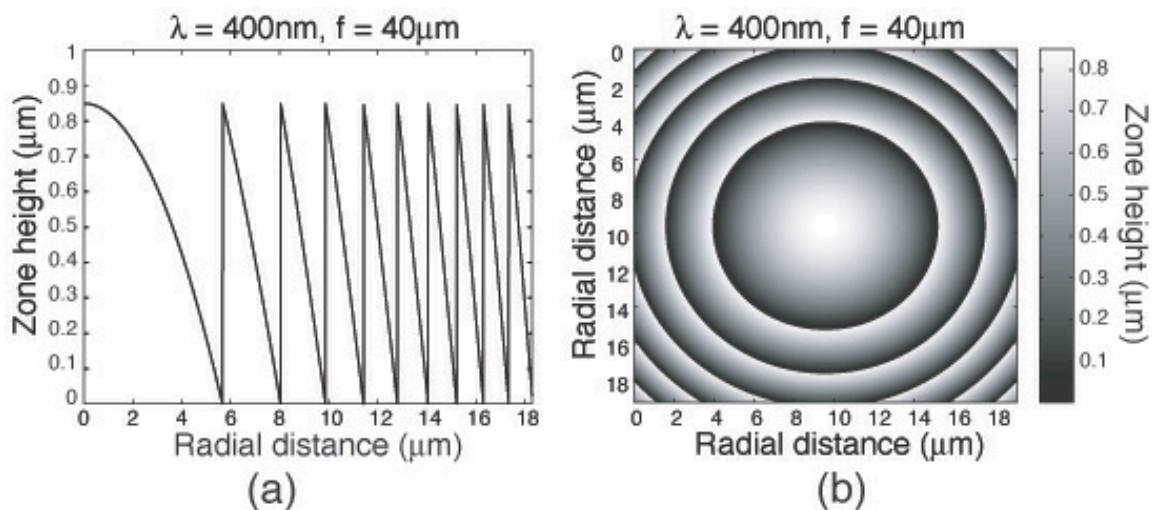


capable of providing sufficient contrast for state-of-the-art lithography. Although multiple diffracted orders exist, the background exposure that they produce is not decisively deleterious. It should be pointed out that orders-sorting apertures, as described in Chapter 3, would further increase the patterning capabilities of zone plates by blocking most of the undesired radiation from reaching the substrate to be exposed.

#### *Alternative Diffractive Optic Designs for Background Reduction*

Diffractive optical elements more efficient than phase zone plates exist that are capable of focusing light into a single diffraction-limited spot with a very high efficiency (and hence with very little background). It is based on a principle of blazed diffraction gratings. The term blazing implies the creation of a sloped profile for alternate zones, folding the phase of the propagating wavefront by  $2\pi$  as it goes through the optical element. In this way, it mimics the effect created by conventional refractive lenses, with the added advantage that it can be fabricated with microfabrication processes.

A “blazed Fresnel phase plate” is depicted in Figure 4-9. Such a diffractive-optical element can focus 100% of the incident radiation into the first-order focus, assuming there is negligible attenuation through the material, which is the case for UV and deep UV radiation in glasses such as fused silica, and single crystals such as calcium fluoride. However, despite the fact that micro-fabrication procedures can be employed for the creation of these elements, high-resolution blazed-elements remain very challenging structures to fabricate. The bottom of Figure 4-9 (c-d) illustrates two of the traditional fabrication procedures for these elements.



### Traditional Fabrication Techniques

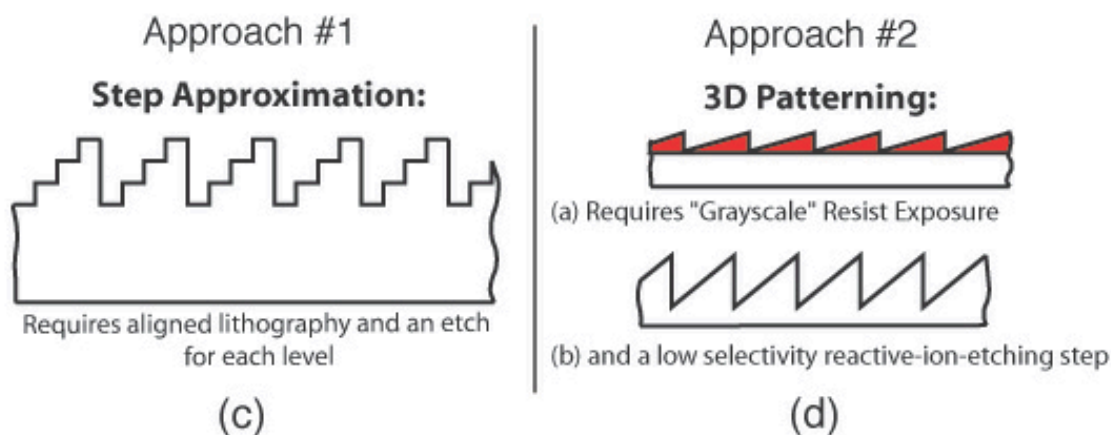


**Figure 4 - 9.** Blazed zone plates can provide close to 100% efficiency into a diffraction-limited spot. Top of figure: (a) Cross-section of a blazed zone plate designed for  $\lambda=400\text{nm}$ . (b) Top-view of the central zones of a blazed zone plate. Bottom of figure: Traditional fabrication techniques for blazed diffractive elements. (c) the blazed profile can be approximated by a series of aligned steps, (d) a “grayscale” resist exposure enables the transfer of a blazed profile into the substrate by means of a low-selectivity reactive-ion-etching step.

Figure 4-9(c) depicts a technique for blazing based on approximating the sloped profile by a series of steps. While four steps can achieve efficiencies into the first order in excess of 80%, each step requires an aligned lithographic exposure, something that can be very challenging for high-resolution zone plates that have outer-zone-widths as small as 100nm (and potentially even smaller). An alternative method is illustrated in Figure 4-9(d). It relies on the use of a “grayscale” resist exposure, which then enables the transfer

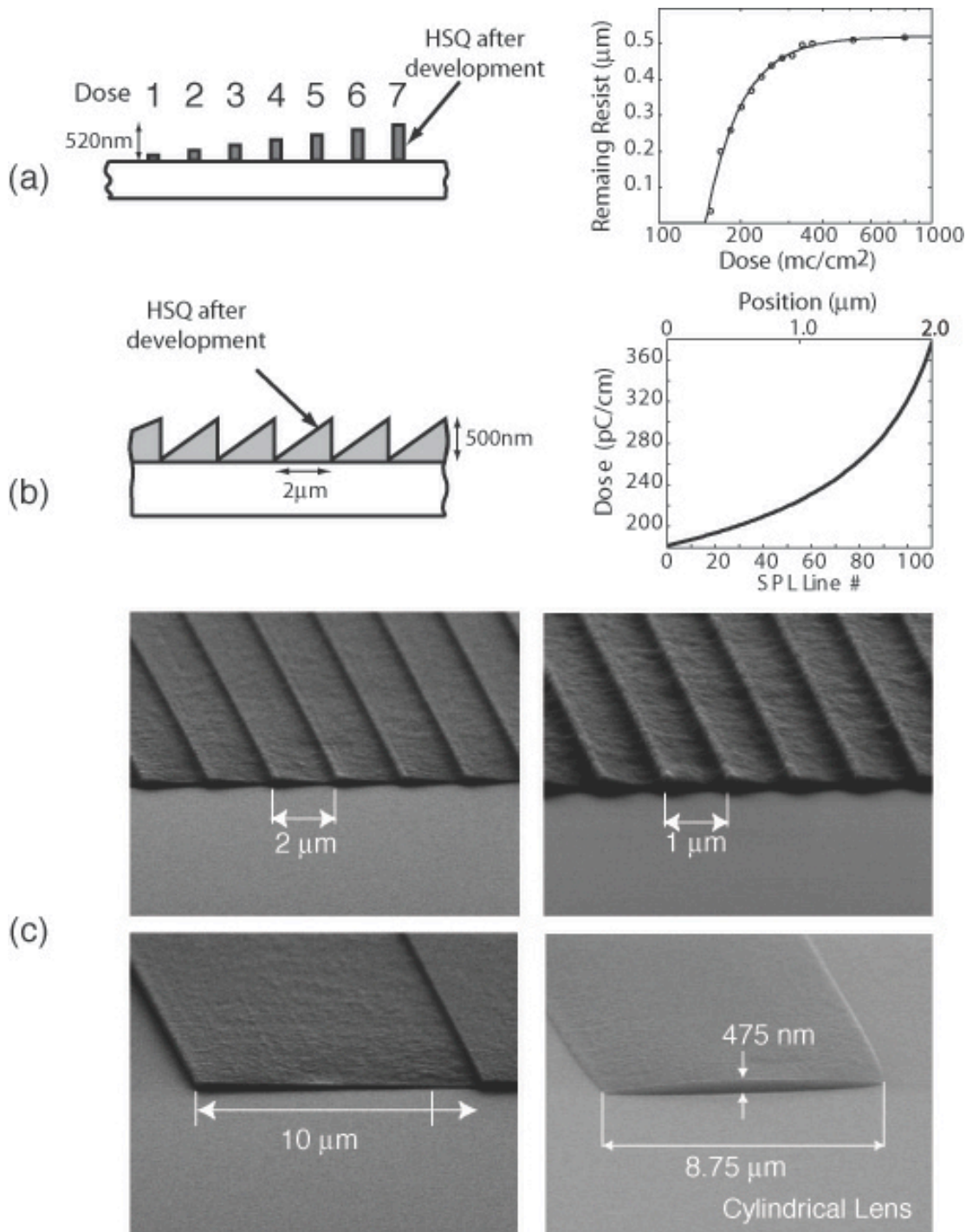


**Figure 4 - 10.** Direct 3D Patterning with HSQ. (a) Left: Schematic illustrating the fact that the thickness remaining of HSQ after development can be controlled, Right: plot of the thickness of remaining resist after development versus dose delivered, (b) Left: Schematic of characteristic blazed structure, Right: Dose required across each tooth of the blazed grating in order to achieve a linear slope (note that the dose required is not a linear function). (c) Scanning electron micrographs of blazed structures fabricated with HSQ

of a blazed profile into the substrate by means of a low-selectivity reactive-ion etching step. Although only one lithography step is required with this process, the reactive-ion etching can be quite tricky, requiring careful control of the etching selectivity of both the resist and the substrate.

An alternative fabrication method for blazed structures requiring a single lithography exposure and no etching was developed through the work reported here<sup>14</sup>. The technique borrows heavily from the self-aligned zone plate fabrication procedure described at the end of Chapter 3, in that it makes use of HSQ (hydrogen silsesquioxane) as the final layer responsible for creating the appropriate phase-shift at each zone. For very thin layers, HSQ, being glass like, will introduce negligible attenuation at UV and deep UV wavelengths. The trick that will allow the creation of sloped profiles with this resist comes from the fact that for a given initial thickness of HSQ, the thickness remaining depends on the electron beam dose, as indicated in Figure 4-10(a). Accordingly, by varying the dose in scanning-electron-beam lithography one can vary the thickness of the zones. Note that, as illustrated in Figure 4-10(b) the dose required in order to achieve a linear slope across each tooth of the blazed grating is not a linear function. Figure 4-10(c) shows a first attempt at creating 3D structures in one step. Among the patterns created were entirely curved structures (mimicking the central zone of a zone plate), as well as gratings with a linear blaze. While much work remains to be done in order to fabricate blazed zone plates, these results provide early indications that such a task might indeed be achievable. As mentioned earlier, this would enable a ZPAL system to obtain nearly 100% efficiency into the first order focus while still utilizing diffractive elements fabricated with the planar process.

One further application of this technique is the apodization of zone plates. Because it is possible to control the thickness of each of the zones by controlling the amount of e-beam dose delivered into the HSQ, we can effectively “attenuate” certain zones. This attenuation, if properly designed, can reduce the size of the sidelobes of the zone-plate PSF, which can have beneficial effects in terms of contrast in ZPAL.

## 4.2. Numerical Aperture Studies

One of the key contributions of the work presented here has been the design, fabrication and testing of the highest-numerical aperture UV zone plates ever reported. The results presented in the following sections are compelling. Zone plates with numerical apertures as high as 0.95 were fabricated and tested. The zone plates were capable of diffraction-limited performance. It is well known that high-numerical-aperture refractive lenses pose enormous design and fabrication challenges, especially for large fields-of-view. With diffractive optics, fabricating high-numerical-aperture optics is not significantly more challenging than low-numerical-aperture elements. Furthermore, the distributed nature of ZPAL bypasses the tradeoff between resolution and wide field-of-view, which is at the core of much of the complexity (and the cost!) of the high-numerical aperture lenses used in many optical systems, including optical-projection lithography.

---

<sup>14</sup> The work on blazed structures was done in collaboration with Todd Hastings

## **4.2.1 Characterization of Numerical Aperture by means of Zone-Plate-Array Microscopy (ZPAM)**

With a minor modification, the ZPAL system can be made to operate as a high-resolution microscope. As will be described in Chapter 5, the microcopy mode of ZPAL (we call it Zone-Plate-Array Microscopy, ZPAM) enables one to set the substrate to be exposed at the right gap (i.e. at the focal plane of the zone plate array), as well as offering the potential for level-to-level alignment.

### **4.2.1.1 The ZPAM Principle**

Zone plates have been used for many decades as imaging elements, primarily for x-ray microscopy. In many respects one can think of a zone plate as a lens, and as such, one should, in principle, be able to image with it. With this concept in mind, if the zone plate is used as the focusing lens of a traditional confocal microscope [Ref 4-3] one would obtain a signal that varies with the gap and that achieves its maximum value exactly at the focal length of the zone plate. The concept is illustrated in Figure 4-11(b).

Any confocal scheme is at a minimum comprised of two lenses (an objective lens and a detector lens), a light source, a pinhole and a detector. The mode of operation is very straightforward. Light (typically from a laser) is passed through a beam splitter cube and is then focused by a lens onto a sample. If the sample is exactly at the focal plane of the lens, the light will be focused to a diffraction-limited spot at precisely the surface of the sample. Assuming for now a specular reflection at the substrate, the light will travel back through the same lens, come out of it collimated, and then travel to the beam splitter to be reflected and go through a second lens (the detector lens). At the focal plane of this last lens a pinhole is placed, followed by a detector. This path is illustrated with a solid line in Figure 4-11(a).

If the sample is not at the focal plane of the objective lens the detector lens will no longer see collimated light, and it will focus the light at a different distance than before. The pinhole's role is now apparent. Its purpose is to improve contrast by allowing only light that comes from the focal plane of the objective lens to go through and reach the detector. The signal obtained as the gap is varied is shown in Figure 4-11(c). The signal allows for the precise determination of the focal length of a zone plate. A peak detection algorithm can be used to find the maximum intensity of the signal. The focal length determination can be further improved by taking the center of gravity of the axial response (Figure 4-11(c)-right). [Ref 4-4].

Since each zone plate provides a signal from the substrate, by processing these signals while scanning the substrate, high-resolution images of the sample can be obtained, as show in Figure 4-11(d).

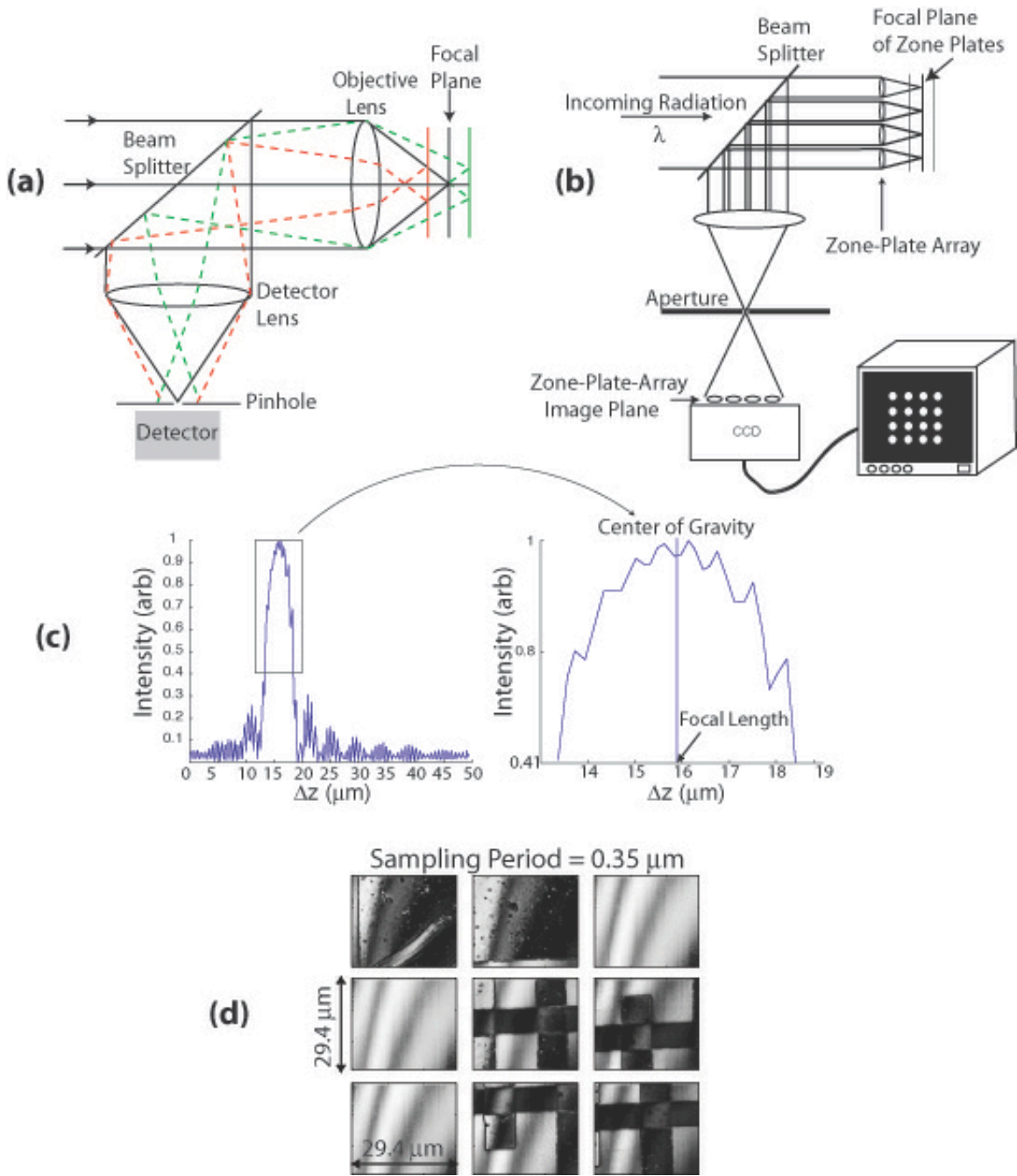


**Figure 4 - 11.** Confocal microscopy. (a) Conventional implementation of confocal microscopy (a single objective lens is used). (b) Schematic of ZPAM. The zone plates are used as an array of objective lenses. The CCD detector is placed at the image plane of the zone-plate array, after the confocal aperture, allowing the light from each zone plate to be analyzed independently. (c) Typical axial confocal signal obtained with ZPAM. The peak of the signal (which gives the exact location of the focal length of the zone plate) is obtained by calculating the Center of Gravity (CoG) of the signal. (d) Nine ZPAM images obtained in parallel (with nine zone plates). The sampling period was 350nm.



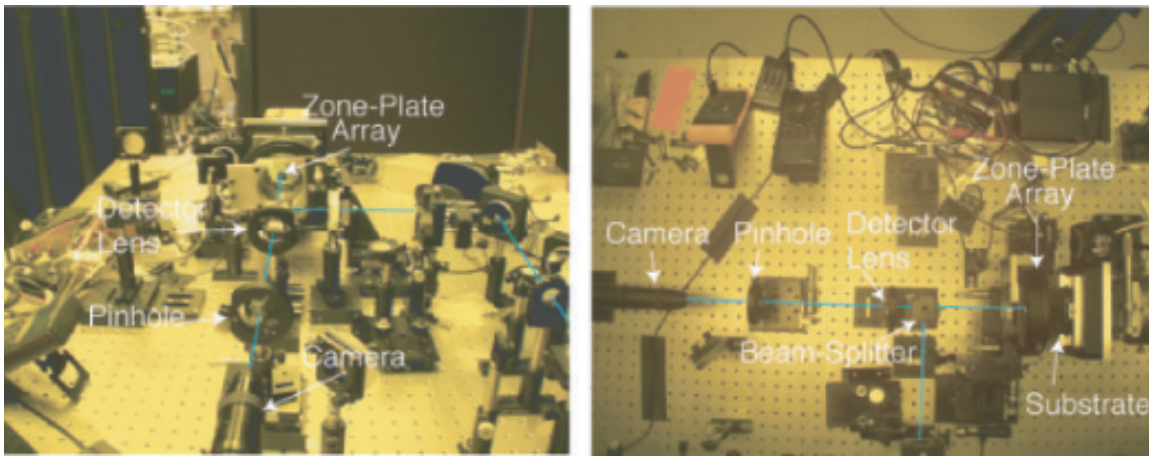


**Figure 4 - 12.** Experimental implementation of Zone-Plate-Array Microscopy.

#### 4.2.1.2 Experimental Setup

The principle of operation of the massively parallel confocal microscope, ZPAM, is schematically depicted in Figure 4-11(b), and its experimental implementation is shown in Figure 4-12. Collimated light coming from a laser goes through a beam splitter and is focused by the zone-plate array, forming a 2-D array of diffraction-limited spots at the focal plane of the zone plates. The 2-D array of points get reflected back and pass through the zone plates one more time, coming out collimated if the substrate is at the focal plane. The array of collimated rays (one for each zone plate) gets reflected off the beam splitter, and is then focused by a lens. After passing through an aperture, the array of light beams reaches the CCD-chip of the camera. One signal per zone plate is obtained. The image of the camera is processed by a computer with a frame-grabber. The image is digitized and stored in memory for subsequent processing.

As in traditional confocal microscopy, if the object that is to be imaged is moved out of the focal plane, the array of spots generated by the zone plates will not form collimated rays when they pass through the zone plates for the second time, causing the detector lens to focus the light from the array into a focal plane that is different than when the substrate was at the focal plane of the zone-plate array. The pinhole will hence block most of the radiation. Again, the objective of the pinhole/aperture is to improve contrast by allowing only light from the focal plane of the zone-plates to reach the detector/CCD.

The CCD is placed in the conjugate plane of the zone-plate array, and therefore, the zone plates themselves are imaged with the camera. As a consequence the pinhole cannot be arbitrarily small in order to maximize contrast as in traditional confocal microscopy. It must be sufficiently large as to enable the image of each zone-plate to reach the CCD.

#### 4.2.1.3 Imaging Results



In an effort to understand the focusing performance of high-numerical-aperture zone plates, a set of five linear arrays of phase zone plates, with NAs ranging from 0.7 to 0.95, were fabricated. The zone plates were then tested, with the ZPAL system operating in microscopy mode, by having the different numerical-aperture zone plates image a chirped circular-grating resolution standard, with linewidths varying from 1  $\mu\text{m}$  to 150 nm (the resolution standard was custom fabricated for this application by means of electron-beam lithography). A schematic of the resolution standard along with two scanning-electron micrographs of the first and last zones of the standard can be seen at the top of Figure 4-13. The figure also includes five ZPAM images of the resolution standard acquired with the various NA zone plates. Note that as the NA increases, even the finest period gratings can be resolved, demonstrating that very high-NA zone plates (all the way up to 0.95) maintain good focusing properties and can hence be utilized for high-resolution imaging. These results represent the first report of such high-NA optical imaging with zone plates.

#### **4.2.1.4 Knife-Edge Results**

With the objective of obtaining a more precise characterization of the PSF of the high-numerical aperture zone plates, knife-edge measurements were performed. This technique, which consists of scanning a sharply defined edge through the focused spot that is intended to be measured, is a well-known procedure routinely used to measure

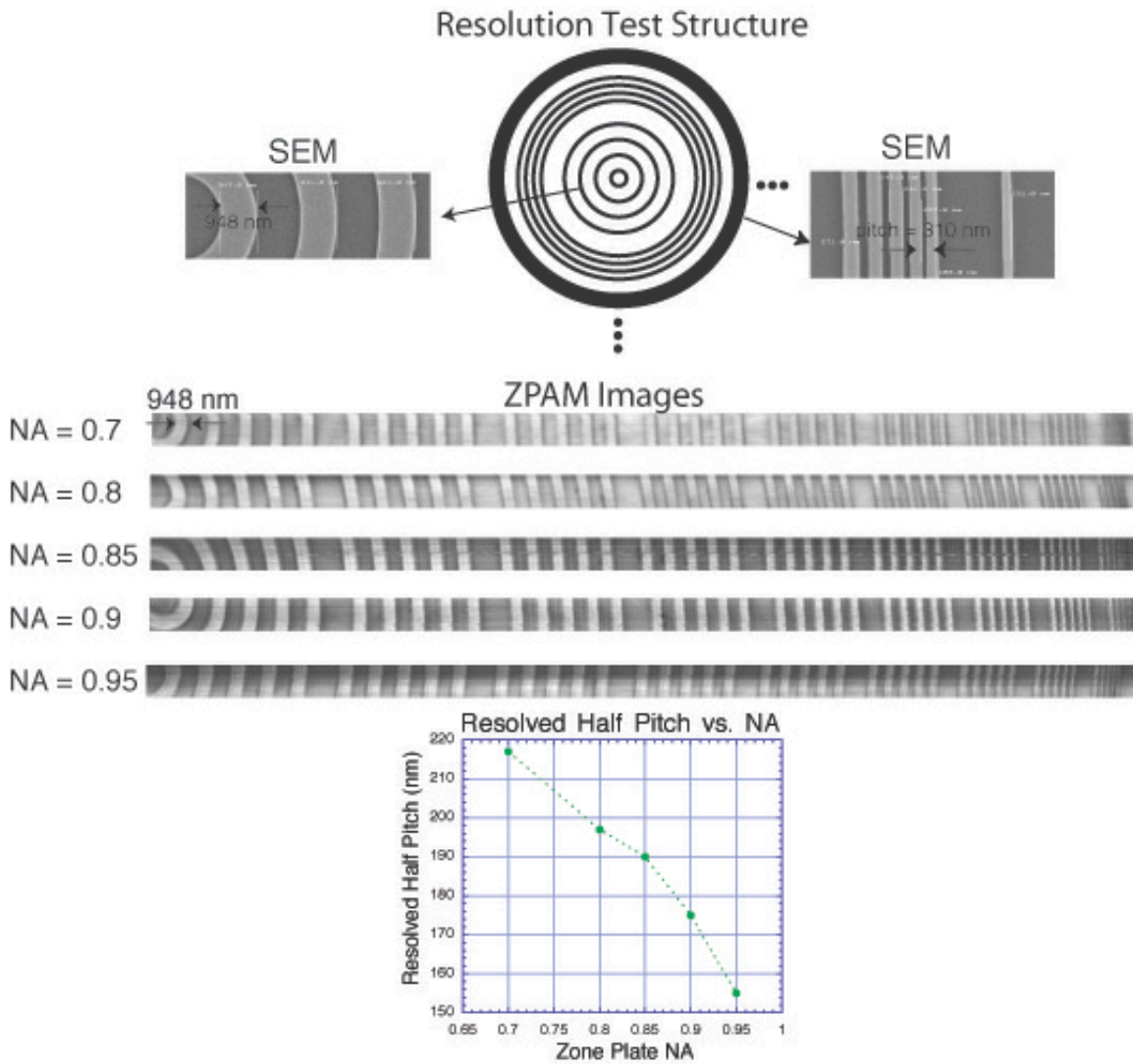


**Figure 4 - 13.** Characterization of high-numerical aperture zone plates by means of confocal microscopy (ZPAM). Top: Schematic representing the resolution structure utilized for characterization. The structure is a chirped circular grating with linewidths varying from  $1\ \mu\text{m}$  to  $150\ \text{nm}$  (see scanning-electron micrographs at the top-right and top-left of the figure). The figure includes five ZPAM images of the chirped grating taken with high-NA zone plates operating at  $\lambda = 442\ \text{nm}$ . Bottom: Plot of the resolved half-pitch of the chirped gratings vs. the Numerical Aperture (NA) of the zone plate. As the numerical aperture increases, all the way to 0.95, the zone plate is able to resolve finer and finer features, demonstrating that very high-NA zone plates can be utilized for imaging.

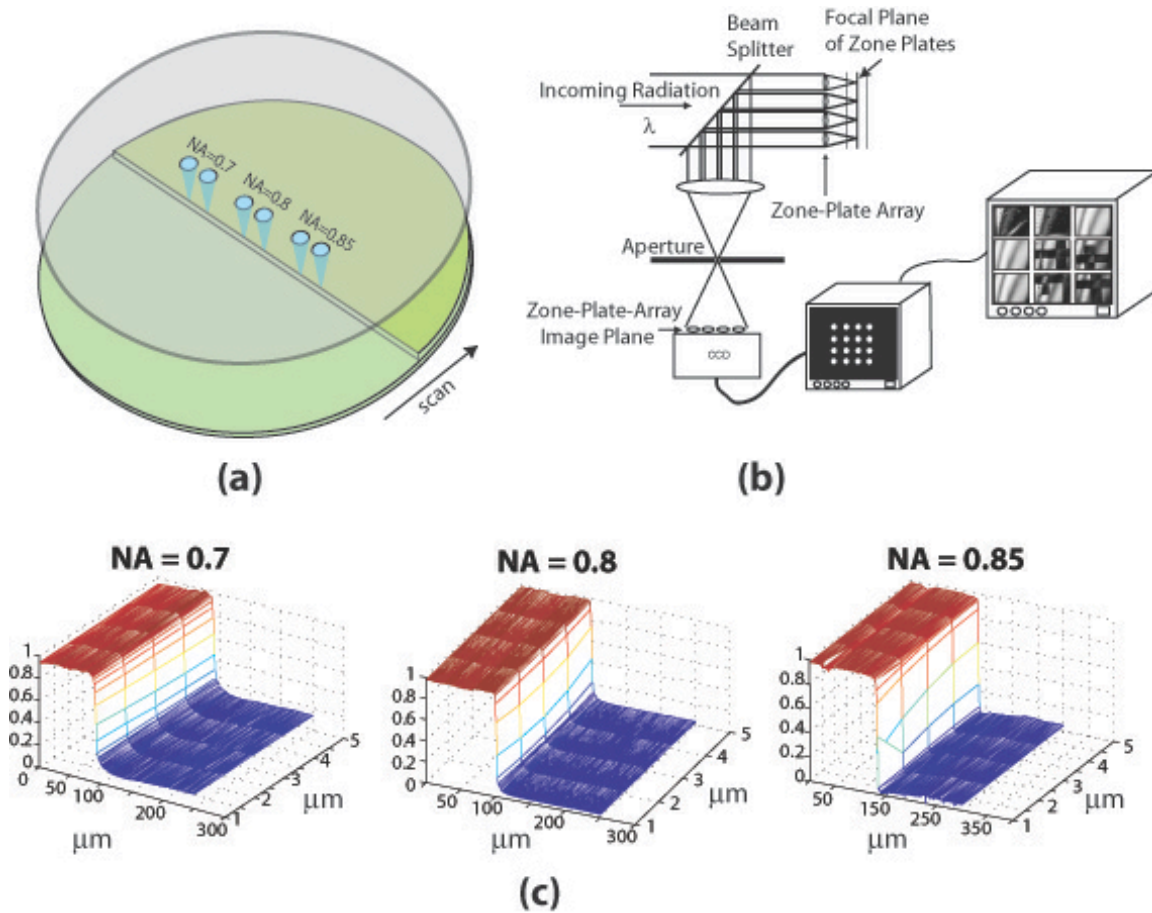


**Figure 4 - 14.** Knife-edge scans for the PSF characterization of zone plates. (a) The focused spot is scanned across a sharp-edge defined by a cleaved Si wafer bonded to a substrate. (b) The signal reflected from the knife-edge scan is collected by means of the ZPAM setup illustrated in the figure. (c) Three knife-edge scans performed with ZPAM with zone plates having numerical apertures of 0.7, 0.8, 0.85. As the numerical aperture increases, the slope of the edge also increases. As can be seen in Figure 4-15, the PSF can be reconstructed from these knife-edge scans.

beam-diameters for both optical and electron-beam focusing systems. Figure 4-14 shows three knife-edge scans obtained with zone plates having numerical apertures of 0.7, 0.8 and 0.85 respectively. Clearly, as the numerical aperture increases, the slope of the edge-transition also increases, indicating that the focal spot was smaller.

In a more quantitative manner, from the knife-edge scans the point-spread function of the high-numerical-aperture zone plates can be reconstructed. This will provide yet another method (the first one was discussed in section 4.1.1) to quantify the characteristics of the PSF.

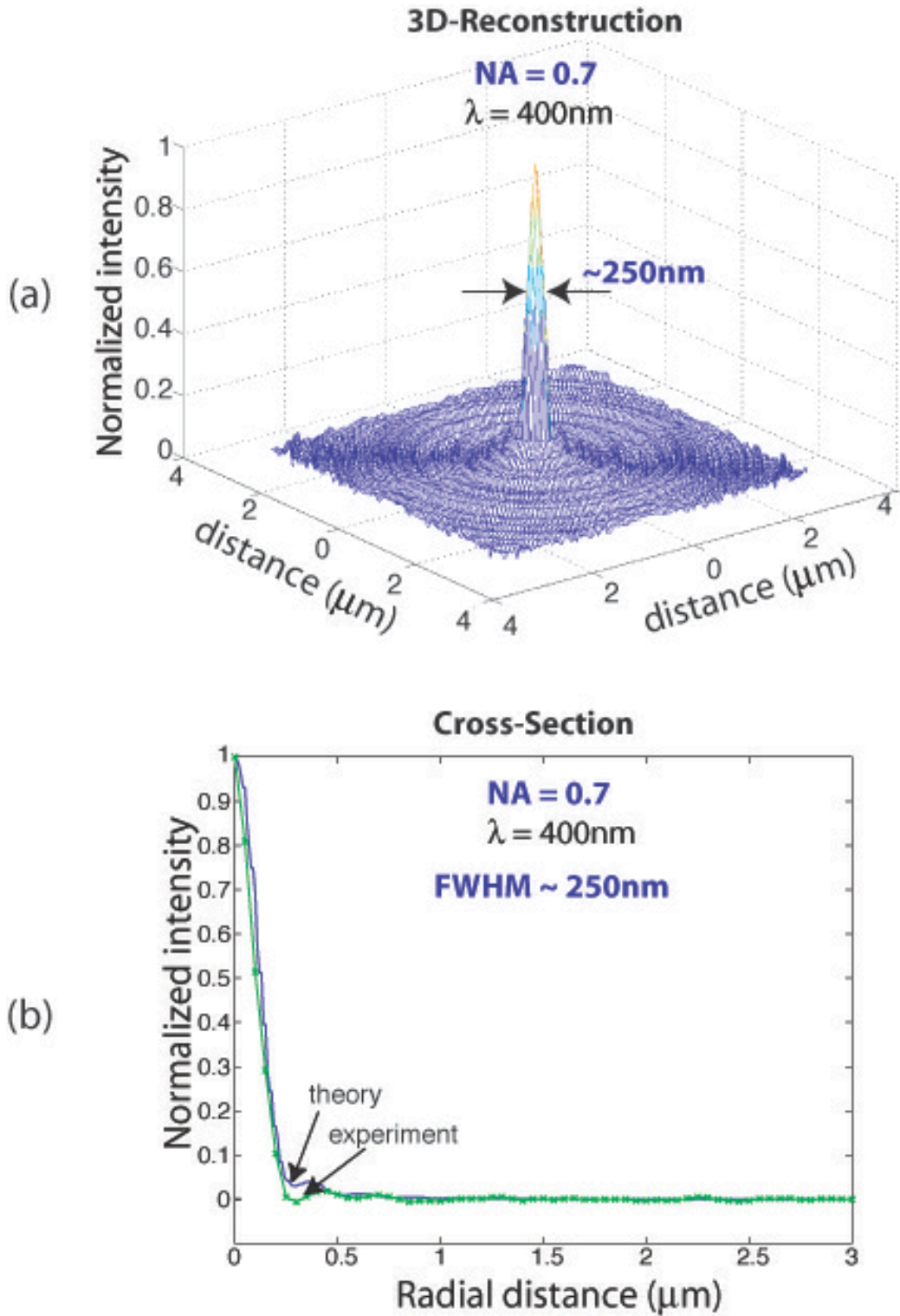


**Figure 4 - 15.** Reconstructed PSF of a 0.7 NA zone plate operating at  $\lambda=400\text{nm}$ . (a) The 3-D reconstruction is obtained from the cross-section and then rotated assuming circular symmetry. (c) Cross-section of the reconstructed PSF. Note that excellent agreement with theory. The spatial resolution of the knife-edge data was 50nm.

We begin by processing the data presented in Figure 4-14. Assuming a perfect confocal microscope, the knife-edge response can be expressed as a convolution of the PSF of the zone plate with the knife-edge [Ref 4-5]. We can then write:

$$U = h^2 \otimes t \quad 4 - 9$$

where  $h$  is the point-spread-function of the zone plate, and  $t$  is the scanned object (i.e. the knife-edge). The PSF appears as a square term since the signal passes through the zone plate twice (once as it focuses the incident radiation onto the object, and the second time as the reflected light is collected on the way back through the zone plate).

Since knife-edge can be modeled as a step function (this is a good approximation, since the sample was a cleaved silicon wafer), carrying out the convolution in equation 4-9 we get:

$$U = - \int_{-\infty}^{+\infty} dy' \int_{-\infty}^{x'} h^2(x', y') dx' \quad 4 - 10$$

by differentiating the above expression, the line-spread function can be obtained:

$$\frac{dU}{dx'} = - \int_{-\infty}^{+\infty} h^2(x', y') dy' \quad 4 - 11$$

The line-spread function is the tomographic projection of the point-spread function along the scan direction. The PSF can be reconstructed by inverting equation 4-11, via an operation known as the *inverse Radon transform*. However, this operation is very sensitive to noise, and hence careful averaging over the area of the scan has to be applied. Figure 4-15 shows the results obtained for a zone plate with a numerical aperture of 0.7 operating at  $\lambda=400\text{nm}$ . Once again, we can see that the zone plates performed as expected, with diffraction-limited focusing that is in excellent agreement with theory.

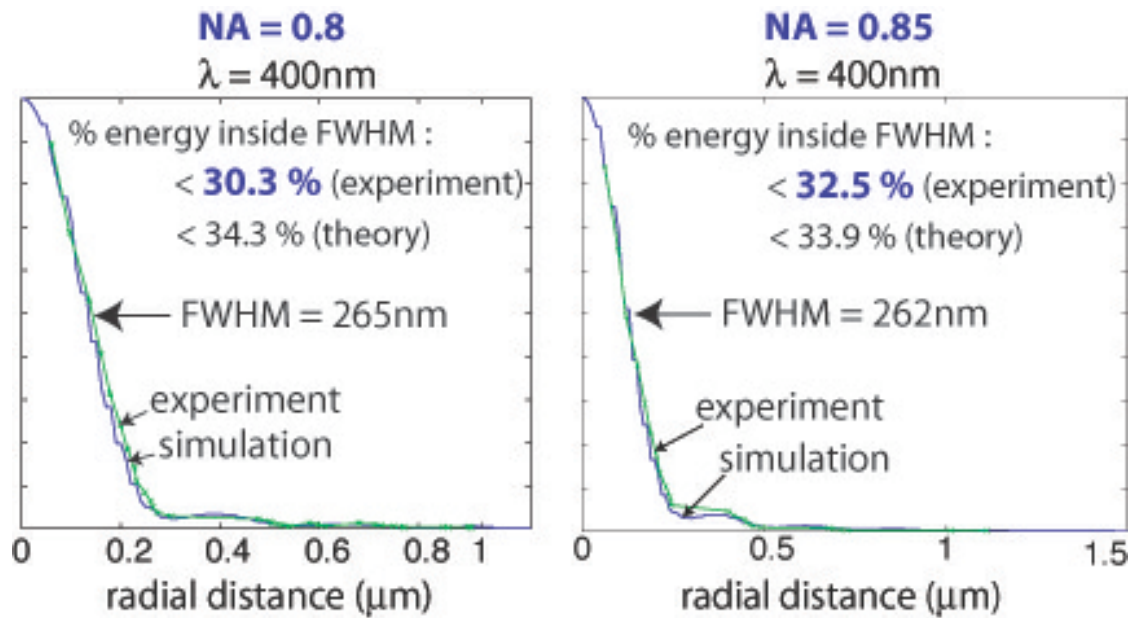


**Figure 4 - 16.** Experimental versus theoretical comparison of the efficiency into the focused spot for two zone plates with numerical apertures 0.8 and 0.85.

#### 4.2.2. Efficiency Measurements

From the experimentally obtained cross-section of the point-spread-function, it is relatively straightforward to calculate the efficiency that was achieved into the focused spot. The method relies on integrating the energy under the area of the PSF from the center of the spot up to the full-width-at-half-maximum (FWHM), and dividing the obtained number by the total energy that is under the entire PSF. This very simple calculation can provide an upper-bound on the efficiency obtained with the fabricated zone plates. A comparison of the experimentally determined and the calculated PSF, along with the expected and achieved focusing efficiencies is plotted in Figure 4-16. Note that the efficiencies that can be achieved are close to the ideal performance.

#### References Chapter 4:

[Ref 4-1] Kwok-Kit Wong A., *Resolution Enhancement Techniques in Optical Lithography*, SPIE Press, Bellingham, Washington, 2001

[Ref 4-2] M.Born and E.Wolf, *Principles of Optics*, Cambridge Univ. Press, New York 1999, 7<sup>th</sup> Ed, pp.441

[Ref 4-3] M.Minsky, US patent 3,013,467, 19 Dec 1961, filed 7 Nov. 1957.

[Ref 4-4] H.J.Tiziani, R.Achi, R.N.Kramer and L.Wiegers, "Theoretical analysis of confocal microscopy with microlenses." Appl. Opt. 35(1). 120-125 (1996).

[Ref 4-5] Rajesh Menon, Optimum volume-holographic confocal microscope: Area Exam Report. Technical Report, 2002. MIT].

Chapter 4.....	71
4.1 Focusing Performance.....	71
4.1.1. Spot Characterization .....	71
4.1.2 Depth of Focus .....	73
4.1.3 Dealing with Multiple Diffraction Orders .....	76
4.1.3.1 The Issue of Background in Lithography .....	76
4.2. Numerical Aperture Studies .....	85
4.2.1 Characterization of Numerical Aperture by means of Zone-Plate-Array Microscopy (ZPAM) .....	86
4.2.1.1 The ZPAM Principle .....	86
4.2.1.2 Experimental Setup .....	88
4.2.1.3 Imaging Results.....	88
4.2.1.4 Knife-Edge Results.....	89
4.2.2. Efficiency Measurements .....	94

## List of Figures

Figure 4 - 1. Methodology for extracting the PSF of a zone plate by means of lithographic exposures on resist.. .....	72
Figure 4 - 2. Comparison of the experimentally determined and the simulated PSF of three zone plates with numerical apertures 0.7, 0.8, 0.85 operating at $\lambda=400\text{nm}$ .....	73
Figure 4 - 3. Two rays (spatial frequencies) contributing to spot formation. ....	74
Figure 4 - 4. Plot of the impact of defocus on image contrast for ZPAL (operating at $\lambda=193\text{nm}$ ). 75	
Figure 4 - 5. Typical contrast curve of a positive photoresist.....	77
Figure 4 - 6. Plot of the minimum resolvable image contrast versus resist contrast.....	78
Figure 4 - 7. Full-field patterning is possible with ZPAL .....	80
Figure 4 - 8. Massive parallelism can be achieved with ZPAL.. .....	81
Figure 4 - 9. Blazed zone plates can provide close to 100% efficiency into a diffraction-limited spot..	83



Figure 4 - 10. Direct 3D Patterning with HSQ. ....	84
Figure 4 - 11. Confocal microscopy. ....	87
Figure 4 - 12. Experimental implementation of Zone-Plate-Array Microscopy.....	88
Figure 4 - 13. Characterization of high-numerical aperture zone plates by means of confocal microscopy (ZPAM).....	90
Figure 4 - 14. Three knife-edge scans performed with ZPAM with zone plates having numerical apertures of 0.7, 0.8, 0.85.....	91
Figure 4 - 15. Reconstructed PSF of a 0.7 NA zone plate operating at $\lambda=400\text{nm}$ .....	92
Figure 4 - 16. Experimental versus theoretical comparison of the efficiency into the focused spot for two zone plates with numerical apertures 0.8 and 0.85. ....	94

# Chapter 5

## *The ZPAL Prototype System*

This chapter presents progress towards the implementation of a prototype ZPAL-system operating at an exposure wavelength of 400 nm, and capable of quick-turn-around, maskless lithography. Extensive lithography results are presented, detailing writing strategy, dose control and proximity-effect correction techniques. The development of a high-speed data delivery system is also discussed, as well as a multiplexing scheme that will enable the ZPAL prototype to achieve 210 nm feature sizes at a moderate but useful throughput of  $\sim 0.25 \text{ cm}^2$  in 20 minutes. The specifications for a high-throughput ZPAL system with sub-100nm resolution are also presented.

### **5.1 The ZPAL Architecture**

As discussed in Chapter 2, zone-plate-array-lithography uses a narrow bandwidth source, an array of Fresnel zone plates, a multiplexing device capable of controlling the illumination to each zone plate in the array, and a scanning stage, to print arbitrary patterns on a wafer without a mask. The entire array of zone plates is illuminated and then shuttered by the multiplexing device. The stage is scanned at the same time, enabling the creation of arbitrary patterns. Aside from the necessary beam-shaping optics needed to properly illuminate the pixels of the multiplexing element such that one pixel illuminates one and only one zone plate (ensuring that there is no crosstalk between zone plates as well as a uniform phase front across each of them), the optical train of the ZPAL architecture is inherently simple and inexpensive. As discussed in Chapter 3, for the UV and deep

UV, the array of zone plates can be fabricated with a planar process that is simple and robust. The micromechanical elements employed are reliable commercial products of modest cost. The more expensive components are the radiation source and the scanning stage, a cost common to all lithography systems. But, with an architecture that offers a radical departure from a century-old tradition of refractive optics, a high-NA system can be built at a cost no higher than a low NA one.

We now proceed with a description of the components utilized in the ZPAL prototype system.

### 5.1.1 The GaN Diode Laser

The invention of the blue-light-emitting diode and blue semiconductor laser in 1991 by Shuji Nakamura<sup>15</sup>, has resulted in the commercialization of compact, versatile, and highly cost-effective blue, violet, and ultraviolet lasers that can be utilized in ZPAL. These new lasers are ideal replacements for bulky, inefficient gas lasers. In terms of cost, the availability of compact GaN-diode lasers has reduced the price of blue lasers from tens of thousands of dollars to a only few thousand dollars. Furthermore, being diodes, no “warming-up” is required when the laser is turned on (as is required with HeCd-gas lasers), and they can be switched ON/OFF electronically at MHz rates. Two pictures illustrating the very significant size reduction achieved with the GaN lasers are included in Figure 5-1.

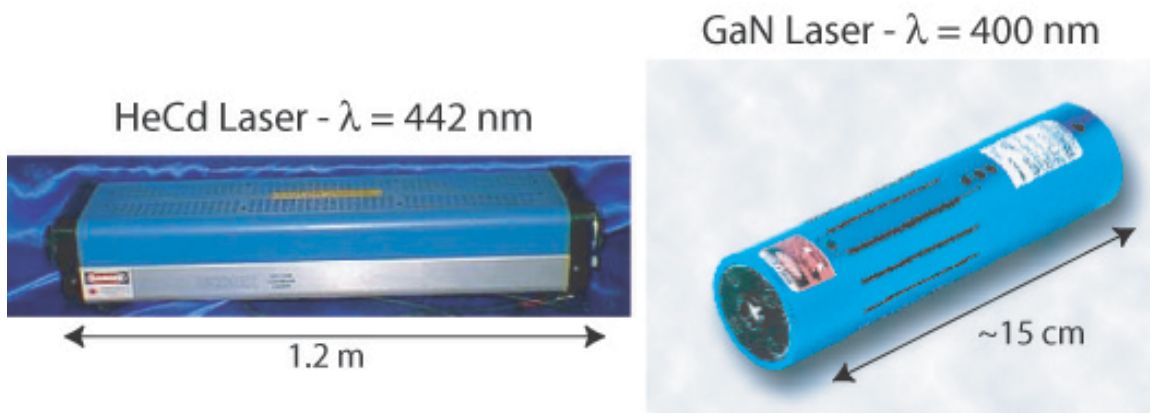


**Figure 5 - 1.** Two of the blue lasers utilized in ZPAL. The availability of compact GaN-diode lasers has reduced the price of blue lasers from tens of thousands to a few thousand dollars. Furthermore, being diodes, no warm-up is required (as is the case with HeCd-gas lasers), and they can be switched ON/OFF electronically at MHz rates.

For all the lithography results presented in this chapter, a  $\lambda = 400\text{nm}$  diode laser manufactured by Power Technology Inc. [Ref 5-1] with a nominal output power of 25mW was utilized. The laser comes with an integrated thermoelectric cooler that maintains the laser diodes operating at 20°C, prolonging the life of the

---

<sup>15</sup> At the time of the invention an employee of Nichia Corporation (who still owns the basic patent) and now a Professor at UC Santa Barbara

diode and achieving wavelength stability<sup>16</sup>, something that is important in ZPAL given the highly chromatic nature of zone plate focusing. In addition, an astigmatic lens placed at the output of the laser module corrects the highly divergent, elliptical, and astigmatic beams typically produced by diode lasers.

For the ZPAL prototype, the output of the laser is fed into an electro-optic feedback loop designed to reduce any noise or amplitude variations that might be present. A low voltage electro-optic light modulator manufactured by ConOptics [Ref 5-2] is then used to achieve dose control and modulation at high speeds. The modulator is connected to the ZPAL control computer via a high-speed input/output board.

In ZPAL, the micromechanical elements are responsible for dose control, bypassing the need for any other dose modulator. However, in order to characterize the lithographic performance of zone plates, as well as to optimize the writing-strategy and proximity-effect correction techniques, it is often preferred to run the system without the micromechanical elements. In this configuration, a dose modulator is required, and hence its presence in the prototype optical configuration.

### **5.1.2 The Silicon Light Machines GLV Module**

As part of our design considerations for the ZPAL prototype, we have switched from our original method of multiplexing the light for ZPAL, the Texas Instruments DMD™ micromirror array, to the Silicon Light Machines Grating Light Valve™ (GLV™) linear array [Ref 5-3]. Although the GLV™ has a smaller number of pixels (1,088) compared to the DMD™ micromirror array (~1 million or more), the higher speed of operation of the GLV™ (20ns rise time as opposed to 20 μs for the DMD™), the fact that gray-scaling is built in, and its diffractive mode of operation (making it compatible with shorter wavelengths, possibly even down to 157nm) made it a superior choice for this ZPAL prototype.

#### **5.1.2.1 Principle of Operation**

The GLV™ is a micromechanical phase grating consisting of parallel rows of reflective Al ribbons. Alternate rows of ribbons can be pulled down electrostatically in a controlled manner to create diffraction effects on incident light. When no force is applied, all the ribbons lie in the same plane. If illuminated, incident light will be reflected from their surfaces at the same angle at which it is incident. When alternate ribbons are pulled down, a grating structure is created. In this state diffraction will produce light at an angle different from that of the incident light. By alternating between these two states (i.e. from flat ribbons to a grating structure)

---

<sup>16</sup> The blue diode has an excellent temperature coefficient of 0.05nm/°C

the GLV™ can switch light ON and OFF. Furthermore, by tuning the applied electrostatic force, the depth to which the ribbons are pulled down can be controlled, impacting the amount of light diffracted into the first order. Grayscaleing of the incident light can be achieved in this manner. Each of the 1088 pixels present in the linear array can accept 8-bits of grayscaleing (256 levels). Since the motion involved in switching the pixels of the GLV™ is small (one-quarter wavelength),

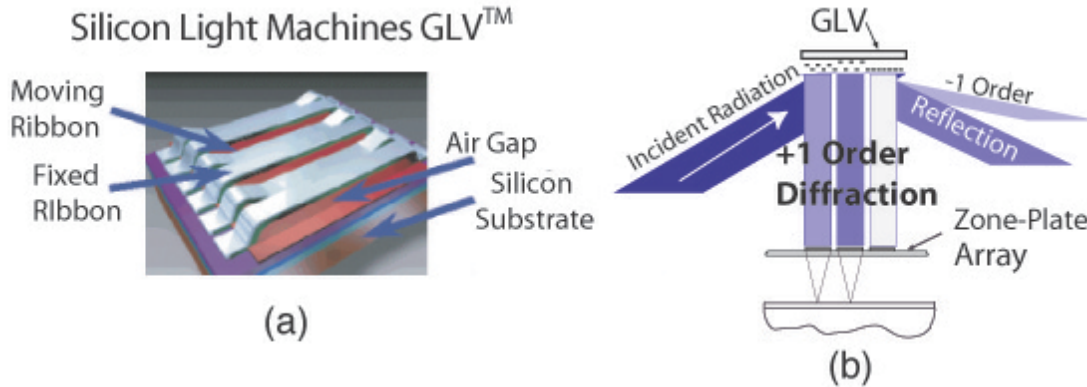


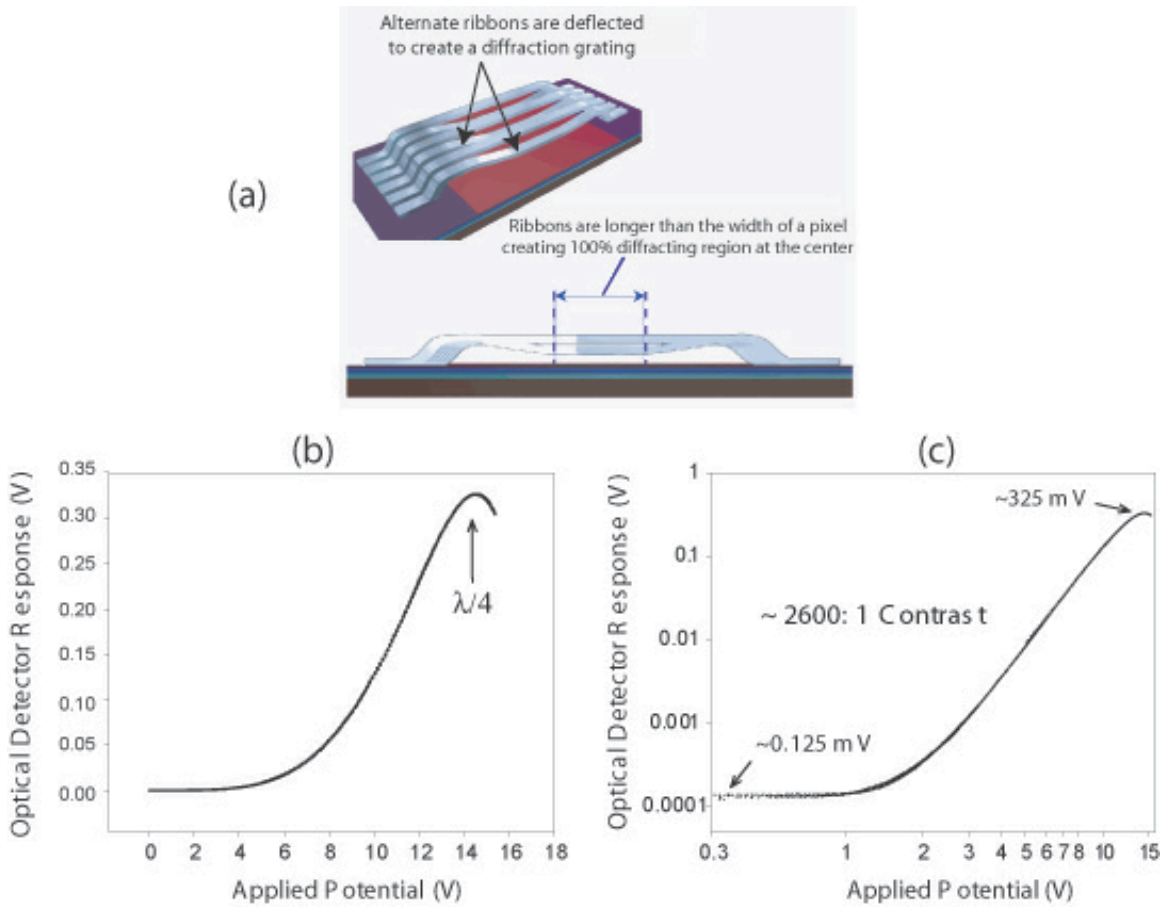
**Figure 5 - 2.** The Silicon Light Machines Grating Light Valve™ (GLV™) (a) one pixel of the GLV™ (each pixel can be thought of as a “mini-grating”), (b) intended implementation of the GLV™ with our linear array of zone plates indicating gray scaling.

the GLV™ is capable of very high switching speeds, with a rise time from the ON to the OFF position of only 20ns [Ref 5-4]. One pixel of the linear array is depicted schematically in Figure 5-2, along with the intended implementation in ZPAL.

### 5.1.2.2 Efficiency

The specific electro-optic response for a GLV pixel is shown in Figure 5-3. The first-order diffracted light intensity is essentially zero when no voltage is applied. Two factors lead to this result. First, most of the incident light is simply reflected specularly by the GLV device, which has a relatively large ribbon width-to-ribbon gap ratio (~6:1). Second, any potentially diffracting features, such as the ribbon gaps, are expressly created at twice the spatial frequency of the alternate ribbon ON state. Thus any undesirable diffraction occurs at larger angles, and does not affect contrast in the first-order diffraction beams. As can be seen in Figure 5-3(c), the GLV device performs smoothly and monotonically for well over three decades of intensity. Under idealized conditions, individual device contrast has been measured at over 4,000:1[Ref 5-5].

The efficiency of the GLV device depends on three main factors: the diffraction efficiency, the aperture ratio (or fill factor), and the reflectivity of the aluminum surface. In an ideal square-well diffraction grating, 81% of the diffracted light energy is directed into the +/- 1st orders.



Source: Silicon Light Machines

**Figure 5 - 3.** A GLV pixel with alternate reflecting ribbons electrostatically deflected to produce a diffraction grating. Note that the ribbons are longer than the width of a single pixel (vertical deflection greatly exaggerated). (b) GLV electro-optic response for 1st order diffraction, (c) GLV electro-optic response for 1st order diffraction on a logarithmic scale.

For maximum efficiency the ribbons have to be vertically deflected by a distance  $d$ , given by:

$$d = \frac{\lambda}{4} \quad 5 - 1$$

where  $\lambda$  is the wavelength of light.

An important design consideration required to achieve the maximum *overall efficiency* for any ZPAL system utilizing the GLV, has to do with how this MEMS device is illuminated. Ideally we would like to illuminate the GLV with a beam as close to a

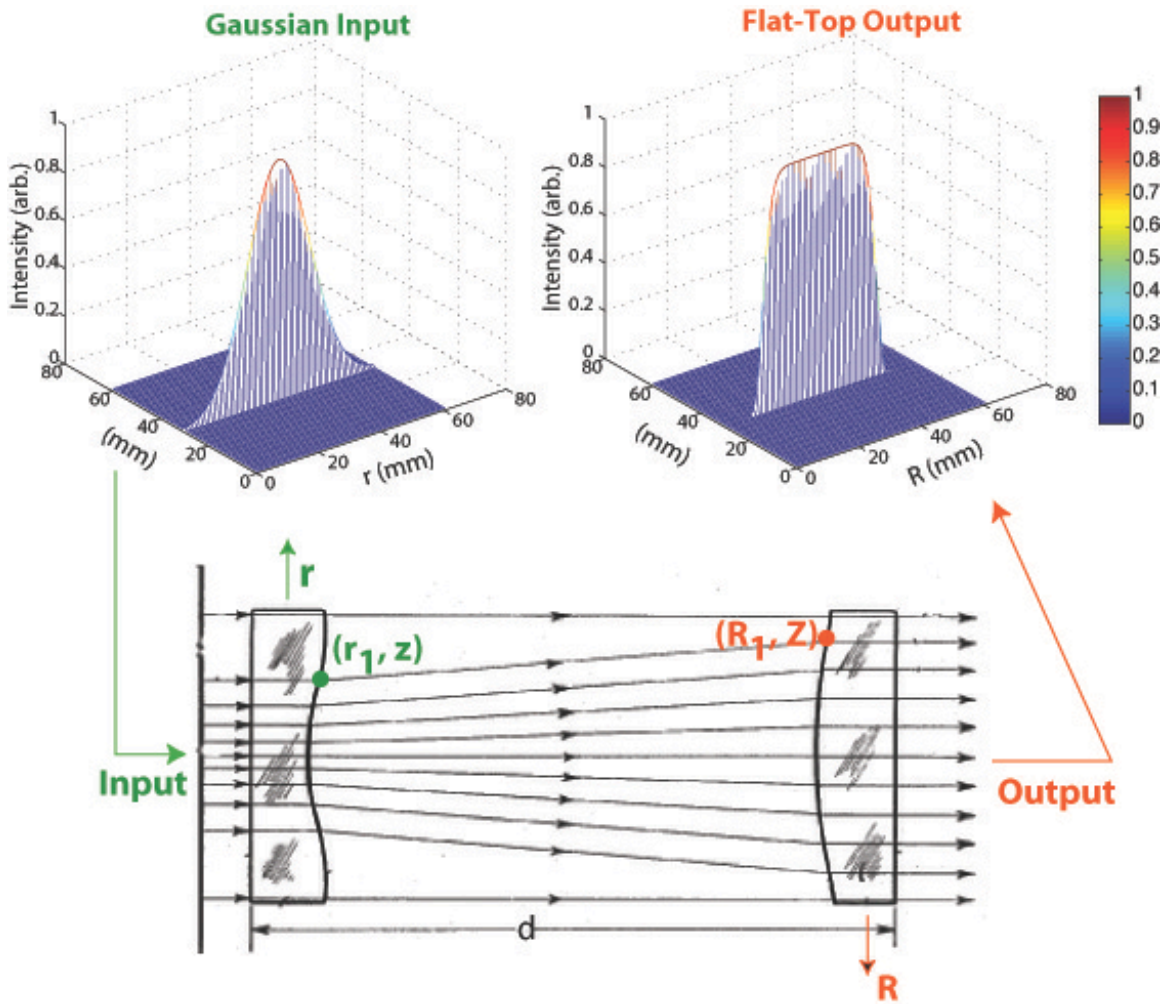


**Figure 5 - 4.** Two properly designed aspheric lenses can convert a Gaussian input intensity profile into a flat-top intensity profile.

flat-top as possible, in order to avoid the Gaussian distribution (typical of most lasers) of intensities across the 1,088 diffracted beams. Such a distribution would result in different zone plates receiving vastly different intensities, resulting in an unacceptable dose control for lithography applications. Although one could always correct for the Gaussian illumination via grayscaling (i.e. lower the efficiency of the central pixels of the GLV to match their diffracted intensities to the pixels at the edges of the device), this would result in a very significant loss of total power. It would be much preferable to properly illuminate the device with a flat-top beam capable of providing a uniform intensity across all 1,088 pixels. A methodology for designing a pair of aspheric lenses capable of converting a collimated Gaussian beam to a flat-top beam is presented below [Ref 5-6, Ref 5-7].

Consider the schematic presented in Figure 5-4. It presents a Gaussian input beam impinging on a lens. By appropriately designing the curvature of this first lens, the rays can be redirected in such a way so as to redistribute the “density of the rays” into a uniformly distributed intensity profile. A second aspheric lens can then be used to collimate the beam to obtain the desired top-hat profile, as shown on the top-right of the figure.

The problem is to find an expression for the curvature of the two aspheric lenses that will achieve such a transformation.

Let us denote by  $d$  the distance between the faces of the two aspheric lenses, as illustrated in Fig.5-4. Lets also define two coordinate systems  $(r, z)$  and  $(R, Z)$ , centered at the intersection of the lens surfaces with the optical axis. We would like to obtain an expression for the curvature of the two lenses through the condition that a ray entering the first lens at  $(r_1, z)$  comes out collimated at  $(R_1, Z)$ . A relation then exists between the rays entering and exiting the optics of the form:

$$R = h(r) \quad 5 - 2$$

Disregarding losses due to absorption and reflections in the lens elements, energy conservation requires that the total power in the input and output beams to be maintained. This condition will allow us to obtain a more explicit relation for equation 5-2. The energy conservation requirement can be expressed as:

$$\int_0^{2\pi} \int_0^{R_o} I_{in}(r) r dr d\theta = \int_0^{2\pi} \int_0^{R_o} I_{out}(r) r dr d\theta \quad 5 - 3$$

The left-side of equation 5-3 is the total energy in an energy beam having a distribution  $I_{in}(r)$ . In our case, this will be a Gaussian distribution, expressed as:

$$I_{in}(r) = e^{-\left(\frac{r}{a}\right)^2} \quad \text{for } r < R_o \quad 5 - 4$$

where  $a$  is a scaling factor, and  $R_o$  is the outer radius of the first aspheric lens.

The right-hand side of equation 5-3 is an expression for the total energy of the output beam. Given that we would like to have an output beam with circular symmetry and a uniform (i.e. constant) energy distribution, the equation can be rewritten as:

$$\int_0^{2\pi} \int_0^{R_o} e^{-\left(\frac{r}{a}\right)^2} r dr d\theta = I_{out} \pi R_o^2 \quad 5 - 5$$

Performing the integration and solving for  $I_{out}$ , we get:

$$I_{out} = a^2 \left( \frac{1 - e^{-\left(\frac{R_o}{a}\right)^2}}{R_o^2} \right) \quad 5 - 6$$

A further constraint can now be imposed. Given the fact that the light rays in the central region in the incident beam are progressively spread out toward the peripheral region of the second aspheric lens, if we



divide the incoming Gaussian beam into annular sections of radius  $r_l$  and width  $dr$ , these sections must map onto a second annular section at the second aspheric lens of radius  $R_l$  and width  $dR$ . We can apply, once again, the conservation of energy principle to each of these pairs of annuli. By also using equations 5-4 and 5-6, we get:

$$e^{-\left(\frac{r_l}{a}\right)^2} r_l dr_l = a^2 \left( \frac{1 - e^{-\left(\frac{R_o}{a}\right)^2}}{R_o^2} \right) R_2 dR_2 \quad 5 - 7$$

integrating equation 5-7, a relationship between  $r_l$  and  $R_l$  can be obtained:

$$R_l = R_o \sqrt{\frac{\left(1 - e^{-\left(\frac{r_l}{a}\right)^2}\right)}{\left(1 - e^{-\left(\frac{R_o}{a}\right)^2}\right)}} \quad 5 - 8$$

Equation 5-8 provides a mapping of where each ray entering the first aspheric surface at  $r_l$ , should end up at the second aspheric surface. Now, applying Snell's law at each of the interfaces, an expression for the curvature of each of the surfaces can be obtained. The curvature will naturally depend on the index of the materials used, the separation and size of the lenses, as well as on the scaling parameter  $a$  regarding the size of the input Gaussian beam. Bypassing the geometrical derivation and application of Snell's law at each interface, a final expression for the curvature of each lens is obtained:

$$z(r) = \int_0^{R_o} \left\{ (n^2 - 1) + \left[ \frac{(n-1)d}{R_l - r_l} \right]^2 \right\}^{-1/2} dr_l \quad 5 - 9$$

by using the expression for  $R_l$  given by equation 5-8, the curvature of the first aspheric surface is defined. For the second surface, Snell's law dictates the following expression:

$$Z(R) = \int_0^{R_o} \left\{ (n^2 - 1) + \left[ \frac{(n-1)d}{R_l - r_l} \right]^2 \right\}^{-1/2} dR_l \quad 5 - 10$$

where an expression for  $r_l$  can be obtained via equation 5-8.

By appropriately computing the integrals of equations 5-9 and 5-10, the profiles can be obtained (i.e. for each radial distance, the amount of lens material that has to be removed is calculated). The resulting table of “location in lens” vs. “amount of material to remove” can be used to fabricate the aspheric lenses via a numerically controlled optical finishing machine. The design presented above, once implemented, should enable an efficient illumination of the GLV for the ZPAL prototype.

### 5.1.2.3 A Data Delivery System for the GLV

Given the fact that the Silicon Light Machines GLV module was purchased without any driving electronics, or software interface, a custom electronic system to deliver the pattern data from the ZPAL control computer to the 1,088 pixels of the GLV™ array at very high speeds had to be built. Very briefly, the implementation is as

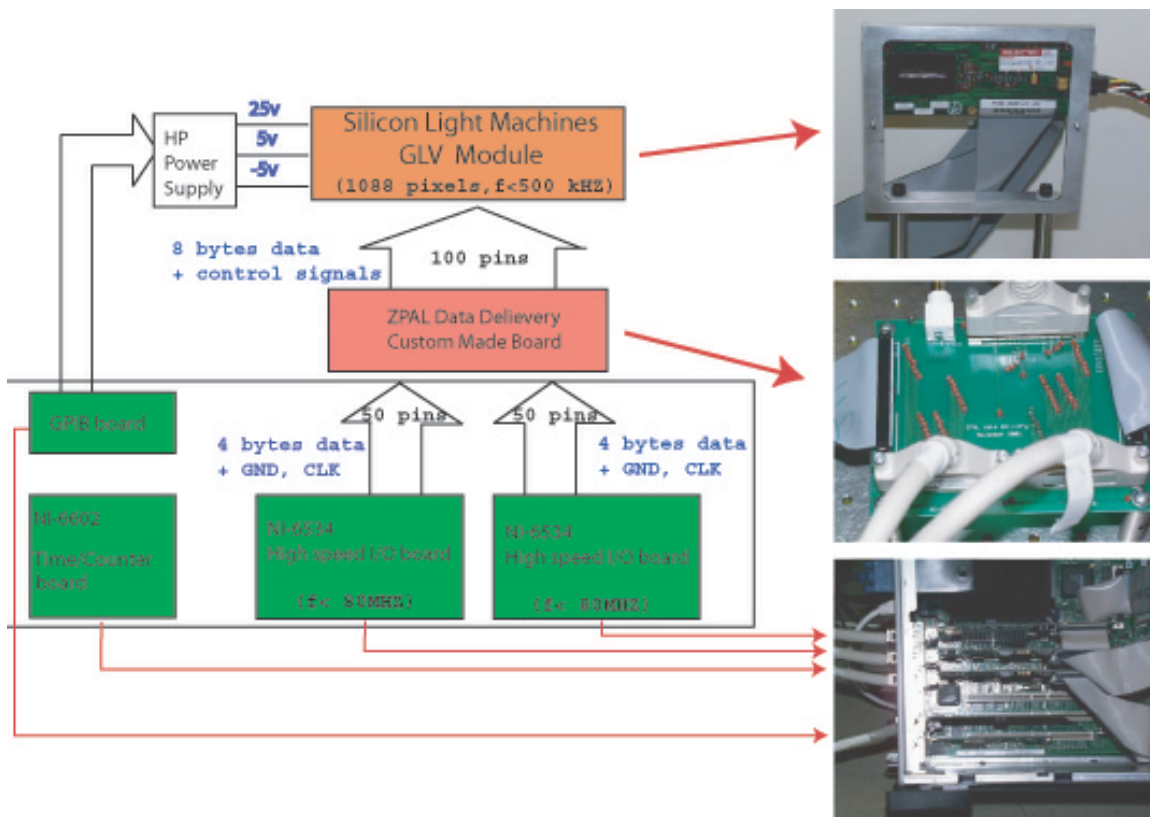


**Figure 5 - 5.** Data delivery implementation for the GLV module in the ZPAL prototype.

follows<sup>17</sup>. Data is first transferred from the computer through the PCI bus to a National Instruments digital I/O board (Model#: 6601). The data is then sent from the I/O board to the GLV™ through a custom made printed circuit board (PCB), which performs the data routing and interpretation as required by the GLV™ electronics.

<sup>17</sup> A much more detailed analysis and description will be the basis of a Master’s thesis by Amil Patel, currently a member of the ZPAL team.

The I/O board, equipped with an 80Mhz clock to enable clocking the data at very high speeds, has the capability of both reading data from the control computer and sending data to the GLV™ simultaneously. In practice, two I/O boards are used in parallel to achieve high data rates. All the software was written in LabView on a Dell windows workstation. Figure 5-5 provides a schematic representation as well as pictures of the system that was built.

In order to test the data delivery system, an experimental setup was assembled, as shown in Figure 5-6 (a). Light from a Helium-Neon laser is collimated and directed onto the GLV™. A lens is used to focus the 1<sup>st</sup> order diffracted beam onto a detector. Data is

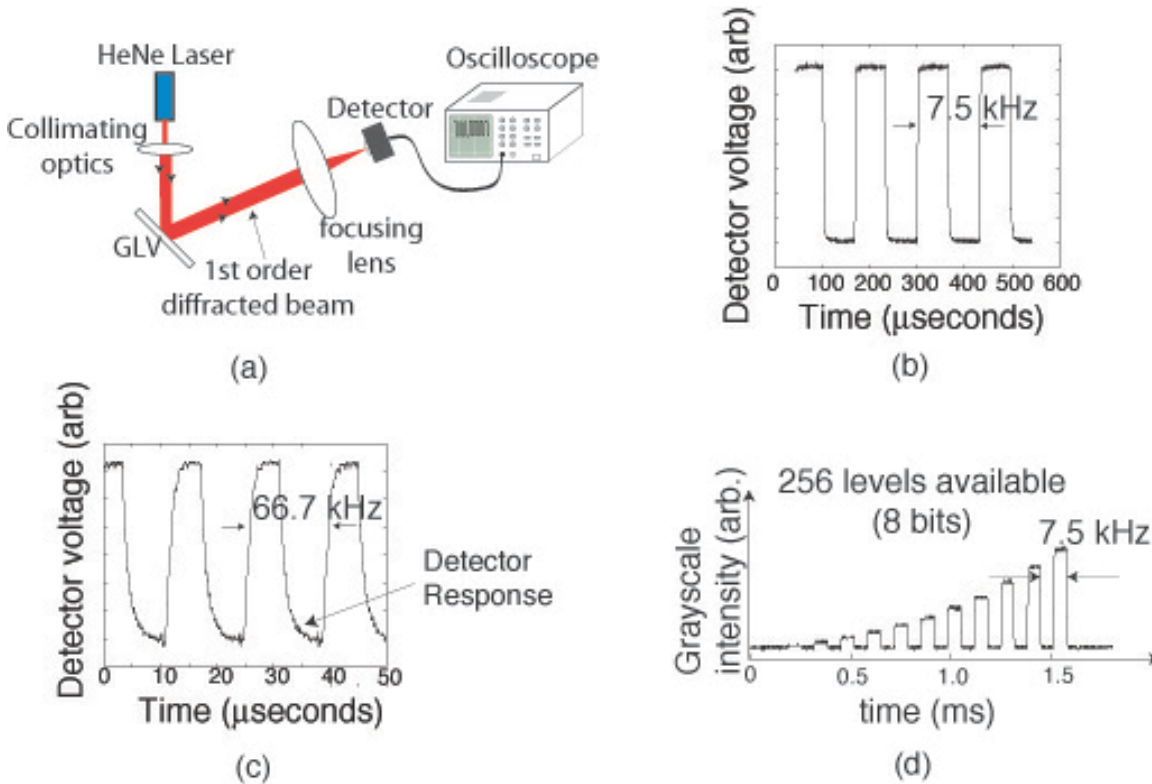


**Figure 5 - 6.** (a) Schematic of the experimental setup for testing the data delivery system for ZPAL. (b) The GLV operating at 7.5 kHz, the required speed for our prototype system. (c) The GLV operating at 66.67 kHz, corresponding to a 1Gbit/sec data rate. (d) Grayscale at 7.5 kHz.

sent to the GLV™ and the modulation of the light on the detector is measured. Figure 5-6(b) shows the detector signal as a function of time when the GLV™ was driven with “ON-OFF” data at a frequency of 7.5 kHz (the specification required for our prototype system), corresponding to an average data transfer rate of 130 Mbits/s. The vertical axis is the detector voltage, but it was not calibrated and hence is not labeled in the figure.

Since the GLV™ is capable of operating at much higher frequencies (~500 kHz), the system was tested in order to determine the limits of the data delivery architecture, even though the achieved requirements are sufficient for the current specifications of the ZPAL prototype. Figure 5-6(c) shows the GLV™ operating at a frequency of 66.67 kHz, corresponding to a data transfer rate of about 1Gbit/s. At the time this experiment was

performed, the response time of the detector used was the limiting factor, but data from a logic analyzer integrated into the system indicates that rates in excess of 100 kHz can be successfully sent with this implementation.

Since dose control is an important requirement for good lithographic performance, the ability to grayscale is paramount in any multiplexing device to be employed in a ZPAL system. The GLV<sup>TM</sup> offers 8-bits of grayscaling (256 levels), 3 bits more than what is needed for the ZPAL writing strategy, which requires 5-bits [Ref 5-8]. As shown in Figure 5-6(d), the data-delivery system is capable of achieving all 8-bits of grayscaling without sacrificing switching speed.

### **5.1.3 The Zone Plate Array**

Although no further discussion is needed with regard to the role of the zone plates in ZPAL, a practical question that is worth addressing is how to experimentally place a photosensitive-resist-coated substrate precisely at the focal plane of the zone-plate array. The two surfaces must be parallel to each other while maintaining the plane of focus as the substrate is scanned. These matters are in practice challenging experimentally, especially for high-numerical-aperture zone plates, which can have focal lengths as short as 30  $\mu\text{m}$ , and very shallow depths of focus.

#### **5.1.3.1 Parallelization and Gapping in ZPAL**

A Michelson interferometer provides a viable technique for parallelizing the zone-plate array and the substrate. The interferometer, as implemented in the ZPAL prototype, is shown in Figure 5-7. A Helium-Neon (HeNe) laser is first passed through a spatial filter and collimated by a lens. The beam is then divided into two beams by means of a beam-splitter cube. One of the beams proceeds by transmission toward the zone-plate array and the wafer, while the other proceeds by reflection towards the mirror (this is the reference arm). The waves are reflected at 3 surfaces (the mirror, the chrome pad on the back of the zone-plate substrate, and the wafer to be exposed with ZPAL).

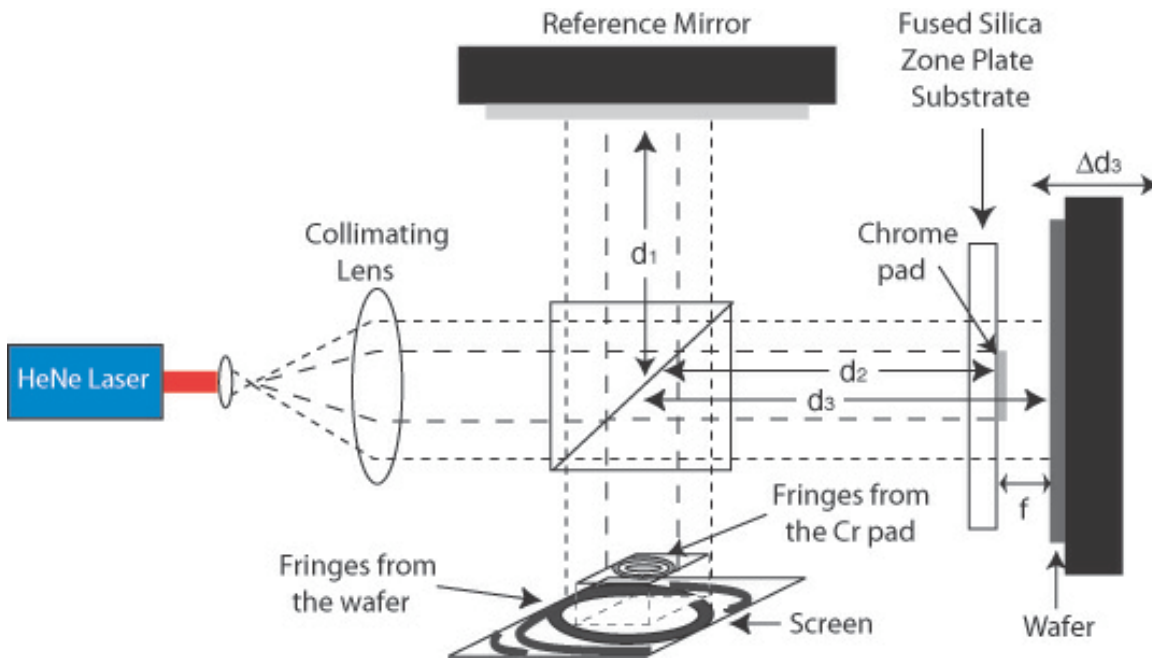


**Figure 5 - 7.** A Michelson interferometer can be used to set the zone plate substrate and the wafer to be exposed parallel to each other.

Interference fringes are observable on the screen (also depicted in the figure) due to all the reflected waves, so long as the optical-path difference between the arms is less than the coherence length of the light used for the interferometer. The very long coherence length of the HeNe laser ensures that the length of the reference arm,  $d_1$ , and those to the zone-plate substrate and wafer need not be matched with any significant precision. By gimbaling the zone plate substrate, observing the change in the fringes, and then adjusting the tilt of the substrate, parallelization can be achieved.

Once parallel, the next step consists on getting the wafer that is to be exposed at the focal plane of the zone plates, with a control that must be better than the depth-of-focus. This can be a considerable challenge for very-high numerical aperture zone plates that can have depth-of-focus of only a few hundred nanometers.

The confocal signal obtained in the Zone-Plate-Array Microscopy (ZPAM) mode of ZPAL, provides an excellent method for positioning the wafer at the focal length of the array. The implementation of a gapping technique with ZPAM is straightforward (see Figure 5-8), with the only constraint that one cannot use for gapping the same radiation that is used for exposing patterns, since in the gapping sequence the resist would be

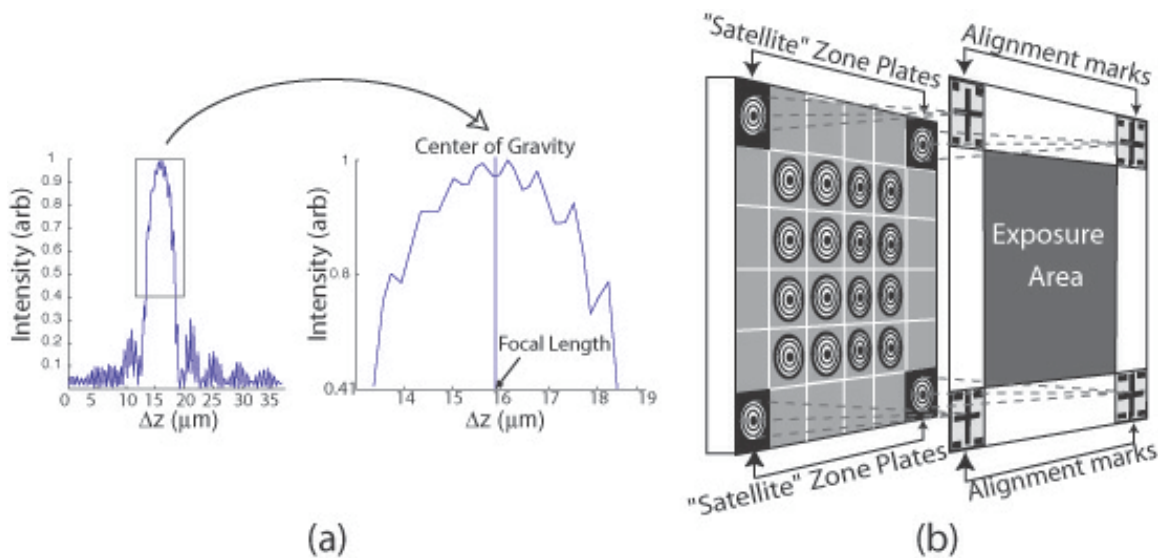


**Figure 5 - 8.** Gapping with confocal microscopy. (a) An experimental confocal signal. A center-of-gravity algorithm enables gap-setting with sub-100nm precision. (b) Illustration of the concept of “satellite” zone plates. These zone plates are designed to have the same focal length as the zone plates in the array, but operate at a non-exposing wavelength (e.g.  $\lambda=633\text{nm}$ ). If the substrate to be exposed is scanned, the “satellite” zone plates can obtain images that can serve to align the exposure to a previous layer.

exposed. The solution lies in fabricating a set of “satellite” zone plates at the edges of the zone-plate array, designed so that they have the same focal length as the exposing zone plates, but operate at a non-exposing wavelength (e.g.  $\lambda=633\text{nm}$ ). The fabrication of these “gapping” zone plates can be readily integrated with that of the exposing zone plates. The scheme allows for sub-100 nm gapping precision, as well as real-time measurements during exposure.

Two other applications can be implemented with the “satellite” zone-plate confocal scheme. The first is achieving parallelization between the zone-plate array and the substrate. This can be done by matching the intensity readings from a set of three “satellite” zone plates spaced sufficiently apart. The readings from each of the three zone plates can be used to feedback to three piezos connected to the zone plate substrate, to then set the array parallel to the substrate.

The second application of ZPAM in ZPAL is level-to-level alignment. If the substrate to be exposed is scanned, the “satellite” zone plates can obtain images that can

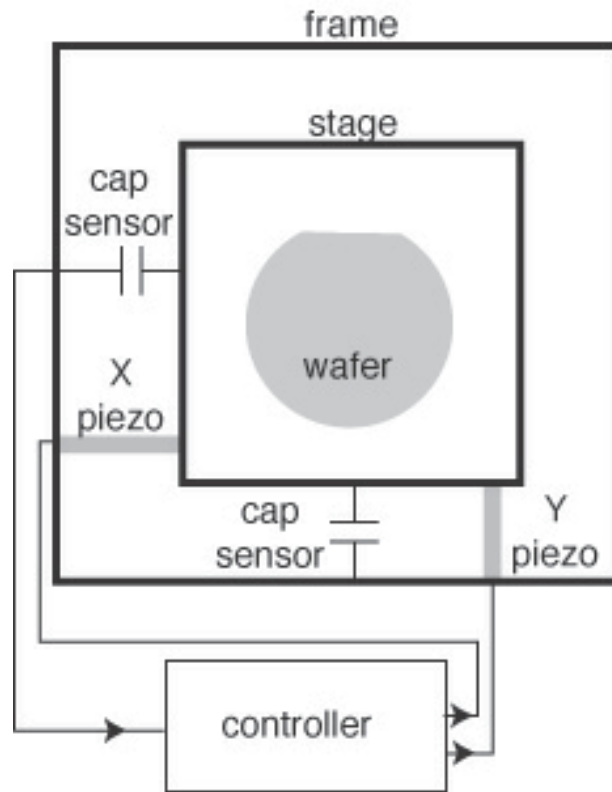


**Figure 5 - 9.** Schematic of the experimental implementation of the continuous-scanning stage in the ZPAL prototype.

be used to align the exposure to a previous layer. This last concept is illustrated in Figure 5-8(b).

#### 5.1.4 The Scanning Stage

The scanning stage in ZPAL is responsible for the creation of complex patterns by displacing the substrate to be exposed to the appropriate positions in synchrony with the flashing laser exposures. Given that zone plates can create high-quality diffraction-limited spots, it is apparent that the quality of ZPAL lithography with ZPAL will be limited by the scanning accuracy and precision of the stage.

Initially implemented as a step-and-settle scanning system (i.e. the stage moves, the stage settles, spots are exposed, the stage moves again, etc), the stage in the ZPAL prototype now has the ability to scan in continuous mode. The scanning system used is a piezo-actuated stage from Physik Instrumente (model P-770), offering a scan range of  $200 \times 200 \mu\text{m}^2$ , with a positioning accuracy of less than 10nm. Capacitive sensors are used for determining position. Custom built velocity feedback circuits were implemented to enable continuous-velocity scanning. The stage scans the substrate in a raster fashion. During exposure, custom-built lithographic pattern generation software ensures that any unwritten rows and repeated pixels are discarded from the pattern, minimizing writing time. A schematic of the experimental implementation of the continuous-scanning stage in the ZPAL prototype can be seen in Figure 5-9.



## 5.2 Lithographic Performance

The results presented in the following sections are the highest quality lithographic patterns ever produced with ZPAL, showing good fidelity, low edge roughness, and the ability to pattern very dense features down to the minimum spot size. As will be described, features as small as 150nm were patterned with ZPAL. This is a remarkable performance for a system operating at  $\lambda = 400\text{nm}$ . The capability of ZPAL to pattern features at a resolution well below half the wavelength, enables ZPAL to compete head-to-head with state-of-the-art multimillion-dollar systems.

### 5.2.1 Writing Strategy

In Zone-Plate-Array Lithography patterns are created through the incoherent addition of spots. The two-dimensional pattern of energy that is deposited in the resist is the result of the convolution of the point-spread function (PSF) of the zone plate with the geometric pattern to be exposed. This concept is illustrated in Figure 5-10.

The convolution has an important consequence: the dose at a given location depends not only on the dose delivered at that location, but also on the dose delivered at nearby locations. Dose from neighboring regions of the pattern can “spill over” and give rise to what are known as proximity effects. A description of the nature of these effects in ZPAL, as well as a methodology for correcting them, is presented in section 5.2.1.2.

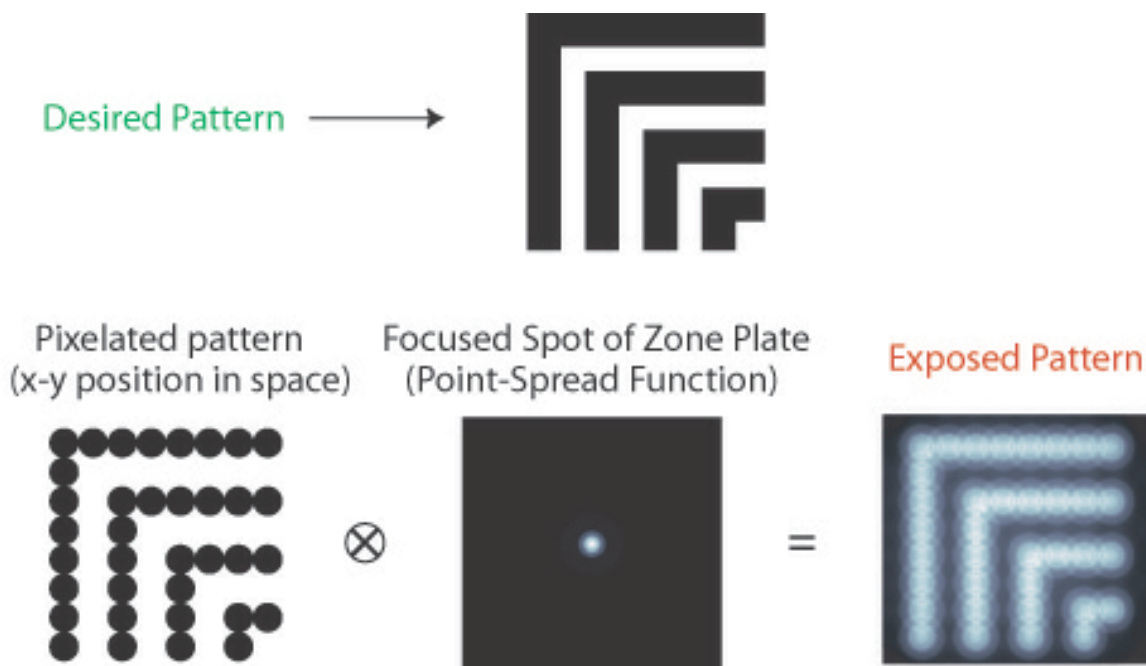


**Figure 5 - 10.** ZPAL writes pattern through the incoherent addition of spots. This addition is the result of the convolution of the pixilated version of the desired pattern and the Point-Spread Function of the zone plate.

### 5.2.1.1 Dose Control and Sub-Pixel Stepping

A lithography system should be able to control linewidth and edge placement of all exposed features with a precision much finer than the minimum feature size (i.e. the spot size in the case of ZPAL). For spot-based lithography systems, this can be done by stepping the exposures on a grid with a spatial period finer than the spot size. This is called sub-pixel stepping. By using this stepping technique, one can envision patterning features as small as the spot size, but with size increments only as small as the stepping grid, e.g., for pattern edge-placement one tenth of the minimum feature size, one would need a grid size one-tenth the spot size. This would severely impact throughput. However, by combining subpixel stepping with gray scaling (i.e the dose to each pixel is controlled) linewidth and edge placement can be controlled to much better than the stepping grid, with minimal throughput impact. This method of patterning has been used for scanning-electron-beam lithography [Ref 5-9, 5-10,5-11] and for scanning laser beam

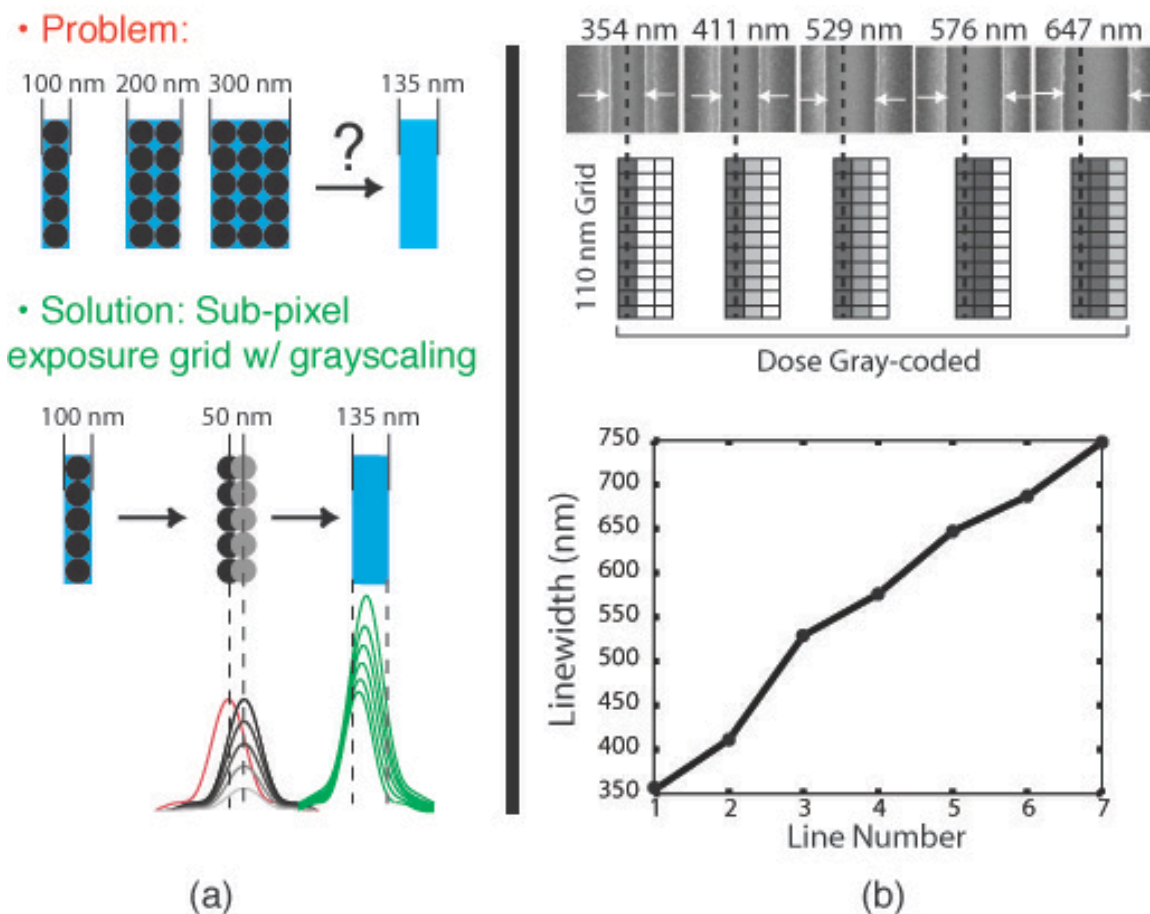


**Figure 5 - 11.** Writing strategy in ZPAL. (a) Since patterns in ZPAL are written by the addition of many spots, the stepping-grid determines the widths that can be created. By stepping a fraction of the spot-size after each spot exposure, while controlling the dose for each exposure, a width and pattern-placement control can be achieved with a resolution that is much better than the size of the spot. (b) Lines of varying width printed with ZPAL with a combination of sub-pixel stepping and gray scaling. Pixels (~330 nm in size) were exposed on a

110 nm grid. To widen the lines, a second line of pixels was exposed at increasing doses, then a third line was added. Top: SEM micrographs of lines. Middle: Schematic of exposure conditions for each line. Bottom: Plot of linewidth vs. line number.

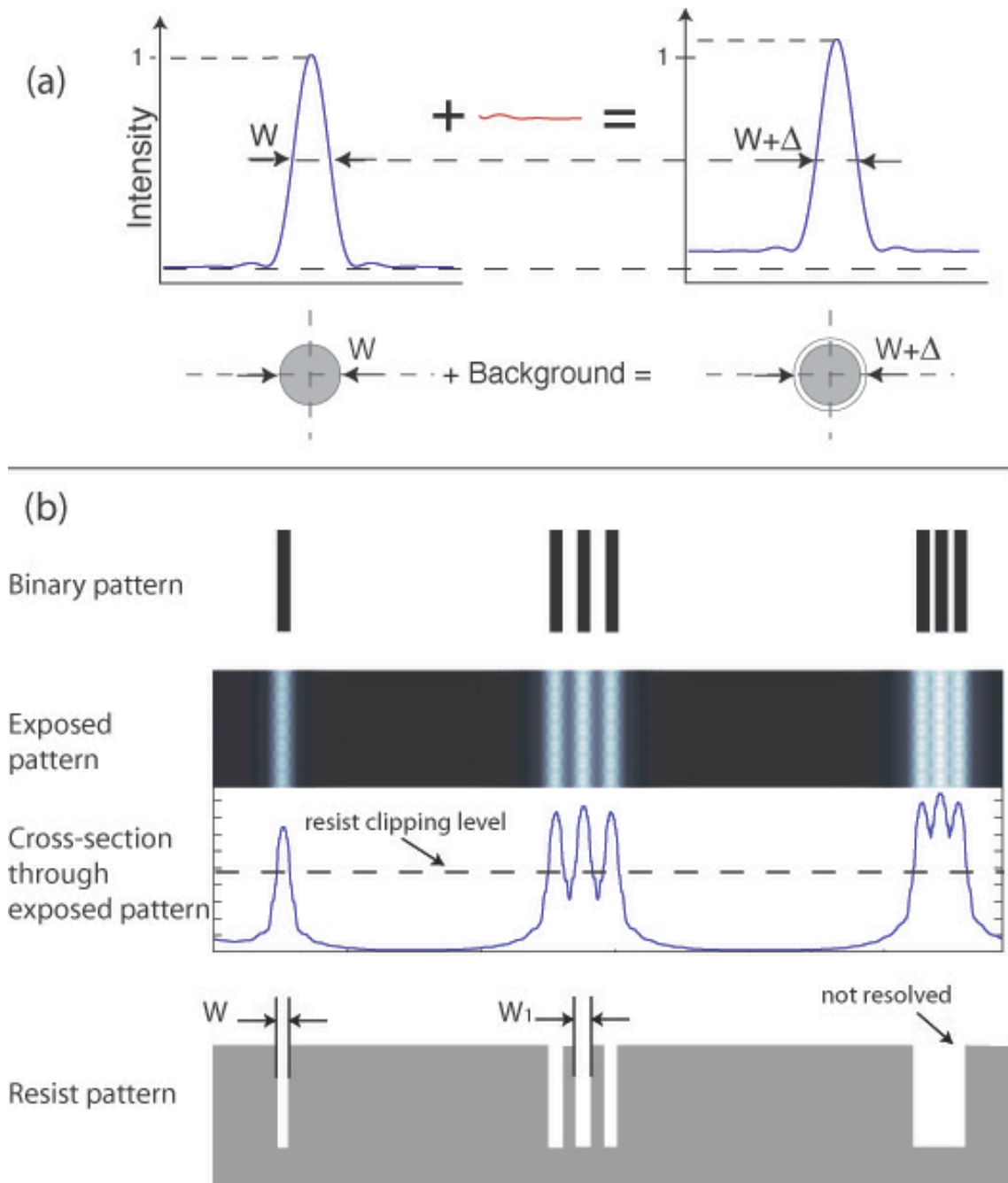
lithography [Ref 5-12, 5-13]. A schematic illustrating what can be achieved with sub-pixel stepping in combination with gray-scaling is presented in Figure 5-11(a).

Figure 5-11(b) shows a series of ZPAL exposures which use sub-pixel stepping (in this case on a 110 nm grid, equal to one third the pixel size), in combination with pixel gray-scaling, to vary linewidth smoothly from a single pixel to greater than two pixels. The leftmost SEM image shows a single-pixel line exposed with a pixel spacing of 110 nm, as indicated in the schematic below the image. The linewidth for this image is plotted as the leftmost data point in the plot at the bottom of Figure 5-11(b). The next three images and data points show the effect of exposing a second column of pixels, 110 nm away from, and parallel to, the first, at increasing dose. The rightmost SEM image and fifth data point show the effect of a third column of pixels exposed at a low dose. Subsequent data points, for which SEM images are not shown, show the effect of increasing the dose of this third pixel column. This result clearly shows that sub-pixel spacing can be used in combination with dose gray scaling to change linewidth with a precision not only finer than the spot size, but also finer than the exposure stepping grid. This can be done starting at a minimum feature size equal to the spot size. Extension to wider lines, or edge placement for large features, is straightforward.

### **5.2.1.2 Proximity Effects and their Correction**

All forms of optical lithography exhibit deterioration in pattern quality due to diffraction and the finite aperture of the optics. In scanning spot systems, this effect arises from the spatial spreading of the focused spot (i.e, the PSF has sidelobes that extend in space and contribute to the dose delivered at other points). In image-projection systems, deterioration arises from the finite aperture of the optics. In this section, the origin of proximity effects in ZPAL as well as methods to compensate for these effects are presented.

As previously described, in ZPAL the exposure dose at a given location depends not only on the dose delivered at that location, but also on the dose delivered at nearby locations. Due to the spatial extent of the PSF, dose from neighboring regions of the pattern can “spill over” and give rise to what are known as proximity effects. The effect is illustrated in Figure 5-12. In Fig.5-12(a) we can see that for a nominal resist-clipping level, the contribution of the background results in adding a DC component to the PSF. The resist will then clip the PSF at a different level, resulting in a wider spot. In Fig.5-12 (b) a simulation shows how background effects (i.e. proximity effects) can result in the inability to print dense features if they are sufficiently close-packed. Proximity-effect correction can alleviate this problem by altering the dose delivered to each pixel to the



**Figure 5 - 12.** Proximity effects in ZPAL. The spatial extent of the PSF contributes to the total dose delivered at nearby exposed pixels. (a) For a nominal resist-clipping level, the contribution of the background results in adding a DC component to the PSF. The resist will then clip the PSF at a different level, resulting in a wider spot. (b) Background effects (i.e. proximity effects) can result in the inability to print dense features if they are sufficiently close-packed. Proximity-effect correction can alleviate this problem by altering the dose delivered to each pixel to the appropriate level, *in anticipation* of the fact that further dose will be delivered to that particular location as a consequence of the exposure of nearby pixels.

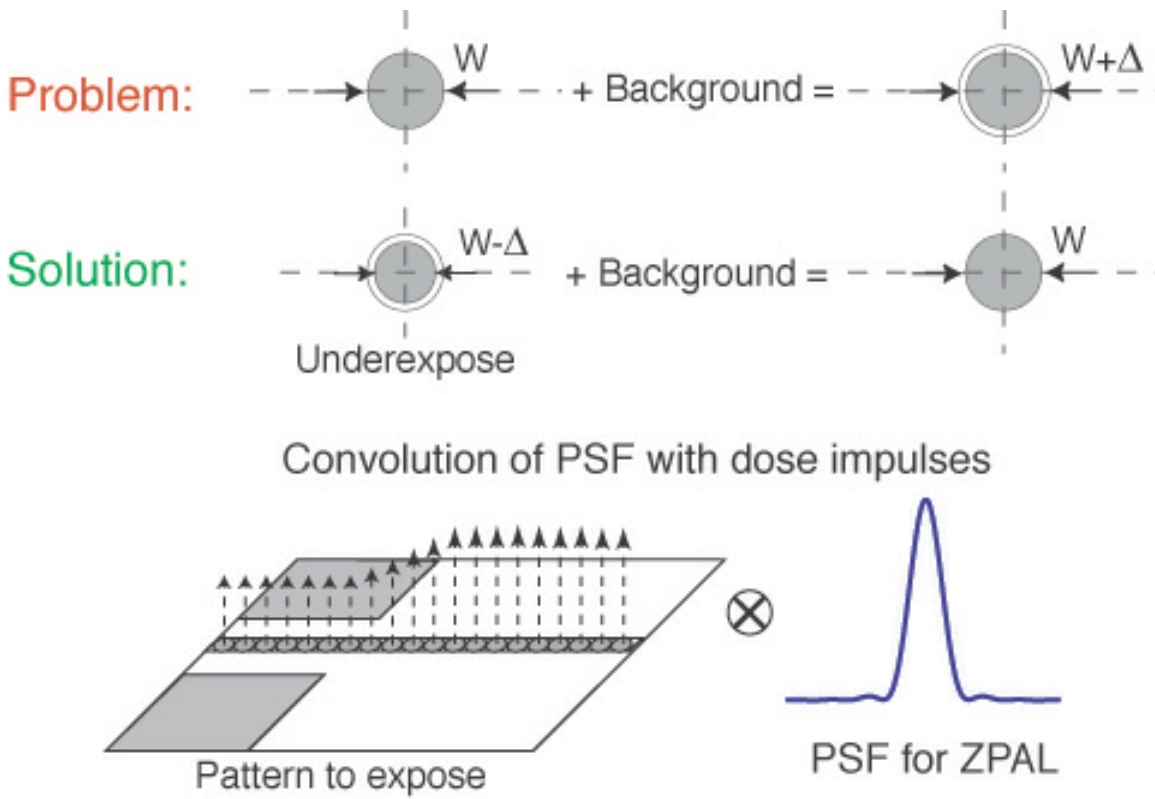


**Figure 5 - 13.** Proximity effects and how to correct them. Background arising from the spatial extent of the PSF contributes to the total dose delivered at nearby pixels. If the PSF is well-known, and given that writing in ZPAL results from the convolution of the pattern to be exposed with the PSF, the exposure dose to each pixel can be calculated in advance to achieve the desired *final* dose at each exposed location. The bottom-left diagram of the figure shows a sample pattern illustrating how the dose delivered at different pixel locations changes for a narrow line placed, for a part of its total length, between two large exposed pads. As expected, the pixels in the line closer to the pads require a different (i.e. lower) dose than the pixels that are far away.

appropriate level, in anticipation of the fact that further dose will be delivered to that particular location as a consequence of the exposure of nearby pixels. The concept is illustrated in Figure 5-13.

Proximity effects in ZPAL can, in general, be corrected by pre-compensating the patterns before writing. This requires accurate knowledge of the point-spread function (PSF) of the zone plate. If we assume a binary-clipping model for the resist, the normalized dose that is to be delivered for a given binary pattern  $B(x, y)$ , intended to be exposed is:

$$B(x, y) = \begin{cases} 1 & \text{inside pattern boundary} \\ 0 & \text{otherwise} \end{cases} \quad 5 - 11$$

The exposed pattern  $E(x, y)$  is then given by:

$$E(x, y) = \sum_{i=1}^{N_{\text{exp}}} B(x_i, y_i) \times P(x - x_i, y - y_i) \quad 5 - 12$$

where  $(x_i, y_i)$  denote the exposed pixel locations,  $N_{exp}$  is the total number of exposed pixels, and  $P(x, y)$  is the two-dimensional PSF of the zone plate. Thus, the exposed pattern is the discrete convolution of the binary pattern and the PSF. From this, we see that there are two degrees of freedom we can change in order to pre-compensate the pattern (i.e. to correct for proximity effects). These are: (1) the location of the points of exposure  $(x_i, y_i)$ , and (2) the exposure dose. In practice, the points of exposure (these are known as pixels) are chosen as a grid of period one-half the spot-size for the reasons explained in section 5.2.1.1, namely to achieve good dimensional control and edge placement. We are then left with dose modulation as the only handle available for proximity-effect correction (PEC).

If we express the dose-modulated pattern as  $D(x, y)$ , then the exposed pattern is given by

$$E(x, y) = \sum_{i=1}^{N_{exp}} D(x_i, y_i) \times P(x - x_i, y - y_i) \quad 5 - 13$$

The problem of PEC then consists of calculating  $D(x_i, y_i)$  for a given binary pattern and PSF. Three methods of solving this problem, as well as an experimental demonstration of the effectiveness of PEC are included below.

#### PEC Method #1: Direct Solution

Equation 5-13 represents a linear system of equations. If we set the exposed pattern,  $E(x, y)$  equal to the binary pattern,  $B(x, y)$ , we can invert this system of equations to calculate the values for  $D(x_i, y_i)$ . The main disadvantage with this method is that it is not easy to put constraints on the values of  $D(x_i, y_i)$ . Care must be taken to consider the negative values of  $D(x_i, y_i)$  since they represent a non-physical quantity, namely, a negative dose. One way to deal with negative values is to add a DC dose value to all pixels so as to “bump up” all the values to 0 or greater. However, this results in a decrease in the process latitude, since the resist has to “clip” features at a higher level to maintain the feature sizes. In practice, this method turns out to be a poor solution, especially for complex and dense patterns.

#### PEC Method #2: Linear Programming

This method takes advantage of the highly non-linear nature of photoresists. Assuming a simple “clipping” model (e.g. after a threshold dose value is delivered at a given location, the resist will clear, creating a binary step profile), the desired pattern must have the following constraint:

$$E(x, y) \begin{cases} > LT & \text{inside pattern boundary} \\ < UT & \text{otherwise} \end{cases} \quad 5 - 14$$

where  $LT$  is the lower threshold dose above which all resist clears, and  $UT$  is the upper threshold dose below which no resist clears. Incorporating the constraints in equation 5-14 into the system of equations 5-13, results

in a linear programming (LP) problem. In this LP problem, the objective is to minimize the difference between the exposed pattern,  $E(x, y)$  and the binary pattern,  $B(x, y)$ , by modifying the exposure doses,  $D(x_i, y_i)$ . The allowed modifications are subject to the constraints imposed by equation 5-14.

Although LP problems are well known and applied in a wide variety of fields, for this application the method was applied with moderate success. The chief problem that arose had to do with computational time; the time required to calculate the optimum doses increased dramatically for larger patterns.

### **PEC Method #2: Iterative Error-Correction Algorithm**

This is a novel technique developed during the course of ZPAL research<sup>18</sup>. It consists of correcting the error contributions of the exposure doses in an iterative manner.

The steps are as follows:

1. We begin with the binary pattern (all doses equal to 1). Then we compute the exposed pattern, through the discrete convolution described in Equation 5-12.
2. The difference between the exposed pattern and the original binary pattern is denoted as the “error”,  $Err(x, y)$ .

$$Err(x, y) = E(x, y) - B(x, y) \quad 5 - 15$$

3. For each point  $(x, y)$ , which has non-zero error, a search is performed to determine its nearest exposed point,  $(x_i, y_i)$ . Then depending on the sign of the error at  $(x, y)$ , the dose at  $(x_i, y_i)$  is modified by a dose quantum. The dose quantum is the dose-control resolution achievable in the system.

$$D(x, y) = d(x, y) + \text{sign}(Err(x, y)) \cdot DQ \quad 5 - 16$$

where  $DQ$  is the dose quantum.

4. Using the dose-modulated pattern,  $D(x, y)$ , the exposed pattern is again calculated. Steps 2-4 are repeated until an acceptable level of error is achieved.

This method is straightforward to implement in software. Since, the dose quantum is automatically taken into account in the calculations, spurious dose quantization effects can be avoided. In practice, this method seems to offer very fast convergence as well. An experimental implementation of these technique in ZPAL is

---

<sup>18</sup> See Rajesh Menon’s Ph.D. thesis for a more extensive discussion of this method [Ref 5-15].



shown in Figure 5-14. The figure shows two scanning-electron micrographs with identical patterns exposed with ZPAL, one optimized (right) and one non-optimized (left). Note the dramatic improvements. Key features are color coded in both micrographs. For instance, the large square was designed to have a single unexposed spot at its center. If all exposed pixels are patterned with the same dose, proximity effects cause the spot to “wash-out” and disappear. By proximity-effect correcting the pattern prior to exposure, the spot can be retained.

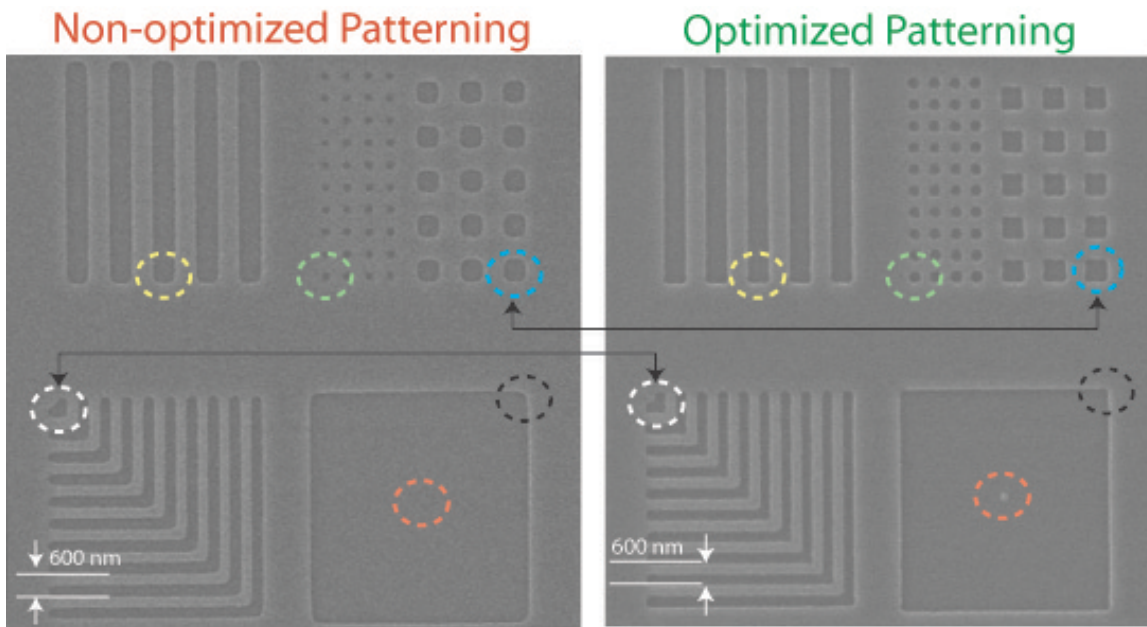


**Figure 5 - 14.** Patterns can be optimized prior to exposure by means of proximity-effect correction techniques. Such techniques allow greatly enhanced patterning capabilities in ZPAL, providing better edge definition and sharper features. The figure shows two scanning-electron micrographs with identical patterns exposed with ZPAL, one optimized (right) and one non-optimized (left). Note the dramatic improvements. Key features are color coded in both micrographs. For instance, the large square was designed to have a single unexposed spot at its center. If all exposed pixels are patterned with the same dose, proximity effects cause the spot to “wash-out” and disappear. By proximity-effect correcting the pattern prior to exposure, the spot can be retained.

### 5.2.2 Lithographic Results

The results that are now presented in the following pages are some of the highest quality lithographic patterns ever produced with ZPAL. A very large number of patterns have been exposed with the system, including many lithographic test structures, optical devices (such as waveguides and 2D photonic bandgap structures), devices for MEMS applications (microcomb structures), as well as diffractive optical elements (zone plates).

All exposures employed a 25 mW GaN laser diode operating at  $\lambda = 400$  nm. For these experiments no multiplexing device was used, i.e., all zone plates in the array wrote the same pattern simultaneously (parallel patterning with active multiplexing has been demonstrated earlier [Ref 5-14]). For all the patterns presented, it is

worth noting that even though all exposed pixels received the same dose, proximity effects are minimal in the exposures.

The confocal gapping technique described earlier was used to set the substrate at the right gap with respect to the zone-plate array. All exposed substrates, unless otherwise indicated in the caption of the figures, were 75cm-diameter silicon wafers, spin-coated with 200 nm of BarLi ARC (spun at 3,000 rpm and baked on a hot-plate at 175° C for 90 seconds), with 150 nm of thinned Shipley 1813 photoresist on top (spun at 5000 rpm and baked on a hot-plate at 90° C for 60 seconds). The exposed patterns were developed in Shipley 351 developer diluted with water in the ratio 1:5 for 45 seconds.

A word about resolution in ZPAL. ZPAL shares with all other optical lithography systems the property that the minimum feature size that can be printed is determined by the following equation:

$$\text{Resolution} = k_1 \frac{\lambda}{NA} \quad \text{5 - 17}$$

where  $\lambda$ , is the wavelength of light,  $NA$  is the numerical aperture, and  $k_1$  is a proportionality factor having to do with the process latitude of the entire lithography process (it includes imperfections on the exposure system, resist and development limitations, etc). From equation 5-17 it is clear that for a given exposure wavelength, in order to achieve the maximum resolution one would like a  $NA$  as high as possible and a  $k_1$  as low as possible. In Chapter 4 we saw that zone plates with numerical apertures in excess of 0.9 were capable of diffraction-limited performance. It is important then to understand what  $k_1$  means for ZPAL, and how low it can be pushed.

Quantitative studies that go beyond obtaining pretty SEM pictures have been undertaken, and for the first time we are able to quantify the process latitude of our current system as well as the  $k_1$  limits of zone plates. Figure 5-15 shows a set of scanning electron micrographs of dense lines and spaces with varying  $k_1$ 's, from 0.56 to 0.32. Systematic characterization of lithographic exposures is allowing us to determine that the process latitude for our current system is in excess of 13% (even when operating at  $k_1$  in the 0.3-0.4 regime).

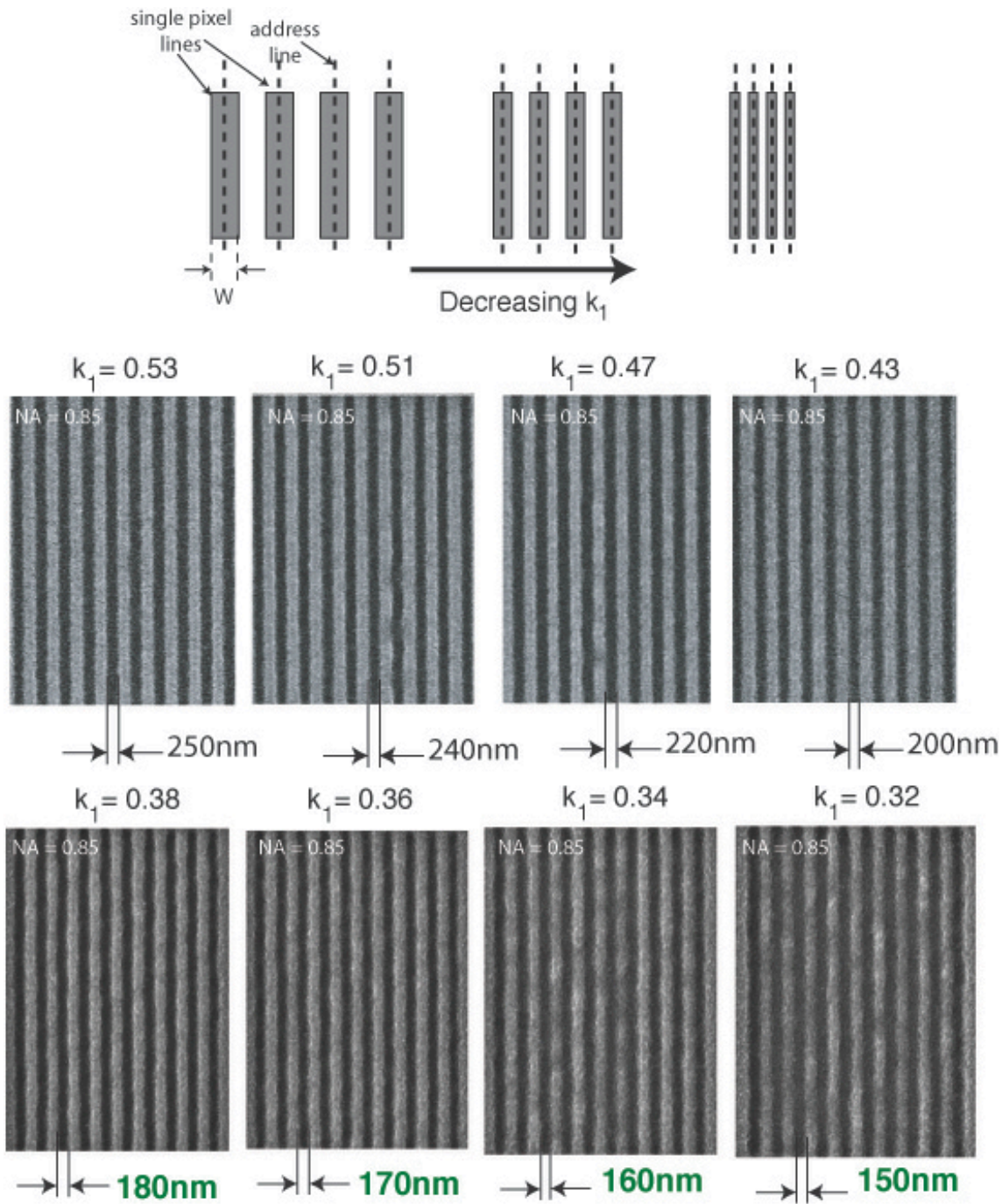


**Figure 5 - 15.** Meaning of  $k_1$  in ZPAL. Top: Decreasing the  $k_1$  factor in ZPAL implies squeezing the address lines (depicted in figure) further and further. The goal is to be able to still pattern dense features with 50-50 duty cycles and an acceptable pattern quality. Bottom: Experimental determination of the limits of  $k_1$  for a 0.85 NA zone plate operating at  $\lambda=400\text{nm}$ . While it is clear that the quality of the printed lines decreases as  $k_1$  is reduced, 150nm lines and spaces can be patterned with  $\lambda=400\text{nm}$  light, a remarkable result.

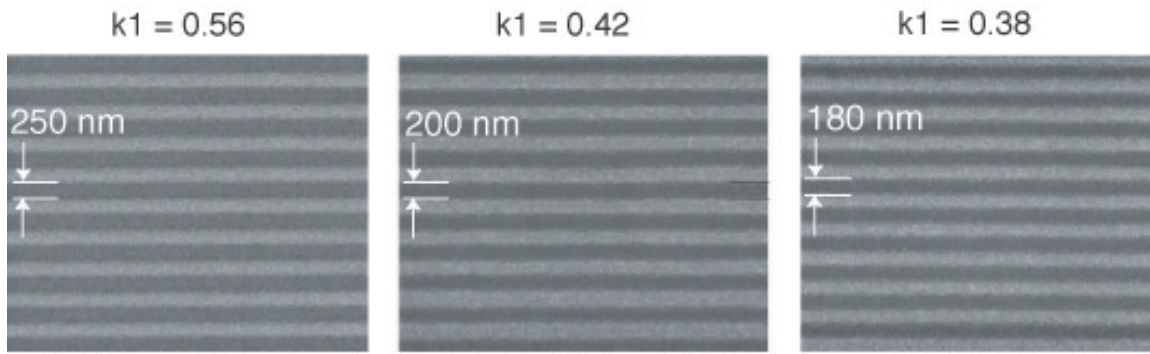


**Figure 5 - 16.** Exploring the limits of  $k_1$  with ZPAL. High numerical aperture zone plates (0.85 and 0.9) can operate at low  $k_1$  factors (even below 0.4). Sub-70 nm patterning should be possible, by operating at the demonstrated  $k_1=0.38$ , with 0.9NA zone plates and  $\lambda = 157\text{nm}$ .

As can be seen in Figures 5-15 and 5-16, the resolution that has been achieved with zone plates operating at  $\lambda=400\text{nm}$  is nothing short of remarkable. Optical lithography systems used in the semiconductor industry are able only to operate at  $k_1$  factors in the 0.3-0.4 range through extraordinarily complex procedures that require phase-shift masks, angular illumination, and optical proximity correction (OPC) in the masks. The implementation of these techniques requires teams of scientist and engineers that optimize patterns, one a time, for each individual tool. The process is very sophisticated, and very costly. Being able to achieve with ZPAL, in a laboratory setup, sub-200nm resolution with  $\lambda=400\text{nm}$ , provides an exciting indication that with the demonstrated  $k_1$  factor of 0.38, 0.9 NA zone plates, and a  $\lambda = 157\text{nm}$  source, sub-70nm dense patterning will be possible. For semi-dense features, the sub-50nm regime will be accessible.

The results included in Figures 5-17 through 5-22 provide a sample of the very-high-quality patterning that can be achieved with ZPAL. The figures include scanning-electron micrographs of lithographic test structures (Figure 5-17), optical devices (Figure 5-18 and Figure 5-19), as well as devices for a number of other applications, ranging from MEMS, to diffractive optics, to magnetic memory (Figure 5-20). Also included are the first field-stitching experiments, which resulted in the creation of large set of 4.5mm-long lines through the combination of 45 zone-plate fields (Figure 5-22).



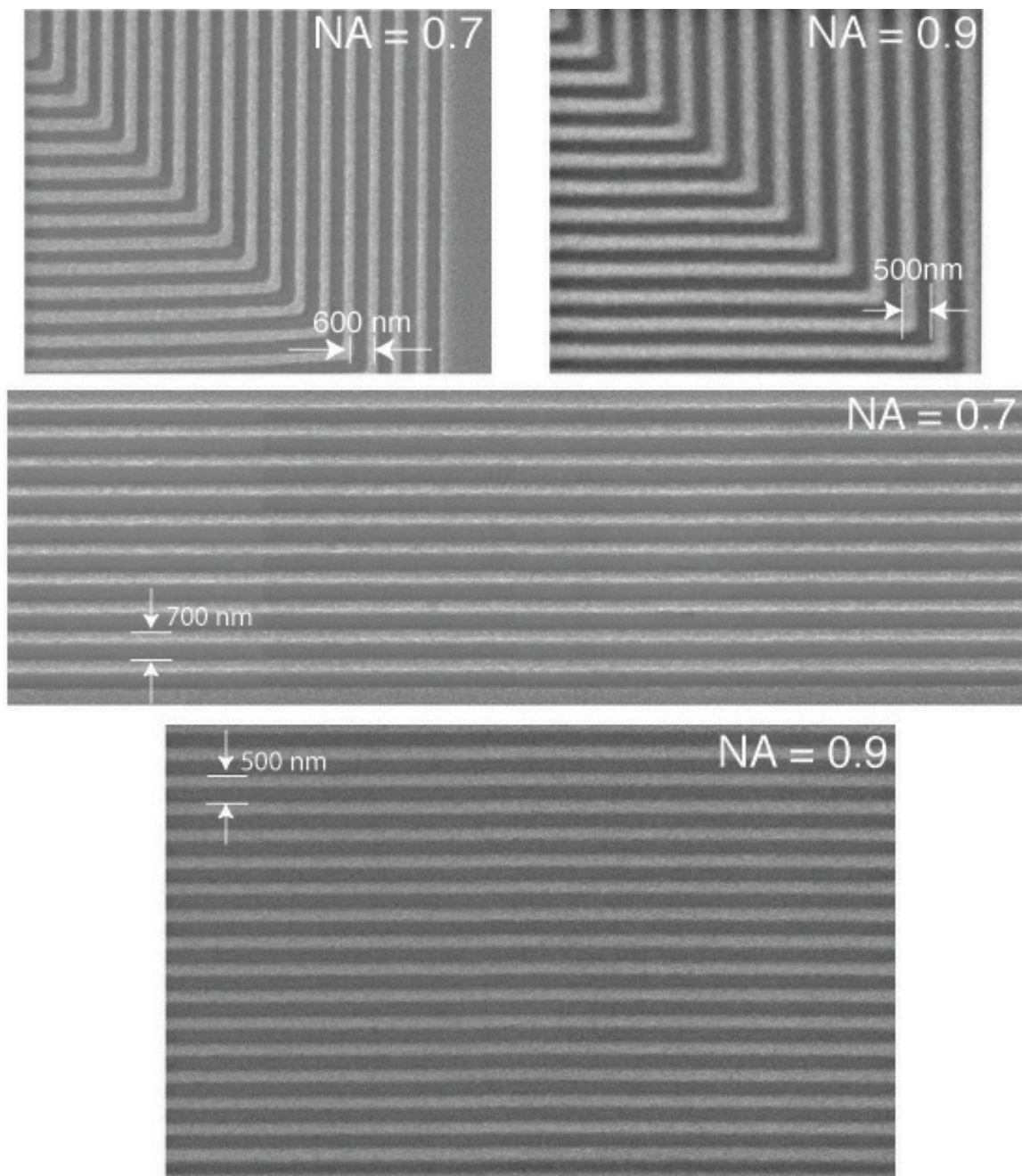


**Figure 5 - 17.** Scanning-electron micrographs of ZPAL patterned lithographic test structures. Top: Nested L's structures created with 0.7 and 0.9 numerical aperture zone plates. Bottom two: Dense 1:1 gratings pattern written with 0.7 and 0.9 NA zone plates.

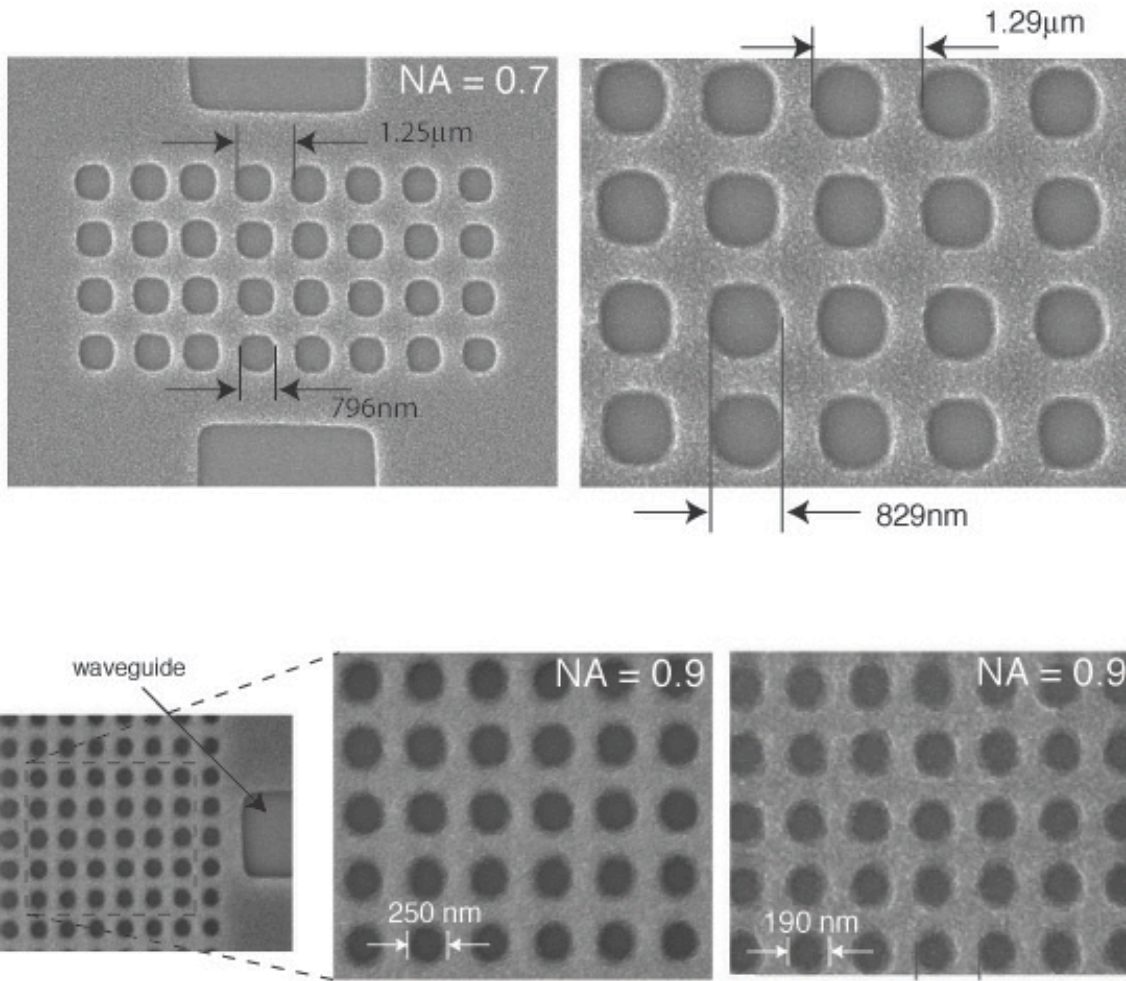


**Figure 5 - 18.** Scanning-electron micrographs of patterns exposed with the continuous-scan UV-ZPAL system. Top: 2D photonic bandgap structures with  $1.29\mu\text{m}$  period, Bottom: 2D photonic bandgap structures with  $500\text{nm}$  period, and also with  $400\text{nm}$  period.

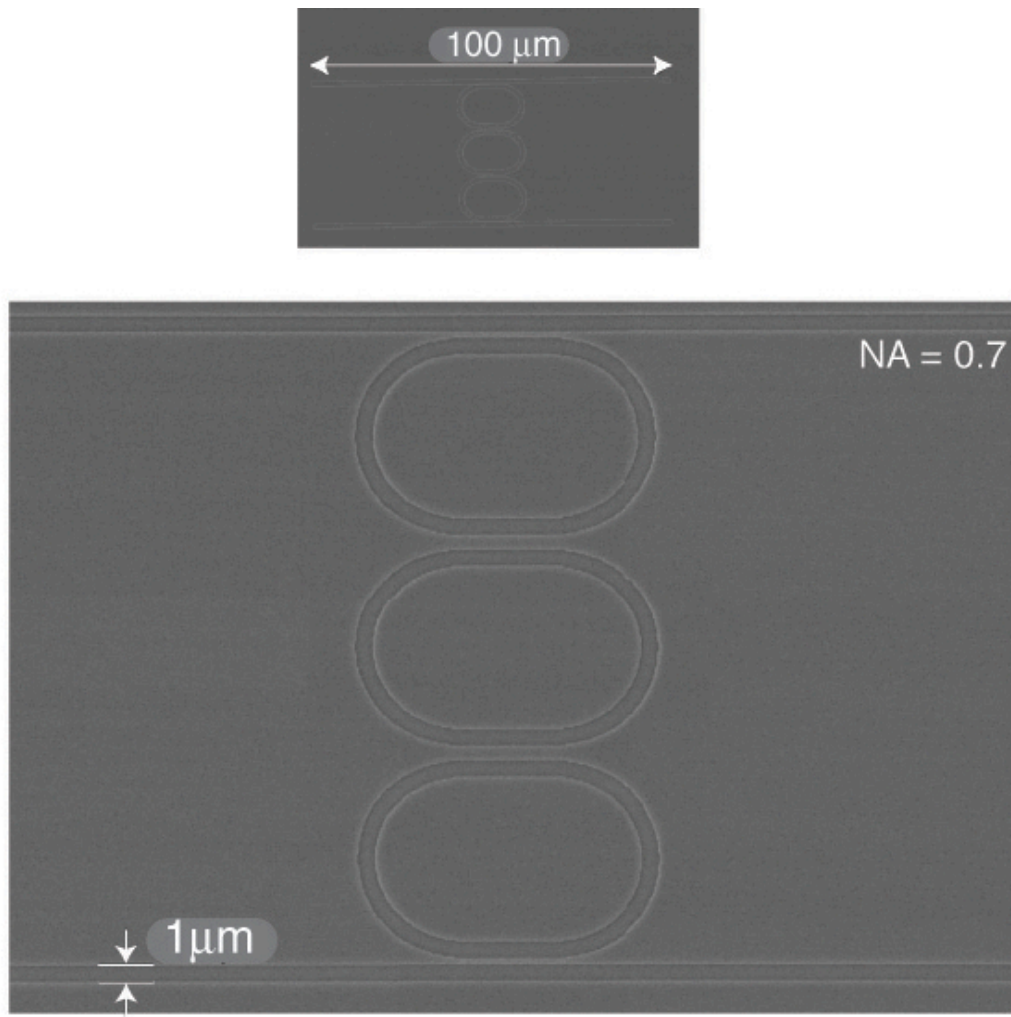


**Figure 5 - 19.** Scanning electron micrograph of a three-ring optical resonator pattern exposed with the continuous-scan UV-ZPAL system, showcasing ZPAL's ability to expose non-Manhattan geometries.



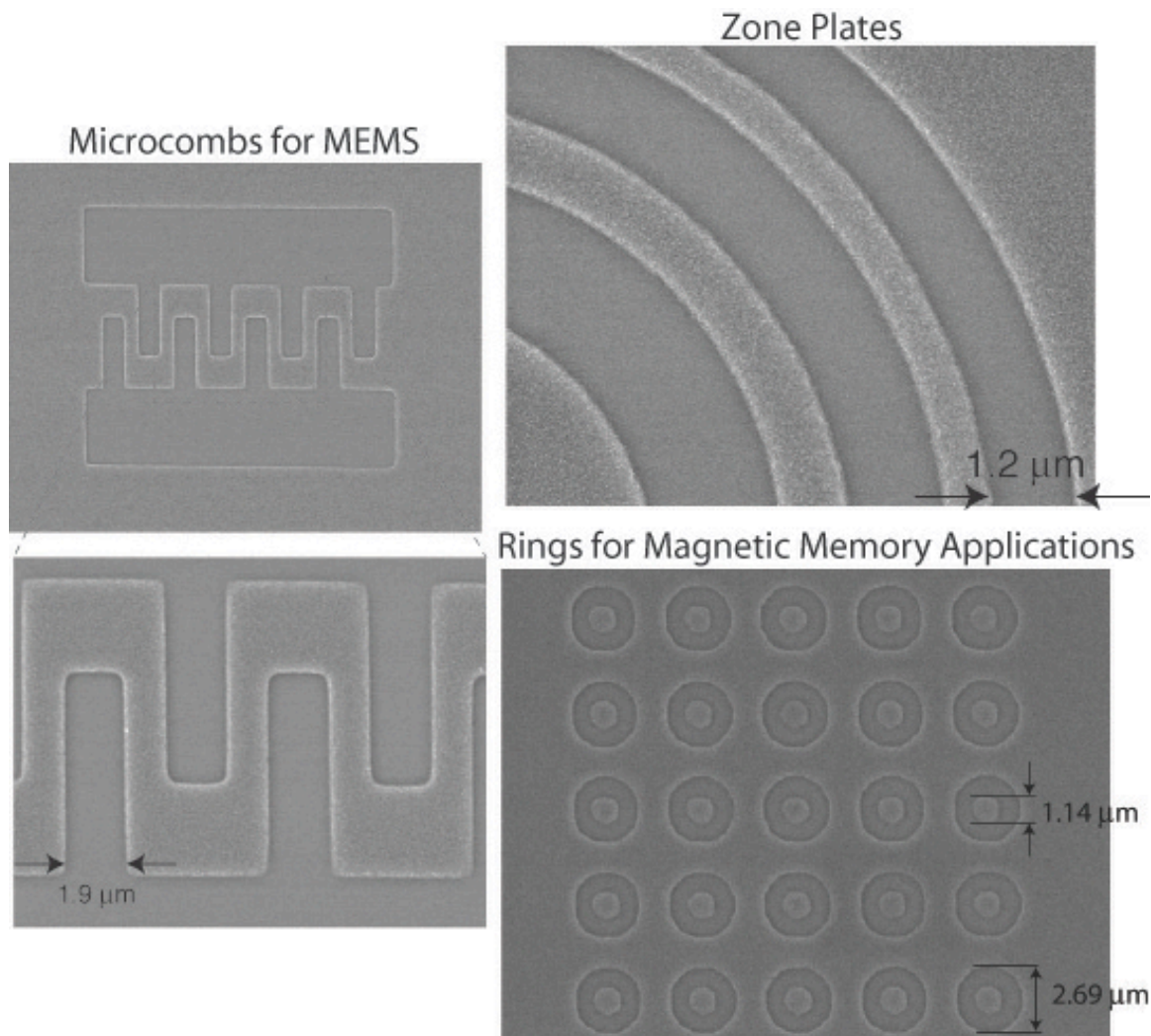


**Figure 5 - 20.** ZPAL is a versatile technique that can satisfy the lithography needs for a wide variety of applications, from MEMS, to diffractive optics, to magnetic memories. Left: Microcomb structure for MEMS. Top-Right: Portion of a zone plate. Bottom-right: Rings for magnetic memory applications.

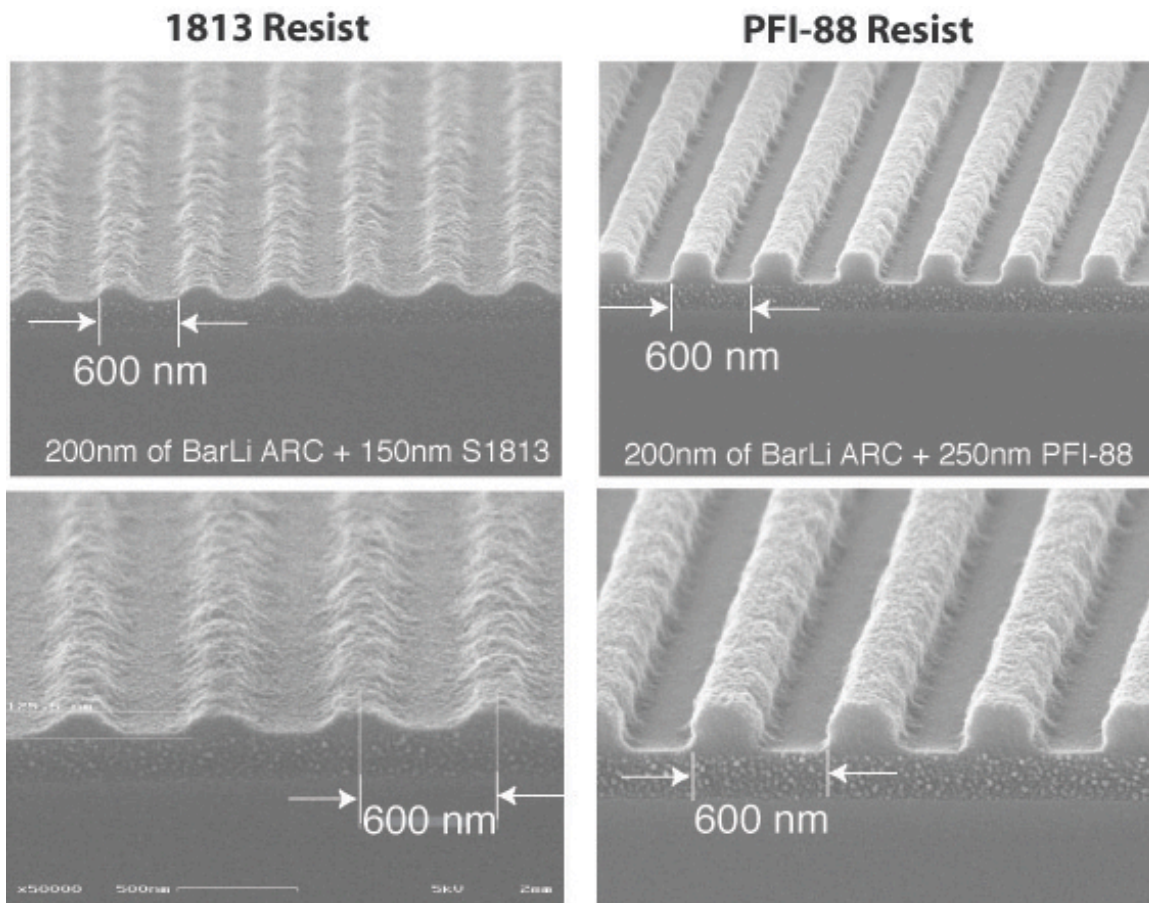


**Figure 5 - 21.** The importance of resist optimization in ZPAL. As was illustrated in Figure 1-9, advancements in resist chemistry are key for high-resolution lithography, and ZPAL is no exception. The same system exposing the same pattern can lead to vastly different results depending on what resist is utilized. Four scanning-electron micrographs of a 600nm-period grating exposed with NA=0.7 ZPAL ( $\lambda=400\text{nm}$ ) are shown in the figure. It is clear that PFI-88 resist yields much better results than the low-resolution 1813 series from Shipley.

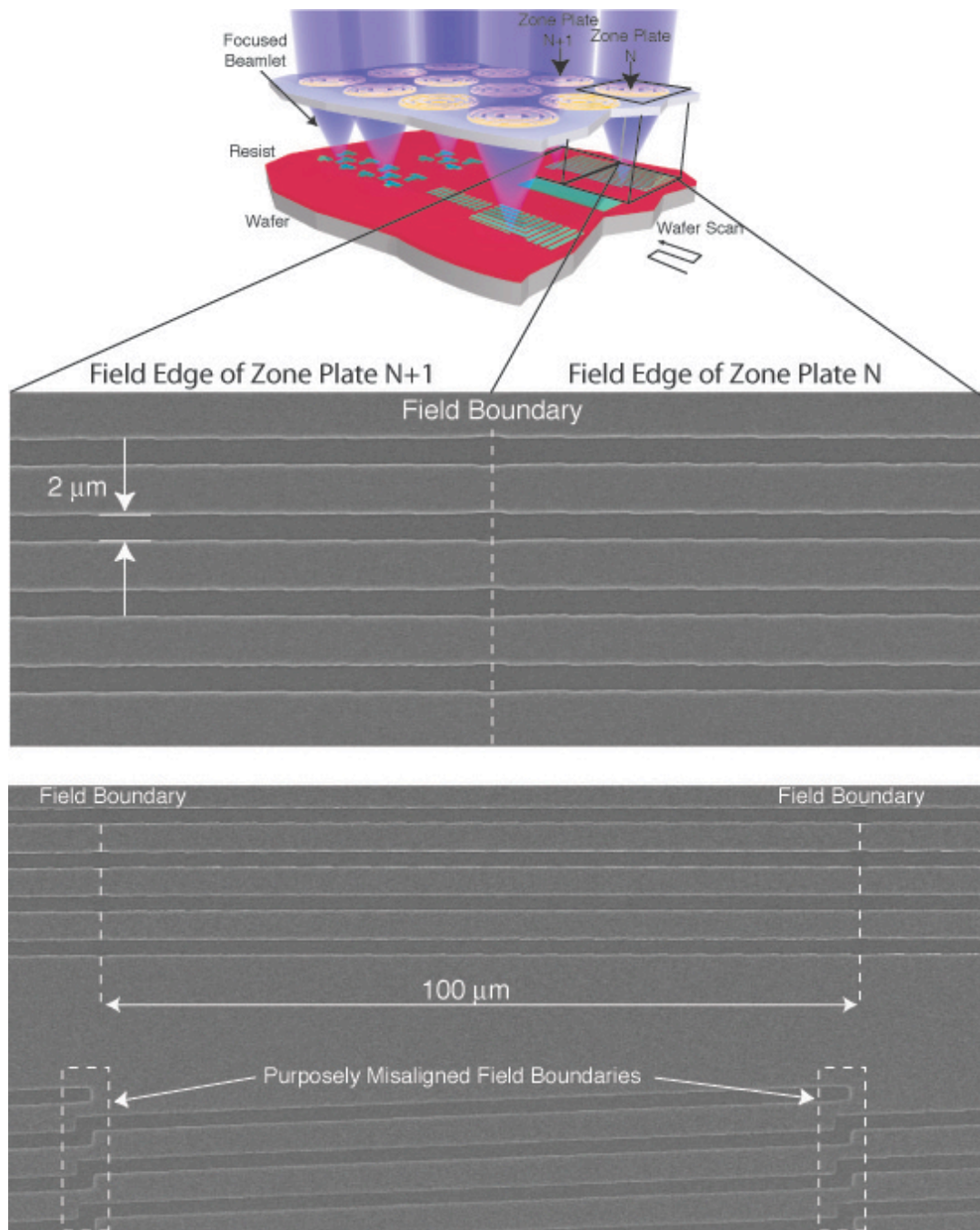


**Figure 5 - 22.** Stitching field boundaries in ZPAL. Top: Schematic of the ZPAL system without the micromechanics. Large-area patterns are created by stitching adjacent fields, with a field defined as the square area located underneath any given zone plate (a field, depicted with black lines, is shown in the figure). Each zone plate is “responsible” for patterning the field that lies directly underneath it, and stitching at the edges of the fields allows features to be connected with patterns written in adjacent fields. Bottom: Experimental demonstration of field stitching, which resulted in the creation of large set of 4.5mm-long lines through the combination of 45 zone-plate fields (each field was 100μm in size).

### 5.3 Specifications for a High-Throughput ZPAL System

For a ZPAL system operating with CW radiation, the only input parameters needed to analyze the throughput of the system are:

- $\lambda$ , the wavelength of the radiation used
- Spot Size: the minimum feature size that the system will be able to resolve.
- $f_m$ , the operating frequency of the micromechanics.
- The number of grayscaling levels.
- $V_{\text{stage}}$ , the stage velocity
- #ZPs, the maximum number of zone plates that can be manufactured with nearly identical characteristics.

The time needed for any given zone plate to expose one pixel is set primarily either by the response time of the micromechanics (if using a CW laser with sufficient power), or by the repetition rate of the laser (in case a pulse source is used). To a smaller extent, the stage velocity also determines the time needed to expose a pixel, since it takes some finite amount of time to travel from one pixel to the next. However, since in ZPAL the distance traveled from pixel to pixel can be as short as 50 nanometers, and given that stages today can travel at speeds in excess of hundreds of mm/s, the contribution of the stage response to the time needed to expose a pixel is negligible compared to the micromechanics addressing time. Given this approximation, it is easy to prove that the number of wafers per hour that can be exposed with ZPAL is determined by the following expression:

$$\text{Wafers/} \text{Hour} = 3600 \cdot \left( \frac{f_{\text{Micromirrors}}}{\# \text{GrayScalingLevels}} \right) \cdot \frac{(\text{SpotSize}^2) \cdot (\# \text{ofZonePlates})}{\text{WaferDiameter}^2} \quad 5 - 18$$

By inspecting equation 5-18 it is easy to get a feeling of how the different parameters affect ZPAL's throughput. The frequency of the micromechanics and the number of zone plates both exhibit a linear behavior. Doubling them doubles the throughput, and so on. The number of grayscaling levels is inversely related to throughput. The remaining two parameters, the spot size and the wafer diameter, provide a quadratic response. Decreasing the minimum feature size by a factor of 2 decreases the throughput by a factor of 4.

As described earlier, in order to achieve appropriate linewidth control and edge placement, sub-pixel stepping is often required in addition to grayscaling. A pixel dimension of one half the spot size, in combination with 5-bits of grayscaling ensures dimensional control that is much finer than the pixel dimension. If sub-spot stepping is employed, the throughput will be reduced by a factor of 4 from the numbers that can be obtained from equation 5-18.

## Case 1: Continuous Wavelength (CW) Source

If a CW source is employed, provided it has sufficient power, the limiting factor in terms of throughput will be the speed at which the micromechanical elements can be switched ON/OFF (the limitation might lie in the data delivery or in the mechanical response time of the individual MEMS device). In order to get a throughput number for a ZPAL system operating with a CW source, let's assume the following parameters:

- Wafer Size = 300mm
- MEMS array size = 1024 x 1024
- Zone Plate array size = 1024 x 1024
- MEMS have built-in grayscaleing
- NA = 0.85
- Focal length of Zone Plates = 25  $\mu\text{m}$
- Sub-spot stepping = 1/2 minimum resolution of system
- $\lambda = 257\text{nm}$

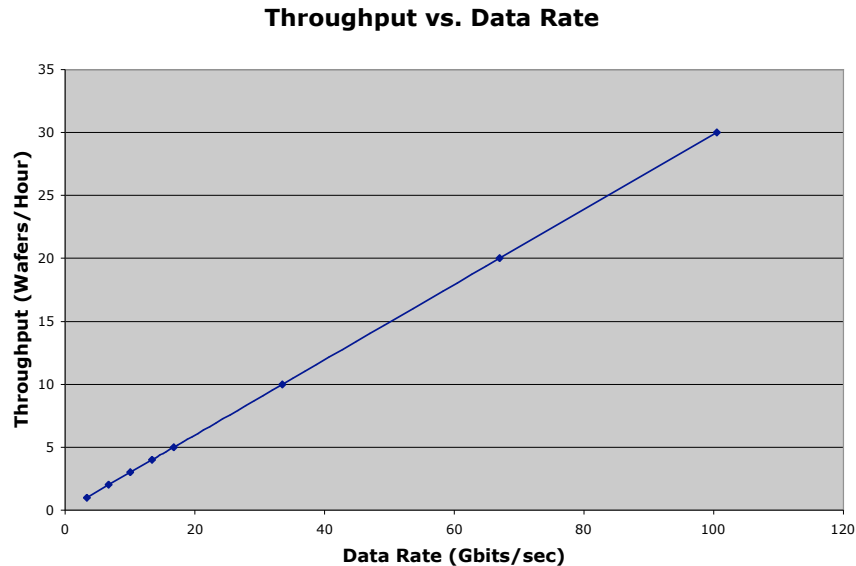


**Figure 5 - 23.** Throughput for ZPAL operating at  $\lambda=257\text{nm}$  (CW) vs. data rate, with sub-150nm resolution

Under these assumptions, Figure 5-23 provides a plot of the number of 300mm wafers that could be exposed per hour as a function of the achievable data rate.

## Case 2: Pulsed Source



If a pulsed source is employed (as will be required for  $\lambda=193\text{nm}$  and  $\lambda=157\text{nm}$ ), the ZPAL system will be chiefly limited by the repetition rate of the laser. In order to get a throughput number for a ZPAL system operating with a pulsed source, let's assume the following parameters:

- Wafer Size = 300mm
- MEMS array size = 1024 x 1024
- Zone Plate array size = 1024 x 1024
- MEMS have built-in grayscaleing
- NA = 0.85
- Focal length of Zone Plates = 25  $\mu\text{m}$
- Sub-spot stepping = 1/2 minimum resolution of system
- $\lambda = 157\text{nm}$

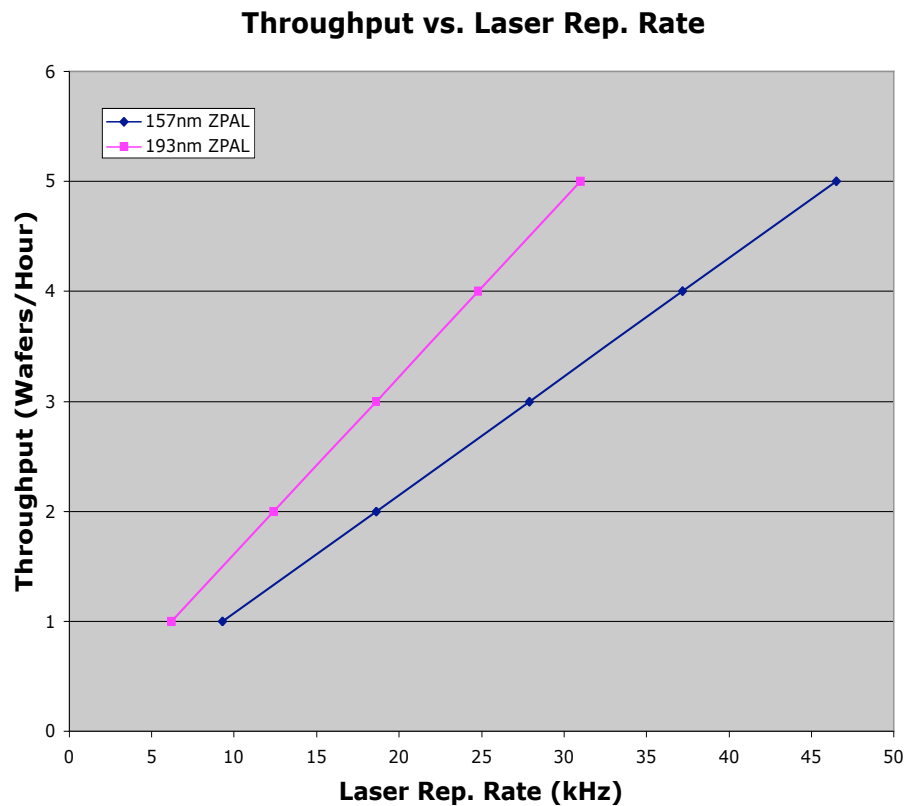


**Figure 5 - 24.** Throughput for ZPAL operating at  $\lambda=193\text{nm}$  and  $\lambda=157\text{nm}$  (pulsed) vs. laser repetition rate. At  $\lambda = 157\text{nm}$ , the system will be capable of sub-90nm resolution (and as small as 60nm, depending on pattern)

Under these assumptions, Figure 5-24 provides a plot of the number of 300mm wafers that could be exposed per hour as a function of the repetition rate of the laser.

In order to compensate for pulse-to-pulse variations (something common in many pulsed lasers) a double-pass strategy might be required. The consequence of such averaging will be a throughput reduction of one half from that presented in Fig.5-24.

Finally, for the numbers presented in this analysis, the assumption was made that all the exposed features are written at the maximum resolution of the system. Were this not to be the case for certain applications (e.g. writing non-critical layers), the required pixel size could be significantly larger, and the throughput will increase quadratically as a result.

As a conclusion, we can see that with current technology, ZPAL will be limited to throughputs that are, at best, a few 300mm wafers per hour.

<b>Chapter 5. The ZPAL Prototype System</b> .....	96
5.1 The ZPAL Architecture.....	96
5.1.1 The GaN Diode Laser.....	97
5.1.2 The Silicon Light Machines GLV Module.....	98
5.1.2.1 Principle of Operation .....	98
5.1.2.2 Efficiency .....	99
5.1.2.3 A Data Delivery System for the GLV .....	104
5.1.3 The Zone Plate Array .....	106
5.1.3.1 Parallelization and Gapping in ZPAL .....	106
5.1.4 The Scanning Stage.....	109
5.2 Lithographic Performance.....	110
5.2.1 Writing Strategy .....	110
5.2.1.1 Dose Control and Sub-Pixel Stepping.....	111
5.2.1.2 Proximity Effects and their Correction.....	112
5.2.2 Lithographic Results.....	117
5.3 Specifications for a High-Throughput ZPAL System.....	126

## List of Figures

Figure 5 - 1. Two of the blue lasers utilized in ZPAL.....	97
Figure 5 - 2. The Silicon Light Machines Grating Light Valve™ (GLV™).....	99
Figure 5 - 3. GLV electro-optic response .....	100
Figure 5 - 4. Two properly designed aspheric lenses can convert a Gaussian input intensity profile into a flat-top intensity profile.....	101



Figure 5 - 5. Data delivery implementation for the GLV module in the ZPAL prototype.	104
Figure 5 - 6. Experimental setup for testing the data delivery system for ZPAL..	105
Figure 5 - 7. A Michelson interferometer can be used to set the zone plate substrate and the wafer to be exposed parallel to each other.	107
Figure 5 - 8. Gapping with confocal microscopy.	108
Figure 5 - 9. Schematic of the experimental implementation of the continuous-scanning stage in the ZPAL prototype.	109
Figure 5 - 10. ZPAL writes pattern through the incoherent addition of spots..	110
Figure 5 - 11. Writing strategy in ZPAL..	111
Figure 5 - 12. Proximity effects in ZPAL..	113
Figure 5 - 13. Proximity effects and how to correct them.	114
Figure 5 - 14. Experimental results of proximity effect correction in ZPAL.	117
Figure 5 - 15. The meaning of $k_1$ in ZPAL.	119
Figure 5 - 16. Exploring the limits of $k_1$ with ZPAL.	120
Figure 5 - 17. Scanning-electron micrographs of ZPAL patterned lithographic test structures..	121
Figure 5 - 18. 2D photonic bandgap structures	122
Figure 5 - 19. Scanning electron micrograph of a three-ring optical resonator pattern exposed with the continuous-scan UV-ZPAL system, showcasing ZPAL's ability to expose non-Manhattan geometries.	123
Figure 5 - 20. ZPAL exposed patterns for MEMS, diffractive optics, and magnetic memory applications.	124
Figure 5 - 21. Scanning-electron micrograph of cleaved ZPAL-patterns.	125
Figure 5 - 22. Stitching field boundaries in ZPAL.	126
Figure 5 - 23. Throughput for ZPAL operating at $\lambda=257\text{nm}$ (CW) vs. data rate.	128
Figure 5 - 24. Throughput for ZPAL operating at $\lambda=193\text{nm}$ and $\lambda=157\text{nm}$ (pulsed) vs. laser repetition rate.	129

## C h a p t e r 6

### Conclusions and Future Work

Given the current industry interest in maskless lithography, it is crucial that the community investigates all the proposed maskless alternatives with an open mind. The work presented here has hopefully proven the efficacy and the advantages of diffractive-optical elements in general, and zone plates in particular, for maskless lithography applications. We have proven that (1) high-NA zone plates work, (2) the contrast in ZPAL is adequate for large-area patterning, and (3) large arrays can be manufactured with close to ideal performance. With  $k_1$  factors that can be pushed into the 0.3-0.4 regime and numerical apertures of 0.9 (and possibly even higher), 157nm lasers will potentially allow ZPAL to reach the 50nm node. Beyond that, zone plates will still be able to function if a source is provided, be it 121nm, EUV or x-rays. It should hence be possible for ZPAL to reach the limits of the lithographic process.

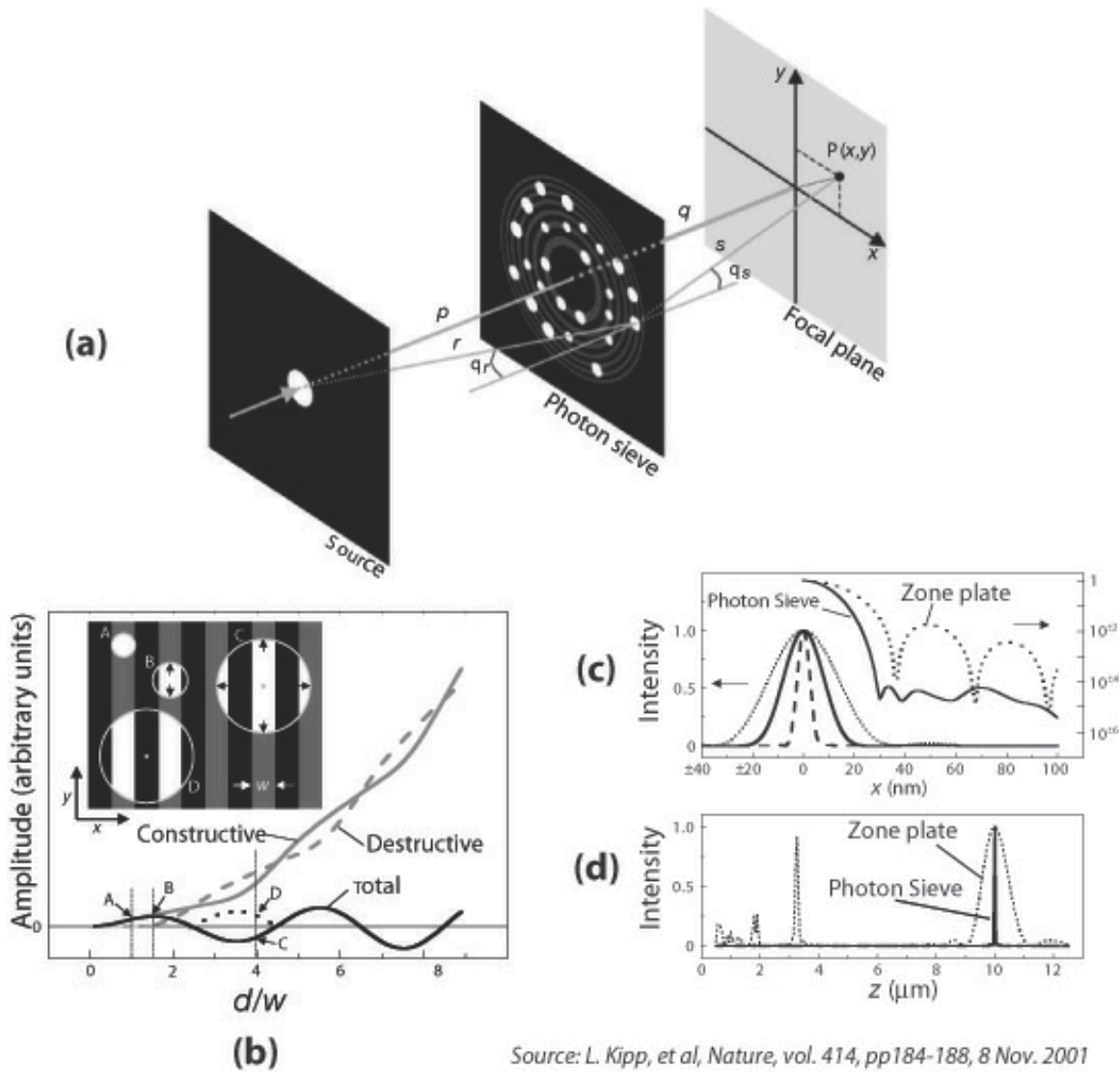
## 6.1 Beyond Zone Plates?

The promise of diffractive optics for maskless lithography applications can, and must, extend beyond the capabilities offered by traditional binary phase zone plates. Optimizing zone plate designs (e.g. apodizing the zones, blazing, etc) can yield diffractive optical elements whose focusing characteristics are particularly suited for certain lithography applications. One could envisage diffractive arrays designed for the lithographic patterning of curved-surfaces (e.g. by having zone plates designed to form spots at different focal lengths such that the curvature of the substrate to be exposed is appropriately matched). Or one could go a step further and envision a totally new form for focusing light.

In an exciting development, a new kind of diffractive-optical focusing element has been indeed proposed recently by Kipp et al.[Ref 6-1]. The new optic has been called a *photon sieve*. In its conception it is related to the familiar amplitude Fresnel zone plate. The photon sieve consists of a large number of pinholes distributed appropriately over the zones of a Fresnel zone pattern (see Figure 6-1). For a given minimum resolution in the fabrication, it achieves a sharper focus than the corresponding amplitude Fresnel zone plate, and, in addition, higher orders of diffraction and secondary maxima are suppressed by several orders-of-magnitude (i.e., they are substantially eliminated) as shown in Figs. 6-1(c-d). In the photon sieve, the distribution of pinholes (and hence the *utilization* of the incident radiation) is adjusted in such a way that the sidelobes or secondary maxima are suppressed (i.e. a form of apodization). Through this apodization, the strength of the *utilization* is varied as a function of radial distance so as to follow approximately the functional form of a Gaussian distribution. As a result, the secondary maxima or sidelobes of the focal spot are reduced or substantially eliminated.

The photon sieve as described by Kipp et al. is less efficient in focusing incident radiation into a first-order focus than an amplitude Fresnel zone plate. However, because of its ability to suppress third and higher-order foci, as well as sidelobes, it is an attractive alternative to conventional Fresnel zone plates for the diffractive focusing elements in those situations where efficiency of focusing is not an important consideration

but sidelobe suppression is. Accordingly, given the concern commonly expressed regarding the inevitable presence of multiple diffracted orders in zone plates, one could conceive



Source: L. Kipp, et al, *Nature*, vol. 414, pp184-188, 8 Nov. 2001

**Figure 6 - 1.** The photon sieve. (a) Diagram showing point-to-point imaging through appropriately positioned pinholes. (b) Examples of photon sieve pinholes together with the underlying zone-plate geometry and the contributions of a single pinhole to the focal amplitude. Constructive and destructive interference contributions from 'white' and 'black' areas inside the pinhole are plotted as solid and dashed grey curves, respectively. The total amplitude at the focus from a single pinhole of diameter  $d$  centered on a transmissive zone (A, B, C) of width  $w$  is given by the solid black curve; the total contribution to the amplitude at the focus from a pinhole centered on an opaque zone (D) is given by the dotted black curve. (c-d) Comparison of calculated intensity distributions of photon sieves and zone plates. Note that sidelobes are suppressed compared to those present in zone plates, and that a single focus is obtained (i.e. no other orders are present).

utilizing an array of photon sieves in substitution for the array of Fresnel zone plates in a maskless lithography system.

With the purpose of verifying the viability of the idea, a set of photon-sieves with high-numerical apertures (0.7 and 0.8) were designed and fabricated. A scanning-electron micrograph of the central pinholes of the 0.7 numerical-aperture sieve is shown in Figure 6-2(a). The sieves were incorporated into the ZPAL system in order to test their focusing capabilities. The results presented in Figure 6-2(b-d) are the very first focusing experiments ever reported with sieves at the UV<sup>19</sup> (and at high numerical apertures!), as well as the first ever use of sieves for lithography.

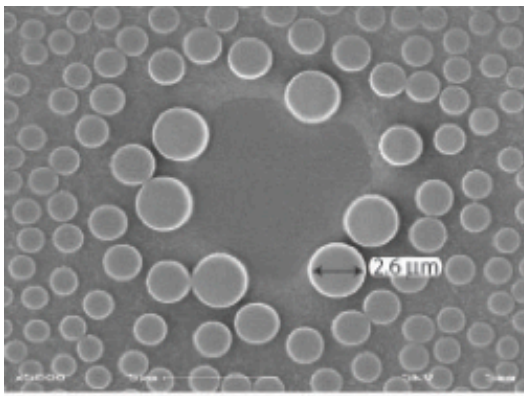
The results are very interesting. As expected, a reduction factor was achieved with respect to the minimum-feature-size present on the sieve. Recall that for the case of a zone plate, the size of the focused spot is roughly determined by the minimum feature size of the zone plate (i.e. the width of the outer-most zone). For the sieve, an appropriate design can result in the creation of a focused spot that is 1/2 the size of the minimum pinhole diameter, as illustrated in Figure 6-2(b). This capability relaxes the fabrication requirements of the diffractive elements, something that can be very beneficial as we progress towards the sub-100nm regime.

As a final note regarding these novel optical elements, although not described by Kipp, et al, one can design a photon sieve based on the principal of phase shifting rather than amplitude modulation. This offers the promise of higher efficiencies while maintaining all of the virtues of the photon sieve: (1) low sidelobes, (2) single diffracted order, (3) minimum feature in the photon sieve is a multiple of the focused spot full-width-at-half maximum (FWHM). This would provide an exciting future research direction with high-potential payoffs. The possibility of creating a diffractive optical element that can be fabricated with a planar process, operate with high-efficiency, while achieving a single diffraction-limited focus (with even some demagnification!) is a promise that is certainly worth pursuing.

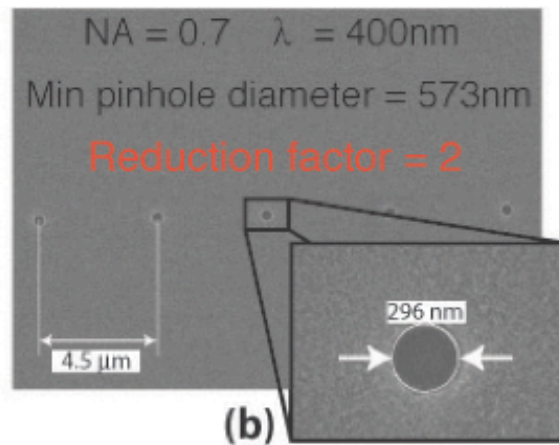
---

<sup>19</sup> The only reported experimental results with photon sieves (by wavelengths, with microscopy applications in mind.

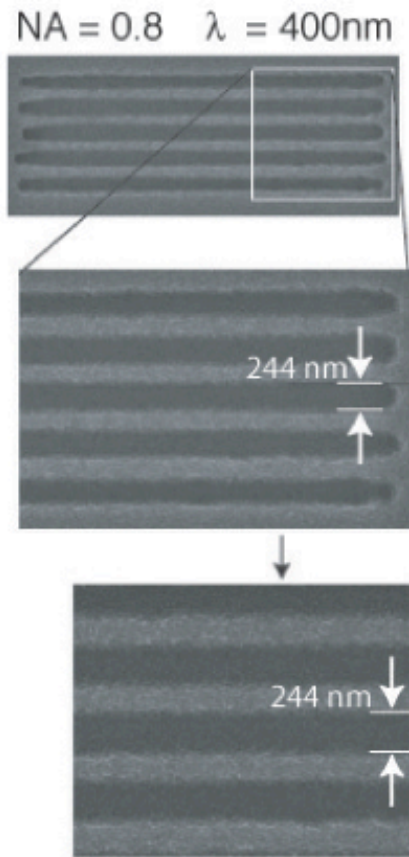
Kipp et al) were performed at x-ray



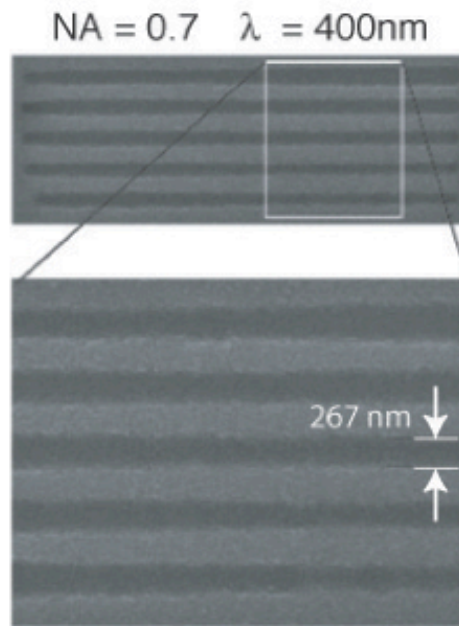
(a)



(b)



(c)



(d)

**Figure 6 - 2.** First ever focusing results with photon-sieves at the UV. (a) Central pinholes of a 0.7 NA sieve with a focal length of 40μm, designed to operate at  $\lambda=400\text{nm}$ . (b) A photon sieve can create a focused spot that is a fraction of the minimum feature size of the sieve. For the results presented, a sieve with a minimum pinhole diameter of 573nm was able to create a 296nm spot, a reduction of a factor of 2. (c-d) Scanning electron micrographs of the first lithography results ever produced with photon sieves. Numerical apertures as high as 0.8 were achieved.

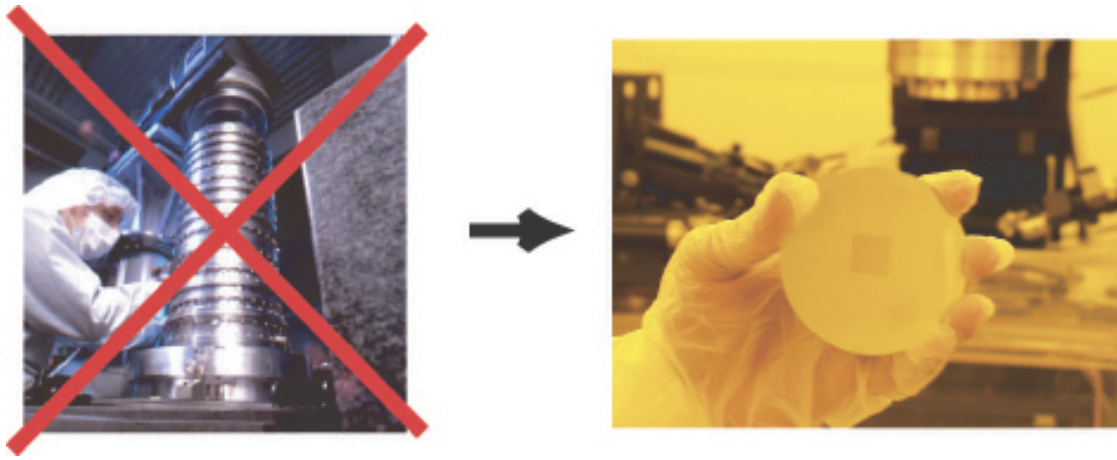


**Figure 6 - 3.** Vision of the power of employing diffractive optics for lithography. Diffractive optics are manufactured using nanofabrication, with techniques similar to those used in chip production

## 6.2 The Dream of Total Integration

In this final section I would like to end with the dream of a maskless lithography system that would function without *any* macroscopic optical elements. In Chapter 2, an image (reproduced in Figure 6-3) illustrating the power of diffractive optics was introduced. The symbolism of this image is very powerful. It represents a new path for optical lithography, a path based on reducing the complexity and cost of systems by taking advantage of the blossoming of our nanofabrication capabilities.

I would like to propose going one step further. ZPAL, in its current implementation, although simpler than other maskless lithography architectures, still requires a relatively large number of conventional refractive optical elements. After all, light from the laser has to be collimated, then shaped appropriately to illuminate the multiplexing device, and then mapped (by more optics) onto the array of diffractive elements. When all is said and done, the ZPAL setup in our laboratory ends up looking as is shown in Figure 6-4. It is still too complicated.

A further step towards total integration, where no macroscopic optical components would be required for the entire optical train, can be envisioned with the recent appearance of diode lasers, and VCSELs (Vertical Cavity Surface Emitting Lasers) capable of operation at UV wavelengths. It is satisfying to see that the existing and mature semiconductor laser technology for the near-infrared and red is finally extending to encompass the blue and near-ultraviolet regions.

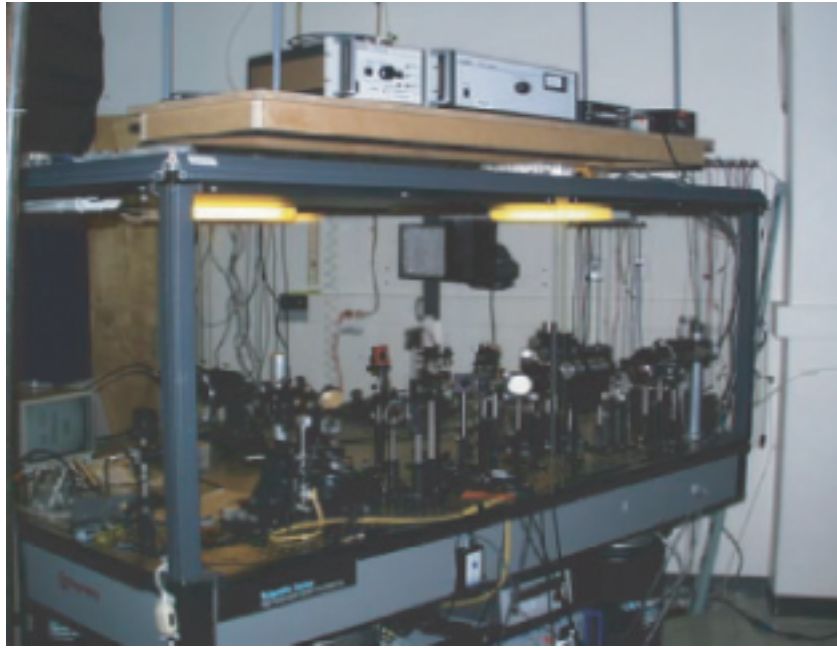


**Figure 6 - 4.** Experimental implementation of ZPAL at M.I.T.'s NanoStructures Laboratory.

These new lasing elements, given their planar fabricated process, can be created into arrays [Ref 6-3], and are capable of dose modulation, high-power, and extremely fast switching rates. In combination with an array of diffractive elements, a multi-optical-column writing technique would result in a high-resolution, high-throughput maskless patterning system. The vision is illustrated in Figure 6-5. The author is hopeful that this vision will become a reality in the not too distant future.



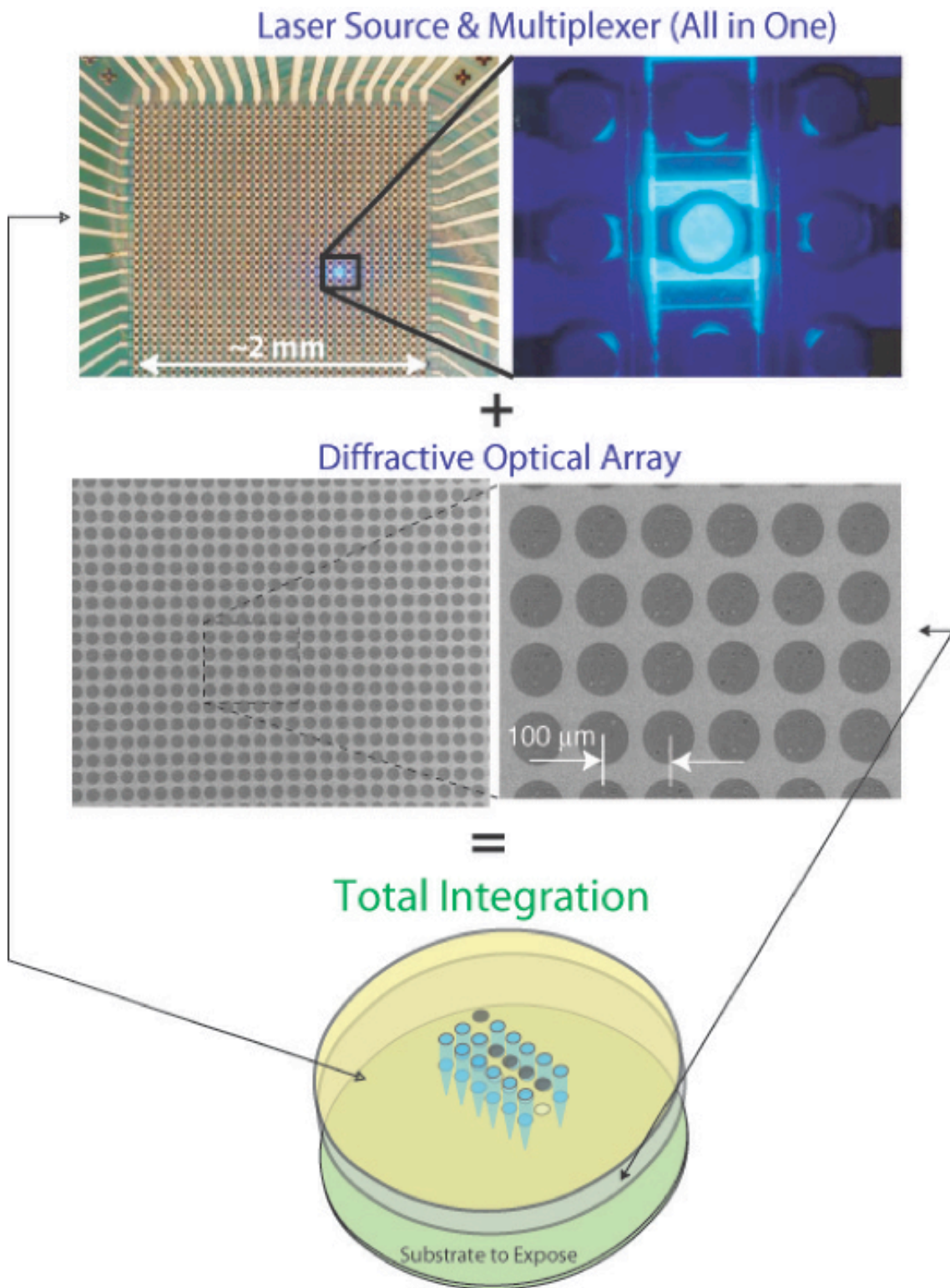


**Figure 6 - 5.** The vision of total optical integration for maskless lithography by combining arrays of laser diodes with diffractive optical arrays. Top-Left : Optical micrograph of at blue emitting 32x32 LED array. Top-right: Close-up view of a single LED element. Source: Ozden et al [Ref 6-3].

<b>Chapter 6. Conclusions and Future Work .....</b>	<b>131</b>
6.1 Beyond Zone Plates?.....	132

6.2 The Dream of Total Integration.....	136
---	-----

## List of Figures

Figure 6 - 1. The photon sieve. ....	133
Figure 6 - 2. First ever focusing results with photon-sieves at the UV. ....	135
Figure 6 - 3. Vision of the power of employing diffractive optics for lithography. ....	136
Figure 6 - 4. Experimental implementation of ZPAL at M.I.T.'s NanoStructures Laboratory. ....	137
Figure 6 - 5. The vision of total optical integration for maskless lithography by combining arrays of laser diodes with diffractive optical arrays.....	138

# A p p e n d i x A

## Zone Plate Processing

This appendix describes the processing necessary to fabricate zone plates by means of scanning-electron-beam lithography and x-ray lithography.

### A.1 Fabrication by means of Scanning-Electron-Beam Lithography

Chronological sequence of steps required:

- 1- **Design zone plates** as described in Chapter 3. Obtain values for:
  - a.  $\lambda$ , the wavelength at which the zone plates are intended to operate.
  - b. The focal length (in microns)
  - c. The Numerical Aperture of the zone plates (or alternatively, the radius in microns)
- 2- **Generate pattern files** that can be read by the electron-beam-lithography system. A custom-software program<sup>20</sup> was written in MATLAB to generate the zone plate files required for patterning with the RAITH-150 and the VS-26 scanning-electron-beam-lithography systems available at MIT's NanoStructures Laboratory. Screen captures of the interface of the RAITH-150 version of the program, as well as the VS-26 version, are respectively included in Figure A-1 and Figure A-2.
- 3- **Prepare zone plate substrate.** The substrate obviously has to be transmissive for the operating wavelength of the zone plates. All the zone plates of this work were fabricated on double-side-polished fused-silica substrates.
  - a. Spin resist. For the Self-Aligned HSQ process, knowing the index of refraction of HSQ (at the intended wavelength of operation of the zone plates) determines the thickness of this layer (for a  $\pi$ -phase shift, the thickness required,  $t$ , is determined by  $t = \frac{\lambda}{2} \cdot \frac{1}{n_r - 1}$ , where  $n_r$  is the real part of the index of refraction, and  $\lambda$  is the wavelength of light). A plot of the index of refraction versus wavelength is included in Figure 3-31 (pg 101).
  - b. Bake the resist. Two bakes are required for HSQ:
    - i. Bake 1: 150<sup>0</sup>C for 2min (on a hot-plate)
    - ii. Bake 2: 220<sup>0</sup>C for 2min (on a hot-plate)
  - c. Evaporate 5nm of Aluminum. This step is required to prevent charging effects during the electron-beam lithography exposure, since the substrate (fused silica) is non-conductive.
- 4- **E-beam exposure.** Load substrate. Create exposure layout by importing the generated pattern files from Step-2 into either the RAITH or the VS-26. The RAITH Code version of the software generates files with the extension **.asc**, which can be readily imported via the RAITH-layout software. The VS-26 version of the software generates files with the extension **.pat**
  - a. **If using the RAITH-150**
    - i. **Create an exposure layout** and transfer it into the position list.
    - ii. **Select acceleration voltage** (30keV will work best for thick HSQ layers)

---

<sup>20</sup> The program can be found on the nano server, under the following directory: **/nano/nsl/dgil/ZonePlateSoftware/**. The directory contains two folders, called **VS-26 Code** and **RAITH Code**. Within each of these directories the main programs running all other sub-programs are called **ZPmainGUI\_VS26.m** and **ZPmainGUI\_RAITH.m** respectively.

- iii. **Select the exposure dose.** Note that the zone-plate files are composed of a large number of single-pixel lines (see section 3.2.2.1). Therefore, it is important to select the exposure dose for single-pixel lines (i.e. line dose) as oppose to area dose. For 475nm-thick HSQ layers (the thickness required for a  $\pi$ -phase shift at  $\lambda=400\text{nm}$ ), the optimum line dose should be  $\sim 225 \text{ pC/cm}$ .
- iv. **Calibrate desired field size.** This requires setting values for the magnification and the field size. It is **very important** that the chosen magnification results in a **magnification range of 2** (this can be checked in the LEO-SEM software under *View/SEM Status*. A *magnification range* of 1 operates the deflection amplifiers under a very noisy gain setting (there are three settings available), with the consequence that the patterns will be extremely rough<sup>21</sup>. The *magnification range* is a function of the acceleration voltage and the working distance. For relatively large field sizes (e.g.  $150\mu\text{m}$  and above) this dependence might require operating at larger working distances in order to obtain the desired *magnification range* of 2. As an example, for  $185\mu\text{m}$  field sizes, at  $30\text{keV}$ , the working distance had to be increased to  $10.2\text{mm}$  to get the desired *magnification range*.
- v. **Expose the zone plates.** Writing times vary depending on zone plate design. As an example, a  $\text{NA}=0.7$ ,  $f=40\mu\text{m}$ ,  $\lambda=400$  zone plate, writing with a  $225 \text{ pC/cm}$  dose, takes  $\sim 2\text{m}15\text{sec}$ /zone plate. For long-writes, use the automatic-beam-current measurement to achieve good dose stability throughout the exposure.
- vi. **Develop patterns.**
  1. **For HSQ exposures.** Develop in any TMAH-based developer. The author always used Microposit MF CD-26. Development time is a very insensitive parameter for HSQ (and very slow!). The author obtained great results with a development time of 1h for thick layers of HSQ. It is **important** to always develop HSQ in a **single development step**.
  2. **For PMMA exposures.** Mix the developer (1:2 MIBK:IPA) in a beaker big enough to fit the wafer. The temperature should drop to  $16^\circ\text{C}$  upon mixing. The developing temperature is  $21^\circ\text{C}$ . To get to this temperature warm beaker with hands while monitoring the temperature. Have the beaker covered to prevent the evaporation of MIBK. Develop for 90 sec. Rinse for 60 sec with IPA + 60 sec  $\text{H}_2\text{O}$ . If the substrate has been coated with a thin metal film to

---

<sup>21</sup> The author learned this problem the hard way, resulting in months of wasted time.

prevent charging, it must be removed with the appropriate metal etchant prior to development.

**b. If using VS-26**

- i. **Convert and transfer files into VS-26.** Login to the nano server via **trajan.mit.edu** and access the following directory: `~/dgil/ZonePlateSoftware`. The directory contains a C program called `pat2vsx.c`, written to convert **.pat** files into **.vsx** files (this is a format that the VS-26 can read). Copy this program into your directory in the nano server and compile the program (by typing `cc -o pat2vsx pat2vsx.c`). Place the previously generated zone-plate files into the directory containing the **pat2vsx** program, and convert to **.vsx** via the following command:

**>./pat2vsx filename.pat filename.vsx**

The files can then be transferred to the VS-26. Make sure that if you use ftp to transfer the files, the transfer is done in binary format.

- ii. **Load files.** It is very important that **Ihsan's** version of the code is used, since this is the only version that can handle circles.
- iii. **Layout the files to be exposed.**
- iv. **Expose patterns.** A good dose for PMMA is  $\sim 330\mu\text{C}/\text{cm}^2$ .
- v. **Develop patterns.**
  1. **For HSQ exposures.** Develop in any TMAH-based developer. The author always used Microposit MF CD-26. Development time is a very insensitive parameter for HSQ (and very slow!). The author obtained great results with a development time of 1h for thick layers of HSQ. It is **important** to always develop HSQ in a **single development step**.
  2. **For PMMA exposures.** Mix the developer (1:2 MIBK:IPA) in a beaker big enough to fit the wafer. The temperature should drop to  $16^\circ\text{C}$  upon mixing. The developing temperature is  $21^\circ\text{C}$ . To get to this temperature warm beaker with hands while monitoring the temperature. Have the beaker covered to prevent the evaporation of MIBK. Develop for 90 sec. Rinse for 60 sec with IPA + 60 sec  $\text{H}_2\text{O}$ . If the substrate has been coated with a thin metal film to prevent charging, it must be removed with the appropriate metal etchant prior to development.

**Zone Plate Parameters**

Wavelength (nm): 400    Focal Length (um): 40    Refractive Index: 1    **Input EITHER Radius or N.A.**

Radius (um):    N.A.: 0.7

Compute ZP Spot Size: 285.714 nm    Compute Number of Zones: 80    Compute Diameter of ZP: 78.4157 um

**Plot Options**

Plot ZP    Plot Zone Widths

**Options for ebeam writing ZPs in RAITH**

☒ Create Zone Plate .asc file?    Name of Zone Plate file (include .asc): ZPtest.asc    E-beam bias of zones (nm): 0    Spacing of sub-circles (nm): 18

☐ Create Big Circle .asc file?    Name of Circle file (include .asc): .asc

**Options for PEC**

Distance from OZ to start correction (um): 10    Extra dose % for last zone: 0    Type of gradation (1=linear, 3=cubic, et): 1

**Plot Options for .asc files**

☐ Plot ZP    ☐ Plot Zone Widths    ☐ Plot Big Circle

**Run**

**Figure A - 1.** Screenshot capture of the interface of the software program capable of generating zone plates for the RAITH-150 scanning-electron-beam lithography system. Once all parameters have been chosen, the program is executed by clicking the Run button. This will generate the desired .asc file (in the example shown in the figure, a file called ZPtest.asc will be created). Comments: (1) the spacing of the sub-circles refers to the spacing of the single-pixel line polygons explained in section 3.2.2.1. The default of 18nm provides excellent results. (2) make sure the *Create Zone Plate .asc file?* box is checked for the file to be created. (3) E-beam bias of the zones accepts positive and negative values, (4) *Options for PEC* refers to proximity effect correction techniques for zone plates (see section 3.2.2.1). (5) If the box of *Create Big Circle .asc file?* is checked and a filename is input, a circle the size of the zone plate will be created. This pattern is necessary for both the *Silicon Process* and the *Chromium Process* (described in Chapter 3).

**Zone Plate Parameters**

WaveLength (nm): -400    Focal Length (um): -40    Refractive Index: 1    Input EITHER Radius or N.A.: Radius (um):    N.A.: 0.7

Compute ZP Spot Size: 285.714 um    Compute Number of Zones: 80    Compute Diameter of ZP: 78.4157 um

**Plot Options**

Plot ZP    Plot Zone Widths

**Options for ebeam writing ZPs in VS-2A**

☒ Create Zone Plate + Alignment Marks .pat file?    Name of Zone Plate + Marks .pat file (include .pat): VS26\_ZP.pat    E-beam bias of zones (nm): 50    E-beam field (um): 100

☐ Create Big Circle .pat file?    Name of Circle (include .pat): .pat    Compute e-beam pixel size: 6.10352 nm    Extra dose % of last zone: 0    Type of gradation (1=linear, 3=cubic, etc): 1

Press for alignment-marks options

**Plot Options for .pat files**

☐ Plot ZP    ☐ Plot Zone Widths    ☐ Plot Big Circle + Marks

Run

**4 Alignment Marks will be placed at the corners of the e-beam field**

Marks distance from corner of field (in um)

X-Coord (um): 4    Y-Coord (um): 4

Select type of mark

☐ Rectangles    ☐ Cross

**Horizontal Bar**

X-Width (um): 1    Y-Width (um): 1    X-Width (um): 1.5    Y-Width (um): 0.5

**Vertical Bar**

X-Width (um): 0.5    Y-Width (um): 1.5

Done

**Figure A - 2.** Screenshot capture of the interface of the software program capable of generating zone plates for the VS-26 scanning-electron-beam lithography system. Once all parameters have been chosen, the program is executed by clicking the Run button. This will generate the desired .pat file (in the example shown in the figure, a file called VS26\_ZP.pat will be created). Comments: (1) Choose an e-beam field size bigger than the zone plate diameter, (2) make sure the *Create Zone Plate... .pat file?* box is checked for the file to be created. The alignment marks (located at the four edges of the field) will only be created if the *Press for Alignment Marks Options* button is pressed and one of the two alignment-mark options (rectangles or crosses) is selected, (3) E-beam bias of the zones accepts positive and negative values, (4) *Extra dose % last zone* provides a form of proximity effect correction (see section 3.2.2.1). (4) If the box of *Create Big Circle .pat file?* is checked and a filename is input, a circle the size of the zone plate will be created. This pattern is necessary for both the *Silicon Process* and the *Chromium Process* (described in Chapter 3).

## A.2 Fabrication by means X-Ray Lithography

1. Start with a clean x-ray mask
2. Evaporate plating base. For all the masks fabricated in this work a “thin-plating base” was used, consisting of 10nm of Ti and 1.8nm of Au.
3. Spin resist, typically PMMA (~250nm).



- a. For PMMA, bake mask in oven at 180°C for 1 hour
4. E-beam write mask, as described in A.1.
5. Flood-expose optically with the OAI the rims of mask (i.e. all areas except the membrane). In our lab this is typically referred to as a “lollipop” exposure, in reference to the shape of the fixture that can be used for this step (the metal fixture is typically by the OAI). A 30 min exposure is more than enough to expose all the resist sitting on top of the Pyrex ring. This optical exposure (once developed) will allow for a clean electrode contact in the plating step.
6. Develop the x-ray mask. Mix the developer (1:2 MIBK:IPA) in a beaker big enough to fit the mask. The temperature should drop to 16°C upon mixing. The developing temperature is 21°C. To get to this temperature warm beaker with hands while monitoring the temperature. Have the beaker covered to prevent the evaporation of MIBK. Develop for 90 sec. Rinse for 60 sec with IPA + 60 sec H<sub>2</sub>O.
7. UV-Ozone for 30sec. Rinse in H<sub>2</sub>O and blow dry. The mask is ready for plating.
8. Electroplate the x-ray mask. To give an idea of plating rates and parameters utilized, the plating sequence of an x-ray mask containing arrays of zone plates is included in Figure A-3. The plating is monitored by means of an atomic-force microscope (AFM).
9. Remove the resist once the desired plating height has been achieved (~200nm of Au is a good goal). For PMMA, an acetone bath for 10min will do it. Ashing is another alternative.
10. Evaporate studs (typically ~3μm tall) onto the mask.
11. The x-ray mask can now be used in an x-ray lithography system to create and/or replicate zone plate arrays.

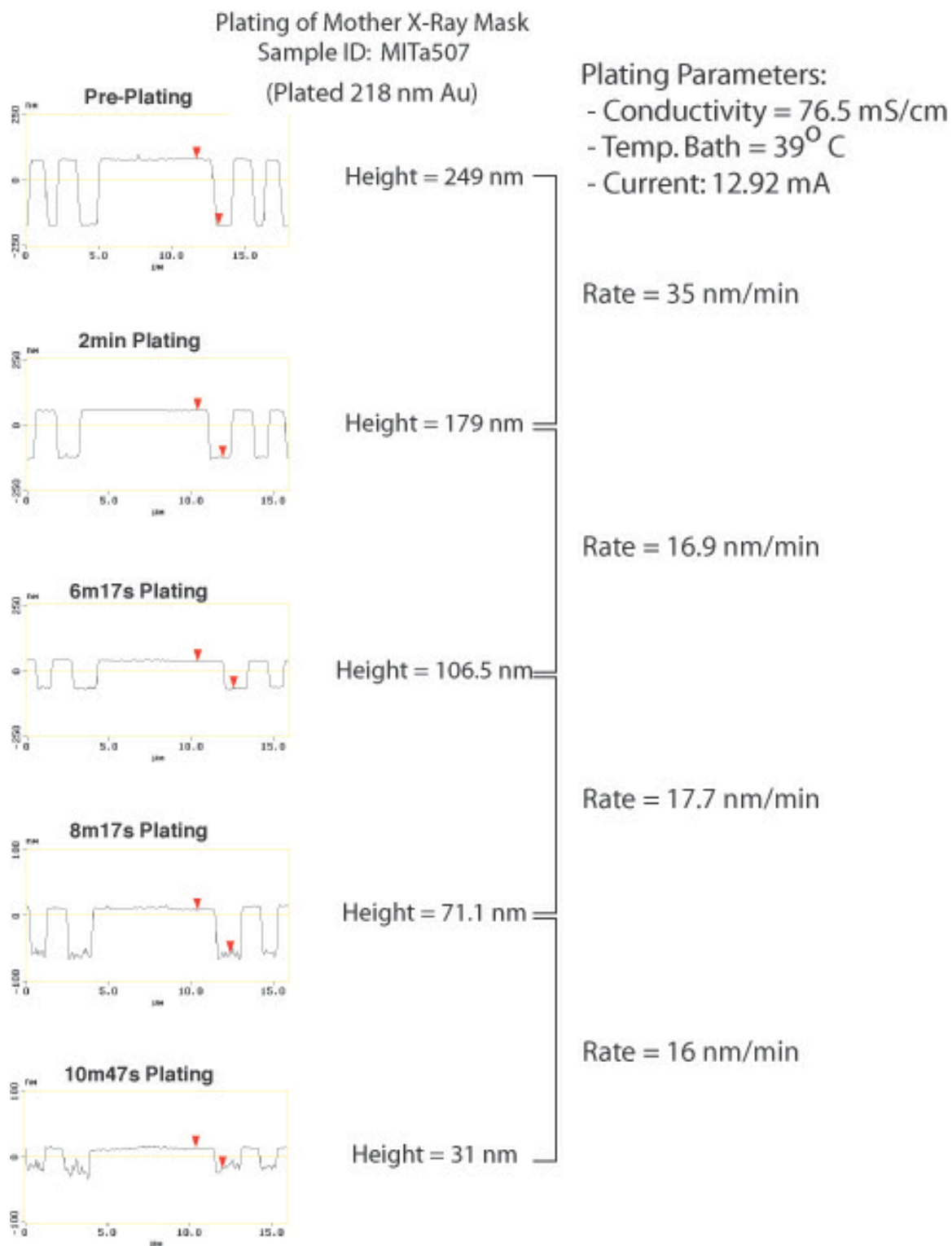


**Figure A - 3.** Sample gold electroplating of x-ray mask containing arrays of zone plates. The plating is monitored by means of an atomic-force microscope (AFM) throughout the process.

# References

## C h a p t e r 1

- [Ref 1-1] Michael Lewis, *The New New Thing*, W.W. Norton & Company; 1999.
- [Ref 1-2] Clayton M. Christensen. *The Innovator's Dilemma*, Harper Business, 200
- [Ref 1-3] H. C. Manoharan, C. P. Lutz, D. M. Eigler, Quantum mirages formed by coherent projection of electronic structure, *Nature* 403, 512 - 515 (2000)
- [Ref 1-4] Bass et al, "The Future of the Microprocessor Business, *IEEE Spectrum*, April 2002].
- [Ref 1-5] Alfred Kwok-Kit Wong, *Resolution Enhancement Techniques in Optical Lithography*, SPIE Press 2001
- [Ref 1-6] Anton, P.S., Silberglitt, R, Schenider, J, *The Global Technology Revolution*, National Defense Research Insitute, RAND Corporation (www.rand.org)
- [Ref 1-7] G.E.Moore, "Cramming More Components onto Integrated Circuits", *Electr.Mag.*, 114 (19 April 1965)
- [Ref 1-8] "DuPont to cut mask costs by dividing offering", *EE Times*, July 24, 2002
- [Ref 1-9] Freye, Jorge, *The Impact of the Photomask on Design* -- *Electronic News*, 6/3/2002
- [Ref 1-10] Willson, C. Grant, Dammel, Ralph A, and Reiser, Arnost, *Photoresist Materials: A Historical Perspective*, SPIE Vol.3049, pg.28-41, 1997.
- [Ref 1-11] <http://www.micronic.se>
- [Ref 1-12] <http://www.amat.com>
- [Ref 1-13] Allen, Paul, DUV Laser Scanning for Mask Pattern Generation at the 130 and 100nm Nodes, White Papers, [www.amat.com](http://www.amat.com)
- [Ref 1-14] E.Spiller, *Soft X-Ray Optics*, pg. 5, SPIE, Bellingham, WA, 1994.
- [Ref 1-15] J.Bjorkholm, "EUV Lithography-The Successor to Optical Lithography?", *Intel Technology Journal* Q3, 1998.]

- [Ref 1-16] E.Spiller, Soft X-Ray Optics, pg. 5, SPIE, Bellingham, WA, 1994.
- [Ref 1-17] N.Choksi et al., "Maskless extreme ultraviolet lithography", J.Vac.Sci.Technol. B 17(6), Nov/Dec 1999
- [Ref 1-18] D.A.Buck and K.R.Shoulders, Proceedings of the Eastern Joint Computer Conference, 1958],
- [Ref 1-19] A.N.Broers and M.Hatzakis, Scientific American 227, 34 (1972)).
- [Ref 1-20] M. McCord, "Electron beam lithography for 0.13 $\mu$ m manufacturing", J.Vac Sci. Technol. B 15(6), Nov/Dec 97
- [Ref 1-21] T.R.Groves and R.A.Kendall, J.Vac Sci. Technol. B 16(6), Nov/Dec 98.
- [Ref 1-22] H.Yasuda, S.Arai,J. Kai, Y. Ooae, T. Abe, S. Maruyama, and T.Kiuchi, J.Vac. Sci. Technol. B 14, 3813 (1996)
- [Ref 1-23] T.H.P. Chang, M.G.R. Thomson, E. Kratschmer, H.S. Kim, M.L. Yu, K.Y. Lee, S.A. Rishton, and B.W. Hussey,"Electron-beam microcolumns for lithography and related applications", J.Vac. Sci. Technol. B 14, 3774 (1996)
- [Ref 1-24] T.R.Groves and R.A.Kendall, J.Vac.Sci.Technol. B 16(6), Nov/Dec 1998
- [Ref 1-25] T.H.P.Chang et al. J.Vac.Sci.Technol. B 14, 3774 (1996)
- [Ref 1-26] S.T.Coyle et al, J.Vac.Sci.Technol. B 20(6), 2657 (2002)
- [Ref 1-27] P.Kruit, J.Vac.Sci.Technol. B 16(6), 3177 (1998)
- [Ref 1-28] <http://www.mapperlithography.com>
- [Ref 1-29] J. T. Hastings, Michael H. Lim, J. G. Goodberlet, and Henry I. Smith, "Optical Waveguides with Apodized Sidewall Gratings via Spatial-Phase-Locked E-Beam Lithography.". J.Vac.Sci.Technol B 20(6), Nov./Dec.2002, 2753-2757.

## C h a p t e r   2

- [Ref 2-1] Doak RB et. al, Physical Review Letters, 83 (21): 4229-4232, 1999
- [Ref 2-2] Henry I. Smith. *A proposal for maskless, zone-plate-array lithography*. J.Vac.Sci.Technol. B, 14(6):4318-4322, Nov/Dec 1996.
- [Ref 2-3]Ihsan J. Djomehri,*Zone-Plate-Array Lithography in the Deep UV*, Master's Thesis, Massachusetts Institute of Technology,1998
- [Ref 2-4]Ihsan J. Djomehri,T.A.Savas, and Henry I. Smith, *Zone-plate-array lithography in the deep ultraviolet*, J.Vac.Sci.Technol. B, 16(6):3426-3429,Nov/Dec 1998.
- [Ref 2-5] D. J. D. Carter, Dario Gil, Rajesh Menon, Mark K. Mondol, H. I. Smith and E. H. Anderson, *Maskless parallel patterning with zone-plate-array lithography*, J.Vac.Sci.Technol. B 17 (6), Nov/ Dec, 1999

[Ref 2-6] Digital Light Processing World Wide Web site: <http://www.dlp.com/>

[Ref 2-7] White papers on Silicon Light Machines GLV technology:  
<http://www.siliconlight.com/htmlpgs/glvtechframes/glvmainframeset.html>

[Ref 2-8] Feldman, M, OSA Proceedings on Soft X-Ray Projection Lithography, 1993, Vol.18

[Ref 2-9] Dario Gil, Rajesh Menon, D. J. D. Carter and H. I. Smith, *Lithographic Patterning and Confocal Imaging with Zone Plates*, J.Vac.Sci.Technol B 18 (6), 2881-2885, Nov/ Dec, 2000

### Chapter 3

[Ref 3-1] *Euvres Completes d'Augustin Fresnel*, Vol. 1, Note 1, pp. 365-372 (1886).

[Ref 3-2] E.Hecht, Optics, Addison-Wesley Publishing (1987).

[Ref 3-3] Max Born and Emil Wolf, Principles of optics, Pergamon Press, 1984.

[Ref 3-4] Rajesh Menon, Diffractive Optics for Mask less Lithography and Imaging, PhD Thesis, M.I.T., June 2003

[Ref 3-5] Myers Jr, Ora E., American Journal of Physics, Vol. 19(6), pp. 359-365 (1951).

[Ref 3-6] Baez, Albert V., Journal of the Optical Society of America, Vol. 51(4), pp. 405-412, April 1961

[Ref 3-7] Baez, Albert V., Journal of the Optical Society of America, Vol. 51(4), pp. 405-412, April 1961

[Ref 3-8] Spiller, E, Soft X-Ray Optics, pp 90-91, SPIE Press, 1994

[Ref 3-9] F.Vasey et al, J.Vac.Sci.Technol.] B 12(6) Nov/Dec 1994

[Ref 3-10] Todd Hastings, Nanometer-Precision Pattern Placement and Applications in Integrated Optics, Ph.D. Thesis, M.I.T., June 2003

[Ref 3-11] Henry I. Smith, Submicron and Nanometer –Structures Technology, 2<sup>nd</sup> edition, NanoStructures Press, Sudbury (1994)

[Ref 3-12] D.L. Spears and H.I. Smith, "High-Resolution Pattern Replication using Soft X-rays", Electronics Lett. 8, 102-104 (1972)

[Ref 3-13] D.L. Spears and H.I. Smith, "X-ray Lithography: A New High Resolution Replication Process", Solid State Technol. 15, No. 7, 21-26 (1972).

[Ref 3-14] D.Attwood, *Soft X-rays and Extreme Ultraviolet Radiation*, pg. 408, Cambridge University Press, 1999.

[Ref 3-15] H.I. Smith, M.L. Schattenburg, S.D. Hector, J. Ferrera, E.E. Moon, I.Y. Yang, and M. Burkhardt, "X-ray Nanolithography: Extension to the Limits of the Lithographic Process", Microelectronic Engineering 32, 143-158 (1996).

[Ref 3-16] L.E.Ocola and F.Cerrina, J.Vac. Sci. Technol. B 12, 3986 (1994) & H.I.Smith, J.Vac. Sci. Technol. B 13, 2323 (1995)

[Ref 3-17] D.Attwood, *Soft X-rays and Extreme Ultraviolet Radiation*, pg. 410, Cambridge University Press, 1999

[Ref 3-18] Ken-ichi Murooka, Michael H. Lim, and Henry I. Smith, J. Vac. Sci. Technol. B 18, 2966 (2000); Ken-ichi Murooka et al, J. Vac. Sci. Technol. B 19, 1229 (2001)

[Ref 3-19] G. Schneider, T. Schliebe, and H. Aschoff, J. Vac. Sci. Technol. B **13**, (1995)

[Ref 3-20] E.Anderson et al, "*Nanofabrication and diffractive optics for high-resolution x-ray applications*", J. Vac. Sci. Technol. B **18**(6), pp. 2970-2975, 2000.

[Ref 3-21] T. Tanaka, M. Morigami, and N. Atoda, Jpn. J. Appl. Phys. **32**, 6059 (1993)

[Ref 3-22] Azalia A. Krasnoperova, et al J. Vac. Sci. Technol. B 13(6), Nov/Dec 1995

[Ref 3-33] Fulton et al, Appl.Phys.Lett., Vol 42, No.8, 15 April 1983.

[Ref 3-34] Dolan et al, IEEE Electron Device Letters, Vol. EDL-4, No.6, June 1983

[Ref 3-35] <http://www.etec.com>

[Ref 3-36] Aboud, F. et al, “*Raster Scan Patterning Solution for 100nm and 70nm OPC masks*”, White Paper, [http://www.appliedmaterials.com/products/mask\\_technical\\_papers.html](http://www.appliedmaterials.com/products/mask_technical_papers.html)

[Ref 3-37] Stephen Y. Chou, Peter R. Krauss, Wei Zhang, Lingjie Guo, and Lei Zhuang, “*Sub-10 nm imprint lithography and applications*,” J. Vac. Sci. Technol. B 15, 2897 (1997)

## Chapter 4

[Ref 4-1] Kwok-Kit Wong A., Resolution Enhancement Techniques in Optical Lithography, SPIE Press, Bellingham, Washington, 2001

[Ref 4-2] M.Born and E.Wolf, *Principles of Optics*, Cambridge Univ. Press, New York 1999, 7<sup>th</sup> Ed, pp.441

[Ref 4-3] M.Minsky, US patent 3,013,467, 19 Dec 1961, filed 7 Nov. 1957.

[Ref 4-4] H.J.Tiziani, R.Achi, R.N.Kramer and L.Wiegers, "Theoretical analysis of confocal microscopy with microlenses." Appl. Opt. 35(1). 120-125 (1996).

[Ref 4-5] Rajesh Menon, Optimum volume-holographic confocal microscope: Area Exam Report. Technical Report, 2002. MIT.

## Chapter 5

[Ref 5-1] <http://www.powertechnology.com>

[Ref 5-2] <http://www.conoptics.com>

[Ref 5-3] White papers on Silicon Light Machines GLV technology:  
<http://www.siliconlight.com/htmlpgs/glvtechframes/glvmainframeset.html>



[Ref 5-4] White papers on Silicon Light Machines GLV technology:

<http://www.siliconlight.com/htmlpgs/glvtechframes/glvmainframeset.html>

[Ref 5-5] D.T.Amm and R.W.Corrigan, "Optical performance of the grating light valve technology", Projection Displays, V.M.H.Wu ed., Proc.SPIE 3634, 71-78 (1999).

[Ref 5-6] J.A.Hoffnagle and C.M.Jefferson, Applied Optics, Vol.39, No.30, 2000.

[Ref 5-7] J.L.Kreuzer, U.S. Patent 3,476,463, 4 November 1969

[Ref 5-8] Dario Gil, Rajesh Menon, D.J.D. Carter, and Henry I. Smith, "Lithographic Patterning and Confocal Imaging with Zone Plates." *Journal of Vacuum Science and Technology B* **18**(6), 2881-2885, Nov/Dec 2000

[Ref 5-9] A. Murray, F. Abboud, F. Raymond, and C. N. Berglund, J. Vac. Sci.Technol. B 11, 2390 (1993)

[Ref 5-10] F. Abboud et al., Photomask and X-ray Mask Technology IV, Proc. SPIE Vol. 3096 (SPIE Bellingham, WA, 1997), pp. 116–124.

[Ref 5-11] R. Dean, D. Alexander, J. Chabala, T. Coleman, C. Hartglass, M. Lu, C.Sauer, and S. Weaver, 15th European Conference on Mask Technology for Integrated Circuits and Microcomponents '98, Proc. SPIE Vol. 3665 (SPIE, Bellingham, WA, 1999), pp. 166–178.

[Ref 5-12] M. L. Rieger, J. A. Schoeffel, and P. A. Warkentin, Laser Microlithography, Proc. SPIE Vol. 922 (SPIE, Bellingham, WA, 1988), pp. 55–64.

[Ref 5-13] B. J. Grenon, D. C. Defibaugh, D. M. Sprout, H. C. Hamaker, and P. D.Buck, 14th Annual BACUS Symposium on Photomask Technology and Management, Proc. SPIE Vol. 2322 (SPIE, Bellingham, WA, 1994), pp.50–55.

[Ref 5-14] D.J.D. Carter, Dario Gil, Rajesh Menon, Mark K. Mondol, Henry I. Smith, and Erik H. Anderson, "Maskless, Parallel Patterning with Zone-Plate Array Lithography." *J. Vac. Sci. Technol. B* **17**(6), 3449-3452, Nov/Dec 1999.

[Ref 5-15].Rajesh Menon, Diffractive Optics for Mask less Lithography and Imaging, PhD Thesis, M.I.T., June 2003

## *Chapter 6*

[Ref 6-1] L. Kipp, et al, Nature, vol. 414, pp184-188, 8 November, 2001

[Ref 6-2] J. W. Goodman, Introduction to Fourier Optics” , McGraw Hill, pp 151-154, (1996).

[Ref 6-3] Ozden I, Diagne M, Nurmikko AV, Han J, Takeuchi T, Physica Status Solidi A-Applied Research, 188 (1): 139-142 Nov (2001)